CZECH TECHNICAL UNIVERSITY IN PRAGUE
Faculty of Electrical Engineering
Department of Control Engineering

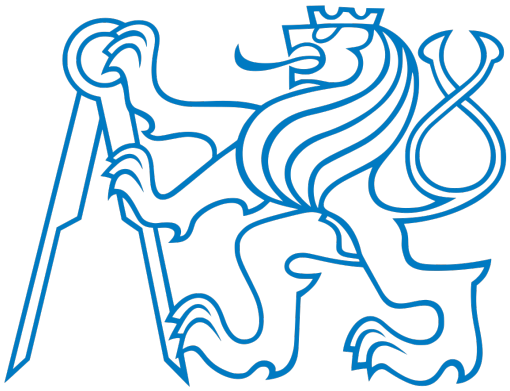

DOCTORAL THESIS

April 2021

Victor E.P. Claerbout

CZECH TECHNICAL UNIVERSITY IN PRAGUE
Faculty of Electrical Engineering
Department of Control Engineering

SOLID LUBRICANTS AT THE NANOSCALE

Frictional behavior *in silico*

DOCTORAL THESIS

by

Victor Emile Phillippe Claerbout

Prague, April 2021

Ph.D. Program:

P0533D110030 APPLIED PHYSICS

supervision

Dr. Paolo Nicolini

The important thing is not to stop questioning. Curiosity has its own reason for existence. One cannot help but be in awe when he contemplates the mysteries of eternity, of life, of the marvelous structure of reality. It is enough if one tries merely to comprehend a little of this mystery each day.

Albert Einstein

Acknowledgments

I dedicate this thesis to my parents,
Fons & Mariëtte.

In the first place, I would like to thank the board of examiners and my opponents for the honor of evaluating my work.

A Paolo, 3 anni e mezzo fa sei diventato il mio supervisore. Ho avuto la possibilità di conoscerti come uno scienziato stimolante, entusiasta e dedicato, ma soprattutto come una persona molto paziente - la qual cosa è notevole, considerate tutte le mie 'solo una domanda veloce'. Sono così grato per tutto il sostegno che mi hai dato e per il fatto che hai creduto in me. Ho appreso da te il mio scopo, non solo riguardo la mia vita professionale; sono lieto di averti conosciuto ed è stato un onore essere un tuo studente. E adesso ti meriti una vacanza!

Štěpě, nebo bych měl říct Mamažerce skupiny, děkuji za organizování mých služebních cest. Děkuji za to, že mě dokázala rozptýlit pokaždé, když jsem potřeboval přestávku. Děkuji za všechnu tu čokoládu. Děkuji za to, že mě přesvědčila, že potřebuji Birbu. Děkuji za všechny ty pěkné výlety, který jsme podnikli. Děkuji za to, že mi ukázala Českou republiku. Děkuji za to všechno!

To Ben, my friend thank you for being and regarding my thesis for your help I thank you. Fond memories of our trip to England I have and forward to Scotland I look. All the best, Yoda

To Tomáš and all my fellow lubricating Minions of the AMG group, thank you for challenging me in a scientific way, a great working environment, and for all the beers on Little Friday.

To the students of SOLUTION, thank you for the amazing conferences, collaborations, and trips. A special thank you to Andrea, I am grateful that we have been able to combine friendship and work into a successful publication and look forward to our next trip!

To my friends from Prague, Katja, Diana, Wouter, Hugo, Leonie, Isold, and Heleen, you have made these past years fly by! Thank you for the amazing memories that I have from our party nights, trips, dinners, and talks. By now, almost like an omen, our times in Prague have for all of us come to an end, but our friendship will prevail. Ondro, chudáku, byl jsi se mnou během nejvíce stresující části mého doktorandského studia, muselo to pro tebe být trochu 'disappointing'. Vážím si toho a těším se na všechna naše budoucí dobrodružství! Ještě jednou moc děkuji.

To my other friends, after five long years, I am finally coming home! I am grateful that all of you have always supported me in following my ambitions.

Finally, aan mijn ouders, broertje en Birba, de afgelopen jaren zijn een rollercoaster geweest maar als het puntje bij paaltje kwam waren we er voor elkaar. Zonder jullie had ik dit nooit bereikt, deze titel is voor ons allemaal!

Abstract

Friction and wear occur when two surfaces are in contact and relative motion, and are considered responsible for approximately 23% of all energy consumed. The types of materials in contact and environmental conditions, such as temperature and humidity, are highly correlated with friction and wear. Introducing a lubricant into the sliding contact can help reduce (or even eliminate) friction, wear, and associated processes – a technique dating as far back as Ancient Egypt. Common everyday classical wet lubricants are either oil- or water-based. However, increasingly strict sustainability standards and rising demands of our modern industrial society have surpassed the application of these wet lubricants in severe operating conditions, such as extremely high/low contact pressures and working temperatures or when used in nanoscale devices.

Starting from the 1940s, solid lubricants, which are layered crystalline materials, have received substantial attention due to their excellent frictional properties. To date, they have mainly been used as additives to impart improved lubrication properties to lubricants. Transition metal dichalcogenides are some of the best-known examples of solid lubricants, of which molybdenum disulfide (MoS_2) is considered prototypical. When applied as a coating (as opposed to an additive), they have the potential to overcome a vast number of problems encountered by wet lubricants. Despite the considerable scientific effort, large-scale industrial implementation of MoS_2, and solid lubricants in general, has not been achieved. A combination of problems lies at the origin of this. We do not possess a fundamental understanding of the actual frictional mechanisms of layered systems, both at the nanoscale and macroscale. Moreover, solid lubricants are highly sensitive to deterioration resulting from interactions with their environments, limiting the exploitation of their promising potential in a wide range of applications.

In this thesis, we make an effort towards elucidating the mechanisms that determine the frictional properties of MoS_2 at the nanoscale by employing computational modeling. This is done by investigating the intrinsic frictional aspects of MoS_2, for example, by studying frictional anisotropy, and considering the effect of external conditions such as water contamination, which is commonly known to deteriorate the frictional properties of MoS_2. The use of prototypical materials allowed us to provide new understandings in the application and design of solid lubricants in general. Novel insights were obtained on the principles of achieving superlubricity in homostructures, where the relevance of the interlayer potential energy surface topology was once more confirmed. Additionally, the results on water contamination highlight the effect of interlayer intercalation of water on the frictional properties of solid lubricants and thus guide the design of nanoscale devices in ambient conditions.

Since 2004 single-layer solid lubricants have been readily available, which has opened the door to a new class of materials, so-called heterostructures. These are layered structures that combine several different types of solid lubricants. Although heterostructures create the potential for tuning the properties of solid lubricants, the actual stability of these structures is often left out of consideration. Therefore, in this work, the twist angle energetic stability of a prototypical heterostructure built from MoS_2 and graphene is extensively explored through epitaxy theory. Our study on heterostructures reveals new insights into the observations made in experiments and the stability of twistronic devices. In conclusion, this thesis has actively contributed to making the next step for large-scale industrial implementation of solid lubricants feasible.

Key Words

friction, tribology, solid lubricants, transition metal dichalcogenides,
molybdenum disulfide, heterostructures, molecular dynamics simulations

Abstrakt

Tření a opotřebení nastává, když jsou dva povrchy v kontaktu a relativním pohybu, a představují přibližně 23 % veškeré spotřebované energie. Použití maziva v kontaktu může snížit (nebo dokonce téměř eliminovat) tření, opotřebení a související procesy. Jedná se o techniku sahající až do starověkého Egypta. Běžná každodenní klasická maziva jsou na bázi oleje nebo vody. Stále přísnější ekologické standardy však omezují další používání olejů, a v náročných provozních podmínkách, jako jsou extrémně vysoké/nízké kontaktní tlaky a pracovní teploty, tekutá maziva nemůžeme používat. Od 40. let 20. století se tuhým mazivům, což jsou vrstvené krystalické materiály, věnuje značná pozornost. Dnes se používají hlavně jako přísady, které tekutým mazivům zlepšují vlastnosti. Dichalkogenidy přechodových kovů jsou některé z nejznámějších příkladů tuhých maziv, z nichž je disulfid molybdenu (MoS_2) hlavní reprezentant. Tyto materiály mají potenciál nahradit tekutá maziva v mnoha aplikacích, a to formou tenké vrstvy. Navzdory značnému vědeckému úsilí však zatím nebylo dosaženo průmyslové implementace MoS_2 a pevných maziv obecně. Důvodem je malá znalost třecích mechanismů vrstevnatých systémů, a to jak v nanoměřítku, tak v makroměřítku. Kromě toho jsou tuhá maziva vysoce citlivá na poškození způsobená interakcemi s jejich prostředím, což omezuje využití jejich slibného potenciálu v široké škále aplikací.

V této práci se pomocí výpočetního modelování snažíme objasnit mechanismy určující třecí vlastnosti MoS_2 v nanoměřítku. To se provádí zkoumáním třecích aspektů MoS_2, například studiem frikční anizotropie a zvážením vlivu vnějších podmínek, jako je kontaminace vodou, o níž je obecně známo, že zhoršuje třecí vlastnosti MoS_2. Byly získány nové poznatky o principech dosažení superlubricity v homostrukturách, a byla potvrzena relevantnost povrchové energie mezivrstvy. Studium interakce s vodou prokázalo interkalaci vody na třecí vlastnosti tuhých maziv.

V tomto tisíciletí jsou dostupná i jednovrstvá tuhá maziva, které otevřely dveře nové třídě materiálů, takzvaným heterostrukturám. Jedná se o vrstvené struktury, které kombinují několik různých typů tuhých maziv. Ačkoli heterostruktury mají potenciál dalšího vylepšení vlastností tuhých maziv, skutečná stabilita těchto struktur je často vynechána. V této práci je proto pomocí teorie epitaxe rozsáhle prozkoumána energetická stabilita úhlu natočení prototypové heterostruktury postavené z MoS_2 a grafenu. Naše studie o heterostrukturách odhaluje nové poznatky o stabilitě těchto struktur a pomohla vysvětlit experimentálně naměřené vlastnosti.

Klíčová Slova

tření, tribologie, pevná maziva, dichalkogenidy přechodových kovů,
disulfid molybdenu, heterostruktury, simulace molekulární dynamiky

Contents

1 Introduction **1**

1.1 Friction 2

1.1.1 Friction Laws 3

1.1.2 Nanotribology 4

1.1.3 Nanoscale Friction Laws 7

1.1.4 Friction Force Microscopy 9

1.1.5 Stick-Slip Dynamics 10

1.1.6 The Prandtl-Tomlinson Model 11

1.2 Lubricants 14

1.2.1 Solid Lubricants 16

1.2.2 Transition Metal Dichalcogenides 17

1.2.3 Graphite and Graphene 20

1.2.4 Van der Waals Heterostructures 22

1.3 Superlubricity 24

1.3.1 Structural Superlubricity 26

1.4 Aims & Outline 30

2 Computational Methods **33**

2.1 Quantum Mechanics 35

2.1.1 Density Functional Theory 36

2.2 Molecular Mechanics 39

2.2.1 Force Fields 39

2.2.2 Molecular Dynamics 45

2.3 In brief 52

3 Pure MoS_2 **53**

3.1 Introduction 53

3.2 Approaches and Problems 55

3.3 Results and Outlook 57

4 MoS_2 & Graphene **67**

4.1 Introduction 67

4.2 Approaches and Problems 69

4.3 Results and Outlook 75

5 MoS_2 & Water **85**

5.1 Introduction 85

5.2 Approaches and Problems 87

5.3 Results and Outlook 89

6 MoS_2 & Diamond 111

6.1 Introduction 111

6.2 Approaches and Problems 112

6.3 Results and Outlook 114

7 Conclusions 119

8 List of Publications 123

8.1 Published Works within the Scope 124

8.2 Submitted Works within the Scope 124

8.3 Published Works outside the Scope 125

Bibliography 126

A SI. Pure MoS_2 143

B SI. MoS_2 & Graphene 149

C SI. MoS_2 & Water 173

D Viewpoint 177

E Joint Study AFM & MD 221

1

Introduction

Estimates indicate that friction and wear are responsible for approximately 23% of the worlds' total energy consumption [1]. The related financial cost and everyday increasing sustainability standards demand a solution. To this end, lubricants can be used to reduce the amount of energy that is lost in processes where friction and wear occur. Historical evidence has shown that lubricants were already used in Ancient Egypt [2, 3]. Generally speaking, we can distinguish between two main classes of lubricants, namely *classical wet lubricants* and novel *dry solid lubricants.* Common everyday classical wet lubricants are either oil- or water-based. Despite their success in the past, the criteria of our modern industrial society have reached their limits of efficient and practical implementation. All sorts of demanding operating conditions present an array of problems to liquid lubricants, e.g., low temperatures resulting in freezing, high temperatures resulting in evaporation, ultra-high vacuum resulting in boiling, ultra-high pressures, or strict confinement in small devices resulting in

solidification. Dry solid lubricants, not to be mistaken with greases, are materials that have exceptional lubricating properties despite being solid. Among others, the most commonly known solid lubricants are graphite and transition metal dichalcogenides (TMDs), of which molybdenum disulfide (MoS_2) can be considered prototypical. They have been studied since the 1940s [4] and their frictional properties are most commonly attributed to their characteristic layered crystal structure. In general, solid lubricants are used as particles dispersed into a liquid, in which the liquid itself can be acting as a lubricant, a 'carrier', or both. More recently, solid lubricants have received substantial attention when used as a lubricating coating, rather than as an additive. As a coating, solid lubricants have the potential to overcome a vast number of problems encountered by wet lubricants. However, despite their enormous potential [5, 6], a large-scale industrial implementation remains elusive. Although this cannot be pinpointed to a single problem, two aspects play a critical role. On the one hand, there is a lack of fundamental understanding of the actual frictional mechanisms of layered systems, both at the nanoscale and macroscale. On the other hand, solid lubricants are highly sensitive to deterioration due to interactions with their environments, limiting the exploitation of their promising potential in a wide range of applications.

The research presented herein elucidates key aspects of the lubrication mechanisms that determine the frictional properties of MoS_2 at the nanoscale through computational modeling. We apply a bottom-up approach, using nanoscale friction as a starting point, from which conclusions may (possibly) be drawn at the macroscale. In this chapter, an overview of the current state of the art will be provided, with an aim of answering two crucial questions: 'what is nanoscale friction?' and 'how can we reduce friction with solid lubricants at the nanoscale?'

1.1 Friction

Plainly said, the goal of this thesis is to study friction. Therefore, let us first define friction. From a scientific point of view, friction, and to be more specific,

dry friction, is a force that thwarts (effectively opposes) the relative motion between two solid surfaces in contact. We distinguish two types of friction, namely *static friction* and *kinetic friction*. One speaks of static friction before an actual motion occurs and of kinetic friction once the two surfaces are in relative motion. Here, the focus will mainly be on kinetic friction, and 'kinetic friction' and 'friction' are used interchangeably. Friction belongs to the wider field of *tribology*, i.e., the study of 'rubbing' – or more specifically, surfaces that are in contact and relative motion – as defined by Jost *et al.* [7]. To illustrate these phenomena, consider the macroscopic example of riding a bike. To stop for a red light, you press the brakes of your bike, causing the rim of the wheel and the brake pad to be in 'contact with' and 'relative motion to' each other, reducing your velocity. In this case, the rim and the brake pad together form a so-called *tribological contact*. Most likely, one has an idea of why one slows down, 'simply' because of the 'friction' between the rim and the brake pad. From this macroscopic point of view, the point where friction occurs can be readily located. However, it does not tell us anything about the origin of this phenomenon. Incisive questions that could now be asked are: Why is the velocity lost when the rim and the brake pad are in contact? Why does the type of materials used influence the velocity decrease? Why is the velocity decrease greater when the brakes are pressed harder? To help to understand and to answer such questions, several laws and models have been derived, of which the most relevant ones for the works presented here will be discussed.

1.1.1 Friction Laws

In the macroscopic world, one way to estimate friction is by the *Amontons-Coulomb (AC) law* [8, 9, 10], the foundations of which were established in 1699 – albeit many years after Da Vinci had first recorded similar observations and relations [11]. The AC law combines three empirical laws:

1. The frictional force and the normal force are proportional,
2. The frictional force is independent of the apparent contact area,
3. The frictional force is independent of the sliding velocity.

In all the works presented here, the normal force is defined as a force acting on the system perpendicularly to the sliding interface; in our reference systems, it acts in the z-direction. The normal force (in Newtons, $1\ N = 1\ kg \cdot m \cdot s^{-2}$) is related to the load (in Pascals, $1\ Pa = 1\ kg \cdot m^{-1} \cdot s^{-2}$) by the area it is acting on:

$$\text{Force / Area} = \text{Load}. \tag{1.1}$$

These laws can be visualized by considering a book lying flat on a table. The friction that is experienced while moving the book over the table is proportional to the weight of the book. The friction is, however, independent of whether the book is lying flat on the table or positioned on its edge. The same accounts for the velocity at which the book is moved. The AC law now states that:

$$F_x = \mu_x F_n, \tag{1.2}$$

with F_x the frictional force, μ_x the coefficient of friction (COF), and F_n the normal force [12]. Here, the subscript x can either relate to static friction or kinetic friction. The COF, a dimensionless parameter, contains all details about the tribological contact, internal properties, such as the type of materials, and the external conditions, such as temperature. Despite some exceptions, the static COF is, in general, larger than the kinetic one [11, 12]. One of the implications of Eq. 1.2 is that when the normal force is zero, frictional forces should be absent. Therefore, in the case of adhering surfaces, an adapted equation should be used [13]:

$$F_x = F_{0,x} + \mu_x F_n, \tag{1.3}$$

where $F_{0,x}$ is the frictional force at zero normal force as a result of adhesion.

1.1.2 Nanotribology

As was stated before, in this thesis, a bottom-up approach is used. This means that instead of considering the macroscopic world (length scales on the order of meters, as observed in daily life), the nanoscale (length scales on the order of angstroms – $10^{-10}\ m$ – at which we can distinguish atoms) is considered. This approach allows us to decompose frictional phenomena into

well-defined, readily calculable quantities that can be concatenated to produce a more complex 'macro'-sized system. For instance, in the earlier example with the rim and the brake pad, one might think of these surfaces as being flat, at least upon visual inspection at the macroscale, resulting in a single contact. However, they are almost certainly not flat, and will appear 'rough' when observed at the nanoscale [12]. As a result, instead of a single contact, it becomes clear that there is a multi-contact interface, where individual contacts or *asperities* interact with one another, as described in Fig. 1.1.

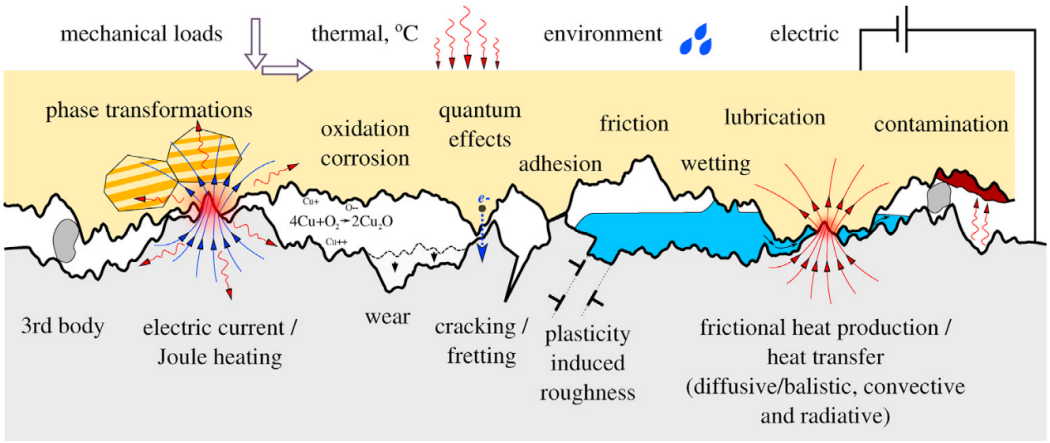

Figure 1.1: Schematic of the phenomena that can take place at the nanoscale when two rough surfaces are put into contact and brought into relative motion. Figure adapted from Ref. [12].

We started this introduction by relating friction to a 'cost', namely, a loss of energy, here this relation will be clarified in more detail. Consider an elementary example where two surfaces are in contact. Next, an external driving force is applied to one of the surfaces, causing a displacement. As a result, this driving force performs mechanical work (in Joule, $1\ J = 1\ kg \cdot m^2 \cdot s^{-2}$):

$$\text{Work} = \text{Force} \times \text{Displacement}. \tag{1.4}$$

Whenever friction is present, only part of the external driving force (and thus work) is converted into actual motion (kinetic energy) of the surface. The other part is used to overcome the frictional force that acts in the opposite direction due to the interaction with the other surface and possibly its surroundings. In

this case, the work consists of two components, $W_{\text{ext}} = \Delta E_{\text{kinetic}} + E_{\text{dissipated}}$. Here, $E_{\text{dissipated}}$ represents the irreversible loss of energy. In other words, frictional force is a dissipative force that performs work when the surfaces are in relative motion. If there is no dissipation, all external work is transformed into kinetic energy, and no friction is present. This automatically clarifies a big difference between static and kinetic friction. In the case of static friction, by definition, no motion occurs, and thus the static frictional force does not perform work, and no energy dissipation arises.

To transform a frictional force into dissipated energy, a so-called *channel of energy dissipation* needs to be present. Various examples are depicted in Fig. 1.1. For example, frictional force can be transferred to heat, phonon excitation, and plastic deformation. A somewhat counterintuitive observation is that not all channels increase friction. Consider, for example, a scenario where the system is thermally activated, either by its surroundings or by (prior) local heating within the tribological contact. Although the frictional properties might be influenced by this, in some instances, the thermal activation of the atoms might induce a decrease in friction during sliding [14]. That said, this observation is very system-specific, and opposite results have been published [15].

It becomes clear that the field of tribology is very complex due to the wide variety of possible physical phenomena that are taking place simultaneously. Whereas some processes occur on a short timescale, such as quantum effects, others require longer timescales, such as wear. Moreover, most of these phenomena are out-of-equilibrium processes, which are more challenging to study because standard thermodynamics no longer always applies [16]. If we consider the rim and brake pad contact at the nanoscale, practically, it is still impossible to directly correlate any observation with one or several of these physical phenomena. One way to circumvent this problem is to zoom in even further and consider only a single asperity, thereby entering the field of *nanotribology*. Using this approach, a single asperity can be considered as two atomically flat surfaces in contact. In practice, this means that system sizes are limited to tens of nanometres. This approximation underpins the approach of all studies carried out within this thesis, all of which aim to improve the

understanding of the mechanisms that determine dry friction at an atomistic level.

1.1.3 Nanoscale Friction Laws

While the AC law is widely used, a word of caution is necessary. Owing to its simplicity, it assumes that μ is constant, i.e., μ appears to be invariant with contact time or sliding velocity, which has already been proven to be false [11, 12, 17]. For static friction, μ increases with the time that the layers have been in contact before applying an external sliding force [18]. For kinetic friction, μ can increase or decrease with increasing sliding velocity, depending on the type of system and the length scale considered [11, 12]. Both phenomena are likely related to the fact that there exists a finite (instead of an instantaneous) formation time of the multi-asperity contact, forming the contact area [11, 12]. Several corrections can account for the issues, as reported above, resulting in the so-called *rate-and-state* friction laws, reported in the literature [12].

One might wonder if the AC law is also applicable at the nanoscale. The general consensus is that the AC relation does not hold on an atomistic level [11, 13, 19]. It is thought that the responses of the system to external factors, such as temperature, sliding velocity, and normal load, are closely related to the length scales at which they are considered. Conversely, some have argued or observed that the AC law might hold at the nanoscale [20, 21, 22]. According to AC, the frictional force should be independent of the macroscopic contact area. However, among others [19, 20], Bowden and Tabor [23] showed that there is a relation to the 'real' contact area. They found that if one considers the total area of the asperities instead of the total apparent contact area, the frictional force is proportional to, rather than independent of, the area. In other words, the frictional force seems to depend linearly on the true contact area (sum of the areas of the individual asperities), according to $F_{\text{fric}} = \tau \sum A_{\text{asperity}}$, where τ is the material-dependent shear strength[1] [20, 23]. As previously mentioned, due to the wide variety and complex na-

[1] Whereas shear stress is the deformation of a material due to external forces, the shear strength of a material defines its ability to resist deformation due to these external forces.

ture of the processes taking place at nanoscale multi-asperity contacts, the studies presented herein consider only single asperity contacts. However, at this length scale and only considering a single asperity, the AC relation no longer holds [19, 20], i.e., $F_{\text{fric}} \neq \tau A_{\text{asperity}}$. In a theoretical contribution, Mo *et al.* [20] showed that the linear AC relation might be valid at the nanoscale, given a correct definition of the area of contact. Their approach is similar to what was done at the macroscale. Instead of considering the total area of the asperity, they consider the sum of the contact areas per atom within the asperity, resulting in the following relation: $F_{\text{fric}} = \tau \sum A_{\text{atom}}$ (see Fig. 1.2). Moreover, their simulations show that $\sum A_{atom}$ is proportional to the load, and they therefore recover the original AC relation. One remark, however, is the fact that in the derivations described above, adhesive forces were not considered. If these are included, a sublinear AC relation is found. The authors explain this behavior by the fact that the van der Waals interactions scale nonlinearly. However, for high loads or two flat surfaces where all interlayer distances are comparable, the AC relation is expected to hold again [20]. This conclusion is confirmed by one of our studies [21], in which we report that for a flat commensurate bilayer of MoS_2, a linear behavior exists between the normal load and the frictional force. Typical examples where adhesive forces might pose a problem include atomic force microscopy experiments, which are explained in the next section.

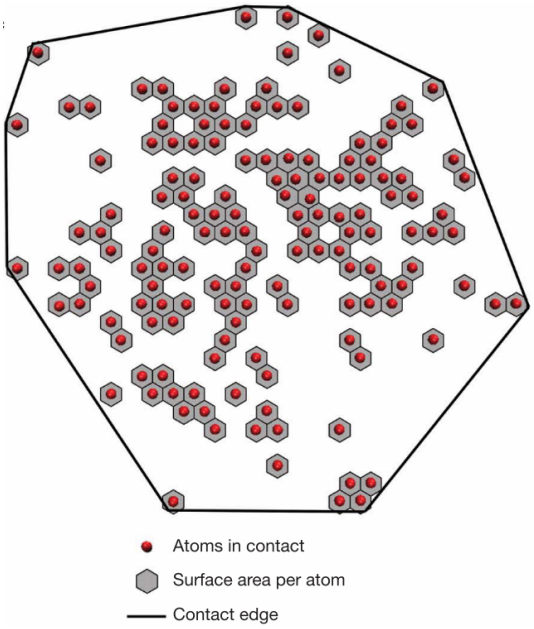

Figure 1.2: Schematic representation of the difference between the asperity contact area and the sum of contact areas of the individual atoms. Figure adapted from Ref. [20].

htbp

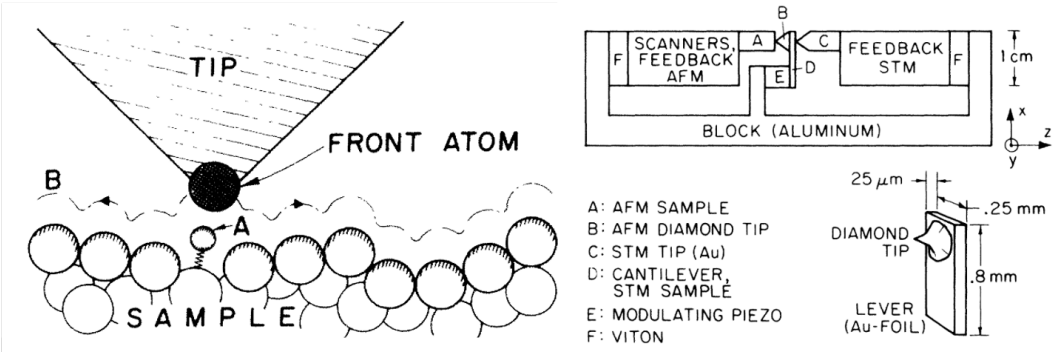

Figure 1.3: Schematic representation of an atomic force microscope, as proposed by Binnig *et al.* from which this figure is also adapted [24].

1.1.4 Friction Force Microscopy

So far, friction has been discussed mainly from a theoretical point of view. Next, one of the main experimental techniques to study friction will be considered. In 1986, Binnig *et al.* [24] developed a novel experimental technique based on the scanning tunneling microscope (STM): the atomic force microscope (AFM). Their goal was to measure ultrasmall interatomic lateral forces (forces that are parallel to the plane of the system) of non-conductive surfaces for single contact asperities. The general idea of the STM is to measure the topography of a surface by scanning the substrate with a sharp (atomic-scale) tip. The interaction between the tip and the surface of the substrate allows for local tunneling of electrons, causing a characteristic current. To keep this tunneling current constant, the tip moves up and down, creating a 2D image. One of the downsides of the STM is the fact that it requires a conducting substrate and tip. Binnig *et al.* used the following simple yet creative approach to circumvent this problem: they placed a cantilever with a diamond tip between the sample and the STM tip resulting in the AFM, as shown in Fig. 1.3 [24]. This way, the cantilever displacement due to electromagnetic forces is recorded via STM, producing an image of the surface topography. However, this approach does not require a conductive substrate, and also produces a 3D image of the surface [24]. Since then, the working principle of the AFM has been updated, where nowadays the most commonly used technique is based on a laser beam deflection system for tracing the movement of the cantilever.

Modern AFMs are no longer only used for topographic imaging and elemental force measurements, but also for manipulating materials and measuring viscoelasticity, conductivity, and electric and magnetic forces. In 1987, Mate *et al.* [25] used a modified AFM to study frictional properties. Later, this work would turn out to be the start of atomic-scale friction studies, nowadays called friction force microscopy (FFM) [11]. In such experiments, the lateral force is measured as the substrate moves underneath the tip [26]. Here, the frictional force can be obtained by taking the average of the instantaneous lateral forces. Typical scanning areas and common tip sizes are in the range of a few to hundreds of nanometres, whereas the scanning velocity is in the order of 1 $\mu m/s$ [16]. Finally, the precision of measuring forces is at the sub-nanonewton scale [26].

1.1.5 Stick-Slip Dynamics

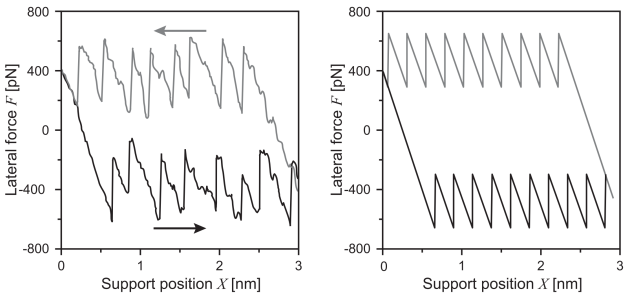

Figure 1.4: Examples of the characteristic saw-tooth shaped lateral forces for a graphite system, exhibiting stick-slip dynamics. On the left, the lateral forces are obtained via FFM while sliding once back and forth along a single line. On the right, similar results are obtained via the theoretical 1D PT model. Figure adapted from Ref. [11].

One of the observations during the earlier mentioned FFM experiment by Mate *et al.* [25] was a distinct type of dynamics. They found that as the tip was scanning the graphite substrate, sudden, instantaneous slips of the tip occurred. The frequency of these slips was matching the structural periodicity of the substrate [25]. During these slips, a drop in the lateral force was observed. In between the slips, the tip moved according to the substrate, and an increase of the lateral force appeared. As a result, these noncontinuous and nonlinear *stick-slip* dynamics express themselves via a characteristic

saw-tooth pattern for the lateral forces. As can be seen in Fig. 1.4, the periodicity of the substrate is easily recognizable [11]. In this figure, half of the area within the friction loop represents the dissipated energy. It turns out that the stick-slip dynamics represent an essential channel of energy dissipation for friction at the nanoscale. One noteworthy observation is that the stick-slip dynamics are not unique to the nanoscale. They are observed at all length scales, from earthquakes to creaking doors, and from violins being played to nanoscale machinery.

1.1.6 The Prandtl-Tomlinson Model

One might wonder, what is the origin of nanoscale stick-slip dynamics? One way to gain insight into this is the use of numerical applications that use simplified assumptions to simulate complex systems. Several modeling techniques exist that are closely related to FFM experiments. In the so-called *minimalistic models*, the tip-substrate system is represented using only a limited number of degrees of freedom [16]. The best known of these models is the mechanical Prandtl-Tomlinson model (PT)[2] [28, 29], wherein stick-slip is a natural outcome [11]. Its success stems from the fact that it provides a fundamental explanation of some of the experimental friction results at the nanoscale, despite being a very simplistic model [16]. Both Krylov *et al.* [11] and Vanossi *et al.* [16] provide excellent overviews detailing the PT model, of which a summary will be given below.

In the 1-dimensional PT model, a point mass m is dragged over a periodic potential [16] (see Fig. 1.5). The mass is connected to a driver via a spring. When the driver is moving, the mass indirectly follows because of the spring. Here, the mass represents the tip, the spring represents the cantilever and the tip, and the potential represents the interaction between the tip and the substrate. The spring has a force constant K, and the driver of the spring moves with a constant velocity v. The interaction potential of the PT model

[2] In fact the model is more commonly known as the Tomlinson model and refers to a 1929 paper by Tomlinson. However, this paper describes a different kind of model and it was Prandtl in 1928 who came up with the current model [27].

consists of two components: i) the elastic interaction between the tip and the driver, represented by the harmonic potential of the spring, and ii) the static periodic interaction between the tip and the substrate, often represented by a sinusoidal function [11]. Consider for example:

$$U_{\text{tot}}^{\text{PT}}(x,t) = \frac{K}{2}(x - vt)^2 + U_0 \; cos\left(\frac{2\pi}{a}x\right). \tag{1.5}$$

Here, x is the position of the tip on the static potential, t is the simulation time, and the sinusoidal function is characterized by an amplitude U_0 and the periodicity a [16]. The lateral force can now be obtained by taking the derivative of this function with respect to the position ($F = -\frac{\partial U}{\partial x}$):

$$m\ddot{x} = -K(x - vt) + U_0 \; \frac{2\pi}{a} sin\left(\frac{2\pi}{a}x\right). \tag{1.6}$$

However, this equation represents a conservative system because of the lack of a dissipative force, i.e., no energy dissipation occurs, and thus, no friction is present.

To include friction in the model, a dissipative force is added to Eq. 1.6, represented by $F = -m\gamma\dot{x}$, where γ represents the damping coefficient [16]. The equation of motion of the point mass now reads:

$$m\ddot{x} = -K(x - vt) + U_0 \; \frac{2\pi}{a} sin\left(\frac{2\pi}{a}x\right) - m\gamma\dot{x}. \tag{1.7}$$

Although this dissipation has a physical meaning, it does not represent a specific channel of dissipation observed in experiments [16]. The frictional force is now defined as the time average of the lateral forces acting on the point mass (Eq. 1.7) [16].

The PT model predicts two types of sliding dynamics, namely smooth and stick-slip dynamics. The parameter $\nu = 4\pi^2 U_0/Ka^2$ can distinguish them, which is the ratio between the stiffness of the spring and the stiffness of the substrate-tip interaction potential [16]. Whenever $\nu < 1$, the energy well of the harmonic potential strongly dominates over that of the corrugation of the sinusoidal function, and $U_{\text{tot}}^{\text{PT}}$ is therefore characterized by one minimum and the resulting dynamics are smooth. Whereas whenever $\nu > 1$, the harmonic potential and the sinusoidal are of the same order and compete, and thus

$U_{\text{tot}}^{\text{PT}}$ contains several local minima, resulting in stick-slip dynamics; this is illustrated in the bottom part of Fig. 1.5.

The PT model now provides a very intuitive way of understanding stick-slip dynamics. Consider a point mass residing in a local energy minimum of the static potential. In the case of a very stiff spring (i.e., $K \to \infty$), the point mass will follow the motion of the driver, irrespective of the corrugation of the static potential. This is confirmed by looking at ν, which will vanish as K approaches ∞. In other words, smooth sliding is observed. In case a soft spring is considered, the point mass will initially remain at rest (the stick phase), and the spring will stretch as the driver moves forward. In other words, potential energy builds up in the spring, a phenomenon also known as 'charging' of the spring. Keep in mind that one can also charge a spring through compression. As a result, the spring exerts a positive force on the point mass. When this force exceeds the maximum energy gradient resulting from the static potential, the point mass starts to accelerate, in accordance with Eq. 1.6. This point marks the start of the slip towards the next local minimum. The slip ends once the point mass has reached the next local minimum, its vibrations have significantly dropped, and is practically at rest again. From Eq. 1.7, it becomes clear that while the point mass is moving during the slip, energy dissipation occurs. This process repeats, resulting in the typical outcome of a lateral force computation using the PT model, as shown in Fig. 1.4.

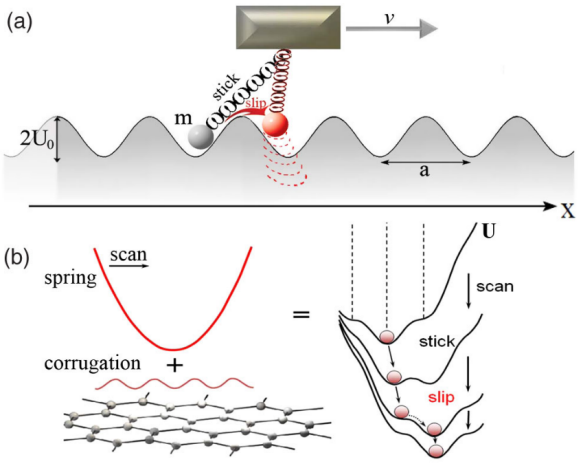

Figure 1.5: The upper panel (a) represents a schematic of the Prandtl-Tomlinson model in 1D. The lower panel (b) represents a schematic of the potential interaction surface resulting in stick-slip dynamics. Figure adapted from Ref. [16].

The original PT model does not include a temperature dependence; however, this can be achieved by adding a random thermal force to Eq. 1.6, satisfying the fluctuation-dissipation theorem [11, 16]. By including the notion of temperature, thermally assisted barrier crossing becomes possible [16]. Based on the outcomes of thermal PT studies, it is believed that the nanoscale stick-slip dynamics in FFM experiments are a result of thermal activation [16].

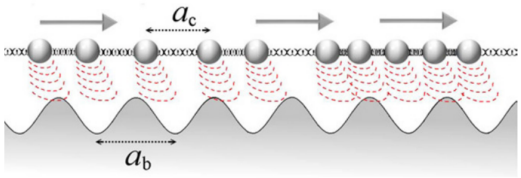

Figure 1.6: Schematic of the Frenkel-Kontorova model in 1D. Figure adapted from Ref. [30].

Although the model has provided valuable insights into FFM results, a word of caution is necessary. The PT model is fundamental and might provide incorrect relations, e.g., the velocity appears to be irrelevant to stick-slip dynamics according to the definition of ν, which has experimentally been proven to be incorrect [11]. Additionally, whereas the PT model exhibits significant overlap with AFM experiments, it fails to describe two sliding solid surfaces [16]. The latter can be resolved by a relatively simple manipulation, resulting in the so-called Frenkel-Kontorova (FK) model [16, 30]. Here, instead of having a single point mass, a chain of N masses (atoms), connected via harmonic springs, are considered [30], as depicted in Fig. 1.6. For more information on this model, please refer to Refs. [16, 30].

1.2 Lubricants

In the previous section, the basic concepts of friction were discussed. In this section, we examine the possibilities of how to reduce friction. In the example of the rim and the brake pad of the bike, friction was needed to slow down. However, friction is often an unwanted (and costly) phenomenon [1, 31]. The general idea of reducing friction (and wear) is by introducing an intermediate medium, a so-called *lubricant*, within the tribological interface – a concept dating back at least as far as the Ancient Egyptians [2, 3]. Hieroglyphs were found, apparently depicting the use of a lubricant to facilitate moving large

and heavy stones. Later, lubricants such as oils were used to reduce friction in all sorts of sliding contacts, such as carriage wheels and other more advanced machinery [3]. More and more, especially in the wake of the industrial revolution throughout Europe and the New World, the importance of effective lubricants was evident, both in respect to altering the friction properties of materials themselves and reducing wear. More recently, climate change has formed an essential motivator for reducing friction, thereby reducing energy consumption, CO_2 emissions, and the use of materials [1, 5].

Lubricants are applied in a wide range of interfaces comprising different types of materials, with metallic ones forming the majority [32]. The idea behind lubricants is simple: reduce or even avoid direct contact between sliding surfaces that might result in friction and wear. The lubricant itself should have low adhesion to at least one or both interfaces, promoting easier sliding. As a result, less energy is required to induce a relative sliding within the system. Moreover, the sliding materials themselves will experience reduced wear, increasing their sustainability. To avoid instant deterioration of a lubricant, it should be characterized by a long fatigue life, high strength, and stiffness [32]. For ease of implementation, it should also have a relatively low sensitivity to thermal expansion [32].

Nowadays, water- and oil-based lubricants are referred to as classical wet lubricants [32, 33]. However, these types of lubricants are no longer able to meet the increasing demands of the industry. On a global scale, these lubricants have been linked to severe environmental problems [5, 34, 35]. Moreover, the increasingly extreme operating conditions under which materials are expected to perform, e.g., contact pressures, high temperatures, and other challenging conditions, result in problems when using these types of lubricants [32]. Consider as an extreme example a space rocket [36]. On the one hand, there is an enormous change in temperature between being on Earth and while being powered by an engine with combustion temperatures of thousands of degrees, and being in space with temperatures in the cryogenic regime (below -150 °C). On the other hand, there is a change in pressure when leaving Earth's atmosphere and entering the vacuum of space. A more common example is an airplane, where the actual flux in temperature and pressure is lower, but

the actual change of conditions occurs more frequently. On smaller scales, wet lubricants also reveal an array of problems. Classically, a particular type of lubricant delivery system (like a pump) introduces the lubricant to the tribological contact [5]. This approach, however, is not always feasible, for example in nano/micro electromechanical systems (NEMS/MEMS), a class of small devices that allow positioning at an atomic scale [5, 31, 37, 38]. Studies have also shown that liquids can change their behavior and properties, e.g., their viscosity, when they are confined to small scales [31].

1.2.1 Solid Lubricants

At the beginning of this chapter, so-called solid lubricants were briefly introduced, with MoS_2 being one of the first to be studied by Bell and Findlay in 1941 [39]. When applied as lubricating coatings, solid lubricants can circumvent the problems experienced by the wet lubricants described above. Based on their properties, different types of solid lubricants can be distinguished. In the works presented here, we focus on 'soft' solid lubricants, characterized by a hardness below 10 GPa and a characteristic layered atomic structure, such as graphite and TMDs [32, 40, 41].

There are several reasons why both the industry and the scientific community have a deep interest in solid lubricants. First of all, solid lubricants have been related to a significant reduction of friction, with COFs ranging between 0.05-0.2 [31, 32, 33, 40]. Secondly, solid lubricants are less prone to degrade under extreme working conditions [40]. Thirdly, it is sometimes desired that the lubricant remains in a specific place, rather than having a natural flow throughout the interface. Finally, when using solid lubricants instead of wet ones, there is a potential weight reduction, since one no longer needs specific mechanical machinery, such as pumps, to deliver the lubricant [5].

However, there are also several reasons why a large-scale industrial implementation is still lacking. First of all, solid lubricants are generally not sustainable because they have low wear resistance [5]; whenever they are found to

have high wear resistance, their frictional properties have weakened, especially when operating under an extensive range of temperatures [40]. Moreover, it has been shown that solid lubricants are very sensitive to environmental conditions [5, 32, 42, 43]. For example, at the macroscale, MoS_2 is found to have increased COFs in the presence of humidity, whereas graphite requires humidity to achieve low COFs [5, 44, 45, 46]. Finally, replenishing a solid lubricant is difficult [40].

From the above, it becomes clear that when we are looking for an excellent soft solid lubricant when used as a lubricating coating, it should have high wear resistance, be insensitive to environmental conditions, and must be easily applied and replenished [5]. Next, we will discuss TMDs in greater detail, with the main focus on MoS_2, alongside graphite and graphene.

1.2.2 Transition Metal Dichalcogenides

An overview of TMDs can be found in Refs. [6, 47, 48, 49, 50], parts of which will be summarized below. Firstly, we will have a closer look at the general structure of TMDs, after which we will discuss some of the lubricating properties of MoS_2. Most of the properties of MoS_2 that are discussed here are similar to other TMDs.

TMDs consist of transition metals (M) and chalcogens (X) with a molecular formula MX_2 [46, 48, 51]. As shown in Fig. 1.7, the metal comes from groups 4-10 in the periodic table, and the chalcogen is either S, Se, or Te. In 1923, the general crystal structure of MoS_2 was determined via X-ray spectral photographs, which was then extrapolated to other TMD family members [52]. This shows the great structural similarity between different TMDs. Although most TMDs have a naturally occurring lamellar structure, groups 8-10 form an exception by being mainly bulk materials and are not considered here [47, 48]. For layered TMDs, the intralayer atoms are held together by strong covalent bonds. Here, a three-fold symmetry is present where the metal is sandwiched in between the chalcogens. Depending on the specific type of TMD, the most common metal coordination is either *octahedral* (1T) or *trigonal prismatic*

(2H), as shown in Fig. 1.7 [6, 48, 49]. This distinction is based on the positions of the chalcogens, which can either be in an AbA configuration or in an AbC configuration, where the capital letters represent the chalcogens and the lower case represents the metal. The resulting in-plane lattice constant a, i.e., the periodicity of the in-plane symmetry, ranges from 3.15 to 4.03 Å [47].

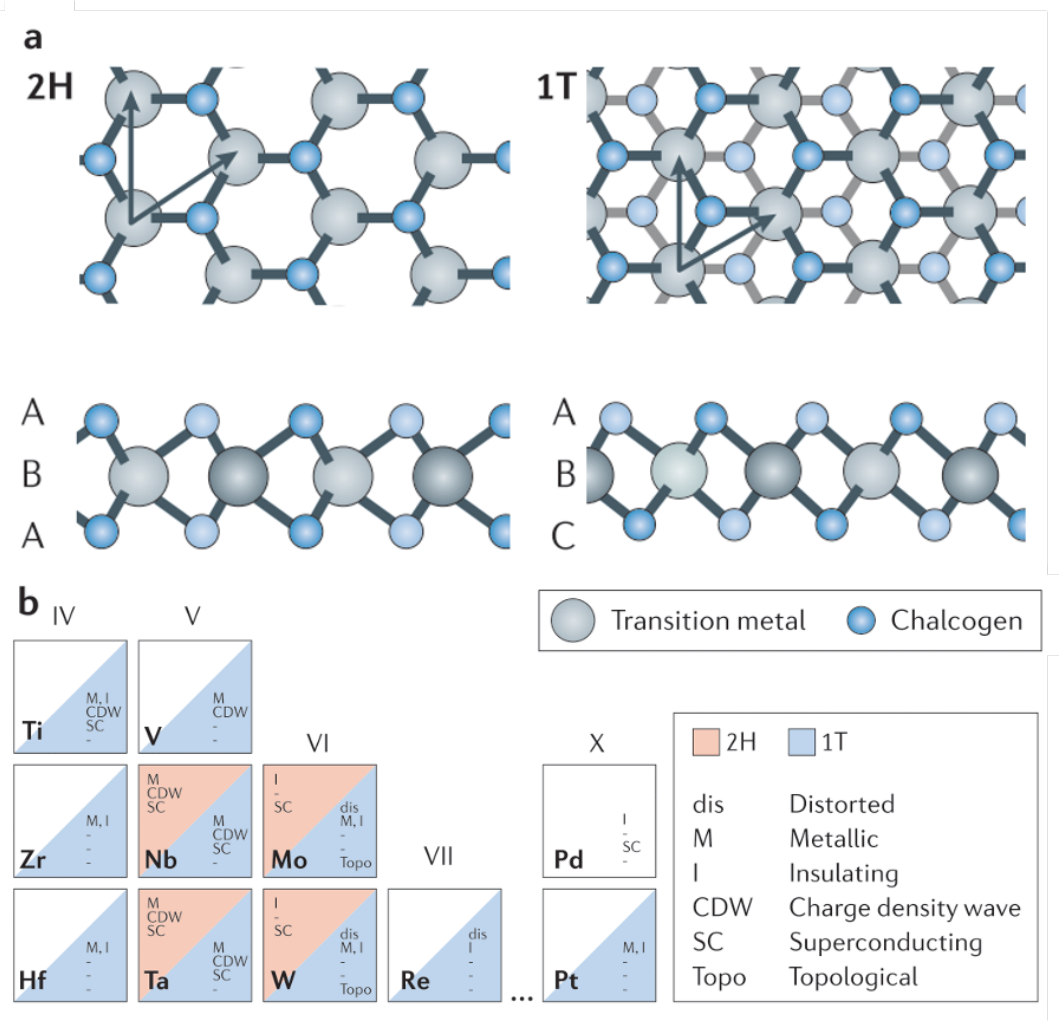

Figure 1.7: Overview on TMDs. In panel (a), two different types of intralayer metal coordination are displayed, on the left trigonal prismatic and on the right octahedral. In panel (b), the metals that form lamellar TMDs are displayed, along with some of the electronic properties. Figure adapted from Ref. [48].

The layers, held together by weak electrostatic and van der Waals interactions, have a thickness of about 6-7 Å [47]. Apart from the intralayer structural configuration, TMDs are characterized by interlayer stacking configurations,

which can be either trigonal (1T), hexagonal (2H), or rhombohedral (3R) [47, 49, 50]. Here, the number reflects the number of layers required to obtain the stacking. The 1T stacking consists of monolayers with an octahedral metal coordination stacked above each other, resulting in an AbC-AbC configuration and a unit cell of three atoms. The 2H stacking consists of monolayers that are rotated by 180° relative to one another. The resulting configuration is most commonly AbA-CbC ($2H_a$) or AbA-BaB ($2H_c$), and the unit cell consists of six atoms. Finally, the 3R stacking is organized in an AbA-CaC-BcB fashion and the unit cell consists of nine atoms. Depending on the type of TMD and its structure, it can be either metallic, insulating, or anything in between [47, 49]. Due to the wide variety of combinations of metals and chalcogens and the possible structural configurations, TMDs are characterized by a wide range of thermal, chemical, electrical, and mechanical properties [6, 47].

Within the TMD family, MoS_2 can be considered prototypical and is a commonly used solid lubricant at the macroscale, where it is usually sputtered onto the substrate of interest [53, 54]. The choice of MoS_2 is partially related to the fact that it is abundant in nature [47]. The most energetically favorable stacking of MoS_2 is $2H_c$, which belongs to the $P6_3/mmc$ space group, and will be the main focus of the works presented here [47, 54]. So far, this introduction has not yet explained the excellent lubricating properties of MoS_2 and solid lubricants, which we will now turn our attention to.

The tribological properties of solid lubricants have been related to their layered structure [51, 54]. In 1928, Bragg *et al.* [55] studied the lubricating behavior of graphite, which will be discussed in the next section. They explained this characteristic behavior by considering the combined structure, composed of strong intralayer covalent bonds with relatively weak interlayer van der Waals interactions, facilitating easy sliding. As was stated above, whereas strong intralayer covalent bonds hold the individual layers together, weak electrostatic and van der Waals interactions maintain the layered structure. It is this unique structural feature that allows easy shearing between the layers [56, 57].

Next, a brief overview will be given on some general factors that underpin

the frictional behavior of MoS_2, such as the effect of thickness, orientation, humidity, temperature, and sliding velocity. The frictional properties of MoS_2 have been related to the number of layers present in the structure, and it was shown that the friction decreases for an increasing number of layers [58]. This observation was related to an out-of-plane deformation present in single or few-layered systems. MoS_2 is also characterized by an anisotropic behavior of the friction when considering a relative rotational mismatch between the layers, i.e., by changing the mismatch, different frictional behavior is observed [57, 59]. This structural argument can lead to the so-called *superlubric regime*, which is explained in more detail later. Although MoS_2 was found to be somewhat hydrophobic, humidity has been related to a significant deterioration of the frictional properties and increased wear of MoS_2 [43, 45, 46, 54, 60, 61, 62, 63]. The actual mechanism for this observation has been strongly debated and, in fact, forms the starting point of one of the works presented here (Chap. 5). On the other hand, MoS_2 is less sensitive to temperatures, remaining a functional lubricant up to approximately 350 °C [64]. Finally, Acikgoz and Baykara used AFM to show a relation between the sliding velocity and friction both for monolayer and bulk MoS_2 [65]. With increasing sliding velocity, the friction increased logarithmically. This ends our brief overview on MoS_2; further frictional characteristics are discussed in Chaps. 3 and 5.

1.2.3 Graphite and Graphene

An extensive review of graphite is given in Ref. [66], parts of which will be summarized below. Graphite is a lamellar material belonging to the $P6_3/mmc$ space group and is made solely of carbon atoms, in which the monolayers have a hexagonal symmetry. The layers are stacked in an AB fashion. For every hexagon of one layer, a carbon atom from the neighboring layer is located in the center of the hexagon within the xy-plane. Whereas the atoms within a layer are covalently bonded with a bond length of ~ 1.42 Å, van der Waals and electrostatic interactions keep the layers together at a distance of ~ 3.35 Å [66, 67, 68]. The unit cell of graphite contains four carbon atoms with a planar and perpendicular lattice constant of $a \approx 2.46$ Å and $c \approx 6.71$ Å, respectively

[66, 67, 68]. Finally, graphite is a zero bandgap semi-metal and conducts both electricity and thermal heat due to the aromatic rings [66]. A structural overview of graphite can be found in Fig. 1.8.

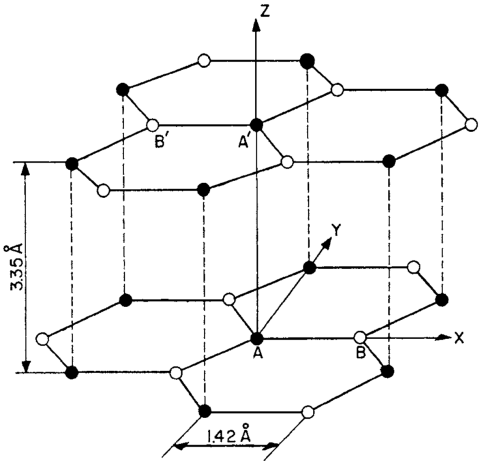

Figure 1.8: Schematic of the crystal structure of bilayer graphite with an AB stacking. Figure adapted from Ref. [66]

As stated above, the lubricating behavior of graphite has been known for a long time [55]. In fact, it is because of this lubricating behavior that we are able to write with graphite-based pencils. As previously mentioned, at the macroscale, this easy sliding has been proven to benefit from humidity [5, 32]. One explanation for this observation is the enhanced easy shearing between graphite sheets as a result of intercalated water molecules [5]. However, at the nanoscale, the dependence of friction on humidity is more complex. Hasz *et al.* [69] performed AFM experiments and found that the friction behavior of graphite has a non-monotonic dependency on humidity. For lower humidities, friction was found to increase with the number of water molecules absorbed. This was related to a pinning behavior of the water in the sliding interface affecting the easy shearing. At high humidities, the friction was found to decrease with the number of water molecules. Here, the water molecules formed a thin layer, thereby increasing the tip-sample distance. Moreover, the hydrogen bonds between the water molecules prevented the water from pinning. The discrepancy between the results at the macroscale and nanoscale has been explained by the fact that at the macroscale graphite exploits the humidity to neutralize dangling bonds [32], whereas at the nanoscale bond breaking/formation and wear were absent [69].

In 2004, Novoselov *et al.* [70] managed for the first time to obtain a stable monolayer of graphite by using a 'Scotch tape' method; and so the graphene

era began. Graphene belongs to the class of so-called *two-dimensional (2D) materials*, which are characterized by their super-thin (one or a few atoms thick) nature [5]. Similar to graphite, it can, in principle, be considered as one big layer of connected aromatic rings, missing the typical hydrogen atoms. One might wonder why this discovery earned them a Nobel prize. As it turns out, when changing from bulk to monolayer thickness, the properties of many materials change significantly, such as high optical absorption (far beyond infrared), extreme mechanical strength, and electrical conductivity (several orders higher than typical polymers or bulk materials) [5, 33, 47, 71, 72, 73].

As is the case for MoS_2, the basal planes of both graphite and graphene are relatively chemically inert, even in the presence of defects [5, 43, 71]. However, when considering finite flakes, it is found that the edges of graphene are less stable than those of MoS_2 and therefore exhibit a greater reactivity with e.g. water [43]. In contrast to MoS_2 where the zig-zag edge termination is most thermodynamically stable, the arm-chair edge termination is more stable for graphene [43, 71]. In general, graphene is not soluble in water due to its hydrophobic nature, which prevents oxidation and corrosion in ambient conditions [5, 43, 71]. Finally, in contrast to graphite, Berman *et al.* [5] found that the frictional properties of graphene are independent of relative humidity. This observation was confirmed by others [33].

1.2.4 Van der Waals Heterostructures

By now, the reader should have an idea of the potential and problems of solid lubricants when used as lubricating coatings. Since the fruitful attempt to isolate a single layer of graphite in 2004, many other 2D materials have been extracted from their bulk. As with graphene, the properties of other 2D materials revealed significant discrepancies from their bulk counterparts [72, 73]. The next step was made in 2011 by Ponomarenko *et al.* [74], who mixed and matched for the first time successfully different types of 2D materials to create stable novel types of so-called *van der Waals heterostructures*. A schematic of the principle of such heterostructures is displayed in Fig. 1.9. The combination of different layers, stacked together by van der Waals interactions, allows

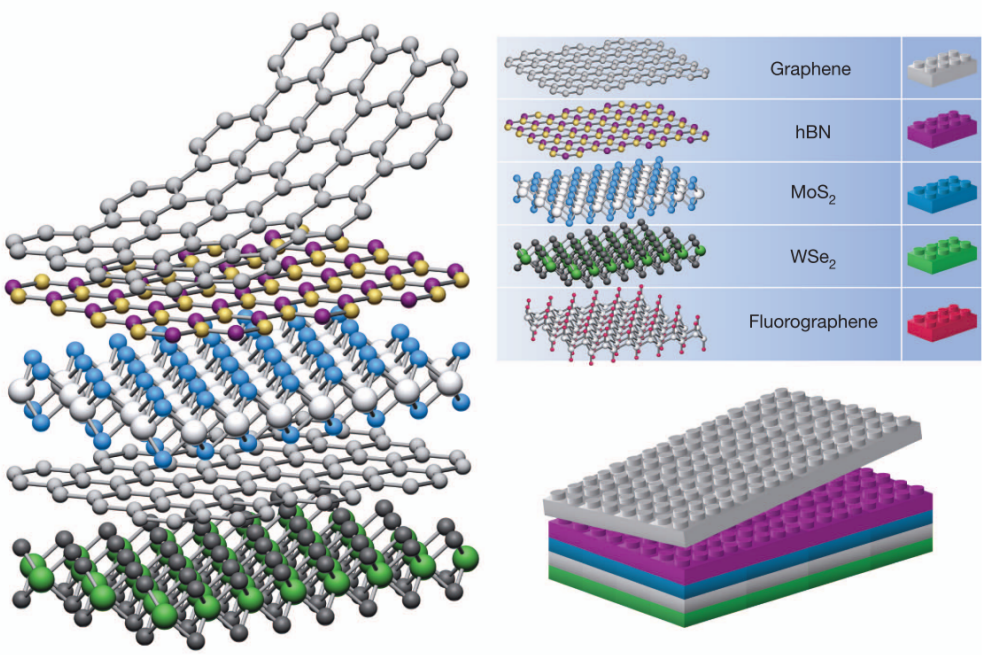

Figure 1.9: Schematic example of the stacking approach of 2D monolayers, used as building stones, resulting into a heterostructure, as if being Lego® blocks. Figure adapted from Ref. [75].

for another level of precision in tuning the characteristics of a material, such as its mechanical and electronic properties [72, 75, 76, 77, 78]. More recently, the intrinsic mismatch angles between individual layers in heterostructures have been explored to further extend the tunability of the properties [79, 80]. Promising results were shown in relation to controlling the electrical conductivity and band gaps. Despite the exciting physics that might be achieved by exploiting the stacking degree of freedom in heterostructures, a proper analysis of the actual energetical stability of these structures is often missing. This aspect will be further discussed in one of the works presented here, namely Chap. 4. More in line with the main topic of this thesis, others have also considered van der Waals heterostructures in frictional studies [34, 60, 81]. Since every 2D material has its own unique in-plane lattice parameter (although they might sometimes be similar to others), the combination of two or more unique monolayers can create a friction regime in which the COF becomes extremely small, so-called *superlubricity* [77], a concept that will be explained next.

1.3 Superlubricity

In the section discussing the PT model, we saw that the characteristic stick-slip dynamics are mainly the result of the corrugation of the underlying static (and periodic) interaction profile in combination with a 'soft enough' spring. We also discussed another type of dynamics, namely smooth dynamics for the case where either the corrugation of the potential flattens out or the spring becomes infinitely stiff. According to the PT model, the latter automatically implies vanishing of frictional forces. Using the AC law, a dimensionless parameter was defined to quantify friction, μ. To give an idea, rubbing two pieces of 'smooth' wood against each other will result in a COF of 0.2 or larger, whereas for two metal surfaces, the COF is 1.0 or larger [76]. For bulk solid lubricants, we saw that the COFs could be in the order of 1.0×10^{-2} [33]. A question that might arise is 'how low can we go'? A more scientific formulation would be: 'how can we decrease the energy dissipation due to sliding as much as possible'?

In 1983, Peyrard and Aubry [82] discussed the possibility of a state in which the COF would vanish for crystalline systems [31], based on the 1D FK model. A little under ten years later, in 1990, Sokoloff continued discussing the possibility of a vanishing COF [83]. However, mainly because the model was one-dimensional and the actual term 'superlubricity' was not mentioned, it are the works of Hirano and Shinjo between 1991 and 1993 [84, 85, 86] that is most often referred to as the start of research on superlubricity [76].

The work of Hirano and Shinjo was purely theoretical, and the idea was to look at friction from the nanoscale instead of the macroscale (as a result of surface roughness), and thus, to study interatomic interactions. As stated before, in the PT model and during FFM experiments, the frictional force is defined as the time average of the lateral forces experienced during sliding. The lateral forces result from interatomic interactions between the sliding surfaces, i.e., electrostatic and van der Waals interactions [76]. According to the model of Hirano and Shinjo, to achieve vanishing frictional forces and thus friction, the sliding surfaces should be: i) weakly interacting (e.g., based on non-covalent interactions), ii) atomically flat and clean, and iii) contain a rela-

tive misfit angle between the orientation of the two surfaces, yielding so-called *incommensurability* [84, 85, 87]. As will become apparent, it is the incommensurability that is related to obtaining a substrate-substrate interaction potential that can be considered corrugation-free, resulting in smooth sliding and the superlubric regime.

In the years after, other conditions for achieving superlubricity were described [87], hence why we now refer to this specific phenomenon as *structural superlubricity*. For a more extensive overview, the reader is directed to Refs. [76, 87]. An overview of the timeline of the discovery of superlubricity can be found in Fig. 1.10. In general, superlubricity is defined by COFs lower than 0.01 [76, 87], whereas some define the regime when the COFs are below 0.001 [31, 34]. One might wonder why superlubricity is defined by a finite number. It has been found that friction never completely vanishes, i.e., certain channels of energy dissipation will always remain present [31].

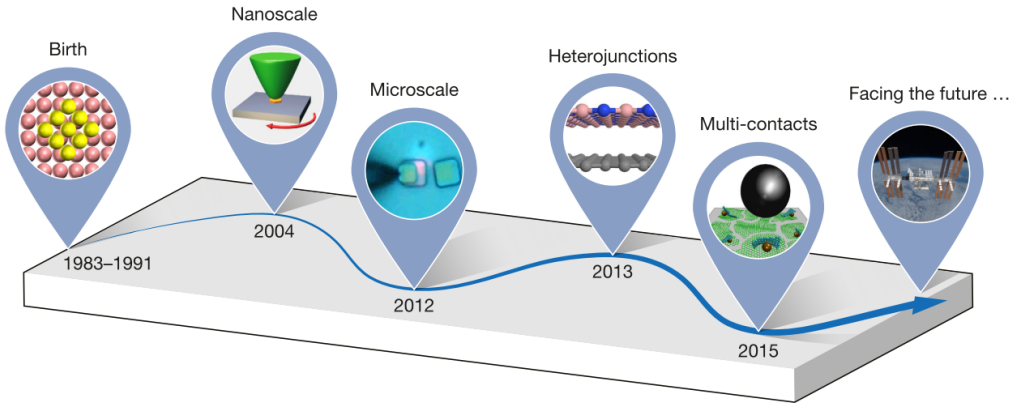

Figure 1.10: Schematic timeline on the scientific progress on superlubricity. 1983, first theoretical prediction of vanishing coefficent of friction [82]. 1991, the term superlubricity was defined [86]. 2004, the first experimental verification of superlubricity at the nanoscale [77]. 2012, the first experimental verification of superlubricity at the microscale [88]. 2013, the first theoretical prediction of superlubricity in heterostructures [89]. 2015, observation of macroscale superlubricity for multi-material, multi-contact systems [90]. Figure adapted from Ref. [31].

1.3.1 Structural Superlubricity

The idea behind structural superlubricity is to achieve vanishing frictional forces due to the relative orientation between the sliding surfaces. The original model of Hirano *et al.* [84, 85] considered ultra-high vacuum and therefore automatically excluded any chemical contribution from surrounding molecules to the frictional forces. Moreover, the model neglects any temperature dependence. That being said, temperature directly affects atomic vibrations, which might have some influence on the friction, and therefore it can be assumed that it is better to avoid high temperatures [76]. Structural superlubricity is considered among the most promising ways to achieve low COFs because it is imparted to the material through structural manipulation alone. As we will see next, it considers a conceptually simple manipulation of the contact surfaces themselves, rather than requiring a specially formulated lubricant [87].

Consider a bilayer system of two atomically flat periodic crystal layers (e.g., bilayer graphene or MoS_2), devoid of any contaminants. There exists a potential energy resulting from interlayer interactions. When one of the layers is translated relative to the other, the energy of the system changes. If one now performs a complete mapping of the relative positions of the layers based on their in-plane symmetry, a *static periodic potential energy surface* with a system-specific corrugation is obtained, the so-called PES [76]. The corrugation of the PES stems from the electrostatic and van der Waals interlayer interactions that result in preferential atomic positions when orientating one surface atop another. Consider, as a conceptual example, two egg cartons. Both cartons have a periodic shape in their plane (representing the basal plane of our layered materials). Next, consider that the cartons are stacked one on top of the other. The characteristic shape will result in relative orientations that are more favorable, where the shape of both cartons exactly coincides when stacked, representing minimum energy configurations, and relative orientations where the cartons do not coincide, i.e., the maximum energy configurations. This way, both cartons can be used to represent a PES between two layers of material.

The left panel (a) in Fig. 1.11 is a schematic of two identical, aligned

structures positioned above each other in a minimum energy configuration. This specific contact between the two layers, where the bottom and top layers are identical and aligned, represents a *commensurate structure*. As one might expect, this configuration is very stable, with relatively high resistance to sliding. This resistance is the result of energy barriers arising from the atomic interlayer interactions. In this case, all barriers have to be overcome simultaneously to allow sliding, causing high frictional forces. This is a natural outcome when considering the egg carton analogy. Consider the cartons when 'positioned' in a minimum energy commensurate configuration. The 'sliding' of the upper carton is now practically unfeasible.

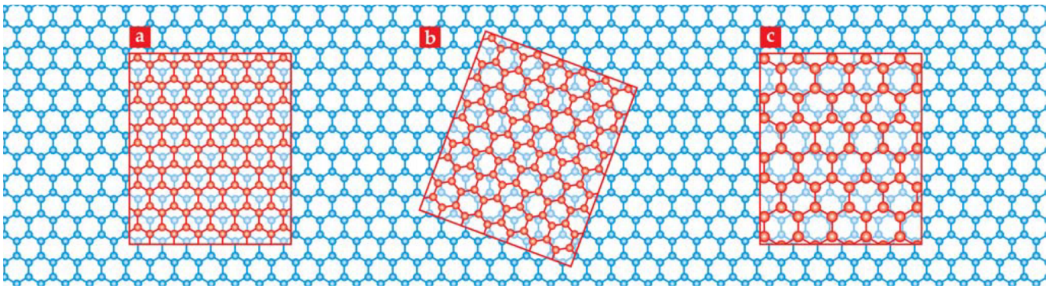

Figure 1.11: Schematic representation of different ways to position periodic surfaces above each other. (a) Homogeneous minimum energy configuration, resulting in a high frictional regime. (b) Homogeneous, incommensurate structure, achieved by means of introducing a relative, orientational, mismatch angle between the layers, resulting in a low frictional regime. (c) Aligned heterostructure, where both surfaces have the same symmetry but have a different lattice constant, resulting in a low frictional regime. Figure adapted from Ref. [76].

What happens if one of the surfaces is rotated with respect to the other so that the global symmetry of the system is lost? A so-called *rotational incommensurate contact* is now obtained, where there is a mismatch angle between the relative orientation of the layers, as depicted in the middle panel (b) of Fig. 1.11. For rotational incommensurate structures that are infinite, there will always be an atom of the top layer located at a local minimum of the PES, for which there is another atom in the top layer positioned at a local maximum of the PES. As a result, any negative contribution to the lateral force will be compensated by a positive contribution to the lateral force, resulting in a net cancellation of the lateral (frictional) forces. From the above, it

becomes clear that breaking the structural (rotational) symmetry is of utmost importance in achieving superlubricity. Whenever this is not the case, the net frictional force resulting from the interlayer interactions will remain finite. For example, one should not rotate according to the rotational symmetry, i.e., 90° for a square symmetry or 60° for a hexagonal symmetry, because this will result in another commensurate structure rather than breaking the symmetry. This can once more be shown by considering the egg cartons. Whenever the cartons are relatively rotated, their shapes will no longer coincide and thus 'sliding' becomes feasible. Rotating one of the two layers is not the only way to achieve contact incommensurability and thus a cancellation of frictional forces. If one, for example, considers a heterostructure of two different materials, each with the same symmetry but with a different in-plane lattice constant (representing the length of periodicity), one obtains a *structural incommensurate contact*. Here, the same effect can be achieved as is the case for rotational incommensurability, as shown in the right panel (c) of Fig. 1.11. In conclusion, when a system is incommensurate (rotational or structural or both), a net cancellation of friction forces results with a COF approaching zero, which is the common pathway to achieve superlubricity.

The concept described above is purely theoretical and required experimental verification. The main difficulty here is four-fold: i) it is incredibly difficult to control the exact orientation between layers at the nanoscale experimentally, ii) an apparatus capable of measuring very low COFs is required, iii) the surfaces should be atomically flat, and iv) to achieve molecular cleanliness, the experiments should be performed in ultra-high vacuum [76, 87]. To this end, Hirano *et al.* provided experimental proof of a dependence between the relative orientation and the COF [85]. Unfortunately, due to the reasons explained before, they could not measure a significant enough vanishing of frictional forces [76]. Another effort by Martin *et al.*, also in 1993, was successful, and they measured for the first time the superlubricity of MoS_2 at the macroscale and in ultra-high vacuum [57]. Furthermore, using transmission electron microscope images, they were able to confirm the origin of the observed vanishing of frictional forces, namely, a relative misfit angle between the layers [57, 76]. A more compelling experimental proof was given in 2004 by Dienwiebel *et al.* [77]. They used atomic force mi-

croscopy (AFM) to study the superlubricity of graphite. Their experiment, performed in high vacuum, measured the friction between a graphite substrate and a graphite-covered tip. By measuring a rotational range of 60°, in correspondence with the hexagonal symmetry of graphene, it allowed them to pinpoint the effect of commensurability on friction. For commensurate orientations, with angles around 0° and 60°, they found high frictional forces, whereas for all incommensurate structures, frictional forces were several orders of magnitude lower [77]. Their findings are summarized in Fig. 1.12.

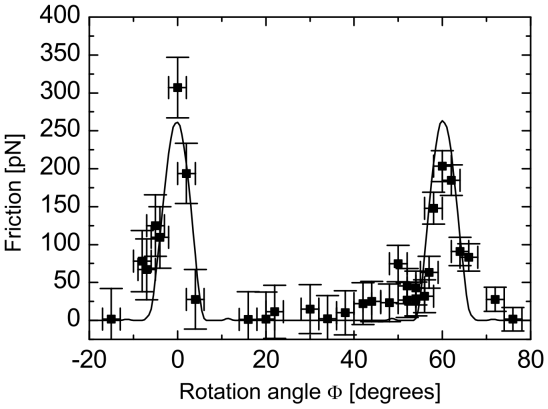

Figure 1.12: Effect of the commensurability of graphite structures on the frictional forces. Figure adapted from Ref. [77].

Due to the complexity of studying structural lubricity experimentally, relatively few observations have been reported, such as those by Liu *et al.* at Tsinghua University, in 2012 [88]. They studied graphite and found ultralow friction for incommensurate structures. And in 2013 by Feng *et al.* [91], at the University of Berkeley, who studied the sliding of graphene flakes on top of graphene. They found that during sliding the flakes orient in an incommensurate fashion. More recently, in 2017, Li *et al.* at Peking University [56] reported on the superlubricity of monolayers of MoS_2. Their novel experimental approach allowed them to measure the friction between monolayers and they found a correlation between the superlubricity and incommensurability of the bilayer systems. Finally, Liu *et al.* at Tsinghua University [92] studied graphene-graphene and graphene-boron nitride structures and found superlubric regimes, even for humid conditions, which was attributed to the incommensurate character of the structures. Although promising, the concept of structural superlubricity does not always apply. Consider, for example, pristine crystalline diamond surfaces. Here, one could also create an incommensurate structure. However, as it turns out, the surfaces are not weakly

interacting due to the unbounded surface electrons [76]. This once more shows the relevance of meeting all criteria outlined in the model by Hirano and Shinjo [84, 85].

1.4 Aims & Outline

In this thesis, the tribological behavior of solid lubricants is investigated by employing computational modeling. The main goal of this thesis is to obtain new insights into the fundamental understanding of the frictional properties of MoS_2 at the nanoscale. This is done by investigating the intrinsic frictional aspects of MoS_2, for example, by studying frictional anisotropy and considering the effect of external conditions such as water contamination. Our choice of prototypical materials enables us to make more broad remarks on the frictional behavior of solid lubricants in general and provide new understandings of their applications. This way, the results of this thesis will actively contribute to making the next step towards large-scale industrial implementation of solid lubricants feasible.

This thesis has received funding from the European MSCA-ITN funding scheme within the Union's Horizon2020 research and innovation program under grant agreement No. 721642: SOLUTION. The goal of SOLUTION is to contribute to large-scale industrial implementation of solid lubricants by:

- Proving the validity of using simulation techniques in the field of solid lubricants,
- Using multi-scale simulation techniques, validated experimentally when possible, for the development of current and new solid lubricants with enhanced properties,
- Familiarizing a new generation of scientists with a cross-disciplinary attitude.

The remainder of this thesis is organized as follows. The second chapter (Chap. 2) briefly presents an overview of the type of modeling techniques that

have been used in the works presented here. In the third chapter (Chap. 3), the superlubric behavior of a commensurate bilayer of MoS_2 is studied and thereby the conditions set by the model of Shinjo and Hirano are challenged. In the fourth chapter (Chap. 4), the rotational energetic behavior of a bilayer heterostructure of MoS_2 and graphene is studied and our findings are used to rationalize experimental results and extend the understanding of epitaxy theory. In the fifth chapter (Chap. 5), the effects of water contamination on the frictional properties of MoS_2 are studied, and the results reveal a peculiar behavior of water, which was found to act either as a lubricant or contaminant. In the sixth chapter (Chap. 6), a contribution is made to a mainly experimental study on MoS_2 and diamond, clarifying our understanding of the observed orientational stacking of MoS_2 atop diamond. And finally, in the last chapter (Chap. 7), we present the main conclusions of this thesis.

2

Computational Methods

In Chap. 1, minimalistic models were discussed in terms of the PT model. PT considers a reduced number of degrees of freedom and aims to describe frictional dynamics, of which stick-slip is one of the most important features. Although these techniques contribute to a qualitative understanding of friction, they fail to describe more subtle features closely related to atomistic behavior [16]. To circumvent this problem, one can resort to atomistic models, also called *in silico* methodologies. Two main branches are distinguished, *quantum mechanics* (QM) calculations and *molecular mechanics* (MM) simulations. In QM calculations, the energy and/or momentum of a configuration of a system is calculated by specifically taking into account the wave-particle duality and the quantized behavior of atoms and their electrons. In MM, the time evolution of a system is modeled by calculating the forces that (charged) atoms

exert on each other according to classical Newtonian mechanics. The type of method used depends on the physical phenomena that are being studied and the computational resources available.

In QM calculations, the interactions and properties of the system are calculated on the fly, without any significant assumptions about the specific interaction, e.g., which atoms are bonded to each other and what the partial atomic charges are. However, assumptions are made about electron behavior, and the atomic interactions that arise from this. As a result, QM calculations allow insights into the electronic structure of the system, i.e., electronic phenomena. That being said, QM calculations are characterized by their high computational cost and are therefore limited to system sizes of less than 1,000 atoms and short (roughly picosecond) timescales. The outcomes of pure QM methods are static (time-independent), which means time-dependent features are not accessible. In the case of friction, which is mainly a dynamical response, time-dependent features are relevant. This can be addressed by considering time-dependent methods that use QM methods as an integral part (e.g., QM/MM methods, time-dependent Density Functional Theory, and *ab initio* molecular dynamics). However, their computational cost remains a problem. Another approach is to resort to more simplified methods, such as pure MM. Among other properties, the main idea of this method is to simulate the time-dependent conformational landscape and the corresponding potential energies. The computational costs are much lower due to the use of so-called *force fields*, which are discussed in Sec. 2.2.1, allowing for systems up to a few million atoms. However, the electronic description is no longer taken into account, and no conclusions can be drawn regarding the electronic behavior. A variety of techniques exist that implement the principles of the methods described above. In this chapter, the techniques used for the projects in this work are briefly introduced. These techniques are *density functional theory* for QM and *classical molecular dynamics* for MM.

2.1 Quantum Mechanics

Among other properties, QM calculations are used to investigate the stability of structures, charge distributions, and potential energy surfaces. In QM, atoms and molecules, including their electrons, are represented by the wavefunction (WF), Ψ [93]. The WF contains all information about the system and thus fully describes it but has no physical meaning [93]. According to the Born interpretation, the squared modulus of the WF, $|\Psi|^2$, does have a physical meaning and gives the probability density of finding the system in a particular state. In theory, the WF can be represented by a mathematical description that has an analytical form. However, only rarely the exact expression is known, and therefore, an expansion of functions is used, a so-called basis set. A basis set is a collection of 'simple' functions whose combinations make up the complex description of a full WF [93].

The partial differential time-dependent Schrödinger equation gives the equation of motion for the WF. In the case of an energy-wise conservative system, this function can be simplified and rewritten in a space- and time-dependent part, where the former is given by the time-independent, second-order differential Schrödinger equation (ti-SE):

$$\hat{H}\Psi = E\Psi, \tag{2.1}$$

which is an eigenvalue equation, where $\hat{H}$ is the Hamiltonian operator, Ψ the WF acting as the eigenstate, and E the energy acting as the eigenvalue [93]. The Hamiltonian operator function corresponds to the total energy (kinetic energy, T, and potential energy, V) of the system [93]. As an example, for a system of N electrons and M nuclei, the total Hamiltonian $\hat{H}$ is given by:

$$\begin{aligned}\hat{H} = &\sum_{i=1}^{N} -\frac{1}{2}\frac{\hbar^2}{m_i}\nabla_i^2 + \sum_{j=1}^{M} -\frac{1}{2}\frac{\hbar^2}{m_j}\nabla_j^2 + \frac{1}{2}\frac{e^2}{4\pi\epsilon_0}\sum_{i=1}^{N}\sum_{i'=1}^{N}\frac{1}{|\boldsymbol{r}_i - \boldsymbol{r}_{i'}|} \\ &+ \frac{1}{2}\frac{e^2}{4\pi\epsilon_0}\sum_{j=1}^{M}\sum_{j'=1}^{M}\frac{Z_j Z_{j'}}{|\boldsymbol{r}_j - \boldsymbol{r}_{j'}|} - \frac{1}{2}\frac{e^2}{4\pi\epsilon_0}\sum_{i=1}^{N}\sum_{j=1}^{M}\frac{Z_j}{|\boldsymbol{r}_i - \boldsymbol{r}_j|} \\ &= T_{\text{elec}} + T_{\text{nuclei}} + V_{\text{elec}} + V_{\text{nuclei}} + V_{\text{elec-nuclei}}\end{aligned} \tag{2.2}$$

Here, $\hbar$ is the reduced Planck's constant, $\boldsymbol{r}$ is the position of the particles, m

is the mass of the particle, e is the elementary charge, ϵ_0 is the vacuum permittivity, and Z is the atomic number of the corresponding nucleus. The main goal is now to obtain values for the energy, which is achieved by solving the ti-SE, i.e., by letting the Hamiltonian 'operate' on the WF. The solution gives the quantized energy levels of the system. The ground-state WF (eigenstate Ψ_0) corresponds to the ground-state energy (eigenvalue E_0).

The simplest molecule, H_2^+, comprises three particles, yet its ti-SE cannot be solved analytically [93]. To overcome this limitation, the Born-Oppenheimer approximation can be applied to the Hamiltonian. This approximation considers the significant relative difference in mass, and thus velocity, between electrons and nuclei, resulting in a timescale separation. As a result, the nuclei can be considered frozen, i.e., T_{nuclei} is set to zero and V_{nuclei} becomes a constant, which can be considered parametrically. The Hamiltonian now becomes the electronic Hamiltonian and the electronic ti-SE reads:

$$\hat{H}_{\text{elec}}\Psi_{\text{elec}} = E_{\text{elec}}\Psi_{\text{elec}}, \tag{2.3}$$

which can be written as,

$$\left(\sum_{i=1}^{N} -\frac{1}{2}\nabla_i^2 + \frac{1}{2}\sum_{i=1}^{N}\sum_{i'=1}^{N}\frac{1}{|\boldsymbol{r}_i - \boldsymbol{r}_{i'}|} - \frac{1}{2}\sum_{i=1}^{N}\sum_{j=1}^{M}\frac{Z_j}{|\boldsymbol{r}_i - \boldsymbol{r}_j|}\right)\psi_{\text{elec}} = E_{\text{elec}}\psi_{\text{elec}}, \tag{2.4}$$

where the Hartree atomic unit system was applied [94]. The eigenvalue of this equation gives the electronic energy contribution to the total energy of the system in a field of fixed nuclei [93].

2.1.1 Density Functional Theory

To solve the ti-SE for more complex systems, several techniques exist. In the following, we will discuss the semi-empirical density functional theory (DFT) method. The main problem with the ti-SE, and more specifically the many-electron WF, is the large degrees of freedom of the systems 'at least three per electron' resulting in an exponential scaling of the computational time. To circumvent this problem, the idea of DFT is to focus on the electron density $\rho(\boldsymbol{r})$. This results in a simplified Hamiltonian, which only depends on three

degrees of freedom [93, 95]. Although the formalism itself is exact, certain experimental-based parameters and approximations are still used to obtain a final result.

The principles of DFT are founded upon two theorems by Hohenberg-Kohn (HK) [96]. Also known as the existence theorem, the first HK theorem states that [93, 96]:

'The ground-state energy and all other ground-state electronic properties are uniquely determined by the electron density':

$$E_0 = E[\rho_0(\boldsymbol{r})]. \tag{2.5}$$

Here, E_0 is the ground-state energy, ρ is the electron density, and $\boldsymbol{r}$ is the position in 3D space. The expectation value of the electronic Hamiltonian is electronic energy, and we can therefore write [93]:

$$\begin{aligned} E[\rho(\boldsymbol{r})] &= T_{\text{elec}}[\rho(\boldsymbol{r})] + V_{\text{elec}}[\rho(\boldsymbol{r})] + V_{\text{elec-nuclei}}[\rho(\boldsymbol{r})] \\ &= E_{\text{HK}} + \int \rho(\boldsymbol{r}) V_{\text{elec-nuclei}}(\boldsymbol{r}) d\boldsymbol{r}. \end{aligned} \tag{2.6}$$

Here, E_{HK} is the HK-functional. This functional is universal for every system and includes the kinetic energy of the electrons and the electron-electron repulsion in the ground-state [93]. The integral is system-dependent and is based on the external potential resulting from fixed nuclei, external fields, etc. Known also as the variational formulation, the second HK theorem states that [93, 96]:

'For a trial density function $\rho'(\boldsymbol{r})$, the energy functional $E_0[\rho'(\boldsymbol{r})]$ cannot be less than the true ground-state energy of the molecule':

$$\text{if} \quad \rho'(\boldsymbol{r}) \neq \rho_0(\boldsymbol{r}); \quad \text{then} \quad E[\rho'(\boldsymbol{r})] > E[\rho_0(\boldsymbol{r})]. \tag{2.7}$$

One of the problems of the HK theorem is the electron-electron interaction, which is a two-body term. Also, the kinetic energy is problematic because there is no analytic form for it in terms of $\rho(\boldsymbol{r})$. In 1965, Kohn and Sham [97]

developed an approach based on non-interacting electrons and a correction term [93]:

$$E[\rho(\boldsymbol{r})]_{\mathrm{KS}} = T_{\mathrm{elec}}^{\text{non-int}}[\rho(\boldsymbol{r})] + V_{\mathrm{elec}}^{\text{non-int}}[\rho(\boldsymbol{r})] + V_{\text{elec-nuclei}}[\rho(\boldsymbol{r})] + E^{\mathrm{xc}}[\rho(\boldsymbol{r})]. \quad (2.8)$$

Here, $T_{\mathrm{elec}}^{\text{non-int}}(\rho)$ is the non-interacting electronic kinetic energy, $V_{\mathrm{elec}}^{\text{non-int}}(\rho)$ is the mean-field replacement of the Coulombic repulsion, and $E^{\mathrm{xc}}(\rho)$ is the so-called exchange-correlation energy, representing the total correction for the assumptions made. In other words, the system of independent electrons is now embedded into two external fields, one representing the external potential resulting from the nuclei, etc., and one representing the electron-electron interaction correction.

When the formalism ascribed above is applied, a set of coupled equations can be derived, each representing a single electron, which are referred to as 'orbitals' [93]. Next, the ti-SE can be rewritten into the Kohn-Sham (KS) equations [93]:

$$\hat{H}^{\mathrm{KS}}\psi^{\mathrm{KS}} = \epsilon^{\mathrm{KS}}\psi^{\mathrm{KS}}. \quad (2.9)$$

Here, ψ^{KS} is the one-electron KS orbital and ϵ^{KS} is the one-electron KS energy. Upon solving the KS equations self-consistently, where an initial guess density is used to obtain a new optimized density, the energy functional is minimized [93]. This procedure is repeated until convergence is reached. Once the 'most ideal' electron density is found, with the lowest corresponding electron energy, the forces on the nuclei can be determined. Finally, several algorithms exist to update the positions of the nuclei until the minimum energy (or force) configuration is found.

One of the reasons DFT can be considered semi-empirical is because of pseudopotentials [93]. While the core electrons of an atom are barely affected by the environment, the valence electrons of an atom may be regarded as 'more important' as they are largely responsible for bonding interactions and physical properties. Pseudopotentials are (simplified) potential functions that represent the interaction between valence electrons with the combined nucleus plus core electrons. They reduce the number of terms required for the plane wave expansion of the wavefunction, thereby reducing the computational cost

of the calculations. Another reason is that the exchange-correlation functional is not known exactly and is approximated by using 'physical intuition'.

2.2 Molecular Mechanics

Whereas QM provides an accurate description of the system based on quantum effects, MM employs a more simplified approach based on classical mechanics. Each atom in the system is considered a point-like (possibly charged) object. All atoms in the system experience different types of forces due to the interaction with other particles and external fields if present. In practice, the different types of interactions are represented by a functional description and a set of parameters, which are combined to produce the *force field*. Generically, the total energy (kinetic energy, T, plus potential energy, V) of a system of N particles can be expressed as:

$$\begin{aligned} E_{\text{tot}}(\boldsymbol{r}_1, ..., \boldsymbol{r}_N) &= T_{\text{tot}}(\boldsymbol{r}_1, ..., \boldsymbol{r}_N) + V_{\text{tot}}(\boldsymbol{r}_1, ..., \boldsymbol{r}_N) \\ &= \sum_i^N \frac{1}{2} m_i \boldsymbol{v}_i^2 + \sum_i^N V_0(\boldsymbol{r}_i) + \sum_{i<j}^N V_1(\boldsymbol{r}_i, \boldsymbol{r}_j) \\ &+ \sum_{i<j<k}^N V_2(\boldsymbol{r}_i, \boldsymbol{r}_j, \boldsymbol{r}_k) + ... + V_{\text{ext}}(\boldsymbol{r}_1, ..., \boldsymbol{r}_N). \end{aligned} \tag{2.10}$$

Here, V_0 is the intrinsic potential energy, V_1 is the pair-wise interaction, V_2 is the many-body interaction, and V_{ext} is the interaction with an external potential. The dots represent possible higher-body interaction terms. One should keep in mind that more elaborate descriptions of total energy exist.

2.2.1 Force Fields

In this section, the basic ideas behind a force field (FF) will be explained in terms of the valence force field (VFF). Then the FFs (also known as empirical potentials) used in this thesis will be briefly explained. As stated before, a FF describes the interactions between atoms based on a functional form with a system-specific set of parameters. From the FF, the potential energy of the

system can be calculated. The actual values of the parameters can be obtained via fitting based on either experimental data or DFT results. Put simply, we can distinguish two types of interactions between any two atoms in a system; i) strong bonded, covalent interactions, ii) weak non-bonded, van der Waals or electrostatic interactions [93, 98]. The idea is now to find a mathematical expression that can give a physical meaning to the interactions present. An example will be given that is loosely based on one of the simplest potentials available, the VFF [99], which was developed in 1975. In the most basic approximation, a covalent bond consists of two main components: i) bond stretching, ii) bond bending [98, 100]. The energy of two bonded atoms as a function of their distance can be expanded in a Taylor series based on virtual displacements. Near the energy minimum, the expansion can be truncated at the second order without a too high error, resulting in a harmonic potential. In the case of a small perturbation of the energy minimum, the system behaves linearly, i.e., if there is a displacement, the force changes linearly with that displacement. For large perturbations, the second-order approximation is inaccurate as nonlinear (anharmonic) contributions become more important. Therefore, in terms of a FF, a harmonic potential can be used [98]:

$$V_{\text{stretching}}(\boldsymbol{r}_i, \boldsymbol{r}_j) = k_b(r_{ij} - r_{0,ij})^2, \tag{2.11}$$

$$V_{\text{bending}}(\boldsymbol{r}_i, \boldsymbol{r}_j, \boldsymbol{r}_k) = k_\theta(\theta_{ijk} - \theta_{0,ijk})^2, \tag{2.12}$$

where k_b and k_θ are the harmonic constants for stretching and bending, respectively, $r_{0,ij}$ and $\theta_{0,ijk}$ are the equilibrium bond length and bond angle between two and three atoms, respectively, and the actual bond length and angle are represented by r_{ij} and θ_{ijk}, respectively. In this example, the physical system is now represented by a model of balls (atoms) connected via springs (bonds). In principle, one could also consider a dihedral torsion of the bonds. However, the energy contributions of this term are generally low [100]; especially when considering the systems that are studied in the works presented here, and are therefore not considered. The benefit of this model is its computational efficiency and the fact that the parameters can be easily fitted to experimental observables [100]. However, only slight deviations of the equilibrium bond distances and angles are correctly predicted, because beyond this regime the interactions are no longer elastic and thus become nonlinear. In practice, this

approach requires a fixed initial topology where all bonds and angles between different atoms need to be stored in a reference data file. This automatically implies that no bond breaking or formation can occur, since the file cannot be updated during the simulation.

While still considering a fundamental approximation, a non-covalent bond also consists of two main components: i) van der Waals interactions, ii) Coulombic interactions. The van der Waals interactions result from a perturbing electrostatic interaction between atoms and are characterized by a repulsive and attractive part. The most common approximation for representing the van der Waals interactions is the Lennard-Jones (LJ) potential [98, 101]:

$$V_{\mathrm{vdW}}(\boldsymbol{r}_i, \boldsymbol{r}_j) = 4\epsilon_{ij}\left[\left(\frac{\sigma_{ij}}{r_{ij}}\right)^{12} - \left(\frac{\sigma_{ij}}{r_{ij}}\right)^{6}\right], \tag{2.13}$$

where ϵ_{ij} represents the depth of the energy well and thus the interaction strength, while σ_{ij} relates to the equilibrium distance. The first part of the LJ potential represents the strong short-range repulsion, whereas the second part represents the weaker long-range attraction. The electrostatic Coulomb potential results from the interaction between charged atoms and can be represented by Coulomb's law [98, 101]:

$$V_{\mathrm{electrostatic}}(\boldsymbol{r}_i, \boldsymbol{r}_j) = \frac{q_i q_j}{4\pi\epsilon_0 r_{ij}}. \tag{2.14}$$

Here, q_i and q_j are the respective charges of each atom, and ϵ_0 is the vacuum permittivity. Coulomb forces are long-range and present computational difficulties concerning energy convergence. One way to deal with this is the commonly used Ewald summation [98]. In this approach, the long-range interactions are split into short-range and long-range contributions. Next, the short-range part is solved in real space, while the long-range part is solved in Fourier space.

For the studies presented in this work, several potentials were employed, which we will briefly discuss. For the calculations presented in Chap. 5, a potential developed by Sresht *et al.* in 2017 [102] was employed to simulate MoS_2 in the presence of water. This potential is based on the VFF potential described above and combines the earlier mentioned harmonic bond stretching

and angle bending potentials combined with an LJ potential. Moreover, it allows for setting fixed partial charges for the atoms. In this specific case, it has been used in combination with a non-polarizable q-SPC/Fw model for water, developed by Paesani *et al.* in 2006 [103]. Here, q-SPC/Fw is an acronym for a Quantum parametrized Simple Point Charge Flexible Water model and simulates water as a three-site molecule. In general, for an SPC water model, each atom has LJ parameters and a fixed partial charge. As will be the case for all potentials, a discussion on the motivation for choosing this specific potential can be found in the chapter related to the study employing that particular potential. In Tab. 2.1 and Fig. 2.1 a benchmark of all potentials used for simulating MoS_2 can be found. For VFF, we find that the local minimum is absent in the PES and the maximum energy barrier is slightly underestimated, whereas the structural parameters are in good agreement.

The Stillinger-Weber (SW) potential [107], developed in 1985, was used for the calculations presented in Chap. 4 to simulate MoS_2. Like the VFF potential, SW has a two-body bond stretching term and a three-body angle bending term. Both terms have an exponential in their definition, ensuring a proper convergence of the potential energy [108]. Compared to VFF, SW is an improvement because it can more accurately describe nonlinear physical properties such as mechanical deformation or thermal conductivity [100, 108]. Moreover, like VFF, its benefits are the clear physical interpretation, its high generality for a wide range of systems, and relatively low computational cost [105, 108]. Although bonds and angles are

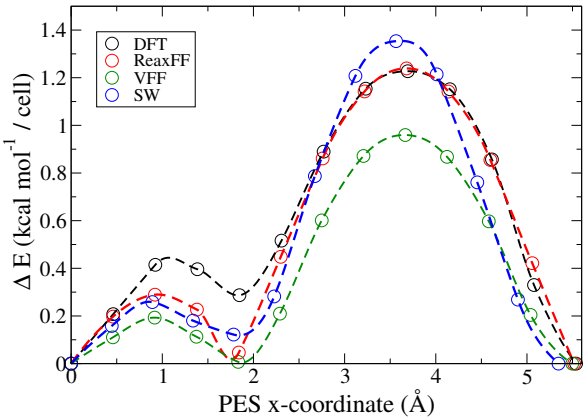

Figure 2.1: Static potential energy surfaces calculated per area of the unit cell for the long diagonal of the hexagonal unit cell. Four different cases are considered: i) in black DFT [104], ii) in red ReaxFF [105]), iii) in green VFF [102], and iv) in blue SW [106]. The dashed lines are obtained via an akima spline interpolation and serve merely as a guide to the eyes.

not required to be stored in a data file, SW is not believed to be suitable to simulate chemical reactivity. In fact, both VFF and SW have been shown to poorly reproduce reliable out-of-equilibrium results [105]. In our study, we used a parametrization by Jiang *et al.* [108], which was fitted to the phonon spectrum of inelastic neutron scattering experiments [105]. In this parametrization, the intralayer bonded interactions of MoS_2 are represented by five terms, representing five different types of bonded interactions present in a single layer of MoS_2, of which two represent a type of angle bending and three represent a type of bond stretching [108] (see Fig. 2.2). From the benchmark (Tab. 2.1 and Fig. 2.1), it can be concluded that it has high accuracy with respect to the PES, but that the structural parameters reveal discrepancies due to a relative in-plane compression.

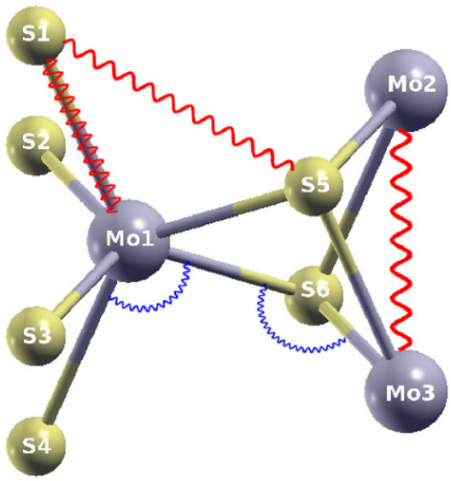

Figure 2.2: Here, the five different types of bonded interactions present in a single layer of MoS_2 are displayed, as described by the SW potential. Figure adapted from Ref. [108].

The reactive empirical bond order (REBO) potential, as parametrized by Brenner *et al.* in 2002 [109], was used for the calculations in Chap. 4 to simulate graphene. This potential allows for active bond breaking and formation. Moreover, atomic hybridization, in which the mixing of atomic orbitals leads to hybrid orbitals, is allowed. Bond order potentials do not consider atom pairs as bonded or non-bonded, but rather allow for different degrees of covalent bond strength. As a result, a practical implication is that the bond order potentials do not require a data file storing all bonds and angles between different atoms present. To determine the bonding state of an atom pair, this potential not only considers the direct pair interaction but also includes the 'local environment'. In other words, the strength of the potential depends on the spatial distance between two atoms and entails a correction for other neighboring atoms. As a result, the REBO potential allows for an improved description of covalently bonded sys-

tems and can simulate actual chemistry, as is the case for DFT, however, at a much lower computational cost [105, 109]. That being said, REBO requires significantly higher computational power than VFF and SW [105]. Importantly, as is the case for SW, REBO does not include Coulomb and van der Waals interactions, resulting in an inadequate description of specific properties of the system, such as the interlayer distance of lamellar systems [110]. A benchmark of this potential, which can be found in Appx. B, shows that the structural parameters are in good agreement with the experimental data and DFT results.

The reactive force field (ReaxFF), developed by van Duin *et al.* in 2001 [110], was used in the calculations presented in Chaps. 3 and 6 to simulate MoS_2 and hydrogen. The main benefit of ReaxFF is its precise prediction of the bonding behavior of a system due to its very complex functional form, where the total energy is subdivided into nine different contributions, each with a vast amount of parameters. The novelty of ReaxFF is that it allows atomic charges to vary based on the local chemical environment of the atoms [105]. As a result, ReaxFF is one of the most accurate potentials currently available. That being said, ReaxFF is also one of the most computationally costly existing classical potentials. The similarity between REBO and ReaxFF is that they are both so-called *second-generation bond-order-based potentials* [105, 109]. This means nothing more than the fact that improved analytical functions are used with a more extensive database to which the parameters are fitted [109]. The difference between REBO and ReaxFF is that the Coulomb and van der Waals interactions, plus several other *ad hoc* terms, are explicitly taken into account for ReaxFF, something which is especially important for a layered system [105]. Moreover, in the specific parametrization of ReaxFF that has been used here, the actual bond dissociation and reaction energy curves match DFT results. They are therefore believed to resemble reality more closely, which is not the case for REBO [105, 110]. The benchmark (Tab. 2.1 and Fig. 2.1) shows that the structural parameters closely resemble experiments and DFT, whereas for the PES, only the global maximum is in perfect agreement, and the local minimum is missing.

	VFF	SW	ReaxFF	Exp.	DFT
Lateral lattice constant (Å)	3.174	3.087	3.184	3.161	3.198
Perpendicular lattice constant (Å)	12.409	12.501	12.034	12.295	12.454
Mo-S distance (Å)	2.397	2.388	2.429	2.366	2.425
Mo-S-Mo (ϕ) angle (°)	82.910	80.524	81.899	83.816	82.504
S-Mo-S (θ) angle (°)	82.910	80.524	81.899	83.816	82.504
S-Mo-S (ψ) angle (°)	80.284	83.465	81.638	79.064	80.829
S-Mo-S (ω) angle (°)	135.057	136.182	135.532	134.634	135.247

Table 2.1: Structural parameters predicted by the VFF [102], SW [106], and ReaxFF [105] potential, together with reference data from X-ray diffraction experiments (Exp.) [111] and DFT calculations [104]. For the meaning of the various internal angles and for more details about the benchmark procedure, please refer to Ref. [112].

2.2.2 Molecular Dynamics

By using the potentials described above in the framework of MM, one can calculate the energy of a system and obtain its optimized structural geometry. Consider, for example, the following basic algorithm for such an MM energy minimization.

1. The energy of an initial configuration is calculated.
2. A minor repositioning of the atoms is performed, resulting in a different energy.
3. The old and new energies are compared, after which the lowest energy configuration is kept, and a new repositioning is performed.

The repositioning of the atoms can be performed in a random or ordered manner until (enough of) the phase space is sampled. Obviously, the above algorithm is far from ideal since a lot of irrelevant configurations are sampled. Far more efficient algorithms exist, of which two have been used in the works presented in this thesis, namely, the *conjugate gradient* algorithm and the *damped dynamics* algorithm. The conjugate gradient uses a combination of force gradients based on the previous and current steps, in search of a new

'direction' towards a minimum energy configuration, whereas in damped dynamics, actual (albeit non-realistic) molecular dynamics are performed based on the atomic force directions (the principle behind molecular dynamics is explained below). In this case, to find the minimum of an energy well, a damping parameter is used. In this type of calculation, one should keep in mind that no 'real' time-dependent dynamics are obtained, e.g., conformational changes of the structure in time. Moreover, although the atoms can possess kinetic energy, the related temperature has no physical meaning.

To simulate the actual dynamics of a system, one can resort to classical *molecular dynamics* (MD). A very comprehensive overview is given in Refs. [98, 101], parts of which will be summarized below. In the schematic below, a basic algorithm is displayed for an MD simulation, as used in the works presented here: [101]

MD simulation	**Simple MD algorithm**
`call init`	Initialize system
`t=0`	Set time to zero
`do while t <= T`	MD loop desired time T
`call force`	Determine system forces
`call integrate`	Integrate equations of motion
`t = t + Δt`	Update time
`call sample`	Obtain desired observable
`enddo`	End loop
`stop`	
`end`	

In this schematic, a possible minimization and equilibration of the system are left out for clarity. In the first step, the system is initialized. Although this can be achieved in different ways, in the case of the works presented herein, experimental data is used to define the initial positions of all atoms, which are subsequently relaxed according to the potential. After that, the actual production run is performed. As long as the running time is below the total desired time, a loop is performed. Firstly, the forces are calculated based on the potential. This is, in fact, the most computationally demanding part of

the simulation and will be explained in more detail below. Next, using the calculated forces, the atomic positions and velocities are updated based on the Newtonian equations of motion. Finally, the observables of interest are stored in an output file.

The previously mentioned calculation of the forces is based on the potential used to describe the atomic interactions and any possible external force. Using Newton's equations of motion, we can relate the energy to the change of positions via the force:

$$\begin{aligned} \vec{F}_i(\mathbf{r}) &= -\vec{\nabla}_i V(\mathbf{r}) \\ \vec{F}_i(\mathbf{r}) &= m_i \cdot \vec{a}_i(\mathbf{r}) = m_i \cdot \frac{d^2\mathbf{r}_i}{dt^2} \\ \vec{\nabla}_i V(\mathbf{r}) &= -m_i \cdot \frac{d^2\mathbf{r}_i}{dt^2} \end{aligned} \tag{2.15}$$

Although the above relation is exact, it is not analytically solvable when V contains nonlinear terms, and so a numerical approach is required. The numerical technique adopted here is the *velocity Verlet* algorithm. Other algorithms do exist, and for more information, the reader is directed to Ref. [101]. The basic principle of the velocity Verlet algorithm is a recasting of a Taylor expansion of the positions, $\mathbf{r}(t)$, with respect to time, resulting in an equation for the update of the position and the velocity:

$$\mathbf{r}(t+\Delta t) = \mathbf{r}(t) + \mathbf{v}(t)\Delta t + \frac{\mathbf{f}(t)}{2m}\Delta t^2, \tag{2.16}$$

$$\mathbf{v}(t+\Delta t) = \mathbf{v}(t) + \frac{\mathbf{f}(t+\Delta t) + \mathbf{f}(t)}{2m}\Delta t, \tag{2.17}$$

where Δt is the time step and m is the mass of the particle. In principle, this integration scheme avoids energy drift along the trajectory. However, because both the expansion and Δt are finite, this time integration is an approximation of reality. To have a reliable outcome of the simulation, the time step size is of great importance and always needs to be carefully benchmarked against the conservation of energy. If the time step is too small, a proper sampling of the time phase space (clearly, this depends on the observable of interest) will not be achieved due to the long simulation time and computational costs. If the time step is too large, e.g., greater than the highest interatomic vibration frequency, the results may be incorrect because the atomic motions and, therefore, interactions are not properly simulated.

In the preceding sections, the basic principles of an MD simulation have been outlined. Several different software packages for performing the MD numerical integration exists. All works presented herein have been performed using the Large-scale Atomic/Molecular massively Parallel Simulator (LAMMPS) [113]. The LAMMPS package was designed in 1995 and is mostly written in C++. LAMMPS is a free and open-source package with a proven computational efficiency achieved via the implementation of the Message Passing Interface (MPI), Open Multi-Processing (OpenMP), etc.

The main idea underpinning the MD simulations presented in this thesis is straightforward, and the components closely resemble those of any real-life experiment. Three main parts can be distinguished: i) energy minimization, ii) temperature and load equilibration, and iii) production run. In all steps, so-called *periodic boundary conditions* are applied to the simulation box in order to simulate an 'infinite' system by replicating the system in every Cartesian direction. The energy minimization process has already been explained. Optionally, the simulation box can also be allowed to expand or compress during this procedure. In the second part, the system is equilibrated to any external conditions, such as temperature and load. In our studies, the temperature is defined based on the relation between the average kinetic energy and the equipartition theorem ($\sum_{i=1}^{N} \frac{1}{2} m_i \boldsymbol{v}_i^2 = \frac{3}{2} N K_b T$), and load is defined as a force applied in z-direction acting on an area parallel to the basal plane of the system. In general, equilibration is performed in two steps. In the first step, a velocity is given to the atoms based on the Boltzmann distribution, resulting in the initial temperature. For the systems and temperatures used, consisting of crystal structures and temperatures of hundreds of Kelvins, it is possible to directly set the temperature instead of slowly heating the system. From a theoretical point of view, pure basic MD simulations sample the microcanonical ensemble, where the number of particles, N, the volume, V, and the energy, E, are kept constant. To circumvent this problem and to keep the temperature constant, a so-called *thermostat* is used, which controls the velocity (temperature) of the atoms in the system. Keeping the temperature constant also improves comparability to real experiments, within which it is not possible to keep the energy of the system constant. In contrast, it is possible to keep the temperature constant [98].

In the works presented here, two types of thermostats have been used, namely the stochastic Langevin thermostat and the deterministic Nose-Hoover thermostat. The Langevin thermostat [114] creates an artificial white noise, e.g., consider a big particle in a medium of small particles modeled as a continuum. The white noise represents an implicit background solvent. The solvent particles give random 'kicks', represented by random forces, to the atoms in the system under study. As a result, the velocity vectors of the atoms change. The Langevin thermostat is controlled by a damping parameter, which sets the timescale of the relaxation of the kicks and thereby represents how it is coupled to the system. The Nose-Hoover thermostat [115, 116, 117, 118] creates one imaginary particle with a certain mass through an extra degree of freedom, representing a heat bath in which kinetic energy can be 'stored'. The actual value of the mass determines the amount of coupling to the system. The system can now exchange heat with the reservoir, which allows for control of the temperature.

Next, it is possible to add constraints to the system in which the degrees of freedom of (some) atoms are reduced. On the one hand, these constraints can be used in order to speed up the simulations (e.g. removing the 'fast' degrees of freedom of the system may allow the use of a larger time step for the integration of the equations of motion), while in some cases they can be exploited in order to simulate e.g. a strong adhesion between the rigid part of the system and a substrate. Moreover, constraints, such as rigidity, sometimes help perform a particular technical 'trick' during the simulation. As an example, consider the sliding of layered systems. In this case, the lowest layer should remain static, which can be achieved by leaving these atoms out of the time integration or by zeroing the forces on the atoms in this layer. For the top layer to move with a constant velocity, the layer is made rigid, an initial velocity is set, and all future forces are zeroed in the desired sliding direction. If the forces were not zeroed, the system would experience fluctuations in the velocity during sliding. During the first part of the equilibration, the force in the z-direction, parallel to the plane of the systems, is increased linearly until the desired load is achieved. In the second step, when the system has the desired temperature and load, it is equilibrated while keeping the external conditions constant.

In the final step of an MD simulation, the actual production run is performed. During the production run, averages of the system can be obtained for any observable that is expressible in terms of position and velocity/momentum [98, 101]. The theory behind this is based on thermodynamics and the ergodicity theorem, which states that the time average of any observable obtained during a long simulation equals the phase space average [98]. To avoid bias from the initial condition of the system or because of undersampling the phase space due to too short production runs, it is good practice to run several unique runs in parallel and combine the averages. In general, two types of simulation can be performed. In *equilibrium MD*, the phase space is sampled to obtain information about, for example, structural fluctuations and thus the conformational behavior. During equilibrium dynamics, no external forces are driving the system in a particular direction. As a result, systems might get trapped in local energy minima because there is not enough energy provided to the system to overcome the energy barriers.

The other type of MD simulations are the so-called *out-of-equilibrium MD*, which are discussed in the works of Vanossi *et al.* [16] and Manini *et al.* [30]. There is a (constant) external force or changing temperature driving the system out of equilibrium in these types of simulations. A perfect example is the simulation of frictional sliding and the resulting stick-slip dynamics. In the case of out-of-equilibrium simulations, the external parameters driving the system provide energy to the system. Here, the thermostat no longer only functions to keep the temperature of the system constant as time evolves, but also as an energy drain for the generation of so-called *Joule heat* from friction to avoid heating the system significantly [16]. In real experiments, the same phenomenon occurs. Joule heat production at the sliding interface results, for example, in phonon excitation, allowing the dispersion of the heat produced into the bulk [16]. However, the problem with a thermostat is that tribological artifacts might be observed due to an unrealistic type of damped dynamics [16]. One can solve this problem by considering larger systems in which only a part of the system, away from the sliding interface, is coupled to a thermostat, as shown in Fig. 2.3.

Next, several drawbacks of MD simulations will be discussed in the case of frictional sliding simulations. As was the case with selecting the time step for the time integration, the sliding velocity should be chosen carefully. The references here are real experiments, where typical velocities of 0.1 to 10.0 m/s are used in macroscopic experiments, and velocities of approximately 1.0 μm/s are used in nanoscale AFM experiments [30]. Although dependent on the property of interest, as a general rule and because typical lattice spacings are around 10 Å (10^{-9} m) [16], one should at least aim to simulate in the nanosecond range (10^{-9} s) in order to obtain relevant statistics.

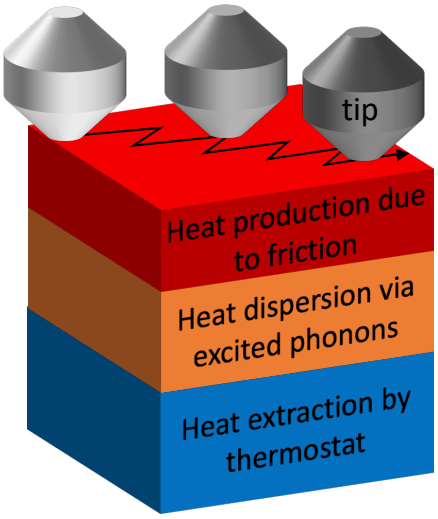

Figure 2.3: Example of a correct way of controlling temperature in an MD system, composed of a substrate over which a tip is sliding, resulting in the production of Joule heat.

Generally speaking (of course this depends greatly on the system size and the type of potential used), it is reasonable to assume to produce 1 μs of production run per day, highlighting the fact that only macroscopic sliding velocities are realistic [30]. Due to the relatively high sliding velocities in MD simulations, the characteristic stick-slip dynamics are no longer believed to result from thermal activation but rather to be the result of other athermal dissipative processes [16]. In fact, it is interesting to note that the transition of stick-slip dynamics to smooth sliding, as a result of increasing the velocity, can occur both in FFM and in MD, but that the values at which this happens differ by six orders of magnitude [30]. The exact reason is still under debate. However, it is considered to be related to the different types of effective mass distribution and spring-force constants [16, 30]. Apart from sliding velocity, the concept of aging, in which the type of interaction between substrates changes according to the time and relaxation of the structure, is not captured by MD, but does influence the frictional behavior in real experiments [16].

2.3 In brief

Although experiments provide a wealth of information, certain drawbacks can currently only be overcome using theoretical modeling techniques at different time and length scales. The main benefit of simulation techniques is the ability to create a setup that can be fully controlled, not only regarding the environment but also regarding the system itself. The basic principles of different modeling approaches to perform such atomistic simulations have been discussed in the above. Firstly, the accurate but computationally expensive QM calculations were reviewed. Although these types of calculations allow valuable insights into the electronic properties of systems, they are, in general, not suitable for dynamical simulations used to study friction. They can, however, be used to fit the parameters of the FFs used in the second type of modeling technique, MD simulations. MD simulations offer a wide variety of properties that can be studied, albeit less accurately than QM. The appropriate choice of the potential used determines the precision of the simulation and its efficiency.

Computational modeling methods have become an integral part of many fields. On the one hand, experimental data can be used to validate computational results. On the other hand, computational results can explain experimental phenomena that would otherwise remain unaccounted for. One approach, be it experimental or theoretical, does not exclude the need and the relevance of the other; it is the synergy between both that creates real scientific power. In the following chapters, these techniques are employed to study the frictional and conformational behavior of MoS_2 in different systems and environments.

3

Pure MoS_2

3.1 Introduction

In Chap. 1, it was mentioned that the motivation to study solid lubricants is multifold. For example, it is estimated that $\sim 23\%$ of the world's total energy consumption is lost to friction and wear [1]. To avoid this from happening and to meet the ever-increasing sustainability demands, lubricants must be used. However, classical wet lubricants have reached the limits of their effective working range due to increasing tough working conditions, such as extremely high/low temperatures and pressures, and increasing dimensional confinement. Here, solid lubricants offer a workaround, mainly due to their 2D layered crystal structures. Furthermore, solid lubricants have been linked to superlubricity. The exact criteria for superlubricity remain, however, a matter of debate. That being said, the consensus of the tribology community is that to achieve

superlubricity, the structure should at least be rotationally or structurally incommensurate. In other words, the layers of the structure should have an intrinsic rotational mismatch angle in the case of homostructures, or be a heterostructure with different lattice constants. Of course, a combination of the above-mentioned criteria would also suffice.

Several studies have already focused on the changing frictional behavior of MoS_2 when varying the intrinsic contact from commensurate to incommensurate. MoS_2 is often chosen because it can be considered a prototypical solid lubricant. In 2010, Onodera *et al.* [59] found that using MD simulations, the mobile layer of a bilayered system follows the minimum energy path (MEP) across the PES. Additionally, they found a relation between the intrinsic commensurability of MoS_2 and the magnitude of the frictional forces by introducing a relative mismatch angle between the layers. For aligned commensurate structures, they found a 'zig-zag' type of sliding dynamics (the sliding did not occur along a straight line), whereas for rotated incommensurate contacts, smooth sliding dynamics along a straight line were observed. Moreover, the zig-zag dynamics were characterized by frictional forces that were two orders of magnitude higher than those found for smooth sliding.

In 2014, Levita *et al.* [104] studied the effect of load on commensurate bilayers of MoS_2, using DFT calculations. It was found that the corrugation of the PES increases for higher loads, as one might expect from the short-range electrostatic interactions. In 2017, Irving *et al.* [51] studied the effect of commensurability on the PES corrugation of bilayer MoS_2 using DFT calculations. By introducing a misfit angle, i.e., changing from a commensurate to an incommensurate structure, it was shown that the PES corrugation vanishes. By considering the results of the three studies presented above, we expected that a change in commensurability or load would induce a change in PES corrugation, and thereby indirectly influence the frictional forces observed during sliding.

In the work presented in this chapter, a different approach to reach a state of superlubricity was considered. Here, we studied the frictional anisotropy of bilayer MoS_2. Frictional anisotropy means that the frictional properties of the

material in question depend on the sliding direction considered. The opposite of frictional anisotropy is called frictional isotropy. We studied the dependence of friction on sliding by considering various sliding directions, instead of a change in contact commensurability. More precisely, we studied the effect of load and sliding direction on the frictional forces of an aligned commensurate bilayer of MoS_2 by performing MD simulations with a computationally expensive but accurate FF, namely the ReaxFF potential [105].

3.2 Approaches and Problems

This was the first project within the framework of this thesis. Therefore, an essential part of this project consisted of getting familiar with the field of computational tribology. An overview of this literature study, with a primary focus on the solid lubricant MoS_2, has been presented in Chap. 1. Moreover, a significant amount of time was spent on getting familiar with the practical use of the modeling software LAMMPS [113] and coding languages such as Fortran for subsequent analysis of the raw data.

The idea for our computational setup was relatively straightforward. We considered an infinite bilayer system of commensurate $2H_c$-MoS_2 by applying periodic boundary conditions. To enforce a relative sliding, the bottom layer was held static by fixing the bottommost sulfur layer in the x-, y- and z-direction. The top layer was made mobile by applying a driving force in the desired sliding direction. During the simulation, the relative orientation between the layers remained unchanged, i.e., the structure remained commensurate. Considering the hexagonal symmetry of our system, a range of 60° in different sliding directions suffices to explore the behavior at any angle. After obtaining the structures, different loads in the z-direction were applied to the system to observe a possible change in frictional forces.

Apart from the general benchmarks of the FF and optimizations of the calculations themselves, the critical step in setting up our calculations was the technical implementation of creating a mobile top layer. Several approaches were considered. In the first approach, a constant external sliding velocity

was applied to the mobile layer in the xy-plane, over a range of 60° and with incremental steps of 10°. This was done by applying a velocity vector in the x- and y-direction to the topmost sulfur atoms in the mobile layer. Moreover, the internal forces in the x- and y-direction were 'zeroed' at every time step by an equal but opposite external force, which prevents a change in velocity. The frictional force is now represented by the average of the negative external instantaneous force. However, an undesired effect of this computational setup is that the mobile layer is forced to slide in a straight line, aligned along the direction of the driving force: this is an unnatural dynamic and constrains the system too much. This had already been shown by Onodera *et al.* [59], who proved that the mobile layer prefers to follow the MEP based on the PES, which is not a straight line in the case of commensurate contacts.

In another attempt to obtain more realistic dynamics, we considered a moving spring with a particular directional velocity, connected to the mobile layer. However, the softness of the spring prevented us from enforcing the sliding in a particular direction. We found that, independently of the sliding direction of the moving spring, the mobile layer would always tend to follow the same path. This path along 30°, where 0° represents sliding along the Mo-S bonds, would later prove to be the lowest frictional path for sliding of a commensurate bilayer of MoS_2, as evidenced by the results in the paper attached below.

Finally, we considered another approach in the spirit of our first attempt. Instead of changing the driving force vector, we rotated the bilayer system as a whole, ranging from 0° to 60°, with steps of 10°, while applying only a single component velocity vector. As a result, only the forces of this component (in our case the y-direction) had to be canceled. Consequently, the frictional force is now represented by a scalar. Moreover, the mobile layer was no longer forced to slide along a straight line and was free to follow the MEP orthogonal to the sliding direction (x-direction).

After obtaining our results, the main challenge was to determine the frictional force along the trajectory, based on the instantaneous external force.

One way to achieve this is by using the dissipated work W, given by:

$$W = \int_0^\tau F_{\text{ext}}(t) v dt, \tag{3.1}$$

with F_{ext} the instantaneous scalar force along the sliding direction and v the sliding velocity. Theoretically, taking the slope of the work versus the traversed distance should give the frictional force. However, due to the significant corrugation of the resulting profile for the dissipated work, it was impossible to define a consistent method to do this.

One could try to circumvent this problem by simply taking the running average of the instantaneous frictional forces along the trajectory. However, similar to the previous approach, statistical uncertainty produced unreliable results. Although we run relatively long simulations (2.5 nanoseconds), the fluctuations of the external forces were high. One way to circumvent this problem is to increase the sampling, which provides more accurate statistics on features with a slowly convergent average. However, computational resources did not allow us to follow this path. Another approach is to apply the so-called *bootstrap method*, which can increase the statistical accuracy of averages that are based solely on a subgroup of a complete dataset [119]. This is an averaging method that is based on random sampling. In our case, the complete dataset would be a very long trajectory, whereas our actual results present the subgroup. By applying this method, we found meaningful results for the frictional forces.

3.3 Results and Outlook

Our study led to several observations and results. Firstly, we found a relation between the sliding direction and the type of sliding dynamics. For sliding along the Mo-S bonds (0° and 60°), which we defined as commensurate sliding of the commensurate contact, we found highly dissipative stick-slip dynamics, with a clear separation of timescales between the 'stick' and 'slip' moments. Here, the slip was characterized by a high-velocity regime, whereas a low-velocity regime characterized the stick. The actual energy dissipation occurred

during the slip phase. For all directions that were not along the Mo-S bonds, which we defined as incommensurate sliding of the commensurate contact, we found smooth sliding dynamics with low energy dissipation. Furthermore, we found a relation between the frictional force and the load imposed on the system, and between the frictional force and the misfit angle between the driving force and the actual sliding direction. Finally, for the first time, we have shown that superlubricity can also be achieved within commensurate contacts from a theoretical point of view. These findings once more indicate that friction, and more specifically superlubricity, is highly complex and determined by more/other nonlinear mechanisms than is currently understood.

I was the main author of this work and was responsible for the conceptualization, data production and subsequent analysis, and the writing of the original draft. All results of this study have been published in the Computational Materials Science journal [21]. This is an impacted journal, which had an impact factor of 2.863 in 2019 and belongs to the quartile category Q2 in the field of materials science. A copy of the manuscript is attached below.

Computational Materials Science 163 (2019) 17–23

Contents lists available at ScienceDirect

Computational Materials Science

journal homepage: www.elsevier.com/locate/commatsci

Superlubricity achieved for commensurate sliding: MoS_2 frictional anisotropy *in silico*

Victor E.P. Claerbout*, Tomas Polcar, Paolo Nicolini*

Department of Control Engineering, Faculty of Electrical Engineering, Czech Technical University, Karlovo náměstí 13, 121 35 Prague 2, Czech Republic

ARTICLE INFO

Keywords:
Molybdenum disulfide
Frictional anisotropy
Superlubricity
Molecular dynamics simulations
Tribology

ABSTRACT

In the past decades, MoS_2 has received substantial attention from the tribology community due to its excellent frictional properties. However, a fundamental understanding of the mechanisms determining friction at the nanoscale is yet to be achieved. The general consensus is that one of the ingredients required for obtaining the superlubric regime when sliding layers of MoS_2 atop each other is incommensurability. Herein, we report on a molecular dynamics study focused on studying the effects of the sliding direction on the frictional properties of commensurate MoS_2. It is found that different types of dynamics are obtained with different sliding directions, with the stick-slip dynamics characterized by a highly dissipative behavior. Also, it is found that there is a relation linking the mismatch angle between the driving force and the actual trajectory and the load-dependence of the frictional force. We show, for the first time with a computational study, that incommensurability is not required for achieving the superlubric behavior of MoS_2.

1. Introduction

It has been estimated that almost one quarter of the world's total energy production is lost in tribological contacts, *i.e.*, due to *friction* and wear [1]. Nevertheless, friction is a complex phenomenon that involves a plethora of events, the exact mechanisms of which are still not fully understood. Roughly speaking, frictional forces are referred to as those effects that thwart the relative motion between two bodies in contact. The general idea to reduce friction and wear is the introduction of a new substance at the interface, called a *lubricant*. The practical implementation goes back as far as the history of mankind, by the application of water or oils in the sliding contact.

Peculiar conditions (*e.g.*, high temperatures, extreme contact pressures) pose problems in the possibility of using liquid lubricants, leading to the introduction of *solid lubricants* [2]. For heavily loaded contacts, the most studied solid lubricants are graphene/graphite [3] and members of the transition metal dichalcogenides (TMDs) family. TMDs are especially intriguing because of their versatile properties and diverse chemistry [4]. They are lamellar crystals with general formula MX_2, M being a transition metal (Mo, W) and X being a chalcogen (S, Se, Te). The sixfold hexagonal symmetry of TMDs, where the metal is positioned between the chalcogens (X-M-X), allows for several crystal forms. The single layer can either be trigonal prismatic or octahedral and the bulk is most commonly found in the trigonal (1T), hexagonal (2H) or rhombohedral (3R) polytypes [4]. Within the TMD family, molybdenum disulfide (MoS_2) is perhaps the most known member, not only for its applications in catalysis [5–7] and microelectronics [8,9] but also as solid lubricant [10]. Abundant in nature [11], MoS_2 is mostly found in the 2H configuration [12]. The weak inter-layer van der Waals and electrostatic interactions (in opposition to the strong covalent intra-layer bonds) allow layers to slide with relatively small effort.

The sliding regime in which the effectiveness of the lubricant makes the friction almost completely vanishing is called superlubricity [10,13,14], with coefficients of friction lower than 0.01. The enormous potential of superlubricity on the reduction of the world's energy consumption have triggered the establishment of a whole new scientific branch. In fact, starting from 1990s, superlubric contacts have been identified for MoS_2 [15], graphite [16] and diamond-like coatings [17]. For the former two mentioned lubricants, the general consensus in the tribology community is that the three following requirements are to be met to obtain the superlubric regime. Namely, (*i*) the atoms at the sliding interface should only experience weak interacting forces (*e.g.*, van der Waals), (*ii*) the sliding surfaces should be free from any contaminants and be atomically flat, and (*iii*) there should be a non-zero misfit angle between the layers [10]. These conditions lead to the cancellation of frictional forces [15] allowing superlubricity. The latter requirement is of particular interest, since a finite misfit angle produces

* Corresponding authors.
E-mail addresses: claervic@fel.cvut.cz (V.E.P. Claerbout), nicolpao@fel.cvut.cz (P. Nicolini).

https://doi.org/10.1016/j.commatsci.2019.03.019
Received 20 December 2018; Received in revised form 28 February 2019; Accepted 11 March 2019

locally incommensurate contacts, and, to the best of our knowledge, incommensurability between the two surfaces in contact is believed to be a necessary condition for achieving superlubricity.

In this regard, Onodera et al. studied the dependence of friction on the misfit angle between two layers of MoS_2 using molecular dynamics (MD) simulations [18]. They found that commensurate structures present frictional forces two orders of magnitude larger than those for incommensurate structures. This difference was explained due to the cancellation of forces in the incommensurate case, which moreover lead to smooth sliding dynamics compared to a zig-zag motion for the commensurate structures. However, the sliding velocity was set at 100 m/s, which is unrealistic for tribological contacts. With increasing velocities the mobile layer tends to "fly" over the static layers, weakening the effect of the interaction with the underlying layer. This is also qualitatively confirmed by the fact that the actual sliding path presents large deviations from the most favorable one, *i.e.*, the minimum energy path (MEP). Moreover, the fact that a small flake (*i.e.*, a flake with high ratio of perimeter to area) was used as a mobile layer automatically introduces unwanted border effects. By means of calculations based on the density functional theory (DFT), Levita et al. studied the sliding properties of commensurate R0 (parallel) and R180 (anti-parallel) MoS_2 bilayers [19]. They found that the corrugation of the static sliding potential energy surface (PES) increases with an increasing load for the R180 stacking. Interestingly, it turned out that, although this corrugation leads to an energetically more favorable configuration, it also results in a overall more unfavorable MEP compared to the R0 case. More recently, some of us elaborated on this and studied incommensurate MoS_2 bilayers [20]. It was found that the PES roughness can drop as much as four orders of magnitude upon introducing a misfit angle of approximately 30°. This observation might be directly related to the earlier observed smooth dynamics of incommensurate structures during sliding [18]. However, one should keep in mind that the latter DFT studies present purely static results, whereas it is known that friction is rather a dynamical response to an external stimulus. Interestingly, we are aware of only one experimental study mentioning the dependence of the frictional behavior on the sliding direction for MoS_2 [21]. Miura et al. found that MoS_2 flakes on top of a MoS_2 substrate tend to remain commensurate during sliding. It was found that the frictional force is proportional to the applied load, in accordance with Amontons' law. Moreover, a correlation between the mismatch angle (between the pulling force and the actual sliding direction) and the frictional forces was observed. Although the authors observed that reducing the value of this angle leads to a reduced frictional force, a detail explanation is yet to be provided. More recently, by applying a novel technique, Li et al. managed for the first time to experimentally quantify the excellent frictional properties of bilayer MoS_2 at nanoscale [22]. They reported coefficients of friction as low as 10^{-4}, clearly proving the superlubricity of MoS_2.

A question that might arise is whether incommensurability is the only way to explain the low energy dissipation observed during sliding in the superlubric regime. Differently from the studies mentioned above, where the effect of structural incommensurability has been investigated, in this paper we focus on the effect of the sliding angle on the frictional behavior of MoS_2. By means of classical MD simulations, we aim to study the tribological properties of a bilayer R180 commensurate configuration. On the one hand the goal of this paper is to provide a novel way to interpret the experimental data [15,22], whilst on the other hand our results might provide a motivation for experiments using a different approach to the problem.

Table 1
Structural parameters predicted by the ReaxFF model, together with reference data from X-ray diffraction experiments and density functional theory (DFT) calculations. For the meaning of the various internal angles and for more details about the benchmark procedure, please refer to Ref. [25].

	ReaxFF [24]	Experimental [12]	DFT [19]
Lateral lattice constant (Å)	3.184	3.161	3.198
Perpendicular lattice constant (Å)	12.034	12.295	12.454
Mo-S distance (Å)	2.429	2.366	2.425
Interlayer distance (Å)	2.841	3.135	3.082
Mo-S-Mo (ϕ) angle (°)	81.899	83.816	82.504
S-Mo-S (θ) angle (°)	81.899	83.816	82.504
S-Mo-S (ψ) angle (°)	81.638	79.064	80.829
S-Mo-S (ω) angle (°)	135.532	134.634	135.247

2. Computational methods

All classical simulations have been performed using the LAMMPS package [23] and the ReaxFF interaction potential for MoS_2 [24]. First of all, the performance of this potential, in predicting the structure and the sliding energetics of a MoS_2 bilayer, was assessed and these outcomes were compared with experimental [12] and first principles [19] results. In Table 1, the results for the structural parameters found in experiment, first principles calculations and via ReaxFF simulations are summarized, whilst in Fig. 1 the comparison between first principles and ReaxFF on the static sliding PES are reported. From Table 1, one can see that the agreement between the structure predicted by the ReaxFF model and both experimental and DFT references is fairly good (for most properties, the ReaxFF description performs almost equivalently to the DFT one). From Fig. 1, it is evident that the heights of the global maximum obtained with the ReaxFF model and DFT calculations are basically coincident. From these outcomes, also taking into account the results reported in Ref. [25], one can conclude that the ReaxFF description is among the best currently available classical potentials.

As a result of the hexagonal symmetry of MoS_2, it suffices to consider any 60° span of the 360° round angle, in order to study the frictional behavior of MoS_2 as a function of the sliding angle. Here, the 0° sliding angle is represented by the projection of the Mo-S bond direction onto a basal plane (see Fig. 2). In fact sliding with an angle of 0° corresponds to sliding with an angle of 60° but in the opposite direction, regardless the orientation of the reference frame. In order not to introduce any artifacts into the sliding dynamics, the system was also allowed to slide in the direction perpendicular to the driving force. In other words, it was avoided to force the system to slide in a straight line. This can be achieved by giving a driving force *e.g.* only in the *y*-direction while keeping the forces in the other directions unchanged. From a practical point of view, this means that one has to rotate the system in order to simulate different sliding angles. To create the periodic supercells of these systems, we used an adapted version of the protocol described in Ref. [26]. A schematic of the practical implementation into LAMMPS is shown in Fig. 2. The bottommost sulfur atoms (S1) were fixed in all directions. Due to the intra-layer covalent bonds, this prevents the whole bottom MoS_2 layer to move in the *xy*-plane during sliding, or to shift vertically when a load is applied in the *z*-direction. In order to make the mobile layer slide, a constant velocity of 5.0 m/s in the *y*-direction was enforced to the topmost sulfur atoms ($S2^{'}$), *i.e.*, this group of atoms was kept rigid during the simulation. This was achieved by setting an initial velocity to all atoms belonging to the $S2^{'}$ group in the *y*-direction and thereafter canceling the forces in the same direction at every step. The forces in the other directions were left unchanged to allow displacements both in the *x*- and *z*-directions.

In total 7 different systems were studied, all consisting of MoS_2 bilayers in the R180 commensurate configuration, but each one rotated with a different angle ranging from 0° to 60° and with increments of approximately 10°. Next, 6 different configurations per system based on a different normal force applied to the system were considered, giving an equivalent pressure which ranges from −1 to 4 GPa and with steps of 1 GPa[1]. Each system consisted of around 1250 atoms and had a size

[1] The negative value of the pressure has to be considered as the result of

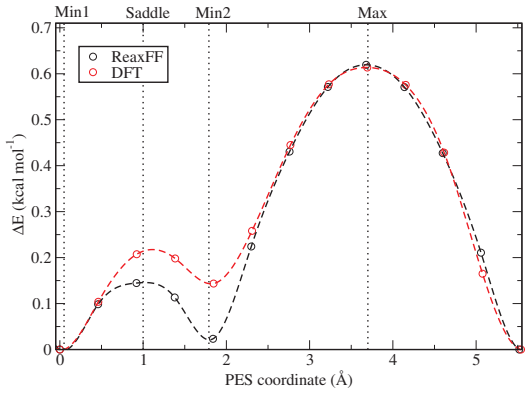

Fig. 1. Lateral potential energy surfaces obtained by translating a MoS_2 layer atop a static one along the long diagonal of the hexagonal unit cell for the R180 stacking. Energy differences are given per MoS_2 unit. Dashed lines are guides for the eye. We distinguish two different minima (min1 and min2) connected via either a saddle point or a maximum. For more details about the used methodology, please refer to Ref. [25].

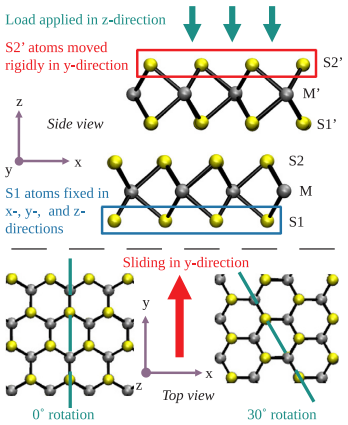

Fig. 2. Schematic of computational setup. In the upper frame a side view is presented. In the lower frame a top view is shown. In order to simulate different sliding angles the system is counter-clockwise rotated from 0° to 60° with approximate steps of 10°. Molybdenum and sulfur atoms are in gray and yellow, respectively. Figure obtained with VMD [27].

of approximately 30 and 50 Å in the *x*- and *y*-directions respectively. 20 Å of vacuum in the *z*-direction was added to every configuration to prevent the interaction with images when applying periodic boundary conditions. After an energy minimization with the conjugate gradient method, the system was equilibrated in two steps: first, linearly increasing the normal pressure from 0 GPa to the set value for 10.0 ps, and then further equilibrating for 100.0 ps under constant load. Next, every 50.0 ps a configuration was sampled; these were the starting points for the subsequent MD production runs. Finally, for each initial configuration, 0.5 ns of dynamics were produced, totaling the sliding dynamics to 2.5 ns per sliding angle-load pair. The equations of motion have been integrated with a timestep of 0.1 fs, while the Langevin thermostat was used to maintain the temperature at 300 K.

(*footnote continued*)
applying a force counteracting the adhesion.

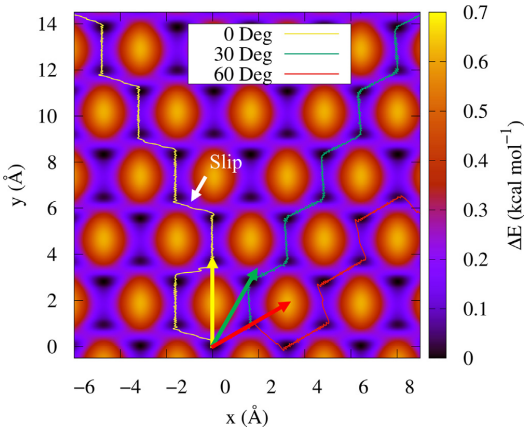

Fig. 3. Projections of MD trajectories in the *xy*-plane of the S2' COM superimposed to the static potential energy surface at zero load, given per unit MoS_2, for 0°, 30° and 60° sliding angles (yellow, green and red lines respectively). The respective arrows show the direction of the driving force. The results for the 10°, 20°, 40°, and 50° systems are not displayed because, in these cases, the taken path is the same as for the 30° case and the trajectories would therefore not be visible. The slip phase for the 0° trajectory is indicated by the white arrow.

3. Results and discussion

3.1. Qualitative analysis of sliding dynamics

We start with a discussion on the dynamical behavior of the different systems during sliding. For the sake of clarity only representative results are shown, whilst additional data can be found in the Supporting Information. In Fig. 3, the trajectories of the center of mass (COM) of the atoms belonging to the S2′ group are reported for three different sliding angles. From the figure, one sees that the mobile layer avoids the maximum energy barriers during sliding and follows the MEP, for all trajectories. The MEP consists of transitions from min1 to min2 passing through the saddle point (see Fig. 1) or vice versa. This is a readily understandable behavior, and it is also consistent with the predictions from static DFT calculations [19]. One can distinguish two types of sliding dynamics, as can been seen from Fig. 4. For systems with the driving force oriented along the 0° or 60° angle, two evident velocity regimes are present. This means that there is a separation of timescales between the events taking place during the dynamics. In particular it is possible to identify certain times at which sudden “jumps” happen,

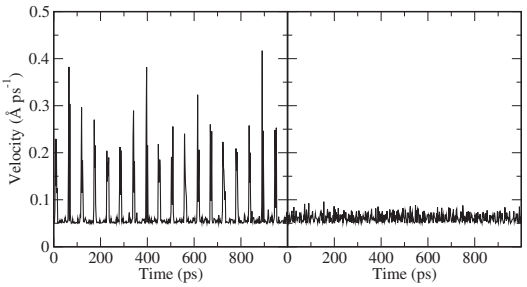

Fig. 4. Profiles of the average velocity of the S2' COM versus time for 0° (left panel) and 30° (right panel) sliding angles at zero load. Averages are obtained by dividing the velocity components along a trajectory into batches of 2 ps and subsequently calculating the amplitude.

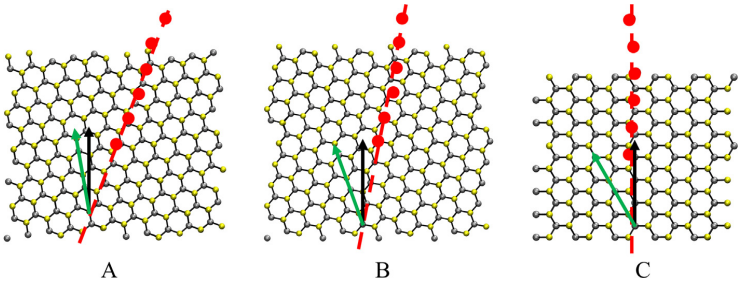

Fig. 5. Pictorial representations of MD trajectories for 10° (Panel A), 20° (Panel B) and 30° (Panel C) sliding angle at zero load. The red circles represent six positions along the trajectory with time intervals of 75 ps of the COM of the S2' group atop the static layer. The green arrows represent the sliding direction for the 0° case, while the black arrows indicate the orientation of the driving force, which is always aligned along the y-axis. Molybdenum and sulfur atoms are in gray and yellow, respectively. Figure obtained with VMD [27].

while for the rest of the trajectory the system evolution is smooth. This behavior is well known in the literature as stick-slip dynamics [28,29]. Having a closer look to the trajectories, one finds that during the stick phase the system is advancing toward the maximum energy barrier, which it will try to climb until the mobile layer experiences a lateral jump almost perpendicular to the driving force (the slip phase), towards the next minimum. In other words, due to the fact that the layer is enforced to advance with a fixed velocity in the *y*-direction, it is more favorable for the system to slide side-wards rather than to climb the energy barrier. During the other parts of the 0° and 60° trajectories the mobile layer smoothly transfers from one minimum to the next minimum, which are aligned along the y-direction.

We have mentioned before that the 10° and 20° (and 40° and 50°) systems follow the same trajectory as the 30° sliding angle. In other words, the trajectory of these systems is not parallel to the driving force. This can been seen in Fig. 5, where the average sliding paths taken for different sliding angles are reported. For the 30° system, one sees that the average sliding path is oriented parallel to the driving force. In contrast, for the 10° and 20° systems, a mismatch angle is observed between the driving force and the average sliding path, with the mismatch for 10° being larger than for 20°. Interestingly, the sliding angle added up to the mismatch angle between the driving force and the average sliding path always gives 30°, furthermore explaining why these trajectories are not visible in Fig. 3. This behavior is consistent with previous experimental results [21], which show that, when the mismatch angle is non-zero, frictional forces increase. It is important to keep in mind that, due to the constraints imposed by the periodic boundary conditions, the systems cannot transform into an incommensurate configuration.

3.2. Quantitative estimation of friction

At each timestep, the instantaneous force $\mathbf{F}(t)$ experienced by the S2′ layer can be calculated by summing up all atomic contributions. In order to enforce the sliding motion at constant velocity v, an external force acting only along the *y*-direction for all systems (*i.e.*, $F_{ext}(t) = -F_y(t)$) is added. The dissipated work W, done by this force, is given by:

$$W = \int_0^\tau F_{ext}(t) v dt \tag{1}$$

where τ is the total time of the simulation. In Fig. 6, the dissipated work is reported for the 0° and 30° sliding angles, both given at two different values of the normal pressure. There are two main observations to be made from this figure. Firstly, one can clearly see the effect of load. With higher loads, an increased corrugation of the profile is observed for both the 0° and 30° case, as expected and in agreement with Ref. [19]. Secondly, the 0° sliding angle is characterized by a more dissipative behavior (*i.e.*, the average slope of the profile is steeper) compared to the 30° one (and to all other angles, apart from 60°), which agrees with the earlier mentioned stick-slip dynamics. Moreover, one sees that the dissipation of the 0° case is affected more by a change in the load than is the case for 30°.

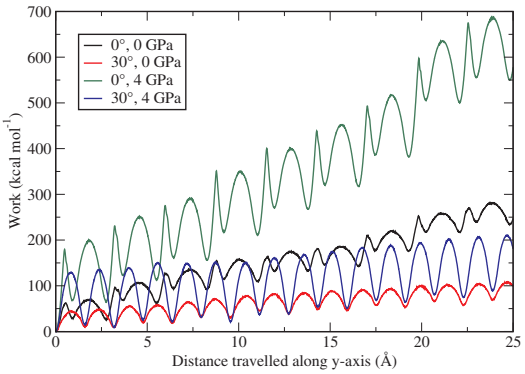

Fig. 6. Work done by the external force versus distance traveled along the *y*-axis as calculated from Eq. (1). Results are displayed for 0° and 30° rotation, both at 0 and 4 GPa normal pressure.

In order to rationalize this behavior, let us imagine an ideal, frictionless situation were the mobile layer slides over a symmetric energy barrier with a constant velocity, both while sliding up-hill and down-hill. In order to slide the mobile layer up-hill, energy (work) has to be provided to the system by applying a positive, external driving force. When the mobile layer is sliding down-hill, this work can be gained back, by means of an equal but negative, driving force. By assumption, the dynamics is conservative and no dissipation takes place. This may be the case of sliding angles different from 0° and 60°. In these latter cases the scenario changes. During the slip phase the system quickly moves from one point in the neighborhood of the global maximum to one close to global minimum. Let us assume that this phase takes place in a very short time, instantaneously in the limit. The driving force does not perform any work during this phase. However, an external work has to be provided to the system and the amount is given by the difference between the potential energy of the final and the initial point of the slip phase. This quantity represents the dissipated work and it can be positive or negative, depending on the actual trajectory. The second principle of thermodynamics states that this quantity has to be positive in average (*i.e.*, energy has to be given to the system and not vice versa) even for this frictionless scenario. Finally, of course the system is not ideal and friction is present.

The time profile of $F_{ext}(t)$ versus time for a representative case is reported in Fig. 7. As one can see from the figure, wide fluctuations are present in the force profile. In order to provide a quantitative estimation of the frictional force, we resort to the so-called bootstrap averaging method [30] (a brief description of the technique including the parameters used in the present study can be found in the Supporting Information). The results for all angles are summarized in Fig. 8, where the frictional force is plotted as a function of the normal load per atom

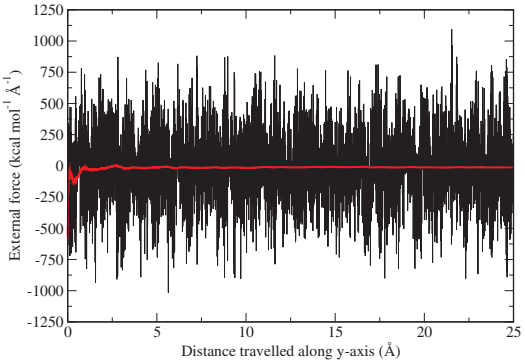

Fig. 7. Profile of the instantaneous external force for the S2′ group for 0° sliding angle at zero load as a function of the distance traveled in the *y*-direction. The red line represents the running average and serves merely as a guide for the eye.

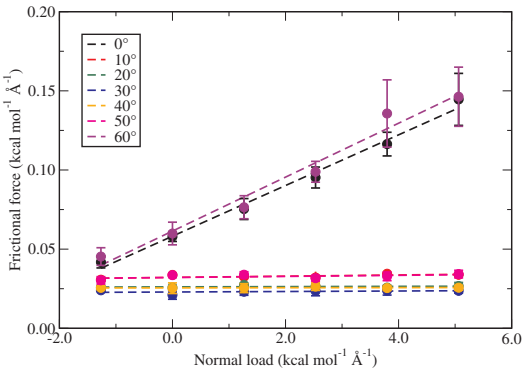

Fig. 8. Profiles of the frictional versus normal force for all sliding angles. The linear fits of the frictional force per S2' atom are reported with dashed lines. The error bars represent the standard deviation calculated on the results of the bootstrap method applied to the individual runs.

in the S2′ group.

To fit the data we use Amontons' law of friction:

$$F_{\parallel} = \alpha_0 + \mu \cdot F_{\perp}. \tag{2}$$

Here, μ is the coefficient of friction, α_0 is the offset of the frictional force per S2′ atom at zero normal load and $F_{\parallel}$ and $F_{\perp}$ are the average forces experienced by single atoms in the S2′ group parallel to the sliding direction and perpendicular to the basal plane, respectively. First of all, all data show linear trends, therefore Eq. (2) is a suitable guess for the fitting. Moreover, Fig. 8 allows us to assess the effect of the load on the frictional force for different sliding angles. For 0° and 60° sliding, one can clearly observe a positive slope, meaning a non-vanishing coefficient of friction. For the other cases, one observes flat profiles, *i.e.*, coefficients of friction close to zero. These latter are somewhat counter-intuitive cases, since the earlier mentioned increased corrugation in the PES profile, while increasing the load, does not necessarily seem to lead to an increased friction.

In order to better rationalize the behavior shown in Fig. 8, let us have a closer look to the trajectory. Let us to divide the trajectory into segments, each ranging from one to the next minimum of the PES. These are the consecutive, approximate straight parts, forming the trajectory as a whole in Fig. 3. It is therefore possible to define a local mismatch angle θ for each segment, with respect to the driving force,

Table 2
Division of all trajectories into segments with corresponding mismatch angles between the actual orientation of the segment and the driving force.

Sliding angle	Segment 1	Segment 2
0°	60°	0°
10°	50°	10°
20°	40°	20°
30°	30°	30°
40°	20°	40°
50°	10°	50°
60°	0°	60°

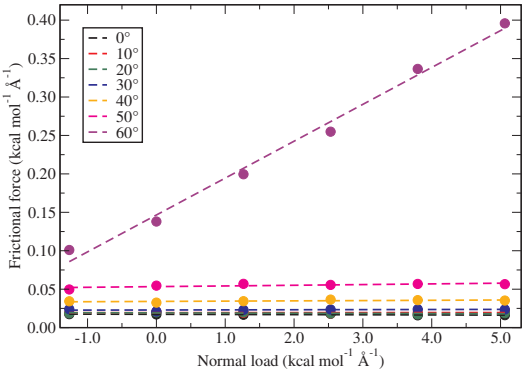

Fig. 9. Profiles of the frictional versus normal force for all mismatch angles θ of the segments. The linear fits of the frictional force per S2' atom are reported with dashed lines.

ranging from 0° to 60° and with a total of seven angles. Every trajectory contains two different types of segments, as summarized in Table 2. Collecting the instantaneous external forces, for all segments having the same mismatch angle (in absolute value) with the driving force and then applying the bootstrap method gives us the frictional force as a function of the mismatch angle. The results are summarized in Fig. 9. First of all, one sees that with an increasing mismatch angle there is an increasing frictional force, as expected. Furthermore, one sees that the load dependence of the 0° and 60° sliding angle, found earlier in Fig. 8, is totally accounted for by the segments with a mismatch angle of 60° only. In fact, these are the segments of the trajectory where the slip event takes place. Finally, the non-zero frictional forces for 0° tell us that, even in the most ideal case, the system suffers from non-conservative dynamics in which dissipation takes place. We define the average of the forces causing this dissipation as the intrinsic frictional force for commensurate bilayer MoS_2. From simple geometrical considerations, it is possible to define the average effective force $\overline{F}_{eff}$ as the force resulting from the average external driving force projected onto the actual sliding direction (Fig. 11):

$$\overline{F}_{eff} = \overline{F}_{ext}\cos\theta \tag{3}$$

where θ is the mismatch angle of the segments. This means that, when the segment is parallel to the driving force, the driving force and the effective force are equal. If the origin of the observed behavior of the frictional force lies solely in the local mismatch angle θ, Eq. (3) should provide the profiles reported in Fig. 10. As it turns out, there remains a part unaccounted for, the light gray part, most significantly present for the 60° case. We attribute such a discrepancy to the change from smooth to the more complex stick-slip dynamics when the mismatch angle increases. Moreover, a change in Amontons' behavior is found for the same change in angle. Finally, slight deviations are found between MEP and the actual sliding path.

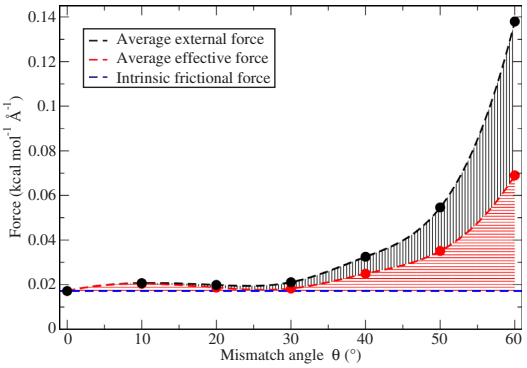

Fig. 10. Values of the effective $\overline{F}_{eff}$ (according to Eq. (3)), external force F_{ext} and the intrinsic frictional force versus the mismatch angle θ for zero load. The black and red dashed lines merely functions as guide for eye. The blue line represents the intrinsic frictional force of commensurate bilayer MoS_2. The filled areas highlight the amount of average forces coming from Eq. (3).

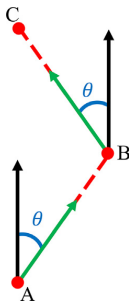

Fig. 11. Schematic of a trajectory. The traits A-B and B-C represent the consecutive segments into which we divide any trajectory. The black arrow represents the average driving force along the *y*-axis, whereas the red dashed line is the actual sliding path. The green arrow is the resulting average effective force due to the mismatch angle θ.

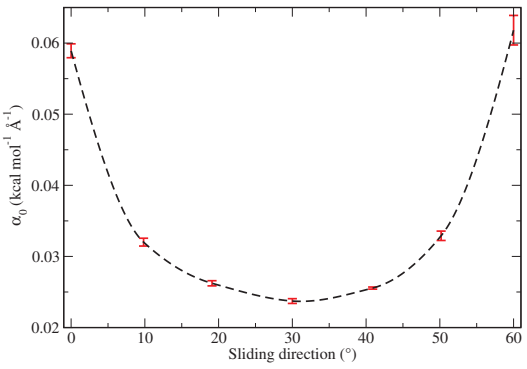

Fig. 12. Offset of the frictional force per S2′ atom (α_0) at zero load plotted versus the sliding angle. The dashed line is provided as a guide for eye. The errors bars represent the standard deviation calculated on the results of the bootstrap method applied to the individual runs.

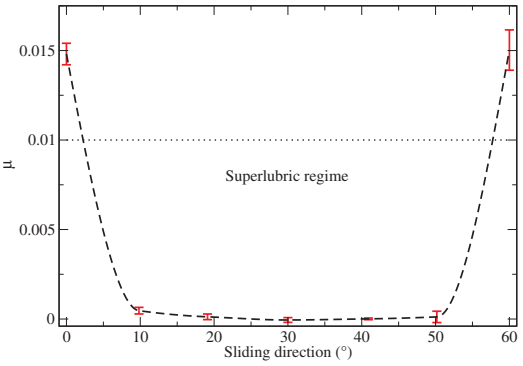

Fig. 13. Coefficients of friction (μ) plotted versus the sliding angle. These values are obtained from the linear fits of Fig. 8. The dashed line is provided as a guide for the eye. The errors bars represent the standard deviation calculated on the results of the bootstrap method applied to the individual runs.

Finally, in Figs. 12 and 13, the profiles of the offset for the frictional force at zero load and the coefficient of friction as a function of sliding angle are reported, respectively. From Fig. 12, one observes an "U"-shape behavior, with a minimum for sliding at 30°. In other words, the frictional force needed to make the mobile layer slide is highest for 0° and 60°, and lowest for 30°. This behavior is in accordance with the experimental finding of Ref. [21], namely that, with an increased mismatch angle between the driving force and the actual trajectory (see Fig. 5), the system experiences an increased frictional force. In Fig. 13, the coefficient of friction is reported as a function of the direction of the driving force. These results are obtained via the linear fits from Fig. 8. As one can see, the effect of the sliding direction on the coefficient of friction is very pronounced and two regimes can be easily identified. When the system is sliding along the Mo-S bonds, which is the case for 0° and 60°, a relatively high frictional regime is found. The dynamics of this regime is characterized by a stick-slip behavior and a high energy dissipation (and Amontons-like dependence of friction on normal force) is observed. In all other cases, when the layer is not sliding along the bond direction, the system experiences superlubricity. Moreover, the dynamical behavior becomes smooth, and the load no longer affects friction. In fact, in combination with the previous observed behavior for the incommensurate case [18,20], our results seem to indicate two things. Firstly, a non-superlubric behavior for MoS_2 is rather unique. In other words, as long as the driving force is not oriented exactly along the Mo-S bond, one will observe superlubricity. Secondly, incommensuration is not required for achieving superlubricity in MoS_2.

4. Conclusion

In this study we investigated the frictional behavior of the commensurate MoS_2 bilayer as a function of the sliding angle by means of molecular dynamics simulations. It was found that despite the fact that all systems prefer to slide along the MEP, we can distinguish two different dynamical behaviors. When the driving force is orientated parallel to the Mo-S bond direction, as in the case of 0° and 60° sliding, a stick-slip behavior is observed. For all other sliding directions, a smooth transition between the stable minima was observed. Moreover, in the latter case, it was found that the minimum energy path taken represents the 30° sliding path, regardless of the sliding angle of the system. Next, it was found that the corrugation profile of the PES increases with an increasing load for all sliding directions, as expected [19]. Also, the stick-slip behavior observed at 0° and 60° is significantly more dissipative compared to all other cases. Stronger still, it was found that an increasing load only affects the frictional force in the case when stick-

slip dynamics are present. This behavior was furthermore confirmed by the increased frictional forces and their load-dependence for the 0° and 60° trajectories as a whole. It was found that the origin of this behavior lies in the segments of the trajectory where the mismatch angle θ is 60°. Although, this mismatch angle cannot fully account for the increase in frictional force. Finally, it was found for the first time in a computational study that there is a dependence on the sliding direction of the superlubric behavior of the bilayer MoS_2.

We believe that our results can open the door to a new approach in explaining the superlubric regime of MoS_2 and of solid layered lubricants in general. It was shown that it is possible to relate the sliding direction to the superlubric regime, something which in general is believed to be related to the commensurability of the system only. That being said, these results do indicate that the explanation of superlubricity might be more complex than so far anticipated. The popular argument, stating that superlubricity is a consequence of the cancellation of forces, might not be able to fully capture the processes underlying this phenomenon. Our results call for an experimental verification, for which the technique applied in Ref. [22] is very promising. Moreover, once our findings will be confirmed experimentally, theoretical approaches like those in Refs. [19,20] should be reconsidered since there the frictional force is based on a straight sliding path along the long diagonal of the unit cell (0° or 60°), whereas our dynamics rather indicate a path taken along the minimum energy path, preferably with a 30° sliding angle. Finally, it is also possible to foresee practical applications of the results described in the present paper for *e.g.* nano/micro electromechanical systems (NEMS/MEMS) [31], where a simple change of orientation of the sliding direction between two moving parts would allow to switch between high- and low-friction regimes.

Data availability

The raw/processed data required to reproduce these findings cannot be shared at this time due to technical or time limitations.

CRediT authorship contribution statement

Victor E.P. Claerbout: Conceptualization, Methodology, Validation, Formal analysis, Investigation, Data curation, Writing - original draft, Visualization. **Tomas Polcar:** Writing - review & editing, Supervision, Funding acquisition. **Paolo Nicolini:** Conceptualization, Methodology, Validation, Writing - review & editing, Supervision, Funding acquisition.

Acknowledgments

The authors are grateful to H.S. Sen and B.J. Irving (Czech Technical University in Prague, Czech Republic) for their valuable time and fruitful discussions. This work was supported by The Ministry of Education, Youth and Sports from the Large Infrastructures for Research, Experimental Development and Innovations project "IT4Innovations National Supercomputing Center – LM2015070". The publication has received funding from the European Union's Horizon2020 research and innovation program under grant agreement No. 721642: SOLUTION. P.N. acknowledges the support of the Czech Science Foundation through the project 16-11516Y. T.P. acknowledges the support from the project Novel nanostructures for engineering applications No. CZ.02.1.01/0.0/0.0/16_026/0008396.

Appendix A. Supplementary data

Supplementary data associated with this article can be found, in the online version, athttps://doi.org/10.1016/j.commatsci.2019.03.019.

References

[1] K. Holmberg, A. Erdemir, Influence of tribology on global energy consumption, costs and emissions, Friction 5 (3) (2017) 263–284, https://doi.org/10.1007/s40544-017-0183-5.
[2] C. Busch, Lubricants, 9. Solid Lubricants, American Cancer Society, 2011. doi:10.1002/14356007.o15_o11.
[3] K. Novoselov, A. Geim, S. Morozov, D. Jiang, Y. Zhang, S. Dubonos, I. Grigorieva, A. Firsov, Electric field effect in atomically thin carbon films, Science 306 (5696) (2004) 666–669, https://doi.org/10.1126/science.1102896.
[4] M. Chhowalla, H. Shin, G. Eda, L.-J. Li, K. Loh, H. Zhang, The chemistry of two-dimensional layered transition metal dichalcogenide sheets, Nat. Chem. 5 (2013) 263–275, https://doi.org/10.1038/nchem.1589.
[5] J. Lauritsen, M. Bollinger, E. Lægsgaard, K. Jacobsen, J. Nørskov, B. Clausen, H. Topsøe, F. Besenbacher, Atomic-scale insight into structure and morphology changes of mos_2 nanoclusters in hydrotreating catalysts, J. Catal. 221 (2) (2004) 510–522, https://doi.org/10.1016/j.jcat.2003.09.015.
[6] X.-R. Shi, S.-G. Wang, J. Hu, H. Wang, Y.-Y. Chen, Z. Qin, J. Wang, Density functional theory study on water-gas-shift reaction over molybdenum disulfide, Appl. Catal. A: General 365 (1) (2009) 62–70, https://doi.org/10.1016/j.apcata.2009.05.050.
[7] X.-R. Shi, H. Jiao, K. Hermann, J. Wang, Co hydrogenation reaction on sulfided molybdenum catalysts, J. Mol. Catal. A: Chem. 312 (1–2) (2009) 7–17, https://doi.org/10.1016/j.molcata.2009.06.025.
[8] B. Radisavljevic, A. Radenovic, J. Brivio, V. Giacometti, A. Kis, Single-layer mos_2 transistors, Nat. Nanotechnol. 6 (3) (2011) 147–150, https://doi.org/10.1038/NNANO.2010.279.
[9] O. Lopez-Sanchez, D. Lembke, M. Kayci, A. Radenovic, A. Kis, Ultrasensitive photodetectors based on monolayer mos^2, Nat. Nanotechnol. 8 (7) (2013) 497–501, https://doi.org/10.1038/NNANO.2013.100.
[10] A. Erdemir, J.-M. Martin, Superlubricity, 1st ed., Elsevier, 2007.
[11] A. Lansdown, Molybdenum Disulfide Lubrication, Elsevier, 1999.
[12] B. Schönfeld, J. Huang, S. Moss, Anisotropic mean-square displacements (msd) in single crystals of 2h- and 3r-mos^2, Acta Crystallographica Section B B39 (4) (1983) 404–407, https://doi.org/10.1107/S0108768183002645.
[13] K. Shinjo, M. Hirano, Dynamics of friction: superlubric state, Surf. Sci. 283 (1–3) (1993) 473–478, https://doi.org/10.1016/0039-6028(93)91022-H.
[14] M. Hirano, Superlubricity: a state of vanishing friction, Wear 254 (10) (2003) 932–940, https://doi.org/10.1016/S0043-1648(03)00295-3.
[15] J. Martin, C. Donnet, T.L. Mogne, T. Epicier, Superlubricity of molybdenum disulphide, Phys. Rev. B 48 (14) (1993) 10583–10586, https://doi.org/10.1103/PhysRevB.48.10583.
[16] M. Dienwiebel, G.S. Verhoeven, N. Pradeep, J. Frenken, J. Heimberg, H. Zandbergen, Superlubricity of graphite, Phys. Rev. Lett. 92 (12) (2004) 126101, https://doi.org/10.1103/PhysRevLett.92.126101.
[17] A. Erdemir, O. Eryilmaz, Achieving superlubricity in dlc films by controlling bulk, surface, and tribochemistry, Friction 2 (2) (2014) 140–155, https://doi.org/10.1007/s40544-014-0055-1.
[18] T. Onodera, Y. Morita, R. Nagumo, R. Miura, A. Suzuki, H. Tsuboi, N. Hatakeyama, A. Endou, H. Takaba, F. Dassenoy, C. Minfray, L. Joly-Pottuz, M. Kubo, J.-M. Martin, A. Miyamoto, A computational chemistry study on friction of h-mos_2. part ii. friction anisotropy, J. Phys. Chem. B 114 (48) (2010) 15832–15838, https://doi.org/10.1021/jp1064775.
[19] G. Levita, A. Cavaleiro, E. Molinari, T. Polcar, M. Righi, Sliding properties of mos_2 layers: Load and interlayer orientation effects, J. Phys. Chem. C 118 (25) (2014) 13809–13816, https://doi.org/10.1021/jp4098099.
[20] B. Irving, P. Nicolini, T. Polcar, On the lubricity of transition metal dichalcogenides: an ab initio study, Nanoscale 9 (17) (2017) 5597–5607, https://doi.org/10.1039/C7NR00925A.
[21] K. Miura, S. Kamiya, Observation of the amontons-coulomb law on the nanoscale: Frictional forces between mos_2 flakes and mos_2 surfaces, Europhys. Lett. 58 (4) (2002) 610–615, https://doi.org/10.1209/epl/i2002-00439-9.
[22] H. Li, J. Wang, S. Gao, Q. Chen, L. Peng, K. Liu, X. Wei, Superlubricity between mos_2 monolayers, Adv. Mater. 29 (27) (2017) 1701474, https://doi.org/10.1002/adma.201701474.
[23] S. Plimpton, Fast parallel algorithms for short-range molecular dynamics, J. Comput. Phys. 117 (1) (1995) 1–19, https://doi.org/10.1006/jcph.1995.1039.
[24] A. Ostadhossein, A. Rahnamoun, Y. Wang, P. Zhao, S. Zhang, V. Crespi, A. van Duin, Reaxff reactive force-field study of molybdenum disulfide (mos_2), J. Phys. Chem. Lett. 8 (3) (2017) 631–640, https://doi.org/10.1021/acs.jpclett.6b02902.
[25] P. Nicolini, T. Polcar, A comparison of empirical potentials for sliding simulations of mos_2, Comput. Mater. Sci. 115 (2016) 158–169, https://doi.org/10.1016/j.commatsci.2016.01.013.
[26] Z. Wang, Q. Chen, J. Wang, Electronic structure of twisted bilayers of graphene/mos_2 and mos_2/mos_2, J. Phys. Chem. C 119 (9) (2015) 4752–4758, https://doi.org/10.1021/jp507751p.
[27] W. Humphrey, A. Dalke, K. Schulten, Vmd: visual molecular dynamics, J. Mol. Graph. 14 (1) (1996) 33–38, https://doi.org/10.1016/0263-7855(96)00018-5.
[28] S. Krylov, J. Frenken, The crucial role of temperature in atomic-scale friction, J. Phys.: Condens. Matter 20 (35) (2008) 354003, https://doi.org/10.1088/0953-8984/20/35/354003.
[29] S.Y. Krylov, J.W.M. Frenken, The problem of critical damping in nanofriction, Colloid J. 74 (5) (2012) 569–572, https://doi.org/10.1134/S1061933X12050067.
[30] B. Efron, R.J. Tibshirani, An Introduction to the Bootstrap, Chapman & Hall/CRC, 1998.
[31] W.M. van Spengen, V. Turq, J.W.M. Frenken, The description of friction of silicon mems with surface roughness: virtues and limitations of a stochastic prandtl-tomlinson model and the simulation of vibration-induced friction reduction, Beilstein J. Nanotechnol. 1 (2010) 163–171, https://doi.org/10.3762/bjnano.1.20.

4

MoS_2 & Graphene

4.1 Introduction

As discussed in Chap. 1, heterostructures are built up from monolayers consisting of at least two different types of 2D materials. Heterostructures allow for the precise tuning of a wide range of (unique) chemical and mechanical properties. For example, it was found that the thermal conductivity and electrochemical properties of a MoS_2-graphene system can be significantly enhanced when changing from a homo- to a hetero-structure [106, 120, 121]. To extend their tunability, the mismatch orientation between monolayers has also been investigated. In the same systems, promising results were shown when studying the electrical conductivity and band gaps. It was found that both features can be tuned with much greater precision than their homologs by manipulating their intrinsic stacking orientation [122, 123]. However, despite the possible

potential that the stacking degree of freedom might offer, the energetic stability of these rotated structures is often left out from the analysis. On top of this, several experimental studies have reported on an intrinsic misfit angle within the heterostructures of graphene and MoS_2, which can be considered as a prototypical configuration. However, the actual values of the misfit angles are discordant between the different studies. For example, some found that the heterostructure is either aligned or characterized by a misfit angle of 30° [124]. Others observed angles from -11° to 18° [125], while again others report angles that are mainly below 3° [126]. Obviously, the techniques used to obtain these structures and the actual size of the layers play a critical role and are different for all the studies mentioned above.

These results made us wonder if we could relate the energetic landscape to the intrinsic mismatch angles and the local deformations of the layers. This chapter summarizes a study on the energy minimization of edge-free bilayer heterostructures composed of MoS_2 and graphene. We performed MM simulations with an in-house optimized FF. The effects of the mismatch angle and other possible mechanisms contributing to the rotational energy landscape for heterostructures were studied. In doing so, a contribution was made to the fundamental understanding of the rotational-dependent energetic behavior of heterostructures. Moreover, our results clarified some of the seemingly contradictory experimental results. Finally, we also considered the orientational ordering of our incommensurate system through epitaxy theory. More specifically, the Novaco-McTague theory predicts misalignment between heterostructures as a pathway to reduce the energy of the system [127, 128].

As per the MSCA-ITN scholarship scheme requirements, part of this work was performed during a secondment at a partner university – in this case, a collaboration between the Czech Technical University in Prague and the University of Southampton was formed. Here, I worked extensively together with another student from the project funding our scholarship, Andrea Silva. He contributed with his expertise in DFT calculations.

4.2 Approaches and Problems

The concept of the computational setup used in this work is straightforward. A set of bilayer heterostructures of graphene and MoS_2 was considered, each with a different relative misfit angle. Since both monolayers are characterized by a hexagonal symmetry, the same accounts for the heterostructure. Therefore, it suffices to consider a rotational range of 60° to explore the complete rotational landscape.

Firstly, an appropriate FF had to be selected. In the case of this system, the FF consists of three parts:

- A part describing the interactions within the graphene layer,
- A part describing the interactions within the MoS_2 layer,
- A part that describes the interactions between the graphene and MoS_2 layers.

The intralayer interactions for graphene and MoS_2 were described by the REBO [109] and Stillinger-Weber [106] potentials, respectively. The results of the benchmark for these FFs can be found in Chap. 2 and Appx. B, where the structural parameters of both are compared to available experimental data and the results of our own DFT calculations. This part of the benchmark was considered to be in reasonable agreement with both the experimental data and the DFT calculations.

In general, the standard LJ potential;

$$V(r) = 4\epsilon \left[\left(\frac{\sigma}{r}\right)^{12} - \left(\frac{\sigma}{r}\right)^{6} \right], \tag{4.1}$$

is used in MM to simulate van der Waals interactions. Here, σ is the distance at which the interaction between the pair of atoms is zero, ϵ is the depth of the energy minimum of the potential, and r is the scalar distance between a pair of atoms. Firstly, to assess the validity of the available LJ parameters, DFT calculations were performed to obtain a reference set. In total, three bilayer

systems were considered; two homostructures of graphene and MoS_2, respectively, and a bilayer heterostructure combining one layer of each type. The creation of the first two structures is relatively straightforward compared to the heterostructure since there is no lattice mismatch. For the heterostructure, a 4x4 MoS_2 unit cell and a 5x5 graphene unit cell were considered, in which the resulting in-plane stress of 2.6% was accommodated by MoS_2. This induced strain is expected to mostly affect the in-plane results. However, our focus was the inter-plane interactions, where only minor deviations were expected, primarily because graphene and MoS_2 are naturally incommensurate. In all cases, only aligned structures were considered. Next, the binding energy profile was obtained by increasing the interlayer distance between the layers in a step-wise manner. For graphene, this was achieved by fixing the carbon atoms in the z-direction, whereas for MoS_2, this was done by fixing the z-coordinates of the outermost sulfur atoms.

Optimized Force Field Parameters			
Pair	ϵ[meV]	σ[Å]	ζ[Å]
C-C	3.26	3.239	0.25
C-S	1.64	3.640	0.30
C-Mo	4.55	4.391	0.30
Mo-Mo	1.60	2.927	0.60
Mo-S	28.00	4.146	0.60
S-S	6.30	3.804	0.60

Table 4.1: Results for the re-parametrization of the LJ parameters. The last column represents the system specific width of the weight function.

After several unsatisfactory results with published parameters, both quantitatively and qualitatively, we decided to perform a refinement based on the parameters in Ref. [106]. Although the focus of this study is heterostructures, we decided to perform an optimization of all three structures for possible future work. To obtain the refined LJ parameters, the Simplex algorithm [129], as implemented in the SciPy software package [130], was used. Here, the N-

dimensional phase space (N = number of LJ parameters) is sampled in an iterative way utilizing a simplex (convex polygon). In the case of bilayer graphene, $N = 2$, whereas for bilayer MoS_2, $N = 6$, and for the heterostructure, $N = 4$. Moreover, a goal function is defined which compares our reference DFT results of the binding energy profile to the current results of the MM simulation obtained with a particular set of LJ parameters. The results of this procedure can be found in Figs. 4.1 (a-c) and Tab. 4.1.

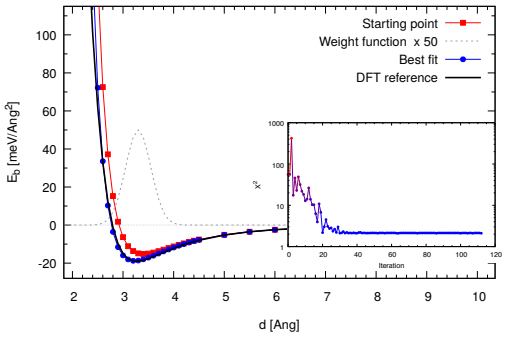

(a) Carbon-Carbon interaction.

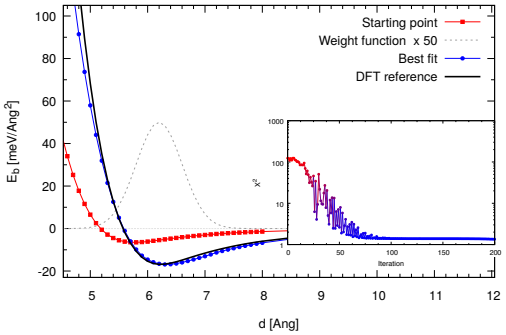

(b) Mo-S interactions.

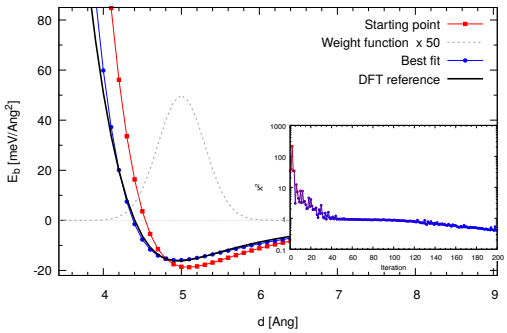

(c) Mo-C-S interactions

Figure 4.1: Graphical representation of the re-parametrization of the LJ parameters obtained via the Simplex procedure for three systems: (a) bilayer grahene, (b) bilayer MoS_2, and (c) heterostructure MoS_2/graphene. Plotted are the original, the optimized, the DFT reference LJ curve and the weight function. The insets depict the chi-squared distribution allowing us to assess the convergence of our minimization.

After obtaining the correct FF parameters, the heterostructures had to be created. To avoid any edge/boundary effects and obtain results that solely

depend on the relaxation of the atoms in the layers, we considered 'infinite' layers instead of a flake on top of a substrate. This was achieved by implementing periodic boundary conditions. However, there is a mismatch between the lattice constants of graphene and MoS_2, which is also the reason why there is a natural incommensurability present within this heterostructure. This means that in order to combine two monolayers, there will be stress introduced to the structure in the xy-plane. This mismatch stress can either be accommodated on one monolayer, or distributed on both. As one might expect, this is an unavoidable artifact in computational studies and might have severe consequences for the outcomes.

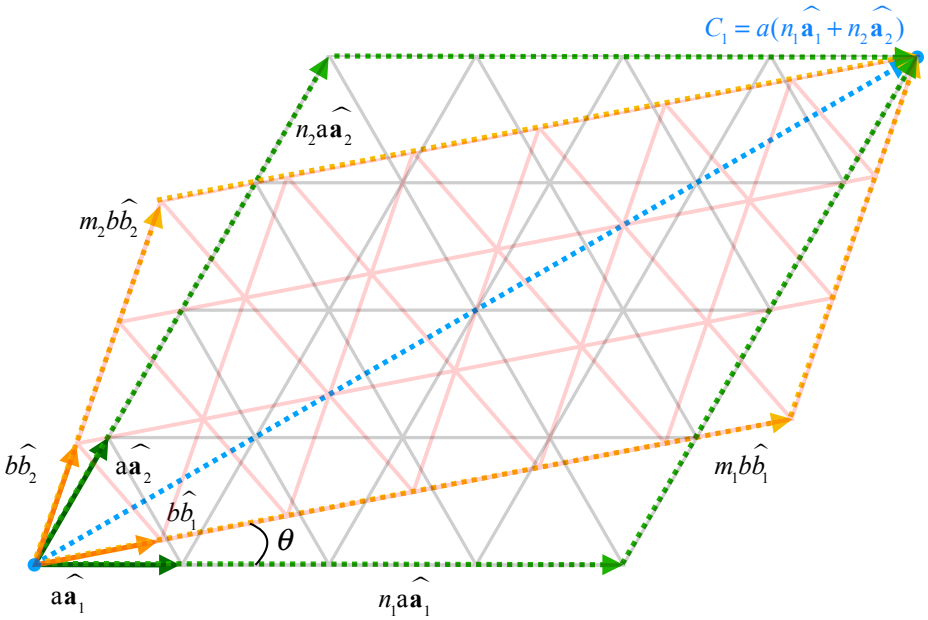

Figure 4.2: Graphical overview of the replication of hexagonal unit cells with different lattice constants in order to create a supercell that matches the symmetry of both.

To maintain the desired precision in the calculations, the effects of this stress must be minimized. Their symmetric structure in the xy-plane characterizes 2D materials. As stated before, graphene and MoS_2 both have a hexagonal symmetry, in which the monolayer unit cell has two atoms for graphene

and three atoms for MoS_2. Every unit cell is defined by two lattice vectors, one along each side: $(l_a\hat{\mathbf{a}}_1, l_a\hat{\mathbf{a}}_2)$ and $(l_b\hat{\mathbf{a}}_1, l_b\hat{\mathbf{a}}_2)$. Here, l_i is the respective lattice constant of layer a and layer b, according to the Bravais lattice definition, $\hat{\mathbf{a}}_1$ is the unit vector along the first side (e.g. the x-axis) and $\hat{\mathbf{a}}_2$ is the unit vector along the second side of the hexagonal cell, with an angle of 60°. The lattice with the desired periodicity is generated by a primitive vector $\mathbf{a}_1 = l_\mathrm{a}\hat{\mathbf{a}}_1$. A heterostructure supercell will be compatible with both periodicities if the individual lattice cells match exactly at the edges, in other words, if the following matching condition is satisfied:

$$l_\mathrm{a}(n_1\hat{\mathbf{a}}_1 + n_2\hat{\mathbf{a}}_2) = l_\mathrm{b}(m_1\hat{\mathbf{b}}_1 + m_2\hat{\mathbf{b}}_2), \tag{4.2}$$

where n_1, n_2, m_1, m_2 represent the repetitions of the unit cell of the first and second lattice along the corresponding versors, respectively. An overview of the matching condition is given in Fig. 4.2.

To obtain a system with the desired misalignment θ, all combinations of integers n_i, m_i within the range $(-200, 200)$ were considered. Thereafter, the supercells which satisfy $\theta \in [0°, 60°]$ and a maximum strain of the order $\epsilon \approx 1 \times 10^{-7}$ were selected. Next, the resulting supercells were binned with a spacing of $\Delta\theta = 0.01°$ and the cell with the fewest Bravais points within each bin was selected. This procedure does not guarantee that the resulting supercell will be evenly spaced according to the mismatch angle. Also, the resulting heterostructures do not have to have the same number of atoms; the sizes varied from 35663 to 343898 atoms. This is because the number of atoms in each lattice is given by the number of Bravais lattice points multiplied by the number of atoms in the crystal basis:

$$N_\mathrm{tot} = N_\mathrm{Bravais} \cdot n_\mathrm{basis}, \tag{4.3}$$

with n_basis equal to 2 and 3 for graphene and MoS_2, respectively.

The final problem encountered during this study occurred while investigating the orientational ordering of our heterostructure in the spirit of the Novaco and McTague theory [127, 128]. This theory considers a soft adsorbate layer treated within the harmonic approximation atop a rigid substrate. To create a similar situation in our system, several constraints were introduced

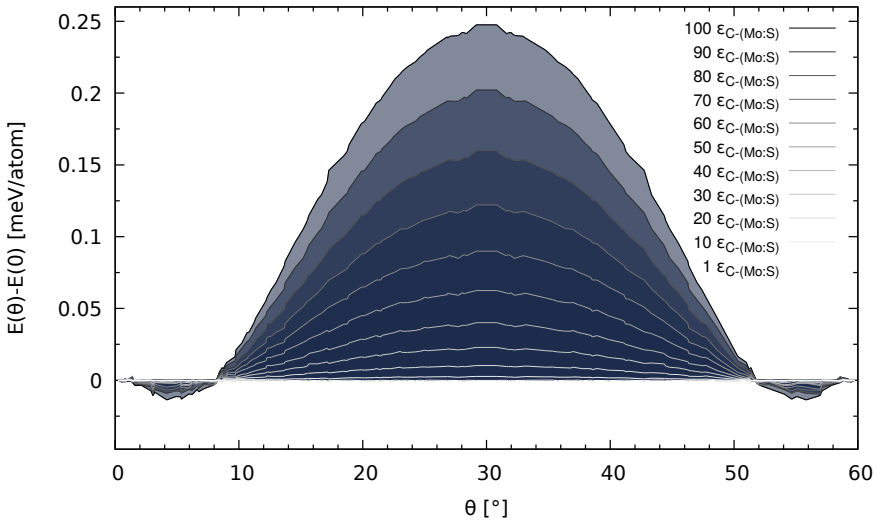

Figure 4.3: Enhancement of the LJ-coupling. The energy (meV/atom) versus angle $E(\theta)$ is plotted for rigid MoS_2 and soft graphene, for increasing values of LJ coupling $f\epsilon_{C-(Mo:S)}$, as reported in the legend.

regarding the degrees of freedom of the atoms, i.e., fixing the atoms in the z-direction. However, due to these constraints, the energy profile plotted versus the rotation angle was not visible due to the noise coming from the residual mismatch stress in the heterostructures. Although the initial structures were relatively big and therefore had a relatively low in-plane stress, the energy differences turned out to be so small that they were easily 'lost'. Firstly, to circumvent this problem, the size of the structures was increased so as to decrease the stress, as explained above. Even though the results improved, the trends were still not clearly visible. Therefore, in a second attempt, the LJ-coupling between the MoS_2 and graphene layers was enhanced during these simulations. In Fig. 4.3, the energy profiles of $E(\theta)$ versus the rotation angle are plotted for different scaling factors. The enhanced LJ values relate to the scaling factor f by $\epsilon' = f\epsilon$. It can be seen that this computational trick does not alter the physics but purely amplifies the energy trends that otherwise get progressively hidden by the noise. In other words, both the minima and maxima remain located at the same angle, whereas their absolute energy value is scaled according to the LJ-coupling. Figure 4.4 reports the scaling relation at $\theta = 30°$, showing an almost quadratic behavior.

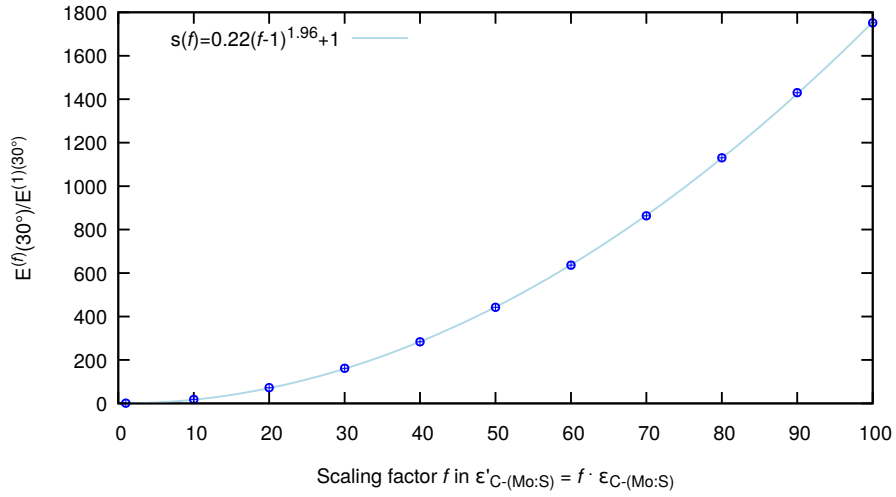

Figure 4.4: Scaling relation between the energy and the LJ parameter ϵ. Blue circles represent the energy at $\theta = 30°$ computed at a given enhancement factor f, with respect to $f = 1$, versus the scaling factor f. The light blue line shows the fitted power-law reported in the legend.

4.3 Results and Outlook

Our study led to several interesting insights and discoveries. First of all, we found a relation between the relative mismatch angle and the energy profile, where for aligned structures (0° and 60°) the lowest energy configuration was found. We found a metastable state for a relative mismatch angle of 30°, where there is a global energy maximum but a locally flat profile. Additionally, we found that for the lowest energy configuration, the structural change was the most significant. This was confirmed by the increased thickness of the graphene layer, defined as the difference between the highest and lowest carbon atoms $(z_{max} - z_{min})$.

Furthermore, we performed an analysis based on the flexural phonon modes and the moiré superlattice. The earlier mentioned out-of-plane distortions have the same periodicity as the moiré patterns. This behavior was well accommodated in the aligned configurations, which are characterized by the largest moiré spacing. It is because of this that the energy cost of the flexural

distortion was almost negligible. Upon decreasing the moiré spacing, the energy gain of local commensuration between graphene and MoS_2 was no longer able to compete with the cost of in-plane rippling. Finally, we have proven that the current available Novaco and MacTague theoretical framework [127, 128] is no longer valid due to the complex three-atom layered structure of MoS_2. Our results introduced a new perspective on the discordance in experimental results and paved the way for future design of twistronics devices.

I was the main author of this work together with Andrea Silva and was responsible for the conceptualization, data production via MM calculations, data analysis, and the writing of the original draft. All results of this study have been published in the ACS Applied Materials & Interfaces journal [131]. This is an impacted journal, which had an impact factor of 8.758 in 2019 and belongs to the quartile category Q1 in the field of materials science and nanoscience & technology. A copy of the manuscript is attached below.

ACS APPLIED MATERIALS & INTERFACES

www.acsami.org Research Article

Exploring the Stability of Twisted van der Waals Heterostructures

Andrea Silva,* Victor E. P. Claerbout,* Tomas Polcar, Denis Kramer, and Paolo Nicolini

Cite This: ACS Appl. Mater. Interfaces 2020, 12, 45214–45221 Read Online

ACCESS | Metrics & More | Article Recommendations | Supporting Information

ABSTRACT: Recent research showed that the rotational degree of freedom in stacking 2D materials yields great changes in the electronic properties. Here, we focus on an often overlooked question: are twisted geometries stable and what defines their rotational energy landscape? Our simulations show how epitaxy theory breaks down in these systems, and we explain the observed behavior in terms of an interplay between flexural phonons and the interlayer coupling, governed by the moiré superlattice. Our argument, applied to the well-studied MoS_2/graphene system, rationalizes experimental results and could serve as guidance to design twistronic devices.

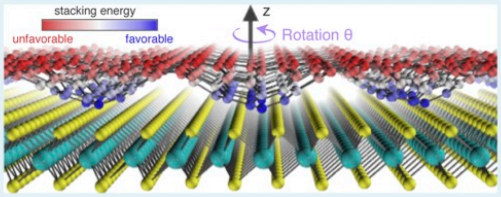

KEYWORDS: *heterostructures, molybdenum disulfide, graphene, twist deformation, molecular dynamics simulations, twistronics*

INTRODUCTION

van der Waals (vdW) 2D materials, such as graphite and the family of transition metal dichalcogenides (TMDs), are a class of compounds characterized by an anisotropic structure. Strong intralayer covalent bonds complement the weak vdW interlayer interactions, which facilitate the lamellar structure of bulk crystals. Because of their diverse chemistry and versatile properties, these materials have received significant attention from the scientific community in the past decades.[1−3] Applications can be found in microelectronics,[4,5] catalysis,[6−8] and tribology.[9,10] Although the attractive properties of the pure compounds are widely known, recent efforts have been focusing on the physics and properties emerging from the stacking degree of freedom offered by these lamellar materials. Different types of single layers can be mixed and matched to create new superstructures, termed *heterostructures*.[11−14] A key feature, affecting the behavior of multilayered structures, is the relative orientational mismatch between layers. Although heterostructures are intrinsically incommensurate because of the different lattice constants of the parent single layers, incommensurability can also arise in homostructures because of a relative misalignment of the single layers.[9]

The relative mismatch between layers, both for homo- and heterostructures, has been related to a range of electronic and mechanical properties.[9,15−20] A flourishing new branch in the field of condensed matter, known as *twistronics*, promises to allow fine-tuning of the electronic properties using the rotational misalignment between layers.[17,21] A notable example is the recent discovery of unconventional superconductivity in bilayer graphene (G) twisted at a *magic angle* of 1.1°.[21] Another study found that the vertical conductivity of bilayer MoS_2/G heterostructures varies by a factor of five when imposing an angle of 30° between the layers.[22] Finally, a pioneering work[9] showed that by switching from commensurate to incommensurate orientation in graphite systems, it is possible to achieve a state in which the coefficient of friction vanishes, the so-called *superlubric* regime.

Despite the interesting physics, which results from these relative mismatches, an often overlooked question is by what their rotational energy landscape is determined and thus which geometries are stable. Indeed, experimental studies are contradictory on this point, with a wide range of misfit angles found, even for the same type of system.[23−26] Below, we give a few examples of heterostructures based on MoS_2 on G. This system may be regarded as the prototypical 2D heterostructure, as it combines two well-known and extensively studied materials, widely reported in the literature. Moreover, it has been reported that MoS_2/G heterostructures show interesting electronic behavior as a function of their mismatch angle.[27,28] Using chemical vapor deposition (CVD), Liu *et al.* epitaxially grew triangles of MoS_2 on top of G, about 0.135 μm in size, with the majority of them (84%) aligned to the substrate and the remainder rotated by 30°.[23] Using the same technique, Shi *et al.* found mismatch angles between MoS_2 and G, on top of a Cu foil, ranging from −11 to 18°, with hexagonal flake sizes of about 1 μm.[24] For CVD-grown flakes of 9 μm, Lu *et al.* found a mismatch with typical angles below 3°.[25] Finally, using an exfoliation protocol, Adrian *et al.* prepared multilayered heterostructures and observed a misfit

Received: August 3, 2020
Accepted: September 8, 2020
Published: September 8, 2020

https://dx.doi.org/10.1021/acsami.0c13971
ACS Appl. Mater. Interfaces 2020, 12, 45214−45221

ACS Applied Materials & Interfaces www.acsami.org Research Article

angle of 7.3°.[26] In addition to different values for the observed mismatch angle, these studies offer different explanations for its origin. Although some attribute the observed (mis)alignment to the vdW epitaxy, accommodating the mismatch in lattice constants,[23,24] others use the structural features of the underlying G and the edges[25] as an explanation.

In a recent theoretical work, Zhu *et al.*[15] explained the orientational ordering of finite size homostructures, for example, MoS_2 flakes on a MoS_2 substrate, using a purely geometrical argument: the lowest energy configuration is the one obtained by the rototranslation of the rigid flake which maximizes the number of locally commensurate regions. Although this argument is solely based on geometry, it provides a satisfactory approximation for finite size systems but in the limit of infinite planes, that is, for large enough flakes, commensurate regions equal incommensurate ones. Therefore, in the limit of extended interfaces, other theoretical frameworks are needed.

In this contribution, we aim to explore the energy landscape originating from the rotational degree of freedom of edge-free, complex layered heterostructures and relate its fundamental origin to incommensurability and layer deformation at imposed angles. This will provide guidance for the design of vdW heterostructures and the control of the twisting degree of freedom. In order to make a more general point about the relative importance of different contributions, in determining the total energy landscape, we focus on a specific but well-studied system, namely, MoS_2/G. Although previous energy analysis focused on commensurate MoS_2/MoS_2 homostructures[29] or near-commensurate 2D-crystal G/hBN heterostructures,[30] the MoS_2/G BL system has a mismatch ratio $\rho = l/l \approx 0.8$ far away from the commensurate value $\rho = 1$ and, moreover, is composed of a mixture of 2D and 3D crystal monolayers. This analysis shows the practical application of our argument and will also allow us to comment on the apparently contradictory experimental observations regarding this particular system.

RESULTS AND DISCUSSION

In order to avoid finite-size effects and harvest information solely from the relaxation of the atoms in the layers, we implemented a protocol to build edge-free geometries. The resulting supercells are simultaneously compatible with the lattice mismatch and a relative imposed angle between the layers. As a result, periodic boundary conditions (PBCs) can be applied to these structures. The starting interface geometry is described by a pair of 2D lattices defined by vectors ($l_a\hat{\mathbf{a}}_1$, $l_a\hat{\mathbf{a}}_2$) and ($l_b\hat{\mathbf{b}}_1$, $l_b\hat{\mathbf{b}}_2$), where l_a and l_b represent the lattice constants and the $\hat{\mathbf{b}}_i$ vectors are rotated by an angle θ with respect to $\hat{\mathbf{a}}_i$. Two layers will be compatible if they satisfy the matching condition $l_a(n_1\hat{\mathbf{a}}_1 + n_2\hat{\mathbf{a}}_2) = l_b(m_1\hat{\mathbf{b}}_1 + m_2\hat{\mathbf{b}}_2)$, where the integer numbers n_1, n_2, m_1, and m_2 are supercell indices, representing the repetition along each lattice vector. In practice, for incommensurate lattice constants, the matching condition yielding PBC-compliant supercells can only be satisfied approximately, that is, the lattice spacing l' of one of the two components needs to deviate from its equilibrium value l. Here, in order to obtain suitable structures with imposed angles between 0 and 60°, we accept supercells satisfying $|l' - l| < 5 \times 10^{-7}$ Å. The resulting strain is applied to the MoS_2 layer, which leads to a maximum strain $\epsilon = \frac{l'-l}{l}$ within the same order of magnitude, four orders less than reported strains in other computational studies.[31−33] This protocol yields a set of supercells, each of which has a different number of atoms of up to 343,893, created according to the four supercell indices resulting in a unique twisting angle, satisfying the matching condition. Details of this protocol and all the parameters of the supercells used are reported in the Supporting Information.

In these supercells, we distinguish intralayer and interlayer interatomic interactions, resulting in the following Hamiltonian

$$H = H_{L_1} + H_{L_2} + H_{L_1L_2} \tag{1}$$

The G layer is modeled with the REBO potential,[34] $H_{L_1} = H_C^{(REBO)}$, while the three-body Stillinger−Weber (SW) potential[33] is used for MoS_2, $H_{L_2} = H_{MoS_2}^{(SW)}$. Interlayer coupling is described by the Lennard-Jones (LJ) potential

$$H_{L_1L_2} = H_{C-Mo,C-S}^{(LJ)} = \sum_{\substack{i\in C \\ j\in Mo,S}} 4\varepsilon_{ij}\left[\left(\frac{\sigma_{ij}}{r}\right)^{12} - \left(\frac{\sigma_{ij}}{r}\right)^{6}\right] \tag{2}$$

Because the interlayer interactions are especially relevant for the aim of this work, we refined the values for the C−Mo and C−S interactions found in ref 33. As a reference set, we computed the binding energy curves at the DFT level, using the Vienna Ab initio Simulation Package (VASP)[35,36] within the projector augmented-wave (PAW) framework.[37] The exchange−correlation potential is approximated using the PBE functional,[38] and the vdW dispersion is described by the DFT-D2 method.[39] After this procedure, we are able to perform energy minimizations using the conjugate gradient algorithm available within the LAMMPS package.[40] More details about the fitting and minimization procedure can be found in the Supporting Information. An overview of the computational setup can be found in Figure 1.

An approximate theory for the orientational ordering of an incommensurate interface was proposed by Novaco and McTague.[41,42] Although developed in the context of epitaxial growth of noble gas layers on metal surfaces, it has been successfully applied to the behavior of mesoscopic colloidal layers in optical lattices[43] and metal clusters adsorbed on G.[44] The assumption of the Novaco−McTague (NM) theory is that two purely 2D systems, linked *via* an interface, may be divided into two separate components: a soft adsorbate layer, treated within the harmonic approximation, atop a rigid substrate. This means that one of the intralayer terms in eq 1 is substituted by its harmonic approximation, while the coordinates of the second layer are frozen at its initial values, r_0. For example, considering G as the adsorbate and MoS_2 as the substrate yields the following Hamiltonian

$$H_{NM} = H_C^{(REBO)}|_{harmonic} + H_{MoS_2}^{(SW)}|_{r_0} + H_{C-MO,C-S} \tag{3}$$

If the substrate and the adsorbate lattices are incommensurate, because of a mismatch in lattice constants, the system is frustrated: the intralayer interactions within the adsorbate favor the intrinsic equilibrium lattice spacing, while the interactions with the substrate drive the atoms away from their equilibrium positions. In the limit of long-wavelength distortions, the NM theory predicts that the system can lower its energy by converting part of the longitudinal stress coming from the

https://dx.doi.org/10.1021/acsami.0c13971
ACS Appl. Mater. Interfaces 2020, 12, 45214−45221

ACS Applied Materials & Interfaces www.acsami.org Research Article

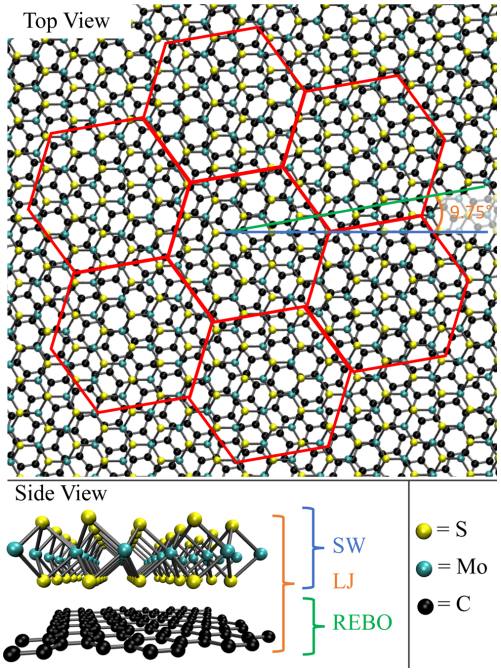

Figure 1. Schematic overview of the computational setup displayed for a mismatch angle of 9.75°. In the top panel, a top view is provided, including a sketch of moiré tiling resulting from the geometrical interference between the two lattices. The mismatch angle between the lattice direction of MoS_2 (blue line) and G (green line) lattices is reported as well. In the bottom panel, a side view is provided, including the corresponding force fields that have been used.

incommensurability into shear stress. This yields a small misalignment angle between the two lattices given by

$$\cos\theta_{NM} = \frac{1+\rho^2(1+2\delta)}{\rho[2+\delta(1+\rho^2)]} \quad (4)$$

where $\rho = l_{substrate}/l_{adsorbate}$ is the mismatch ratio between the two lattices and $\delta = (c_L/c_T)^2 - 1$, with c_T and c_L being the transverse and longitudinal sound velocities of the adsorbate, respectively.

The result of NM in eq 4 can be applied to our system by extracting the sound velocity of each single layer from the phonon dispersion, as reported in the Supporting Information. There are two possible scenarios: G can be treated as the rigid substrate, while MoS_2 acts as a soft adsorbate or vice versa. In the first case, the theory predicts $\theta_{NM}^{MoS_2} = 8.0°$, while if G is the adsorbate, the minimum-energy angle is $\theta_{NM}^{G} = 8.6°$. The prediction of the NM model can be verified by minimizing the total energy of the twisted geometries described above under suitable constraints. We froze the atoms of the heterostructures in the direction perpendicular to the surface, that is, the z axis, effectively reducing the dimensionality of the system to 2D. Furthermore, we also froze the atoms of the substrate layer in the in-plane directions x and y, enforcing a fully rigid substrate.

As mentioned at the beginning of this section and explained in detail in one of the sections of the Supporting Information, the edge-free geometries used in this work inevitably retain a degree of stress resulting from the matching condition for the two lattices in order to be able to apply PBCs. The slightly different strains, unique to every geometry, result in different offsets in the obtained energies. Because these offsets are of the same order as the energy gain arising from in-plane displacement of the atoms, this residual strain leads to a significant noise in the signal of the energy profile as a function of the imposed angle. To overcome this problem and to obtain a clear signal from our simulations, we enhanced the LJ-coupling strength between the MoS_2 and G layers. In other words, we set the LJ parameters ϵ_{ij} in eq 2 to $\epsilon'_{ij} = 100\ \epsilon_{ij}$ during geometry optimization. Next, the applied bias is corrected by scaling back the energy profile, as if simulated with the original value of ϵ_{ij}. As is shown in section three of the Supporting Information, this computational trick solely reduces the noise without affecting the actual physics of the problem.

Figure 2 shows the optimized energy E (meV/atom) as a function of the angle θ (°), with respect to the energy of the

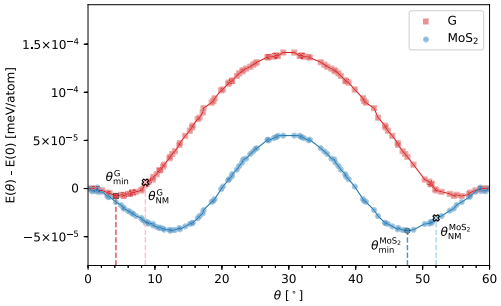

Figure 2. Energy E (meV/atom) as a function of the imposed angle θ (°) for different 2D models: red squares refer to flexible G on top of rigid MoS_2; blue circles refer to flexible MoS_2 on top of rigid G. The labels in the legend indicate the flexible ML. The reference value of the energy scale is set to $E(0)$. The minimum-energy point along each curve is highlighted by a dashed line and a label. Red and blue crosses (accompanied by a label) mark the minimum angle predicted by the NM theory for the first and second cases, respectively. The minimum-energy and NM-predicted angles for flexible MoS_2 are reported starting from 60° for easiness of reading.

aligned structures, $E(0)$. The two curves refer to the following models: 2D-adsorbed G atop rigid MoS_2 (red) and 2D-adsorbed MoS_2 atop rigid G (blue). Both cases reveal a minimum at a nonzero angle: for the adsorbed G case, the minimum is found at $\theta_{min}^{G} = 4.2°$, while for the adsorbed MoS_2 case, it is at $\theta_{min}^{MoS_2} = 12.3°$. Because of the intrinsic hexagonal symmetry of our system, each curve has two symmetrical minima centered at around 30°. The simulations show that the physics described by the approximation of eq 4 is still valid, that is, a nonzero minimum angle is observed for both cases. However, the absolute values of the predicted and observed angles are not in agreement, yielding a discrepancy of $\theta_{min}^{G} - \theta_{NM}^{G} = -4.4°$, in the case of 2D-adsorbed G, and $\theta_{min}^{MoS_2} - \theta_{NM}^{MoS_2} = 4.3°$, in the case of 2D-adsorbed MoS_2.

https://dx.doi.org/10.1021/acsami.0c13971
ACS Appl. Mater. Interfaces 2020, 12, 45214−45221

A previous study of G and h-BN heterostructures showed[30] that the NM model quantitatively describes the relaxation of the constrained system of these purely 2D materials. Here, the NM theory captures the basics of the physics but is not able to describe satisfactorily the complex geometry of the bilayer system, especially in the case of the flexible MoS_2 layer. We attribute the poor prediction of the theory in our case to the internal 3D structure of the MoS_2 monolayer, which indeed is unaccounted for in the NM model. This suggests that the NM theory is generally of limited utility for any bilayer comprising TMDs or other systems with a 3D monolayer structure. Another difference between our results and the results found for G/hBN heterostructures[30] is the quantitative difference in the energy values. In fact, our results report energy differences of 1 order of magnitude less. We explain this difference by the earlier mentioned relatively large MoS_2/G BL system mismatch ratio $\rho = l/l \approx 0.8$. Because of this significant incommensurability between the MoS_2 and G, present for all rotations, the atom displacements and energy differences are expected to be less pronounced. In fact, a similar observation has been carried out experimentally by Diaz *et al.*[27] and Pierucci *et al.*[28] For example, Diaz *et al.* found that the MoS_2/G moiré pattern obtained *via* AFM measurements was less pronounced compared to the one of hBN/G.

Considering another case, one in which all degrees of freedom are considered, that is, all atoms are free to move in the 3D space, the NM theory is even qualitatively inadequate. Figure 3 shows the energy E (meV/atom) as a function of the angle θ (°) of the system without rigid substrate, but with two soft, interacting layers. Naturally, the LJ coupling between the two layers has been restored to the values obtained from fitting against the DFT data to correctly reproduce interlayer forces. The behavior that we found is both quantitatively and qualitatively different from the constrained system presented previously. The introduction of the out-of-plane dimension (z) changes the response qualitatively. The energy minima at nonzero angles have disappeared, and the energy now increases symmetrically from the global minima at the aligned cases (0°,60°) toward the global maximum at a mismatch angle of 30°. From Figure 3, one can thus deduce that at 0 K, the fully flexible bilayer system will be stable when aligned at 0 or 60°. The energy profile around a misalignment of 30° is flat, and the misaligned geometry at this angle could therefore be characterized as metastable, as a vanishing force $F = -dE(\theta)/d\theta$ drives the system toward the global minima at 0 or 60°. In the thermodynamic limit, this orientation should not occur, considering it is the global energy maximum. The fact that nonaligned structures are observed experimentally[23] can be explained by the fact that this type of geometry can be temporarily stabilized by a small internal friction, for example, because of local defects, creating energy barriers that need to be overcome first.

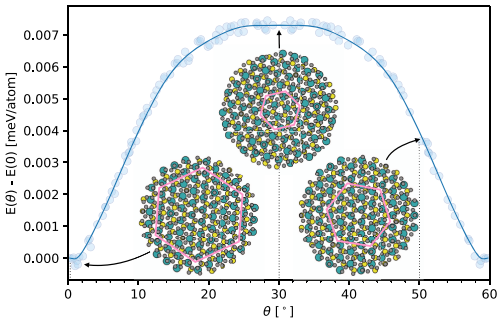

Figure 3. Energy per atom $E(\theta)$, in meV, as a function of the imposed angle θ. Each point in the energy landscape represents a distinct geometry at a different imposed angle, and the blue line is a Bézier fit. The small oscillations at $\theta = 0°$, 60° are due to numerical noise in the energy simulations. The circular insets show top views of the relaxed structures at $\theta \approx 0°$ (bottom left), $\theta \approx 50° \equiv 10°$ (bottom right), and $\theta \approx 30°$ (top center). The atoms are colored according to the scheme in Figure 1. The pink hexagons sketch the moiré tile in each configuration.

The NM theory does not hold when structural distortions perpendicular to the interface are allowed. Our results indicate that these are important for MoS_2/G heterostructures, and we believe that this is also the case for other complex heterostructures. The core of the NM argument is that the collective misalignment arises because of the excitation of the transverse phonon branch in the xy plane, which lies lower in energy than the longitudinal branch. This static distortion, which results in an increased internal energy of the adsorbate layer, is counterbalanced by a better interdigitation of the two lattices, that is, the displaced atoms are locally displaced to an overall more favorable stacking, with respect to the interlayer potential.[41,42] If out-of-plane distortions, unaccounted for in the NM theory, lead to a better interplay between the two layers, that is, if there is a gain in the interlayer coupling energy that is larger than the intralayer energy penalty from out-of-plane modulations, the system will lower its total energy. Different from the NM theory, the lowest-energy distortion in this scenario would not result in a misalignment between the components but in the formation of ripples, creating locally commensurate zones at the equilibrium distance and incommensurate zones at a larger interlayer distance.

Here, we characterize the out-of-plane deformations, disregarded in NM theory, in terms of the flexural phonon branch, which describes excitations perpendicular to the ML plane. In line with our edge-free geometries, the phonon picture is independent of sample size, and because the phonon eigenvectors represent a complete basis set,[45] any distortion in the crystal may be expressed as a linear combination of phonons. Moreover, treating the distortions of a layer in terms of its phonon spectrum decouples the intralayer energetics from interlayer interaction. Our analysis, reported in section seven of the Supporting Information, shows that deformations in the MoS_2 ML are 2 orders of magnitude smaller than the deformation of G. This signals that the distortion governing the energy economy of the system happens in the G layer, and we therefore focus the following analysis on this part only. As shown by the blue solid line in Figure 4, the flexural band is flat near the center of the Brillouin zone (BZ) (Γ point), that is, the long-wave modulations perpendicular to the basal plane can occur essentially without an energy penalty. Transverse (dashed gray in Figure 4) and longitudinal (dash-dotted gray in Figure 4) bands, which are the basis of NM theory, are higher in energy, resulting in more expensive modulations of the G layer.

Although the phonon spectrum describes the energy penalty compared to an isolated ML at equilibrium, the energy gain from interlayer interactions can be quantified in terms of moiré patterns. The moiré superlattice is a geometrical construction

https://dx.doi.org/10.1021/acsami.0c13971
ACS Appl. Mater. Interfaces 2020, 12, 45214−45221

ACS Applied Materials & Interfaces www.acsami.org Research Article

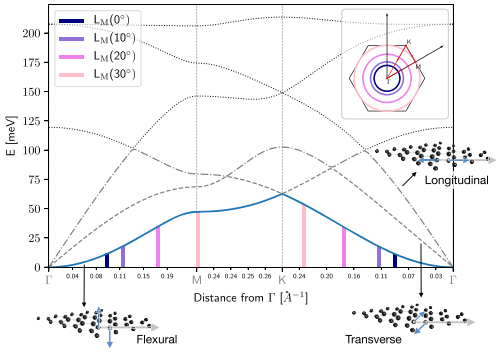

Figure 4. Phonon band structure of the G monolayer. The y axis reports the phonon energy, while the x axis marks the distance from the origin along the path $\Gamma \rightarrow M \rightarrow K \rightarrow \Gamma$, shown in the top right inset and marked along the x axis by gray dashed lines. The flexural branch is reported by a solid blue line, the transverse branch by is reported by a dashed gray line, and the longitudinal branch is reported by a dash-dotted gray line, while other branches are shown in dotted black lines. Colored segments along x increasing from $y = 0$ to the flexural branch mark wavevectors matching the moiré spacing $L_M(\theta)$ for the geometries in the insets of Figure 5, as highlighted by the color code. The moiré wavevector k_M corresponding to real-space wavelength L_M is shown in the top-right inset following the color code in the legend in the top left. The insets marked by black arrows show the characteristic displacement pattern for the three acoustic branches: the gray arrow indicates the direction of the wavevector $\vec{k}$ and the blue arrow indicates the displacement of the atoms in a unit cell.

describing the interference between two lattices and can be used to identify geometrical correspondence between lattices, that is, zones of local commensuration versus incoherent stacking. The symmetry of the moiré superlattice reflects the one underlying Bravais lattices, and its lattice parameter L_M is given by[46]

$$L_M(\theta) = \frac{l_G}{\sqrt{1 + \rho^{-2} - 2\rho^{-1}\cos\theta}} \quad (5)$$

Figure 5 shows the correlation between out-of-plane modulations, that is, rippling in the z dimension, and the moiré pattern in the G sheet. At $\theta = 0$, the moiré spacing and the average displacement along z are at a maximum, and they both decrease as the misalignment increases. As θ increases, the length of the pattern shrinks with the displacement along z: at $\theta = 30°$, the moiré shrinks to a couple of unit cells and the monolayer remains basically flat. The rippling patterns follow the moiré superlattice perfectly, as shown in the insets of Figure 5 for selected values of θ, that is, the nearest configurations having approximately angles of $\theta = 0°$ (0.23°), 10° (9.75°), 20° (19.89°), and 30° (29.17°). The local information expressed in the ripples of the carbon sheet is condensed in the thickness of the G layer

$$\tau(\theta) = \max_{\vec{r}_i \in G} z_i - \min_{\vec{r}_i \in G} z_i \quad (6)$$

which is a global parameter with a single value for each twisted geometry, as reported by black circles on the left y axis in Figure 5.

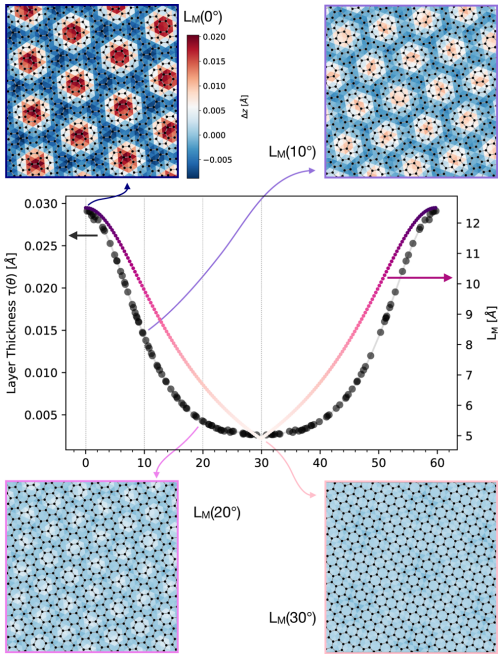

Figure 5. Thickness of the G layer $\tau(\theta)$ resulting from the displacement of C atoms (black circles, left axis) and spacing of the moiré pattern $L_M(\theta)$ (colored dotted line, right axis) as a function of θ for equivalent configurations at 0 and 60° rotating toward 30°. The insets show the local distortion following the moiré lattice in a square of sides 60 Å at the nearest configuration having approximately angles of $\theta = 0°$ (0.23°, dark purple), 10° (9.75°, purple), 20° (19.89°, dark pink), and 30° (29.17°, pink). The color of each triangle reports change in height $\Delta z = z - z_{eq}$ coordinate of the corresponding C atom (black points) following the color code reported in the top left. For example, the moiré pattern can be seen in the inset for $L_M(0°)$ as the lattice defined by the red regions.

Combining the geometrical construction shown in Figure 5 and the G phonon dispersion in Figure 4, we can explain the energy profile in Figure 3. The moiré spacing $L_M(\theta)$ can be mapped to wavevectors into the BZ by $k_M(\theta) = \frac{2}{\sqrt{3}L_M(\theta)}$. The wavevectors k_M, corresponding to the spacing L_M of the geometries in the insets of Figure 5, are highlighted in Figure 4. All wavevectors in the BZ at the moiré spacing are shown by vertical segments along the path and as circles in the inset and follow the same color code. A modulation of the G sheet, with wavelength $L_M(\theta)$, can be represented as a combination of phonon modes of matching wavevectors $k_M(\theta)$. Because the modulation of the G layer essentially takes solely place in the z direction, the major contribution in the decomposition on phonon modes will come from the flexural branch. Within small displacements from the equilibrium positions, the energy price of such modulations can be estimated by the corresponding phonon energy. As θ varies from 0 to 30° and the moiré shrinks, like is shown in Figure 5, the associated wavevector $k_M(\theta)$ assumes the values between $k_M(0°) = 0.09$ Å^{-1} (dark-purple lines in Figure 4) and $k_M(30°) = 0.24$ Å^{-1} (pink lines in Figure 4), at increasing flexural-phonon energies.

https://dx.doi.org/10.1021/acsami.0c13971
ACS Appl. Mater. Interfaces 2020, 12, 45214−45221

Next, we describe these limiting cases in more detail. At $\theta = 0°$, the spacing of the moiré is $L_M = 12.5$ Å, which is the distance between the locally commensurate patches, the red regions in Figure 5. As signaled by the dark-purple line in Figure 4, flexural phonon modes of this length in G are close to the flat region around Γ and therefore energetically inexpensive. This allows commensurate regions to stay at the equilibrium interlayer position, while incommensurate ones are pushed away from MoS_2 ML, perpendicular to the basal planes. As θ increases to 30°, L_M decreases, and thus, the distance between locally commensurate areas reduces. As a result, the deformation needs to occur over a shorter distance, and its energy cost therefore increases. At $\theta = 30°$, $L_M = 4.88$ Å, which is about two G unit cells. As shown by the pink line in Figure 4, deformations of this length scale are described by phonons at the edges of the BZ and are energetically more expensive than the gain coming from the interdigitation with the substrate. Therefore, the G sheet remains flat, at the expense of the interlayer coupling, resulting in a higher total energy of the heterostructure compared to the aligned case. The flattening of the flexural branch near the edges of the BZ, as shown by the solid blue line between M and K in Figure 4, is mirrored by the plateau in the energy profile in Figure 3 around $\theta = 30°$: in the whole region, moiré modulations are too expensive and the system cannot obtain any energy gain.

To sum up, the unconstrained 3D heterostructure lowers its energy by out-of-plane distortions according to the moiré pattern. This is particularly evident at $\theta = 0$, where $L_M = 12.5$ Å: here, the flexural distortion is almost without any energy penalty and the system lowers its energy by improving the interdigitation between G and the MoS_2 layers. As θ increases, L_M decreases and the cost of the ripples overtakes the gain in energy because of local commensuration, yielding flat G and an increased total energy. Finally, the region of the BZ spanned by the moiré spacing as a function of θ (the region between purple and pink segments in Figure 4) shows that the approximation of the long wavelength used to derive eq 4 is unsuited in the large-mismatched heterostructures. Because of the fact that also phonon excitation near the border of the BZ is involved in the energy economy of the system, a modified epitaxy theory is needed in these cases to predict and to understand the phase stability of imposed twist angles.

CONCLUSIONS

We explored the stability of twisted vdW heterostructures. Although often overlooked, this phenomenon is of particular importance in the emerging field of twistronics, as it can be a decisive factor in the real-life application of such systems. The energy as a function of an imposed angle determines whether a device is at risk of rotating away from a prepared angle. Our analysis of MoS_2/G heterostructures helps to clarify the scattered experimental data. We find a single global minimum at $\theta = 0$ and 60°, that is, only epitaxial stacking is expected for the system at 0 K. However, experiments always present defects or intrinsic friction that might result in the emergence of activation energies, potentially trapping a system in a metastable (or even unstable) state. In the limit where such effects become negligible, that is, activation energy approaching zero, one would mostly observe heterostructures aligned at $\theta = 0$ and 60° and few 30°-rotated, in agreement with the results of Liu *et al.*[23] A possible experiment, to test the validity of our results, would be to perform a systematic repetition of the aforementioned experiments, focused upon reducing deviations resulting from working conditions, for example, annealing temperature. We expect that the results of such an effort will confirm our findings: with a high enough annealing temperature and large enough flakes of significant quality, the bilayer system should be found in the aligned configuration, with possibly some outliers at around 30°.

The relevance of our results becomes clear when considering the fact that interesting physics is observed at certain unstable mismatch angles.[28] Our findings show that care must be taken when designing nanodevices as properties observed in studies at a specific angle might fade over time because of the system spontaneously rotating toward the real thermodynamic equilibrium. In fact, others[19] also suggest that aligned structures are most suitable for optospintronic applications.

Finally, we explain the origin of the observed energy economy in terms of the interplay between flexural phonon modes of the pristine compounds and the moiré superlattice. This insight is general in nature and can be applied to all layered materials and heterostructures, serving as a design tool for twistronic devices. Stiffness in the out-of-plane direction should be considered as a critical property in the design of such devices. It is for example known that rippling can affect the Schottky junctions, which are directly related to the performance of optoelectronic devices such as photodetectors and solar cells.[47] Soft flexural phonon modes might be a lower energy route out of frustration than twisting, hindering the possibility of stable rotated configurations. Furthermore, our results show the need for a novel theory of epitaxy for layered materials, incorporating the flexural branches ignored in the NM theory and taking into account all phonon wavelengths. The insights presented here can serve as a starting point for developing such a theory of the epitaxial growth for vdW heterostructures.

METHODS

Classical MD all-energy minimizations of the rotated heterostructures have been performed using molecular dynamics by means of the LAMMPS package[40] using the conjugate gradient algorithm, where the energy tolerance was set to 1×10^{-15}. The REBO potential[34] was used for G, whereas an adapted version of the three-body SW potential[33] was used for MoS_2. To model the vdW interactions, we used an interlayer LJ potential. To obtain the explicit values of the parameters, we refined the values that can be found in the paper by Ding *et al.*,[33] of which we provide an elaborate description in the Supporting Information.

DFT ab initio calculations used to reparametrize the force field were carried out using DFT as implemented in the VASP[35,36] within the PAW framework.[37] The exchange−correlation potential is approximated using the PBE functional,[38] and the vdW dispersion is described by the DFT-D2 method.[39] A plane wave cutoff of 800 eV is adopted, and the BZ was sampled using a $13 \times 13 \times 1$ mesh.

Phonon calculation phonon bands were computed with the aid of Phonopy,[48] which was coupled to LAMMPS using phono-LAMMPS.[49] In both cases, the phonon dispersion was computed using the frozen method employing a $5 \times 5 \times 1$ supercell.

ASSOCIATED CONTENT

Supporting Information

The Supporting Information is available free of charge at https://pubs.acs.org/doi/10.1021/acsami.0c13971.

Details on the protocols, force field, and geometry parameters (PDF)

https://dx.doi.org/10.1021/acsami.0c13971
ACS Appl. Mater. Interfaces 2020, 12, 45214−45221

AUTHOR INFORMATION

Corresponding Authors

Andrea Silva − *Engineering Materials, University of Southampton, Southampton SO17 1BJ, U.K.; national Centre for Advanced Tribology Study at University of Southampton, Southampton SO17 1BJ, U.K.;* orcid.org/0000-0001-6699-8115; Email: a.silva@soton.ac.uk

Victor E. P. Claerbout − *Department of Control Engineering, Faculty of Electrical Engineering, Czech Technical University in Prague, Technicka 2, Prague 6 16627, Czech Republic;* Email: claervic@fel.cvut.cz

Authors

Tomas Polcar − *Engineering Materials, University of Southampton, Southampton SO17 1BJ, U.K.; Department of Control Engineering, Faculty of Electrical Engineering, Czech Technical University in Prague, Technicka 2, Prague 6 16627, Czech Republic*

Denis Kramer − *Engineering Materials, University of Southampton, Southampton SO17 1BJ, U.K.; Mechanical Engineering, Helmut Schmidt University, Hamburg 22043, Germany*

Paolo Nicolini − *Department of Control Engineering, Faculty of Electrical Engineering, Czech Technical University in Prague, Technicka 2, Prague 6 16627, Czech Republic;* orcid.org/0000-0003-1324-7566

Complete contact information is available at: https://pubs.acs.org/10.1021/acsami.0c13971

Author Contributions

A.S. and V.E.P.C. carried out all calculations and data analysis and conceptualize the study in the first place. P.N. and D.K. supervised extensively the study and T.P. guided the project. All authors contributed to the writing of this work. Finally, P.N., D.K., and T.P. secured funding acquisition.

Notes

The authors declare no competing financial interest.

ACKNOWLEDGMENTS

The authors are thankful to E. Tosatti, A. Vanossi, D. Mandelli, and M. Liao for the helpful discussions. This project has received funding from the European Union's Horizon2020 research and innovation programme under grant agreement no. 721642: SOLUTION. The authors acknowledge the use of the IRIDIS High Performance Computing Facility and associated support services at the University of Southampton in the completion of this work. This work was also supported by The Ministry of Education, Youth and Sports from the Large Infrastructures for Research, Experimental Development and Innovations project "e-Infrastructure CZ − LM2018140" and by the project Novel nanostructures for engineering applications no. CZ.02.1.01/0.0/0.0/16_026/0008396.

REFERENCES

(1) Mannix, A. J.; Kiraly, B.; Hersam, M. C.; Guisinger, N. P. Synthesis and Chemistry of Elemental 2D Materials. *Nat. Rev. Chem.* **2017**, *1*, 0014.

(2) Chhowalla, M.; Shin, H. S.; Eda, G.; Li, L.-J.; Loh, K. P.; Zhang, H. The Chemistry of Two-Dimensional Layered Transition Metal Dichalcogenide Nanosheets. *Nat. Chem.* **2013**, *5*, 263−275.

(3) Vazirisereshk, M. R.; Martini, A.; Strubbe, D. A.; Baykara, M. Z. Solid Lubrication with MoS_2: A Review. *Lubricants* **2019**, *7*, 57.

(4) Radisavljevic, B.; Radenovic, A.; Brivio, J.; Giacometti, V.; Kis, A. Single-Layer MoS_2 Transistors. *Nat. Nanotechnol.* **2011**, *6*, 147−150.

(5) Lopez-Sanchez, O.; Lembke, D.; Kayci, M.; Radenovic, A.; Kis, A. Ultrasensitive Photodetectors Based on Monolayer MoS_2. *Nat. Nanotechnol.* **2013**, *8*, 497−501.

(6) Lauritsen, J. V.; Bollinger, M. V.; Lægsgaard, E.; Jacobsen, K. W.; Nørskov, J. K.; Clausen, B. S.; Topsøe, H.; Besenbacher, F. Atomic-Scale Insight into Structure and Morphology Changes of MoS_2 Nanoclusters in Hydrotreating Catalysts. *J. Catal.* **2004**, *221*, 510−522.

(7) Shi, X.-R.; Jiao, H.; Hermann, K.; Wang, J. CO Hydrogenation Reaction on Sulfided Molybdenum Catalysts. *J. Mol. Catal. A: Chem.* **2009**, *312*, 7−17.

(8) Shi, X.-R.; Wang, S.-G.; Hu, J.; Wang, H.; Chen, Y.-Y.; Qin, Z.; Wang, J. Density Functional Theory Study on Water-Gas-Shift Reaction over Molybdenum Disulfide. *Appl. Catal., A* **2009**, *365*, 62−70.

(9) Dienwiebel, M.; Verhoeven, G. S.; Pradeep, N.; Frenken, J. W. M.; Heimberg, J. A.; Zandbergen, H. W. Superlubricity of Graphite. *Phys. Rev. Lett.* **2004**, *92*, 126101.

(10) Vazirisereshk, M. R.; Ye, H.; Ye, Z.; Otero-de-la-Roza, A.; Zhao, M.-Q.; Gao, Z.; Johnson, A. T. C.; Johnson, E. R.; Carpick, R. W.; Martini, A. Origin of Nanoscale Friction Contrast between Supported Graphene, MoS_2, and a Graphene/MoS_2 Heterostructure. *Nano Lett.* **2019**, *19*, 5496−5505.

(11) Geim, A. K.; Grigorieva, I. V. Van der Waals Heterostructures. *Nature* **2013**, *499*, 419−425.

(12) Novoselov, K. S.; Mishchenko, A.; Carvalho, A.; Castro Neto, A. H. 2D Materials and van der Waals Heterostructures. *Science* **2016**, *353*, aac9439.

(13) Liu, Y.; Weiss, N. O.; Duan, X.; Cheng, H.-C.; Huang, Y.; Duan, X. Van der Waals Heterostructures and Devices. *Nat. Rev. Mater.* **2016**, *1*, 16042.

(14) Zhang, K.; Fang, X.; Wang, Y.; Wan, Y.; Song, Q.; Zhai, W.; Li, Y.; Ran, G.; Ye, Y.; Dai, L. Ultrasensitive Near-Infrared Photodetectors Based on a Graphene-$MoTe_2$-Graphene Vertical van der Waals Heterostructure. *ACS Appl. Mater. Interfaces* **2017**, *9*, 5392−5398.

(15) Zhu, S.; Pochet, P.; Johnson, H. T. Controlling Rotation of Two-Dimensional Material Flakes. *ACS Nano* **2019**, *13*, 6925−6931.

(16) Du, L.; Yu, H.; Liao, M.; Wang, S.; Xie, L.; Lu, X.; Zhu, J.; Li, N.; Shen, C.; Chen, P.; Yang, R.; Shi, D.; Zhang, G. Modulating PL and Electronic Structures of MoS_2/Graphene Heterostructures via Interlayer Twisting Angle. *Appl. Phys. Lett.* **2017**, *111*, 263106.

(17) Huang, Y. L.; Chen, Y.; Zhang, W.; Quek, S. Y.; Chen, C.-H.; Li, L.-J.; Hsu, W.-T.; Chang, W.-H.; Zheng, Y. J.; Chen, W.; Wee, A. T. S. Bandgap Tunability at Single-Layer Molybdenum Disulphide Grain Boundaries. *Nat. Commun.* **2015**, *6*, 6298.

(18) Martin, J. M.; Erdemir, A. Superlubricity: Friction's Vanishing Act. *Phys. Today* **2018**, *71*, 40−46.

(19) Du, L.; Zhang, Q.; Gong, B.; Liao, M.; Zhu, J.; Yu, H.; He, R.; Liu, K.; Yang, R.; Shi, D.; Gu, L.; Yan, F.; Zhang, G.; Zhang, Q. Robust spin-valley polarization in commensurate MoS_2/graphene heterostructures. *Phys. Rev. B* **2018**, *97*, 115445.

(20) Zan, R.; Ramasse, Q. M.; Jalil, R.; Tu, J.-S.; Bangert, U.; Novoselov, K. S. Imaging Two Dimensional Materials and their Heterostructures. *J. Phys.: Conf. Ser.* **2017**, *902*, 012028.

(21) Cao, Y.; Fatemi, V.; Fang, S.; Watanabe, K.; Taniguchi, T.; Kaxiras, E.; Jarillo-Herrero, P. Unconventional Superconductivity in Magic-Angle Graphene Superlattices. *Nature* **2018**, *556*, 43−50.

(22) Liao, M.; Wu, Z.-W.; Du, L.; Zhang, T.; Wei, Z.; Zhu, J.; Yu, H.; Tang, J.; Gu, L.; Xing, Y.; Yang, R.; Shi, D.; Yao, Y.; Zhang, G. Twist Angle-Dependent Conductivities Across MoS_2/Graphene Heterojunctions. *Nat. Commun.* **2018**, *9*, 4068.

(23) Liu, X.; Balla, I.; Bergeron, H.; Campbell, G. P.; Bedzyk, M. J.; Hersam, M. C. Rotationally Commensurate Growth of MoS_2 on Epitaxial Graphene. *ACS Nano* **2016**, *10*, 1067−1075.

(24) Shi, Y.; Zhou, W.; Lu, A.-Y.; Fang, W.; Lee, Y.-H.; Hsu, A. L.; Kim, S. M.; Kim, K. K.; Yang, H. Y.; Li, L.-J.; Idrobo, J.-C.; Kong, J.

https://dx.doi.org/10.1021/acsami.0c13971
ACS Appl. Mater. Interfaces 2020, 12, 45214−45221

Van der Waals Epitaxy of MoS_2 Layers Using Graphene As Growth Templates. *Nano Lett.* **2012**, *12*, 2784−2791.
(25) Lu, C.-I.; Butler, C. J.; Huang, J. K.; Hsing, C. R.; Yang, H. H.; Chu, Y. H.; Luo, C. H.; Sun, Y. C.; Hsu, S. H.; Yang, K. H. O.; Wei, C. M.; Li, L. J.; Lin, M. T. Graphite Edge Controlled Registration of Monolayer MoS_2 Crystal Orientation. *Appl. Phys. Lett.* **2015**, *106*, 181904.
(26) Adrian, M.; Senftleben, A.; Morgenstern, S.; Baumert, T. Complete Analysis of a Transmission Electron Diffraction Pattern of a MoS_2-Graphite Heterostructure. *Ultramicroscopy* **2016**, *166*, 9−15.
(27) Diaz, H. C.; Avila, J.; Chen, C.; Addou, R.; Asensio, M. C.; Batzill, M. Direct Observation of Interlayer Hybridization and Dirac Relativistic Carriers in Graphene/MoS_2 van der Waals Heterostructures. *Nano Lett.* **2015**, *15*, 1135−1140.
(28) Pierucci, D.; Henck, H.; Avila, J.; Balan, A.; Naylor, C. H.; Patriarche, G.; Dappe, Y. J.; Silly, M. G.; Sirotti, F.; Johnson, A. T. C.; Asensio, M. C.; Ouerghi, A. Band Alignment and Minigaps in Monolayer MoS_2-Graphene van der Waals Heterostructures. *Nano Lett.* **2016**, *16*, 4054−4061.
(29) Naik, M. H.; Maity, I.; Maiti, P. K.; Jain, M. Kolmogorov-Crespi Potential for Multilayer Transition-Metal Dichalcogenides: Capturing Structural Transformations in Moiré Superlattices. *J. Phys. Chem. C* **2019**, *123*, 9770−9778.
(30) Guerra, R.; van Wijk, M.; Vanossi, A.; Fasolino, A.; Tosatti, E. Graphene on h-BN: to Align or Not to Align? *Nanoscale* **2017**, *9*, 8799−8804.
(31) Wang, Y.; Xiao, J.; Zhu, H.; Li, Y.; Alsaid, Y.; Fong, K. Y.; Zhou, Y.; Wang, S.; Shi, W.; Wang, Y.; Zettl, A.; Reed, E. J.; Zhang, X. Structural Phase Transition in Monolayer $MoTe_2$ Driven by Electrostatic Doping. *Nature* **2017**, *550*, 487−491.
(32) Wang, Z.-J.; Ma, T.-B.; Hu, Y.-Z.; Xu, L.; Wang, H. Energy Dissipation of Atomic-scale Friction Based on One-Dimensional Prandtl-Tomlinson Model. *Friction* **2015**, *3*, 170−182.
(33) Ding, Z.; Pei, Q.-X.; Jiang, J.-W.; Huang, W.; Zhang, Y.-W. Interfacial Thermal Conductance in Graphene/MoS_2 Heterostructures. *Carbon* **2016**, *96*, 888−896.
(34) Brenner, D. W.; Shenderova, O. A.; Harrison, J. A.; Stuart, S. J.; Ni, B.; Sinnott, S. B. A Second-Generation Reactive Empirical Bond Order (REBO) Potential Energy Expression for Hydrocarbons. *J. Phys.: Condens. Matter* **2002**, *14*, 783−802.
(35) Kresse, G.; Hafner, J. Ab Initio Molecular Dynamics for Open-Shell Transition Metals. *Phys. Rev. B: Condens. Matter Mater. Phys.* **1993**, *48*, 13115−13118.
(36) Kresse, G.; Joubert, D. From Ultrasoft Pseudopotentials to the Projector Augmented-Wave Method. *Phys. Rev. B: Condens. Matter Mater. Phys.* **1999**, *59*, 1758−1775.
(37) Blöchl, P. E. Projector Augmented-Wave Method. *Phys. Rev. B: Condens. Matter Mater. Phys.* **1994**, *50*, 17953−17979.
(38) Perdew, J. P.; Burke, K.; Ernzerhof, M. Generalized Gradient Approximation Made Simple. *Phys. Rev. Lett.* **1996**, *77*, 3865−3868.
(39) Grimme, S. Semiempirical GGA-type Density Functional Constructed with a Long-Range Dispersion Correction. *J. Comput. Chem.* **2006**, *27*, 1787−1799.
(40) Plimpton, S. Fast Parallel Algorithms for Short-Range Molecular Dynamics. *J. Comput. Phys.* **1995**, *117*, 1−19.
(41) Novaco, A. D.; McTague, J. P. Orientational Epitaxy-The Orientational Ordering of Incommensurate Structures. *Phys. Rev. Lett.* **1977**, *38*, 1286−1289.
(42) McTague, J. P.; Novaco, A. D. Substrate-Induced Strain and Orientational Ordering in Adsorbed Monolayers. *Phys. Rev. B: Condens. Matter Mater. Phys.* **1979**, *19*, 5299−5306.
(43) Brazda, T.; Silva, A.; Manini, N.; Vanossi, A.; Guerra, R.; Tosatti, E.; Bechinger, C. Experimental Observation of the Aubry Transition in Two-Dimensional Colloidal Monolayers. *Phys. Rev. X* **2018**, *8*, 011050.
(44) Panizon, E.; Guerra, R.; Tosatti, E. Ballistic Thermophoresis of Adsorbates on Free-Standing Graphene. *Proc. Natl. Acad. Sci. U.S.A.* **2017**, *114*, E7035−E7044.
(45) Wallace, D. C.; Callen, H. Thermodynamics of Crystals. *Am. J. Phys.* **1972**, *40*, 1718−1719.
(46) Mandelli, D.; Vanossi, A.; Manini, N.; Tosatti, E. Friction Boosted by Equilibrium Misalignment of Incommensurate Two-Dimensional Colloid Monolayers. *Phys. Rev. Lett.* **2015**, *114*, 108302.
(47) Tomer, D.; Rajput, S.; Li, L. Spatial inhomogeneity in Schottky barrier height at graphene/MoS_2 Schottky junctions. *J. Phys. D: Appl. Phys.* **2017**, *50*, 165301.
(48) Togo, A.; Tanaka, I. First Principles Phonon Calculations in Materials Science. *Scr. Mater.* **2015**, *108*, 1−5.
(49) Carreras, A. phonoLAMMPS. https://github.com/abelcarreras/phonolammps, 2019.

https://dx.doi.org/10.1021/acsami.0c13971
ACS Appl. Mater. Interfaces 2020, 12, 45214−45221

5

MoS_2 & Water

5.1 Introduction

A drawback of MoS_2, and solid lubricants in general, is their sensitivity to humidity, which can induce a significant change in the tribological properties [32, 42, 43, 63]. In the case of MoS_2, water contamination generally tallies with an increase in the COF, alongside an increase in the wear behavior [45, 46, 61, 62, 63]. This has already been addressed in Chap. 1. In a significant number of (potential) applications, however, ambient conditions are unavoidable. Therefore, in the specific case of MoS_2, the current effective working range as a solid lubricating coating is minimal, i.e., vacuum. To fully profit from the enormous potential of MoS_2 and solid lubricants in general, it is of great importance not only to understand in what way humidity affects their frictional properties but also to understand the mechanism behind it.

The consensus that humidity deteriorates the frictional properties of MoS_2 is widely accepted [62, 132, 133]. However, the underlying mechanism is vigorously debated. Whereas some ascribe it to contamination of the surface due to the physical interaction with water [44, 63], others relate it to oxidation of MoS_2 to MoO_3 [134, 135]. Recently, it was found that only physisorption of, instead of oxidation by, H_2O occurs on the stable basal planes of MoS_2 [43]. Furthermore, H_2O increased the interlayer distance when present at the interface, and MoS_2 acted rather hydrophobically [43]. In another study, it was found that for infinite basal planes, increasing the water coverage within the interface reduced the distance traversed after an initial kick, and that hydrogen bonds (H-bonds) were formed between the interacting water molecules [63]. The formation of a highly ordered H-bond network when intercalated in 2D materials has also been observed by others [136].

Although the earlier mentioned results are relevant, some questions remain unanswered. For example, how are the frictional properties of MoS_2 quantitatively affected by the presence of water during sliding, and what is the function of the H-bond water network? Furthermore, how are the frictional properties of MoS_2 in the presence of water affected by sliding velocity and the load applied to the system? In this chapter, a paper is presented that focused on the frictional properties of commensurate pseudo-bulk MoS_2 during sliding in the presence of water, employing non-equilibrium MD simulations. Based on previous results [44, 63], no tribochemical reactions were expected to occur; therefore, we resorted to a nonreactive FF. This allows for the simulation of larger systems, longer timescales, and a more comprehensive range of (external) conditions, such as a range of normal loads and water coverage. The main aim of this study was to quantify friction in the presence of water. More specifically, the effects of normal load and sliding velocity were evaluated for different amounts of water coverage, ranging from dry sliding to bulk water.

5.2 Approaches and Problems

The computational setup in this system consisted of six 'infinite' layers of commensurate $2H_c$-MoS_2, which was achieved by applying periodic boundary conditions to the simulation cell. Within the center interface, varying numbers of water molecules were inserted, ranging from dry sliding to full coverage, and one configuration with bulk water. The number of water molecules required to represent the total coverage adequately was estimated using the definition of the perpendicular crossing diamond network [136]. Next, a range of normal loads were applied to the top layer, perpendicular to the plane of the monolayers (in the z-direction). Finally, the lowest layer was held static by fixing the bottommost sulfur layer in the x-, y-, and z-direction. In contrast, the top layer was made mobile by introducing a driving force to the topmost sulfur layer.

Although the concept of this study is closely related to the previous study presented in Chap. 3, several problems were encountered. Here, we decided to work again with a driving force instead of a spring. To do so, and to mimic a strong adhesion to a moving support (e.g., like in an atomic force microscopy experiment) as closely as possible, the topmost layer of sulfur atoms was made rigid. However, during the minimization, an in-plane structural deformation of the layers was caused by the interaction with the water molecules located at the center interface in the low coverage regime. This out-of-plane puckering also reached the outermost layers. If the top layer had been made rigid during sliding, an unnatural behavior would result in the deformed shape of the top layer, which would cause a deformation of the neighboring layers and the water cluster. In reality, however, the water is the driving factor for the puckering. To circumvent this problem, the topmost layer of sulfur atoms was already made rigid in the xy-plane during the minimization. As a result, the inner layers are still allowed to deform, whereas the top layer only breathes in the z-direction and remains flat.

In the above, the structural deformation as a result of the water cluster is discussed. In a first attempt, several trial runs were performed in which the

water molecules were randomly spread within the center interface instead of modeling them as a cluster. However, sliding of the layers led to a repositioning of the water molecules causing them to cluster, although at a different speed depending on the initial configuration. Once a cluster was formed, it reshaped and showed a drift, but was never found to fall apart. Therefore, in the actual runs, clusters were selected to build the systems to save computational time and make all trajectories comparable.

Finally, during the analysis of the results and specifically the frictional forces, a large discrepancy was observed between different runs for the high coverage regime. This was even seen between runs for which the number of water molecules, the velocity, and the load were equal. Several explanations were considered, namely a configuration-dependent longer run-in period, an out-of-plane positioning of the water layer, and a stronger reshaping of the water network. However, none of the explanations were valid; the type of water network was comparable for all different runs and present along the whole trajectory. Moreover, the H-bond breaking/formation speeds were found to be practically the same, as well as the lifetime of the H-bonds and the drift velocities. Strangely enough, some trajectories that initially started with high frictional forces would end with low frictional forces, but the opposite transition was never observed. Additionally, it was found that the type of sliding dynamics of the trajectories with high/low frictional forces was different. In the trajectories with lower frictional forces, and thus lower dissipation, smooth dynamics were observed. In the trajectories with higher frictional forces and dissipation, stick-slip dynamics were observed, as was the case for the low water coverage regime. This observation hinted at the presence of a type of corrugated PES, which is directly related to the observation of stick-slip dynamics. Therefore, the orientation of the water network in the xy-plane was analyzed. From this, it was found that two possible orientations existed, which we defined as *parallel* and *anti-parallel*. Here, parallel and anti-parallel refer to the orientation of the H-bonds with respect to the sliding direction. Whereas for the parallel-oriented water network the corrugation of the PES was found to be of the same order as that of pure MoS_2, the anti-parallel PES was relatively flat. This observation explained the different types of dynamics and the difference in frictional force and dissipation. Because the parallel case was found to be

less energetically favorable, only the trajectories with an anti-parallel-oriented water network were selected in the quantitative analysis, making all results comparable.

5.3 Results and Outlook

The outcomes of this study led to several conclusions. It was found that when water is intercalated between layers of MoS_2, a single layer of water is formed, where a highly organized H-bond network holds the molecules together comparable to a solid 2D structure. Additionally, there exist preferential orientations of this water network when located above/beneath the MoS_2 layer that can be either parallel to the Mo-S bonds or anti-parallel. The parallel orientation can be considered a meta-stable state. The amount of water coverage can also be related to the type of sliding dynamics that are observed. From a side view, card-deck shearing of the MoS_2 layers was observed for dry sliding and low water coverage. For high coverage, block sliding was observed where the bottom three layers remained fixed, and the top three layers moved as one block according to the set velocity. From a top view, stick-slip dynamics for MoS_2 were observed for dry sliding and low water coverage, whereas for high coverage, smooth dynamics were found.

Finally, at odds with the common understanding, we found that there exist three frictional regimes due to the presence of water. The first two regimes concern the case where a thin layer of water is present. Here, water acts as a contaminant for low water coverage, characterized by stick-slip dynamics and high energy dissipation. For the high water coverage regime, water acts as a solidified lubricant, where smooth dynamics with low energy dissipation were found. The third regime is related to bulk water, where water acts as a liquid lubricant with a substantial velocity dependence, which is a standard feature. Our results contribute to the general understanding of the frictional mechanisms at play for solid lubricants in the presence of water, and can also serve as guidance for the design of nanoscale devices in ambient conditions.

I was the main author of this work and carried out the conceptualization,

data production and subsequent analysis, and writing of the original draft. All results of this study have been submitted as a contribution to a special issue of the Frontiers in Chemistry journal. This is an impacted journal, which had an impact factor of 3.693 in 2019 and belongs to the quartile category Q2 in the field of chemistry. A copy of the submitted manuscript is attached below.

Exploring nanoscale lubrication mechanisms of multilayer MoS_2 during sliding: the effect of humidity

Victor E.P. Claerbout [1], **Paolo Nicolini** [1,*] **and Tomas Polcar** [1,2]

[1] *Department of Control Engineering, Faculty of Electrical Engineering, Czech Technical University in Prague, Prague, Czech Republic*
[2] *Engineering Materials, University of Southampton, Southampton, United Kingdom*

Correspondence*:
Paolo Nicolini
Department of Control Engineering
Faculty of Electrical Engineering
Czech Technical University in Prague
Technicka 2, 16627 Prague 6, Czech Republic
nicolpao@fel.cvut.cz

ABSTRACT

Solid lubricants have received substantial attention due to their excellent frictional properties. Among others, molybdenum disulfide (MoS_2) is one of the most studied. Humidity results in a deterioration of the frictional properties of MoS_2. The actual mechanism at the nanoscale is still under debate, although there are indications that chemical reactions are not likely to occur in defect-free structures. In this study, we performed non-equilibrium molecular dynamics simulations to study the frictional properties of multilayer MoS_2 during sliding in the presence of water. Moreover, we also investigated the effect of sliding speed and normal load. We confirmed earlier results that a thin layer of water organizes as a solidified, ice-like network of hydrogen bonds, as a result of being confined in a two-dimensional fashion between MoS_2. Moreover, we found that there exists an energy driven, rotational dependence of the water network atop/beneath MoS_2. This orientational anisotropy is directly related to the dissipative character of MoS_2 during sliding. Finally, three distinct frictional regimes were identified, two for a thin layer of water and one for bulk water. In the case of a thin layer and low coverage, water represents a solid-like contaminant, causing high energy dissipation. For a thin layer and high coverage, water starts to act as a solid-like lubricant, reducing dissipation during sliding. And finally, a regime where water acts as a liquid lubricant, characterized by a clear velocity dependence.

Keywords: molybdenum disulfide, friction, water, hydrogen bond network, molecular dynamics simulations, tribology

1 INTRODUCTION

The presence of friction and wear has been linked to a loss of almost a quarter of the world's total energy consumption (Holmberg and Erdemir, 2017). The current demand of our industry has surpassed the application of 'classical' liquid lubricants in peculiar conditions, such as ultra-high vacuum, extreme contact pressures, super low/high temperatures, and extremely small dimensions. A new generation of

lubricants, so-called solid lubricants, offer new possibilities. Moreover, solid lubricants have been linked to superlubricity, a state in which the frictional forces vanish (Martin and Erdemir, 2018; Baykara et al., 2018). Among others, transition metal dichalcogenides (TMDs), and in particular molybdenum disulfide (MoS_2), are prototypical examples. TMDs are layered materials, where the monolayers have a so-called two-dimensional (2D) crystal structure with a transition metal covalently bound between chalcogens. The layers are held together by weak electrostatic and van der Waals interactions. As a result of this unique binding character, easy shearing between the layers is accommodated, creating an enormous potential for achieving low coefficients of friction (COF) (Martin et al., 1993; Scharf and Prasad, 2013). This is confirmed by numerous studies on their remarkable tribological characteristics (Evaristo et al., 2008; Mutafov et al., 2015; Pimentel et al., 2011; Martin et al., 1993; Cho et al., 2006; Watanabe et al., 2004). This, in combination with their low toxicity (Teo et al., 2014; Chng and Pumera, 2015), versatile chemistry, (Chhowalla et al., 2013) and peculiar electronic properties, has resulted both in macroscale applications, such as the automotive, aerospace, and space industries (Cho et al., 2006; Nian et al., 2017; Vazirisereshk et al., 2019) and nanoscale applications, such as photovoltaic and optoelectronic devices, transistors and solar cells (Li and Zhu, 2015; Choi et al., 2017).

In a significant number of (potential) applications, ambient conditions, such as humidity, are unavoidable, resulting in contaminated surfaces. Humidity, however, has shown to induce a significant alteration of the tribological properties of TMDs and other 2D materials, such as graphite/graphene (Evaristo et al., 2008; Levita et al., 2016; Levita and Righi, 2017; Scharf and Prasad, 2013; Hasz et al., 2018). In the case of MoS_2, humidity not only leads to an increase in wear, but also to a significant degradation in frictional properties (Khare and Burris, 2013; Arif et al., 2019; Panitz et al., 1988; Zhao and Perry, 2010; Chhowalla and Amaratunga, 2000; Levita and Righi, 2017; Serpini et al., 2019, 2017). For example, it has been found that clusters of contaminating adsorbates can induce a static friction, seemingly 'locking' surfaces in relative motion, that would otherwise slide smoothly (Ouyang et al., 2018). As a result, MoS_2 solid lubrication currently has a relatively small effective working range, limited to outer space or vacuum (Hasz et al., 2018). To extend its applicability, one should fully understand how humidity affects the lubricating mechanisms at the nanoscale during sliding.

Although the scientific community agrees that the beneficial frictional properties of MoS_2 deteriorate in case of increasing humidity (Dudder et al., 2011; Zhao and Perry, 2010; Khare and Burris, 2014; Serpini et al., 2017), the actual mechanism at the nanoscale is still under debate (Hasz et al., 2018). Some ascribe it to oxidation, whereby MoS_2 oxidizes to MoO_3 (Curry et al., 2017; Tagawa et al., 2007; Panitz et al., 1988). Others showed that humidity does not necessarily lead to oxidation, but that water physically interacts with the surface, thereby increasing interlayer friction (Khare and Burris, 2013; Levita and Righi, 2017; Serpini et al., 2017; Arif et al., 2019). Some use an argument based on adhesion, when explaining the changing frictional properties as a result of humidity (Hasz et al., 2018). In an experimental study, Lee *et al.* (Lee et al., 2020) showed that when a layer of water is intercalated between mica and exfoliated MoS_2, the frictional properties deteriorated. Interestingly, similar results were found for graphene and mica (Lee et al., 2017), contradicting previous reports that humidity leaves the frictional behavior unchanged (Berman et al., 2014). These results hint at a universal frictional mechanism for intercalated water layers, that is independent of the type of solid lubricant itself (Lee et al., 2020).

The frictional response of a material is highly complex and characterized by nonlinear, out-of-equilibrium dissipative processes (Vanossi et al., 2013). Simulation techniques offer possibilities to gain insights by disentangling the phenomena and using simplified models. Among others, Levita *et al.* made several computational contributions (Levita et al., 2016; Levita and Righi, 2017). In one study, (Levita et al.,

2016) the type of interaction between MoS_2 and water was determined using first principles calculations (FPC). Literature was discordant on whether this should be depicted as hydrophobic or hydrophilic (Late et al., 2012; Gaur et al., 2014). In addition, the tendency of MoS_2 towards 'adsorption of' versus 'being oxidized by' water was investigated. Due to the stable basal plane of MoS_2 (lacking any dangling bonds and characterized by low chemical reactivity), it was found that also in case of defects only physisorption occurs, such as S-vacancies. This observation was confirmed by others (Arif et al., 2019). Upon introducing water within the bilayer interface, the interlayer distance was found to increase, weakening the interlayer binding energy and destabilizing the structure. It was confirmed that MoS_2 does not favor oxidation (e.g. to MoO_3) and acts rather hydrophobically (Levita et al., 2016). This conclusion has been shared by others (Luan and Zhou, 2016) using molecular dynamics (MD) simulations.

To study the frictional properties, sliding should be considered; after all, kinetic friction is a dynamical response. In another study, based on *ab initio* MD, the chemical and physical interactions taking place during sliding of a single asperity of MoS_2, in the presence of water, were studied (Levita and Righi, 2017). At high temperature and load, it was found that an increasing water coverage present within the interface reduces the distance traversed after an initial kick. Again, and as expected from previous studies (Levita et al., 2016; Khare and Burris, 2013), no oxidation occurred. Furthermore, it was found that the water molecules formed a water network of H-bonds. Finally, S-vacancies did not induce significant deviations in the results. These observations were confirmed by a mainly experimental study (Arif et al., 2019), indicating that the main mechanism affecting the frictional properties of MoS_2, in the presence of water, is physisorption.

The earlier mentioned results are relevant, but some remarks are in place. Levita and Righi (Levita and Righi, 2017) used a high load (11 GPa) and temperature (320 K) to provide enough energy to the system to overcome potential energy barriers, which might affect the outcomes. Additionally, the simulation time was limited to the picosecond range, affecting the statistical precision of the results. Moreover, a structural analysis of the water network was not properly considered. When liquids, and water in particular, are confined in a small space, their properties might alter significantly (Bampoulis et al., 2016); this is in fact one of the problems of classical lubricants. In the case of water confined between two hydrophobic layers, ice-like water films have been found (Bampoulis et al., 2016), raising the question whether water acts as a (solid) lubricant or as a friction inducer (Lee et al., 2020). In the case of MoS_2, Kwac *et al.* (Kwac et al., 2017) found that, using MD, a characteristic tile-like pattern of squares and diamond forms, resulting from the MoS_2 surface charge. However, the sliding of the MoS_2 layers was not considered in this study.

The main aim of this study is to present a qualitative and quantitative analysis of the nanoscale frictional properties when sliding multilayer MoS_2 in the presence of water. More generically, our goal is to reveal broader features of the frictional behavior of solid lubricants in the presence of contaminants. Based on previous results (Levita and Righi, 2017; Khare and Burris, 2013), tribochemical reactions were not expected to occur. Therefore, classical non-equilibrium MD simulations were performed. This was done by considering the intercalation of various numbers of water molecules, varying from dry sliding to bulk water, located at the center interface. Furthermore, the effects of normal load and of sliding speed were investigated. Apart from gaining insight into the conformational landscape of water, this setup allows for insight into the mechanisms of the additional channel of dissipation, present when considering intercalated water, in the case of bulk MoS_2 and that of solid lubricants in general.

2 COMPUTATIONAL METHODS

The simulations have been carried out by means of the LAMMPS package (Plimpton, 1995), employing a force field developed by Sresht *et al.* (Sresht et al., 2017) for MoS_2. Its foundation is based upon harmonic bonds and angles, with partial charges set to $Mo = +0.50\ e$ and $S = -0.25\ e$, in combination with the Lennard-Jones (LJ) potential (Sresht et al., 2017). Water was modeled through a non-polarizable q-SPC/Fw model (Paesani et al., 2006), characterized by a three-site water molecule, where the charges were set to $O = -0.84\ e$ and $H = +0.42\ e$. Using Lorentz-Berthelot mixing rules, $\sigma_{ij} = \frac{\sigma_{ii}+\sigma_{jj}}{2}$ and $\epsilon_{ij} = \sqrt{\epsilon_{ii}\epsilon_{jj}}$, cross-term parameters were obtained. A cut-off of 12 Å was used for the LJ potential. To account for electrostatic interactions, the particle-particle particle-mesh (PPPM) method was used, with a threshold of $1.0 \cdot 10^{-6}$ for the relative error in the forces. In Fig. 1 and in the Supplementary Material, a benchmark of this force field is presented against FPC results (Levita et al., 2014) and experimental data (Schönfeld et al., 1983), by means of the sliding potential energy surface (PES) and structural parameters, respectively. The PES was obtained by performing static calculations on a partially rigid MoS_2 bilayer. Here, only the top layer was allowed to breath in the z-axis and was translated along the x-axis and the y-axis in twelve steps, for a total distance equal to the size of the period in that direction (for more details we refer to Ref. (Nicolini and Polcar, 2016)). The employed force field shows good agreement with both *ab initio* and experimental data.

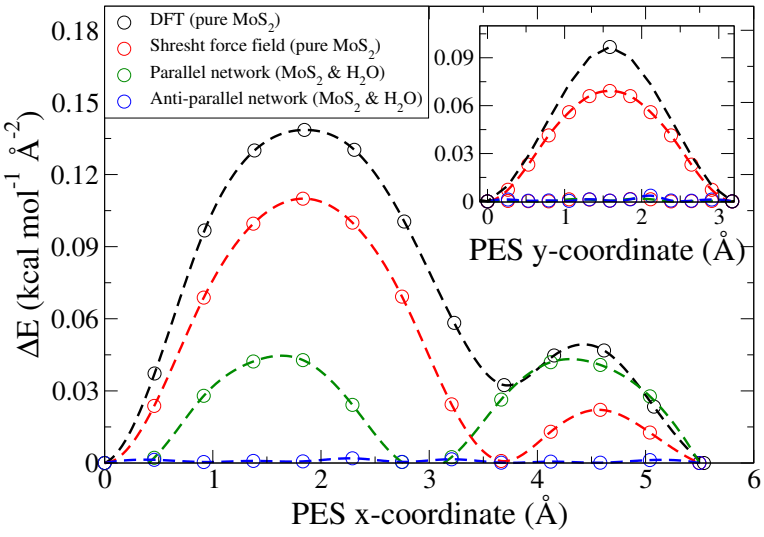

Figure 1. Static potential energy surfaces calculated per area for the long (inset: short) diagonal of the hexagonal unit cell. Four different cases are considered: i) in black pure MoS_2 obtained via DFT (Ref. (Levita et al., 2014)), ii) in red pure MoS_2 obtained with the force field employed in this study (Sresht et al., 2017), iii) in green MoS_2 and an ideal, parallel water network via MD and iv) in blue MoS_2 and an ideal anti-parallel water network via MD. The dashed lines are obtained via akima spline interpolation and serve merely as a guide to the eyes.

Firstly, the six-layered $2H_c$-MoS_2 system was built using the initial coordinates from Ref. (Schönfeld et al., 1983). The resulting structure consists of 4608 atoms and a surface of approximately 44 Å by 51 Å. An energy minimization was performed using a sequence of conjugate gradient (CG) algorithm, with a relative energy tolerance of $1 \cdot 10^{-15}$, and damped dynamics (DD) algorithm, with a relative energy

tolerance of $1 \cdot 10^{-10}$; the simulation box was also allowed to relax. Secondly, an isolated water molecule was optimized according to the force field using CG. The resulting structure was replicated in three dimensions to create a large cube, with a density equivalent to that of liquid water at room temperature, and optimized using both CG and DD, while relaxing the box. Thirdly, the cube of water was put atop three layers of MoS_2 and subsequently optimized using both CG and DD. Thereafter, the water cube was heated up to 300 K using the Nose-Hoover thermostat (Martyna et al., 1994), with a temperature damping parameter of 100 time steps. In the fourth step, the actual structures were created. Random clusters of water molecules of the melted cube, located within a 5 Å cutoff above the nearest sulfur layer, were selected. The reason that we chose clusters instead of randomly spread water molecules had to do with the fact that in preliminary simulations we found that the sliding of MoS_2 drives the formation of clusters and therefore are the best representation. Finally, the missing three top layers of MoS_2 were pasted above. By considering the 'tiled' structure of the water network mentioned in Ref. (Kwac et al., 2017), full coverage requires 304 H_2O molecules. In total, 11 different systems were created consisting of either 0 (dry), 1, 2, 5, 10 (3% coverage), 26 (8.5%), 52 (17%), 103 (33%), 206 (67%), 304 (100% full coverage) or 1236 (bulk) water molecules. Finally, a vacuum of 20 Å was added above each structure in order to avoid interaction with the repeated images while applying periodic boundary conditions.

After obtaining the structures, all were once more optimized using CG and DD, while keeping the box dimensions fixed. This time, the bottommost sulfur layer was held fixed in the x-, y- and z-direction. Moreover, the topmost sulfur layer was made rigid in the xy-plane and the forces in the z-direction were averaged over all sulfur atoms in this layer. This restriction on the top sulfur layer was added to mimic adhesion to the substrate and to be able to control the sliding. After the minimization, a 2-step equilibration was performed, in which seven configurations of every system were created, each with a different normal load applied to the topmost sulfur layer. The normal load was ranging from 0.0 GPa to 3.0 GPa, with increments of 0.5 GPa. In the first step (100 ps), the load was slowly increased from 0 GPa to the target value, whereas in the second step (100 ps) was held constant. During the equilibration, the system was thermalized by initializing the temperatures for every atom using the Boltzmann distribution. Moreover, the bottom and top layers of MoS_2 were coupled to a Nose-Hoover thermostat (Martyna et al., 1994). On the one hand, this allows for maintaining the temperature during equilibration, while on the other hand, this avoids overheating from Joule heat production during the actual sliding runs (Vanossi et al., 2013).

Three independent production runs for every configuration were created. In all runs, the bottommost layer of sulfur atoms was held fixed in the x-, y-, and z-direction. Next, the topmost sulfur layer was moved rigidly in the x-direction, along the Mo-S bonds, with three different velocities (20.0, 2.0, and 0.2 m/s) and for a total of ∼27.5 Å. For the analysis, the first part of the MD trajectories was discarded and considered as the run-in phase, and only the last ∼22 Å were used, which is the distance based on four periods of the cell in that direction (∼5.5 Å). The velocities were maintained constant along the trajectories, which was achieved by setting an initial velocity and canceling the force in this direction. On the one hand, this setup allows for the study of the effect of velocity in the sliding direction, and on the other hand, the system keeps the freedom to slide the MoS_2 layers in the y-direction and to breath in the z-direction. The reason to slide along this direction is because this direction represents the highest friction (Claerbout et al., 2019) and therefore the most interesting dynamics was expected to be observed. Along all runs, a time integration step of 0.1 fs was used. In Fig.2, the computational setup is depicted.

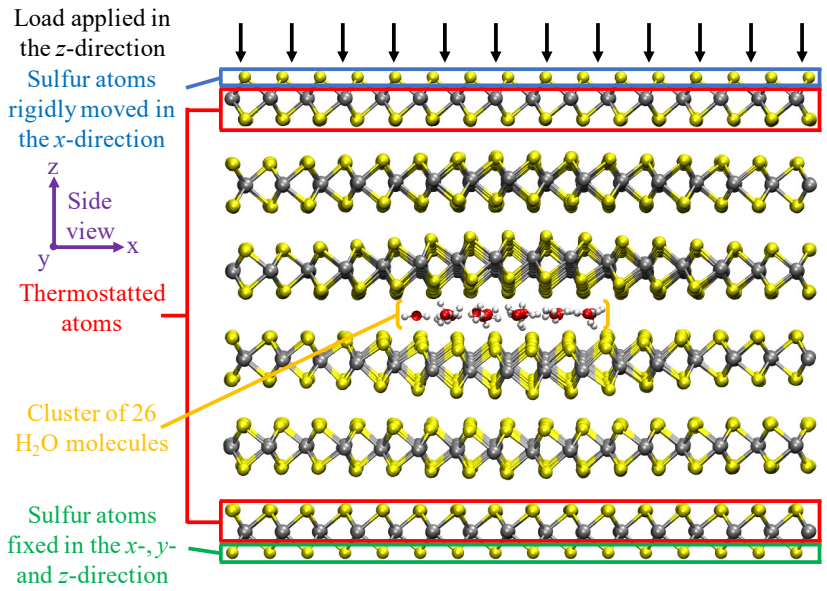

Figure 2. Schematic overview of the computational setup. The side view of the six-layered MoS_2 structure, with a cluster of 26 H_2O molecules intercalated in the center interface, is displayed. Molybdenum, sulfur, oxygen, and hydrogen atoms are displayed in silver, yellow, red, and white, respectively. This specific case resembles the system after equilibration at 0.0 GPa load and 300 K. From this picture, there is a clear structural deformation visible in the MoS_2 layers directly encapsulating the H_2O cluster. Figure obtained with VMD (Humphrey et al., 1996).

3 RESULTS AND DISCUSSION

3.1 Sliding dynamics

We present a full analysis of the results obtained for 2.0 m/s and describe some of the differences and similarities to sliding with 20.0 and 0.2 m/s. Firstly, a qualitative analysis on the water dynamics is presented, followed by MoS_2. As stated above, the water molecules in the clusters were randomly selected from a melted ice cube. This allows to observe the naturally resulting water network after being transferred from a 3D 'free' space to an encapsulated 2D confinement. In general, a flat, single layer of water molecules was formed, see Fig. 3(**A-J**). For bulk water, the formation of two water layers was observed, facing the MoS_2 on either side, between which water molecules in a more disordered state were found.

In Fig. 4(**A-C**), a top view of the water network for three systems is displayed. For up to 8.5% coverage, we found single clusters, kept together by a network of H-bonds. In the present study, a hydrogen bond (H-bond) is defined as two oxygen atoms, between which there is a maximum distance of 3.5 Å, and where the O-H-O angle is $150^\circ < \alpha < 210^\circ$ (Kwac et al., 2017). Through this H-bonds, rings of either three or four molecules were formed. Similar observations were made for increasing water coverage; however, the majority of the rings now consist of four molecules. In fact, a similar type of water network as described in Ref. (Kwac et al., 2017) can now be distinguished. This ice-like, so-called perpendicular crossing diamond network (pcd) consists of rings with four molecules, which are either diamond-like shaped, where the four H-bonds are 'donated' by two of the water molecules, or square-like shaped, where each water molecule

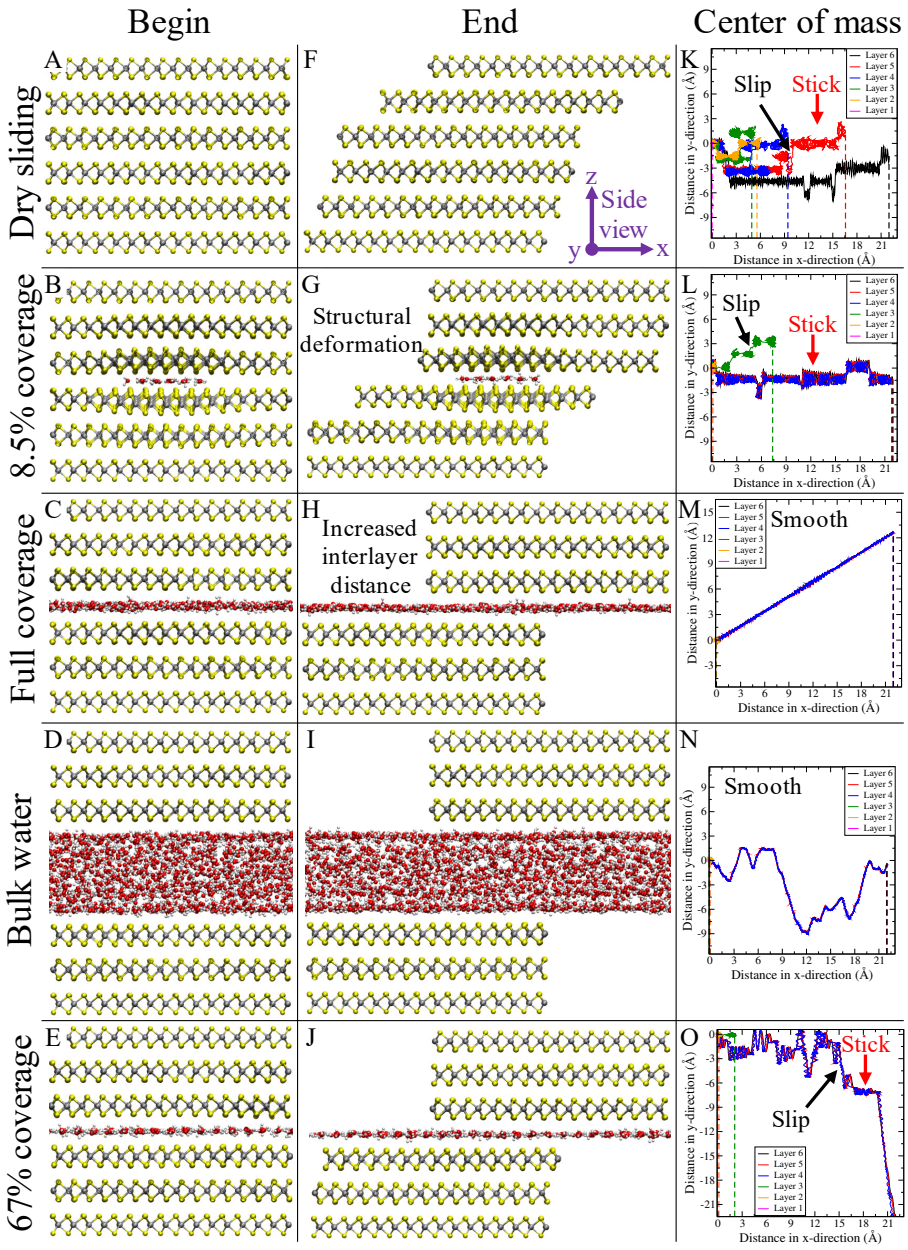

Figure 3. Snapshots for different configurations taken at 0 Å (panel **A-E**) and 22 Å (panel **F-J**), presented from a side view perspective. Respective configurations are dry sliding, 8.5% coverage, full coverage, bulk water, and 67% coverage. In the final column (panel **K-O**), the center of mass for every layer is depicted in the xy-plane. The vertical dashed lines in this column represent the final x-position for every layer. Figure obtained with VMD (Humphrey et al., 1996).

188 contributes with one H-bond. As an example, we put the diamond shapes atop the water network in case of
189 full coverage and 67% coverage. From these observations, it can be concluded that water acts as a solidified
190 film when strictly confined, despite of temperatures above the melting point. Changing the load or the
191 sliding velocity did not alter significantly the formation of the structure.

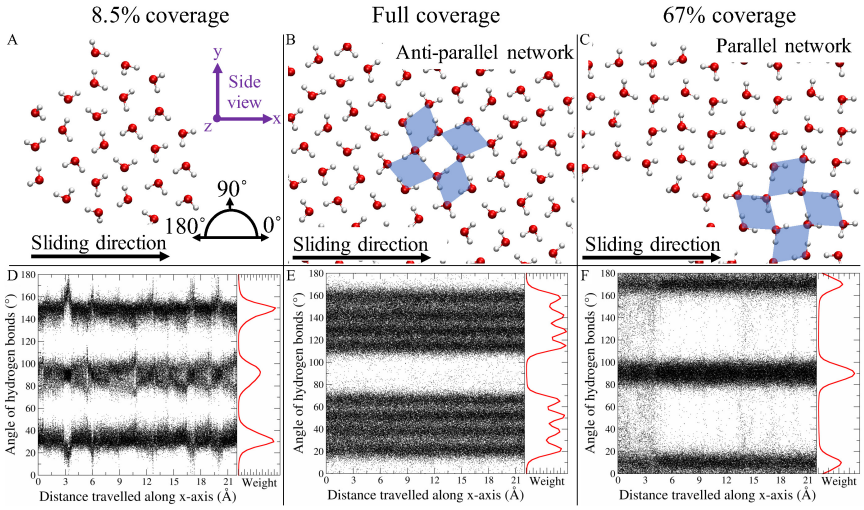

Figure 4. Top view representation of the water network for 8.5%, full and 67% coverage (panel **A-C**). The black arrow represents the sliding direction. The blue diamonds serve as a guide to the eyes in distinguishing the pcd configuration. The bottom row (panel **D-F**) represents the angles of all hydrogen bonds, at every time step, with respect to the x-axis, in red the corresponding histograms are depicted. Figure obtained with VMD (Humphrey et al., 1996).

192 In an 'ideal' water network, the pcd configuration should result in four different H-bond angles, two
193 per diamond orientation, which sum up to $180°$. We found two main orientations of the water network
194 with respect to the simulation box. We define the first orientation, which was the most common in our
195 sliding MD simulations, as the anti-parallel one, where none of the H-bonds align along the sliding
196 direction. We define the second orientation, which was only present in a few cases, as the parallel one,
197 where half of the H-bonds are oriented practically along the sliding direction. More specifically, in the
198 anti-parallel case, these angles are $\sim 37.5°$, $\sim 52.5°$, $\sim 127.5°$ and $\sim 142.5°$ (obtained by doing a separate
199 simulation using an ideal 'defect-free' water structure without MoS_2, see the Supplementary Materials.),
200 whereas in the parallel case, these angles are $\sim 7.5°$, $\sim 82.5°$, $\sim 97.5°$ and $\sim 172.5°$. In Fig. 4(**D-F**),
201 the angles of the H-bonds with respect to the x-axis, present at every time step are displayed, including
202 the corresponding histograms. In the case of 8.5% coverage or less, three main angles (the middle one
203 with a wider distribution) could be distinguished, which are $\sim 30°$, $\sim 90°$ and $\sim 150°$. This is consistent
204 with the fact that in this case both three- and four-molecule rings are present. Overall, the H-bonds were
205 not aligned along the sliding direction. By increasing the number of water molecules, the pcd network
206 started to form, showing up in six different angles for a water coverage up to 67%, which are $\sim 30.0°$,
207 $\sim 50.0°$, $\sim 70.0°$, $\sim 110.0°$, $\sim 130.0°$ and $\sim 150.0°$ (data not shown). Here, the summation of one of
208 the three lower angles combined with one of the three higher ones gives $180°$, resulting in a diamond
209 shape. Once more, none of the H-bonds were aligned along the sliding direction. For full coverage, four

sets of angles were found, again whose sum totals $180°$, see Fig. 4(**B,E**). On the contrary, in the parallel case as depicted in Fig. 4(**C,F**) as an example, three angles were found which are $\sim 10°$, $\sim 90°$ and $\sim 170°$, and where the central one is the superposition of the two distinct peaks found in the ideal case. The parallel orientation is less energetically favorable (by about 0.04 kcal mol^{-1} Å^{-2}, with respect to the static calculations presented in Fig. 1) than the parallel one, and generally, along a sliding MD trajectory parallel to anti-parallel transitions (but not vice versa) were observed. The deviation between the actual and the expected angles is due to the sliding energy provided to the system, which allows several metastable states where the H-bond network experiences a breathing motion. Moreover, the discrete character of the relative orientation of the clusters above/beneath the MoS_2 hints at a rotational disorder energy dependence, which was also revealed by the energy difference between the two ideal cases, referred to above. At any rate, to have a consistent quantitative comparison in terms of the frictional properties, only anti-parallel configurations were considered. Finally, considering bulk water, we note that this is the only case where the water actually behaves as a liquid.

Next, we analyze the MoS_2 dynamics, firstly from a top view and thereafter from a side view perspective. From the top view, we found a typical characteristic observed in nanoscale friction for 2D solids, the so-called stick-slip dynamics (Lee et al., 2010). In the case of stick-slip, two velocity regimes can be distinguished, a high speed one during which a sudden jump in position occurs, and a stick phase. Stick-slip happens as a result of the underlying interactions between two surfaces relative in motion, represented by the potential energy surface (PES), and can be explained using the principles of the Prandtl-Tomlinson (PT) or the more generalized Frenkel-Kontorova model (Socoliuc et al., 2004; Vanossi et al., 2013). Consider a ball being dragged over a PES by a moving spring. When encountering an energy barrier, the ball will stay trapped in the minimum and the spring will be stretched, i.e., the stick phase. At a certain point, the energy stored in the spring will be sufficient to pass the energy barrier, the ball 'slips' to the next local energy minimum, and as a result the energy stored in the spring is dissipated. The higher the barrier, the higher the dissipation. In general, it is believed that in the temperature-extended PT model and in friction force microscopy experiments, stick-slip is a thermally activated process, whereas in MD simulations this is only believed to be true for very low sliding speeds (Vanossi et al., 2013).

In our case, the moving spring is indirectly represented by the topmost sulfur layer, which was moved with a constant velocity, and the van der Waals interactions between the layers. From the above, it becomes clear that whenever the PES has no effective corrugation, stick-slip will not occur. It is found that the corrugation of the PES goes hand-in-hand with the commensurability of the system (Wang et al., 2017; Irving et al., 2017), as is the case considered in this study. Whenever there is a mismatch, be it a rotational, structural, or a combination of both, the PES flattens out due to the cancellation of forces. In this case, one will observe smooth dynamics, characterized by low energy dissipation.

We observed the stick-slip dynamics for the low water coverage regime (up to 17%), as can be observed in the third column of Fig. 3(**K-O**). Here, the position of the center of mass of each layer is presented along the course of the trajectory. From the trajectories, it becomes clear that the actual slip is directed in the y-direction, perpendicular to the sliding direction. This is in line with the PES of commensurate MoS_2, displayed in Fig. 1. When the load was increased, stick-slip is enhanced and present for higher water coverage. This observation is in line with earlier results. In 2014, Levita *et al.* (Levita et al., 2014) studied the sliding properties of dry MoS_2, using first principle calculations. With an increasing load, the corrugation of the PES increased as a result of changing van der Waals, electrostatic, and Pauli interactions. Moreover, purely by considering the functional form of the force field, especially the LJ part describing the interactions between MoS_2 layers and between MoS_2 and water, one could also have predicted this

outcome. Increasing the load reduces the interatomic distances and therefore results in a regime with more repulsive LJ interactions. When the velocity was increased, we found that the stick-slip dynamics disappear, even for dry sliding. A possible explanation for this observation is that the adhesion between the layers is reduced due to the increased velocity. This lowers the probability for the atoms to relax to their local minimum energy positions (Onodera et al., 2010). In other words, the layers tend to 'fly' over each other, without experiencing a strong interlayer interaction. Although not presented in Fig. 3, we also found that the water clusters themselves display stick-slip dynamics up to this low coverage regime.

In general, when the water coverage was increased, we observed a transition to smooth dynamics, both for the MoS_2 layers and the water clusters. However, in the special case of a parallel water network orientation, stick-slip dynamics persisted again both in the MoS_2 and the water clusters. This behavior is also suggested by the static PES profiles (Fig. 1), where the PES is displayed for the 'ideal' parallel and anti-parallel water network compared to 'pure' MoS_2. The anti-parallel PES is flat due to a lattice incommensurability with MoS_2. The parallel PES, however, shows that there is in fact a commensurability present along the sliding direction, where twice the length of the H-bond gives the lattice period of MoS_2.

Next, we analyze the MoS_2 dynamics from the side view perspective. For low water coverage up to 3%, we observed a 'card-deck' shearing behavior, where the bottommost layer remains in place, while the topmost layer moves according to the driving velocity. The intermediate layers present increasing displacements, depending on their relative position in the layered system. At the value of 8.5% water coverage, there is a transition towards a new type of dynamics, where we found that the MoS_2 starts to divide into two blocks, one above and one beneath the water molecules. For moderate coverage (17% and above), the layers in the bottom block, where the bottommost sulfur atoms are fixed in the x-, y- and z-direction, remain together and do not reposition. Additionally, the layers in the top block stick together; however, this block slides as a whole according to the driving velocity given to the topmost sulfur layer. This is confirmed by Fig. 3(**A-J**), where snapshots at the begin and end of the trajectory are displayed for different amounts of water coverage. In these specific examples, the water network is oriented in an anti-parallel fashion for full coverage, whereas for 67% this is parallel. We found that for the low water coverage regime, increasing the velocity slightly shifts the transition from the card-deck shearing to higher water coverage; the same accounts for increasing the load. In other words, card-deck shearing is more pronounced for higher loads and velocities.

Using the PES profiles once more, we can also explain the card-deck shearing versus block sliding. Let us consider the six layers of MoS_2 in a minimum energy configuration and start sliding solely the top layer. At a certain moment, an energy barrier will be reached according to the PES resulting from the interaction with the fifth layer. In this case, instead of passing the barrier, it is energetically more favorable to slide both the top and the fifth layer until the fifth layer reaches the energy barrier from the interaction with the fourth layer. This process continues until the bottom layer is reached, which is static, resulting in the card-deck shearing. We saw that, upon introducing water at the interface, the card-deck shearing diminishes until it completely disappears. This behavior can be explained by means of the actual values of the LJ parameters. The interlayer interaction between MoS_2 is stronger than that between a layer of MoS_2 and water. Thus, when the top layer slides, the two layers beneath will follow since their adhesion is stronger compared to that with the water layer. For the low water coverage regime, the third and fourth layers are still able to interact, albeit less compared to dry sliding, by means of local bending of the layers around the water cluster. Once the threshold is reached, the layers increase the interlayer distance instead of local bending, at which point the interaction between water and MoS_2 dominates.

Finally, we comment on the structural behavior of MoS_2. For the low coverage regime, we found a structural distortion of the MoS_2, representing a puckered shape (out-of-plane elastic deformation), most strongly pronounced in the layers directly facing the water. The MoS_2 layer bends outwards from the center interface creating a locally enhanced interlayer distance. A similar observation was already visible in the computational setup (Fig. 2). Increasing the number of water molecules increases the intralayer structural distortion up to a threshold, after which the MoS_2 no longer bends around the water cluster but increases more significantly the interlayer distance of the center interface. This reveals the delicate interplay between the energy cost of the structural distortion and maintaining the interlayer van der Waals interactions. In other words, the LJ interactions between the layers are replaced by LJ contributions between water molecules and the MoS_2 layers.

3.2 Frictional behavior

Using the same analysis as described in Ref. (Claerbout et al., 2019), we can make an estimation of the dissipated energy as a result of friction coming from the PES corrugation and other channels such as structural distortion. By considering the instantaneous force that is required to slide all the atoms in the uppermost sulfur layer rigidly with a constant velocity along the sliding direction, we can calculate the dissipated work:

$$W = \int_0^\tau F_{ext}(t) v dt, \tag{1}$$

where $F_{ext} = -\sum_{i=1}^{N} F_{i,y}$ is the sum of the atomic contributions of the top sulfur layer along the sliding direction. The integral ranges along time τ, the total time of the trajectory, and v is the sliding velocity. In Fig. 5(**A**), the work profiles at 0.0 GPa and 3.0 GPa load are displayed for dry sliding and 8.5% water coverage. Furthermore, in this panel, the dissipation is displayed for the parallel water network in the case of 67% coverage. In Fig. 5(**B**), the full coverage with an anti-parallel orientation and bulk water, again at 0.0 and 3.0 GPa load, are displayed. From these graphs, several observations can be made. First of all, an increasing load leads to higher dissipation. This observation was expected, and it can be explained with the same argument used earlier. Increasing the load reduces the interlayer distance, resulting in a more repulsive regime of the LJ interactions and a more corrugated PES. A second observation is the dependence of the energy dissipation on the number of water molecules. Starting from dry sliding, increasing the water coverage results in an increasing dissipation. In other words, water acts as a contaminant that increases the frictional forces This continues up to 3% coverage, after which the dissipation starts to decrease. Reaching moderate coverage (17%), the dissipation falls below dry sliding where the water starts to act as a friction weakening lubricant. It should be noted that the dissipation behavior follows the same trends as the card-deck shearing versus block sliding, with respect to the amount of water coverage. These observations can be explained as follows. For dry sliding and low water coverage, a PES corrugation is present resulting in a significant dissipation during sliding, as explained above. When the number of water molecules are increased in the low coverage regime, an additional dissipation occurs due to the fact that the number of degrees of freedom and the possible channels for energy dissipation increases. This can, for example, be seen by the puckering of the layers in the low water coverage regime. The water causes a puckered shape, resulting in an enhanced strain in the structure, which comes with an energy cost. Next, the puckered shape promotes a deformation of the neighbouring layers during sliding. The PES profiles can also explain the frictional behavior in the high coverage regime. There is no effective corrugation in the PES in the case of an anti-parallel water network, compared to that of dry MoS_2; thus when increasing the water coverage the dissipated energy decreases. However, in the case of a parallel oriented network, the PES corrugation is of the same order as that of dry MoS_2, which is translated in a similar dissipation behavior.

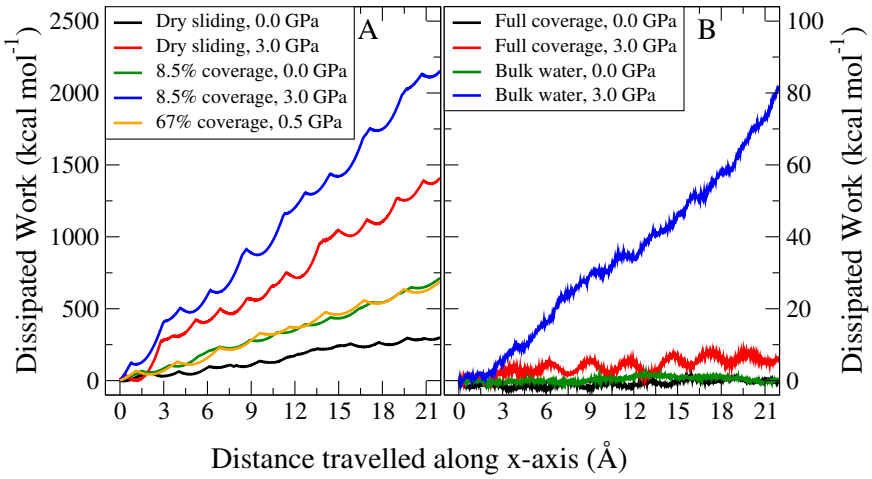

Figure 5. Profiles of the dissipated work for MD trajectories sliding in the x-direction. The left panel **A** represents the case with dry sliding (black and red) and 8.5% coverage (green and blue) at zero and 3.0 GPa load, respectively, and one case with 67% coverage (orange) at 0.5 GPa load and characterized by a parallel water network. The right panel **B** represents the dissipation at zero and 3.0 GPa load for full coverage with an anti-parallel water network (black and red), and bulk water (green and blue).

Considering different velocities, an interesting behavior was observed. In the case of dry sliding and the low water coverage regime (below 17%), increasing the velocity decreased the dissipation. Above this coverage threshold, increasing the velocity increased the dissipation, with the most pronounced signature for bulk water. To explain this phenomenon, we divided the coverage into three regimes. The first regime, which we termed the contamination regime, is characterized by low water coverage and is governed by stick-slip dynamics, where, as stated above, a higher velocity results in a possible reduced adhesion and a lower probability for the atoms to move to local minimum energy positions. These factors reduce the energy dissipated during the slip phase. An explanation provided by Zeng *et al.* (Zeng et al., 2018) on the frictional velocity dependence of graphene studied by using atomic force microscopy, entailed an aging argument, resulting in a stronger interlayer contact state for lower velocities. Although this case might not directly relate to our computational study (Vanossi et al., 2013), it corroborates the fact that for an enhanced slip more energy is irreversibly and instantaneously transformed into vibrations and heat. We defined the second regime (ranging roughly between 17% and full coverage) as the solidified water lubrication regime. Here the lubrication type changes: stick-slip is no longer present and the block sliding mechanism is dominant. Despite the smooth dynamics and the seemingly flat PES compared to dry MoS_2, some corrugation still remains. Here, thermal activation can be exploited to overcome the low energy barriers, reducing the dissipation. However, with increasing velocity, the system might not explore the local energy minima long enough to benefit from thermal fluctuations towards overcoming the barriers (Szlufarska et al., 2008). Moreover, high velocity regimes are in general further away from equilibrium and characterized by more complex and nonlinear processes, and thereby more dissipative. The third regime (which we termed the liquid water lubrication regime) considers bulk water lubrication, where an enhanced signature of increased dissipation was observed. Apart from the discussion above, here one should take into account the fact that we are no longer only dealing with solids but also with liquids. Whenever the hydrodynamic fluid film creates enough MoS_2 interlayer separation, the MoS_2-water interaction dominates.

Liquids are characterized by viscosity, which is known to be strongly affected by the sliding velocity (Ni et al., 2019; Vanossi et al., 2013).

In the final part of the analysis, we computed the coefficients of friction. To do so, we employed Amontons' law of friction (Amontons, 1699; Coulomb, 1821):

$$F_{\parallel} = \alpha_0 + \mu \cdot F_{\perp}, \tag{2}$$

where $F_{\parallel}$ is the average over the external force in the sliding direction, α_0 is the frictional force at zero load, μ is the coefficient of friction and $F_{\perp}$ is the normal load applied to the system. Although this law is in general valid only at the macroscopic scale, Mo *et al.* (Mo et al., 2009) have shown that, in the case of a single asperity contact, it can work at the nanoscale. To obtain the average lateral force, we used a procedure applied before in one of our other studies (Claerbout et al., 2019), the so-called bootstrap method. More details on this averaging technique can be found in the Supporting Information.

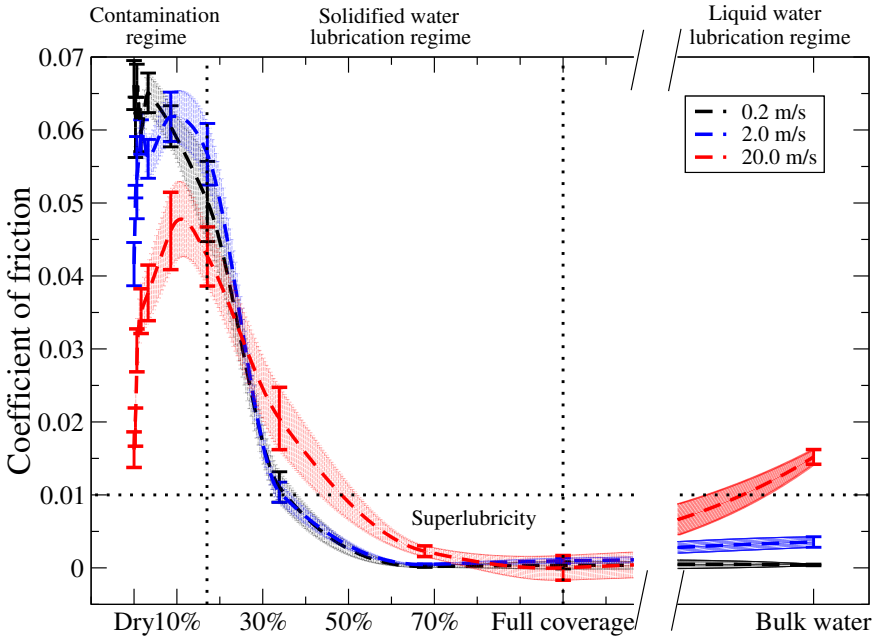

Figure 6. Coefficients of friction for different sliding velocities, 0.2 (black), 2.0 (blue), and 20.0 (red) m/s, plotted versus water coverage. The dashed lines and the area around it result from akima interpolation and serve as a guide to the eyes. The error bars result from the linear fit taking into account the errors obtained via the bootstrap method.

In Fig. 6, we present the coefficients of friction as a function of the water coverage for all three velocities. In this analysis, we selected only the trajectories in which the water network for the high coverage regime was characterized by an anti-parallel orientation. This approach is justified since this orientation is more energetically favorable. Again, three frictional regimes can be distinguished. In the first contaminated regime, the coefficient of friction increases with the water coverage, reaching a maximum at a coverage of 3%, after which the coefficient of friction decreases and drops below the dry sliding value for a coverage

of 17%. When the water coverage increases further (solidified water lubrication regime), the coefficient of friction monotonically decreases, eventually falling below the superlubricity threshold (COFs below 0.01) (Martin and Erdemir, 2018; Baykara et al., 2018). After 70% water coverage (liquid water lubrication regime), the friction remains seemingly stable till bulk water; at this point the water molecules are no longer solely in a solid form but they are also present as a liquid, bearing the usual velocity dependence (Popov, 2017). We found similar trends for the other velocities, albeit that for the contamination regime, the lower velocity has higher coefficients of friction (and vice versa), in agreement with the earlier discussion about energy dissipation.

4 CONCLUSION

In this study, we investigated the frictional properties of bulk commensurate MoS_2 in the presence of water. By employing non-equilibrium MD simulations, the effects of load, sliding velocity and the number of water molecules were elucidated. Several conclusions can be drawn from our simulations. Firstly, when placed within a 2D confinement, water acts as a solidified lubricant. The resulting ice-like structure, where the H-bonds lead to a characteristic tile-like network, has a discrete (e.g., parallel or anti-parallel) orientation above/beneath MoS_2. Secondly, two classes of sliding dynamics were distinguished, namely card-deck shearing versus block sliding and stick-slip dynamics versus smooth dynamics. Both show a dependence on the amount of water coverage and the sliding velocity. Within the low water coverage regime, card-deck shearing and stick-slip dynamics are dominant. These types of dynamics are characterized by a high dissipative signature and strong load dependence. For moderate to high water coverage, block sliding and smooth dynamics were observed, with low energy dissipation and low load dependence. One exception is the metastable case, where the water network aligns along the sliding direction. In this case, a behavior comparable to that of low water coverage is observed. Combining the results above, we found that three lubrication regimes could be identified. In the first one (contamination regime, low water coverage), water acts as a contaminant and a friction strengthening was observed with increasing coverage. In the second one (solidified water lubrication regime, high water coverage), water acts as a solid-like lubricant and superlubricity was observed. In the third one (liquid water lubrication regime, bulk water), water acts as a liquid lubricant and low coefficients of friction were found, also showing a more pronounced viscosity-like velocity dependence. Finally, we showed and quantified that, due to the solidified structure of water, there was a rotational dependence present for the frictional behavior of water between a multilayer system of MoS_2.

Our results directly contribute to strengthen the general understanding of the nanoscale frictional mechanisms at play when considering MoS_2 (and 2D materials in general) in the presence of humidity. Once more, it was confirmed that the processes defining friction at this scale are anisotropic and complex in nature. Our results shed light upon the design of nanoscale devices, such as nano- and micro-electromechanical systems (NEMS/MEMS), in which humidity might play an important role, to ramp up the efficiency of the devices. In future work, the scalability of our results to the multi-asperity macroscale will be studied.

CONFLICT OF INTEREST STATEMENT

The authors declare that the research was conducted in the absence of any commercial or financial relationships that could be construed as a potential conflict of interest.

AUTHOR CONTRIBUTIONS

V.E.P.C. carried out the conceptualization, methodology, validation, calculation, formal analysis, investigation, data curation, visualization, and writing of the original draft. P.N. supervised the study,

contributed to the conceptualization, methodology and validation, and reviewed and edited the manuscript. T.P. guided the project and reviewed and edited the manuscript. The funding was secured by P.N and T.P.

FUNDING

This work was supported by The Ministry of Education, Youth and Sports from the Large Infrastructures for Research, Experimental Development and Innovations project "e-Infrastructure CZ – LM2018140". The publication has received funding from the European Union's Horizon2020 research and innovation program under the grant agreement No. 721642: SOLUTION. P.N. acknowledges the support of the Czech Science Foundation through the project 16-11516Y. T.P. acknowledges the support of the project Novel nanostructures for engineering applications No. CZ.02.1.01/0.0/0.0/16_026/0008396.

ACKNOWLEDGMENTS

The authors are grateful to G. Levita and M.C. Righi for the DFT data used for the benchmark.

DATA AVAILABILITY STATEMENT

The datasets of this study can be obtained upon request to the authors.

REFERENCES

Amontons, G. (1699). De la resistance causée dans les machines. *Mémoires de l'Académie royale des sciences (Paris)* , 275–282

Arif, T., Yadav, S., Colas, G., Singh, C. V., and Filleter, T. (2019). Understanding the independent and interdependent role of water and oxidation on the tribology of ultrathin molybdenum disulfide (MoS_2). *Advanced Materials Interfaces* 6, 1901246. doi:10.1002/admi.201901246

Bampoulis, P., Teernstra, V. J., Lohse, D., Zandvliet, H. J., and Poelsema, B. (2016). Hydrophobic ice confined between graphene and MoS. *The Journal of Physical Chemistry C* 120, 27079–27084. doi:10.1021/acs.jpcc.6b09812

Baykara, M. Z., Vazirisereshk, M. R., and Martini, A. (2018). Emerging superlubricity: A review of the state of the art and perspectives on future research. *Applied Physics Reviews* 5, 041102. doi:10.1063/1.5051445

Berman, D., Erdemir, A., and Sumant, A. V. (2014). Graphene: a new emerging lubricant. *Materials Today* 17, 31–42. doi:10.1016/j.mattod.2013.12.003

Chhowalla, M. and Amaratunga, G. A. (2000). Thin films of fullerene-like MoS_2 nanoparticles with ultra-low friction and wear. *Nature* 407, 164–167. doi:10.1038/35025020

Chhowalla, M., Shin, H. S., Eda, G., Li, L.-J., Loh, K. P., and Zhang, H. (2013). The chemistry of two-dimensional layered transition metal dichlacogenide nanosheets. *Nature Chemistry* 5, 263–275. doi:10.1038/NCHEM.1589

Chng, E. L. K. and Pumera, M. (2015). Toxicity of graphene related materials and transition metal dichalcogenides. *RSC Advances* 5, 3074–3080. doi:10.1039/C4RA12624F

Cho, M. H., Ju, J., Kim, S. J., and Jang, H. (2006). Tribological properties of solid lubricants (graphite, Sb_2S_3, MoS_2) for automotive brake friction materials. *Wear* 260, 855–860. doi:10.1016/j.wear.2005.04.003

Choi, W., Choudhary, N., Han, G. H., Park, J., Akinwande, D., and Lee, Y. H. (2017). Recent development of two-dimensional transition metal dichalcogenides and their applications. *Materials Today* 20, 116–130. doi:10.1016/j.mattod.2016.10.002

454 Claerbout, V. E., Polcar, T., and Nicolini, P. (2019). Superlubricity acheived for commensurate sliding:
455 MoS_2 frictional anisotropy *in silico*. *Computational Materials Science* 163, 17–23. doi:10.1016/j.
456 commatsci.2019.03.019
457 Coulomb, C. (1821). Théorie des machines simples en ayant égard au frottement de leurs parties et à la
458 roideur des cordages. *Bachelier*
459 Curry, J. F., Wilson, M. A., Luftman, H. S., Strandwitz, N. C., Argibay, N., Chandross, M., et al. (2017).
460 Impact of microstructure on MoS_2 oxidation and friction. *ACS Applied Materials & Interfaces* 9,
461 28019–28026. doi:10.1021/acsami.7b06917
462 Dudder, G. J., Zhao, X., Krick, B., Sawyer, W. G., and Perry, S. S. (2011). Environmental effects on the
463 tribology and microstructure of MoS_2-Sb_2O_3-C films. *Tribology Letters* 42, 203–213. doi:10.1007/
464 s11249-011-9764-z
465 Evaristo, M., Polcar, T., and Cavaleiro, A. (2008). Tribological behaviour of C-alloyed transition metal
466 dichalcogenides (TMD) coatings in different environments. *International Journal of Mechanics and*
467 *Materials in Design* 4, 137–143. doi:10.1007/s10999-007-9034-2
468 Gaur, A. P., Sahoo, S., Ahmadi, M., Dash, S. P., Guinel, M. J.-F., and Katiyar, R. S. (2014). Surface energy
469 engineering for tunable wettability through controlled synthesis of MoS_2. *Nano Letters* 14, 4314–4321.
470 doi:10.1021/nl501106v
471 Hasz, K., Ye, Z., Martini, A., and Carpick, R. W. (2018). Experiments and simulations of the humidity
472 dependence of friction between nanoasperities and graphite: the role of interfacial contact quality.
473 *Physical Review Materials* 2, 126001. doi:10.1103/PhysRevMaterials.2.126001
474 Holmberg, K. and Erdemir, A. (2017). Influence of tribology on global energy consumption, costs and
475 emissions. *Friction* 5, 263–284. doi:10.1007/s40544-017-0183-5
476 Humphrey, W., Dalke, A., and Schulten, K. (1996). Vmd: Visual molecular dynamics. *Journal of*
477 *Molecular Graphics* 14, 33–38. doi:https://doi.org/10.1016/0263-7855(96)00018-5
478 Irving, B. J., Nicolini, P., and Polcar, T. (2017). On the lubricity of transition metal dichalcogenides: an ab
479 initio study. *Nanoscale* 9, 5597–5607. doi:10.1039/c7nr00925a
480 Khare, H. and Burris, D. (2013). The effects of environmental water and oxygen on the temperature-
481 dependent friction of sputtered molybdenum disulfide. *Tribology Letters* 52, 485–493. doi:10.1007/
482 s11249-013-0233-8
483 Khare, H. and Burris, D. (2014). Surface and subsurface contributions of oxidation and moisture to
484 room temperature friction of molybdenum disulfide. *Tribology Letters* 53, 329–336. doi:10.1007/
485 s11249-013-0273-0
486 Kwac, K., Kim, I., Pascal, T. A., Goddard, W. A., Park, H. G., and Jung, Y. (2017). Multilayer two-
487 dimensional water structure confined in MoS_2. *The Journal of Physical Chemistry C* 121, 16021–16028.
488 doi:10.1021/acs.jpcc.7b05153
489 Late, D. J., Liu, B., Matte, H. R., Dravid, V. P., and Rao, C. (2012). Hysteresis in single-layer MoS_2 field
490 effect transistors. *ACS Nano* 6, 5635–5641. doi:10.1021/nn301572c
491 Lee, C., Li, Q., Kalb, W., Liu, X.-Z., Berger, H., Carpick, R. W., et al. (2010). Frictional characteristics of
492 atomically thin sheets. *Science* 328, 76–80. doi:10.1126/science.1184167
493 Lee, D., Lee, H., Lee, H., and Park, J. Y. (2020). Nanotribological effect of water layers intercalated
494 between exfoliated MoS_2 and mica. *The Journal of Physical Chemistry C* 124, 16902–16907. doi:10.
495 1021/acs.jpcc.0c01848
496 Lee, H., Ko, J.-H., Choi, J. S., Hwang, J. H., Kim, Y.-H., Salmeron, M., et al. (2017). Enhancement of
497 friction by water intercalated between graphene and mica. *The Journal of Physical Chemistry Letters* 8,
498 3482–3487. doi:10.1021/acs.jpclett.7b01377

499 Levita, G., Cavaleiro, A., Molinari, E., Polcar, T., and Righi, M. (2014). Sliding properties of MoS_2
500 layers: Load and interlayer orientation effects. *The Journal of Physical Chemistry C* 118, 13809–13816.
501 doi:10.1021/jp4098099
502 Levita, G., Restuccia, P., and Righi, M. C. (2016). Graphene and MoS_2 interacting with water: A
503 comparison by *ab initio* calculations. *Carbon* 107, 878–884. doi:10.1016/j.carbon.2016.06.072
504 Levita, G. and Righi, M. C. (2017). Effects of water intercalation and tribochemistry on MoS_2 lubricity:
505 An ab initio molecular dynamics investigation. *ChemPhyschem* 18, 1475–1480. doi:10.1002/cphc.
506 201601143
507 Li, X. and Zhu, H. (2015). Two-dimensional MoS_2: Properties, preparation, and applications. *Journal of*
508 *Materiomics* 1, 33–44. doi:10.1016/j.jmat.2015.03.003
509 Luan, B. and Zhou, R. (2016). Wettability and friction of water on a MoS_2 nanosheet. *Applied Physcis*
510 *Letters* 108, 131601. doi:10.1063/1.4944840
511 Martin, J., Donnet, C., Mogne, T. L., and Epicier, T. (1993). Superlubricity of molybdenum disulphide.
512 *Physical Review B* 48, 10583–10588. doi:10.1103/PhysRevB.48.10583
513 Martin, J. M. and Erdemir, A. (2018). Superlubricity: Friction's vanishing act. *Physics Today* 71, 40–46.
514 doi:10.1063/PT.3.3897
515 Martyna, G. J., Tobias, D. J., and Klein, M. L. (1994). Constant pressure molecular dynamics algorithms.
516 *The Journal of Chemical Physics* 101, 4177–4189. doi:10.1063/1.467468
517 Mo, Y., Turner, K. T., and Szlufarska, I. (2009). Friction laws at the nanoscale. *Nature* 457, 1116–1119.
518 doi:10.1038/nature07748
519 Mutafov, P., Evaristo, M., Cavaleiro, A., and Polcar, T. (2015). Structure, mechanical and tribological
520 properties of self-lubricant W-S-N coatings. *Surface & Coatings Technology* 261, 7–14. doi:10.1016/j.
521 surfcoat.2014.11.074
522 Ni, K., Fang, H., Yu, Z., and Fan, Z. (2019). The velocity dependence of viscosity of flowing water.
523 *Journal of Molecular Liquids* 278, 234–238. doi:10.1016/j.molliq.2019.01.055
524 Nian, J., Chen, L., Guo, Z., and Liu, W. (2017). Computational investigation of the lubrication behaviors
525 of dioxides and disulfides of molybdenum and tungsten in vacuum. *Friction* 5, 23–31. doi:10.1007/
526 s40544-016-0128-4
527 Nicolini, P. and Polcar, T. (2016). A comparison of empirical potentials for sliding simulations of MoS_2.
528 *Computational Materials Science* 115, 158–169. doi:10.1016/j.commatsci.2016.01.013
529 Onodera, T., Morita, Y., Nagumo, R., Miura, R., Suzuki, A., Tsuboi, H., et al. (2010). A computational
530 chemistry study on friction of h-MoS_2. part ii. friction anisotropy. *The Journal of Physical Chemistry B*
531 114, 15832–15838. doi:10.1021/jp1064775
532 Ouyang, W., de Wijn, A. S., and Urbakh, M. (2018). Atomic-scale sliding friction on a contaminated
533 surface. *Nanoscale* 10, 6375–6381. doi:10.1039/C7NR09530A
534 Paesani, F., Zhang, W., Case, D. A., Cheatham III, T. E., and Voth, G. A. (2006). An accurate and simple
535 quantum model for liquid water. *The Journal of Chemical Physics* 125, 184507. doi:10.1063/1.2386157
536 Panitz, J., Pope, L., Lyons, J., and Staley, D. (1988). The tribological properties of MoS_2 coatings in
537 vacuum, low relative humidity, and high relative humidity environments. *Journal of Vacuum Science &*
538 *Technology A* 6, 1166–1170. doi:10.1116/1.575669
539 Pimentel, J., Polcar, T., and Cavaleiro, A. (2011). Structural, mechanical and tribological properties of
540 mo-s-c solid lubricant coating. *Surface & Coatings Technology* 205, 3274–3279. doi:10.1016/j.surfcoat.
541 2010.11.043
542 Plimpton, S. (1995). Fast parallel algorithms for short-range molecular dynamics. *Journal of Computational*
543 *Physics* 117, 1–19. doi:https://doi.org/10.1006/jcph.1995.1039

544 Popov, V. L. (2017). *Contact Mechanics and Friction: Physical Principles and Applications* (Springer-
545 Verlag Berlin Heidelberg), 2 edn.
546 Scharf, T. and Prasad, S. (2013). Solid lubricants: a review. *Journal of Materials Science* 48, 511–531.
547 doi:10.1007/s10853-012-7038-2
548 Schönfeld, B., Huang, J. J., and Moss, S. C. (1983). Anisotropic mean-square displacements (msd) in
549 single-crystals of 2H- and 3R-MoS_2. *Acta Crystallographica Section B* B39, 404–407. doi:10.1107/
550 S0108768183002645
551 Serpini, E., Rota, A., Ballestrazzi, A., Marchetto, D., Gualtieri, E., and Valeri, S. (2017). The role of
552 humidity and oxygen on the MoS_2 thin films deposited by rf pvd magnetron sputtering. *Surface &*
553 *Coatings Technology* 319, 345–352. doi:10.1016/j.surfcoat.2017.04.006
554 Serpini, E., Rota, A., Valeri, S., Ukraintsev, E., Rezek, B., Polcar, T., et al. (2019). Nanoscale frictional
555 properties of ordered and disordered MoS_2. *Tribology International* 136, 67–74. doi:10.1016/j.triboint.
556 2019.03.004
557 Socoliuc, A., Bennewitz, R., Gnecco, E., and Meyer, E. (2004). Transition from stick-slip to continuous
558 sliding in atomic friction: Entering a new regime of ultralow friction. *Physical Review Letters* 92,
559 134301. doi:10.1103/PhysRevLett.92.134301
560 Sresht, V., Rajan, A. G., Bordes, E., Strano, M. S., Pádua, A. A., and Blankschtein, D. (2017). Quantitative
561 modeling of MoS_2–solvent interfaces: Predicting contact angles and exfoliation performance using
562 molecular dynamics. *The Journal of Physical Chemistry C* 121, 9022–9031. doi:10.1021/acs.jpcc.
563 7b00484
564 Szlufarska, I., Chandross, M., and Carpick, R. W. (2008). Recent advances in single-asperity nanotribology.
565 *Journal of Physics D: Applied Physics* 41, 123001. doi:10.1088/0022-3727/41/12/123001
566 Tagawa, M., Yokota, K., Matsumoto, K., Suzuki, M., Teraoka, Y., Kitamura, A., et al. (2007). Space
567 environmental effects on MoS_2 and diamond-like carbon lubricating films: Atomic oxygen-induced
568 erosion and its effects on tribological properties. *Surface & Coatings Technology* 202, 1003–1010.
569 doi:10.1016/j.surfcoat.2007.07.069
570 Teo, W. Z., Chng, E. L. K., Sofer, Z., and Pumera, M. (2014). Cytotoxicity of exfoliated transition-metal
571 dichalcogenides (MoS_2, WS_2, and WSe_2) is lower than that of graphene and its analogues. *Chemistry –*
572 *A European Journal* 20, 9627–9632. doi:10.1002/chem.201402680
573 Vanossi, A., Manini, N., Urbakh, M., Zapperi, S., and Tosatti, E. (2013). Colloquium: Modeling friction:
574 From nanoscale to mesoscale. *Reviews of Modern Physics* 85, 529–552. doi:10.1103/RevModPhys.85.
575 529
576 Vazirisereshk, M. R., Martini, A., Strubbe, D. A., and Baykara, M. Z. (2019). Solid lubrication with MoS_2:
577 A review. *Lubricants* 7, 57. doi:10.3390/lubricants7070057
578 Wang, L., Zhou, X., Ma, T., Liu, D., Gao, L., Li, X., et al. (2017). Superlubricity of a graphene/MoS_2
579 heterostructure: a combined experimental and dft study. *Nanoscale* 9, 10846–10853. doi:10.1039/
580 c7nr01451a
581 Watanabe, S., Noshiro, J., and Miyake, S. (2004). Tribological characteristics of WS_2/MoS_2 solid
582 lubricating multilayer films. *Surface & Coatings Technology* 183, 347–351. doi:10.1016/j.surfcoat.2003.
583 09.063
584 Zeng, X., Peng, Y., Liu, L., Lang, H., and Cao, X. (2018). Dependence of the friction strengthening of
585 graphene on velocity. *Nanoscale* 10, 1855–1864. doi:10.1039/c7nr07517k
586 Zhao, X. and Perry, S. S. (2010). The role of water in modyfying friction within MoS_2 sliding interfaces.
587 *ACS Applied Materials & Interfaces* 2, 1444–1448. doi:10.1021/am100090t

FIGURE CAPTIONS

Figure 1: Static potential energy surfaces calculated per area for the long (inset: short) diagonal of the hexagonal unit cell. Four different cases are considered: i) in black pure MoS_2 obtained via DFT (Ref. (Levita et al., 2014)), ii) in red pure MoS_2 obtained with the force field employed in this study (Sresht et al., 2017), iii) in green MoS_2 and an ideal, parallel water network via MD and iv) in blue MoS_2 and an ideal anti-parallel water network via MD. The dashed lines are obtained via akima spline interpolation and serve merely as a guide to the eyes.

Figure 2: Schematic overview of the computational setup. The side view of the six-layered MoS_2 structure, with a cluster of 26 H_2O molecules intercalated in the center interface, is displayed. Molybdenum, sulfur, oxygen, and hydrogen atoms are displayed in silver, yellow, red, and white, respectively. This specific case resembles the system after equilibration at 0.0 GPa load and 300 K. From this picture, there is a clear structural deformation visible in the MoS_2 layers directly encapsulating the H_2O cluster. Figure obtained with VMD (Humphrey et al., 1996).

Figure 3: Snapshots for different configurations taken at 0 Å (panel **A-E**) and 22 Å (panel **F-J**), presented from a side view perspective. Respective configurations are dry sliding, 8.5% coverage, full coverage, bulk water, and 67% coverage. In the final column (panel **K-O**), the center of mass for every layer is depicted in the xy-plane. The vertical dashed lines in this column represent the final x-position for every layer. Figure obtained with VMD (Humphrey et al., 1996).

Figure 4: Top view representation of the water network for 8.5%, full and 67% coverage (panel **A-C**). The black arrow represents the sliding direction. The blue diamonds serve as a guide to the eyes in distinguishing the pcd configuration. The bottom row (panel **D-F**) represents the angles of all H-bonds, at every time step, with respect to the x-axis, in red the corresponding histograms are depicted. Figure obtained with VMD (Humphrey et al., 1996).

Figure 5: Profiles of the dissipated work for MD trajectories sliding in the x-direction. The left panel **A** represents the case with dry sliding (black and red) and 8.5% coverage (green and blue) at zero and 3.0 GPa load, respectively, and one case with 67% coverage (orange) at 0.5 GPa load and characterized by a parallel water network. The right panel **B** represents the dissipation at zero and 3.0 GPa load for full coverage with an anti-parallel water network (black and red), and bulk water (green and blue).

Figure 6: Coefficients of friction for different sliding velocities, 0.2 (black), 2.0 (blue), and 20.0 (red) m/s, plotted versus water coverage. The dashed lines and the area around it result from akima interpolation and serve as a guide to the eyes. The error bars result from the linear fit taking into account the errors obtained via the bootstrap method.

6

MoS_2 & Diamond

6.1 Introduction

Although independent of the main theme of this thesis, complementary results are presented of a collaborative study on MoS_2 grown on a diamond substrate. This predominantly experimental work aimed to study the optoelectronic properties of MoS_2 nanosheets synthesized on nanocrystalline diamond films. Firstly, silicon substrates were coated with diamond films. Next, the diamond was covered by a pristine coating of different thicknesses of molybdenum (Mo). Finally, the Mo was annealed in the presence of a sulfuric environment, yielding sheets of MoS_2.

Using a scanning electron microscope, it was evident that the MoS_2 layers orient differently atop the diamond depending on the initial thickness of the pristine Mo. For pristine Mo with an initial thickness of 1 nm, the MoS_2 layers

tended to orient parallel to the diamond surface. For pristine Mo with an initial thickness of 6 nm, the MoS_2 was found to orient vertically atop the diamond surface. Finally, for an intermediate thickness of about 3 nm, a mixture of these two scenarios was found. In all cases, the morphology of the underlying diamond substrate remained unchanged. One of the proposed explanations for this observation is based on the mechanism for MoS_2 growth on planar substrates [137, 138]. The idea here is that with a thinner initial pristine Mo coating, the MoS_2 will form in a planar fashion because there is enough space to do so. In contrast, for an initially thicker pristine Mo coating, a vertical formation of MoS_2 is favored since the individual layers of MoS_2 grow rapidly, and compress and extrude each other [139, 140].

6.2 Approaches and Problems

The manuscript of this work has not yet been finished. Therefore, this chapter contains a more detailed overview of the computational details and an extended discussion of the results obtained. To identify the driving force behind the change of the preferred orientation of MoS_2 nanosheets on a diamond substrate, we performed MM simulations. We performed these simulations by employing the LAMMPS package [113] and using the ReaxFF interaction potential [105, 141]. Structure and energy optimizations were based only on the final configurations obtained via the experimental growth processes. This approach is based on the assumption that the growth process is controlled by thermodynamics and not by kinetics. Therefore, the final structures represent the most stable configurations and not the structures that formed the quickest. This assumption can be justified by considering the high temperature and the long deposition time (allowing structural rearrangements in order to form the most stable product) in play for the experimental technique used to make these structures.

The current availability of FFs restricted our freedom in establishing the computational setup. More specifically, although there are reactive FFs (allowing bond breaking and formation) available for hydrogen-terminated dia-

mond [141] and for hydrogen in the presence of MoS_2 [105], to the best of our knowledge, a FF which covers both systems was still lacking at the time of performing this study. Therefore, we decided to use an alternative approach in which the heterostructure, consisting of diamond and MoS_2, is simplified. In doing so, a 12.5 Å thick slab of diamond was prepared with a hydrogen-passivated (111) surface, using the FF of Ref. [141]. A crystal structure [142] from the American Mineralogist Crystal Structure Database [143] was used. This specific surface was selected since it is the most representative for diamond. Firstly, after an initial energy minimization, the top layer of hydrogen atoms was retained, whereas the nearest neighbor bonded carbons were replaced by hydrogen atoms, and all other atoms were removed, resulting in a 'surface of H_2 molecules' characterized by the orientation and spacing of an H-terminated diamond surface. During this optimization and all further minimizations, the conjugate gradient algorithm was employed. The relative energy tolerance was set to 1.0×10^{-15} (energy change between two successive iterations, divided by the energy magnitude). Secondly, the resulting structure was optimized while keeping the topmost hydrogen atoms fixed to maintain the surface topology. Thirdly, a supercell was created by covering the plane of hydrogen atoms with crystalline MoS_2 layers. For this, the commensurate $2H_c$-MoS_2 crystal structure [111] from the Inorganic Crystal Structure Database [144] was used.

The MoS_2 coating was oriented in either a horizontal or perpendicular fashion. Furthermore, the coating thickness in the z-direction varied, ranging from roughly 10 to 250 Å, to match the length scale of the experimental results. It is important to note here that there is an unavoidable mismatch between the passivated diamond surface and the MoS_2 structure. The configurations were chosen such that the lattice mismatch stress is fully accommodated within the MoS_2 coating and is always below 1%. The reader should also keep in mind that for the horizontal case, the atoms facing the interface solely consist of sulfur atoms. In contrast, for the perpendicular case, each layer either ends with sulfur or molybdenum atoms, as per the structure of the $2H_c$ polytype. Finally, these structures were optimized while keeping the bottommost layer of hydrogen atoms fixed in the x-, y- and z-direction. An overview of the computational setup can be found in Figs. 6.1 (a-b).

6.3 Results and Outlook

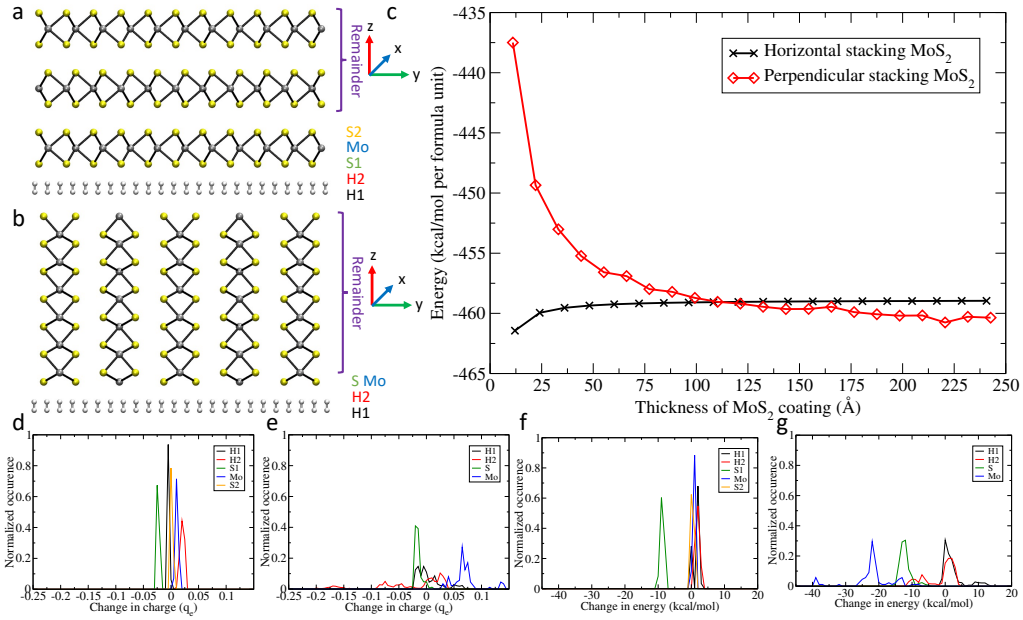

Figure 6.1: Overview of the computational results. Schematic of the computational setup of the (a) horizontal and (b) perpendicular stackings. (c) Normalized total energy profile of minimized horizontal and perpendicular stacking structures plotted against the coating thickness of MoS_2. The energy is normalized per formula unit (H_2 and MoS_2) in order to account for differences in area of the hydrogen surface and MoS_2 thickness. Finally, distributions of the change in per-atom charge and energy for the horizontal (d, f) and the perpendicular (e, g) configurations, respectively, are displayed.

In Fig. 6.1-c, the results of the energy minimization for both systems are presented. From these results, it can be observed that for a thin coating thickness (<105 Å, which is equivalent to $\sim$ 3 nm of pristine Mo), the MoS_2 layers prefer to orient parallel atop of the diamond (111) surface. For thicker coatings (>125 Å, which is equivalent to $\sim$ 3.5 nm of pristine Mo), the MoS_2 layers prefer to orient perpendicularly above the diamond surface. These results are in perfect agreement with the experimental findings.

To further elaborate on these findings, we compared the fully interacting H_2-MoS_2 system with the two isolated subsystems composed of either H_2

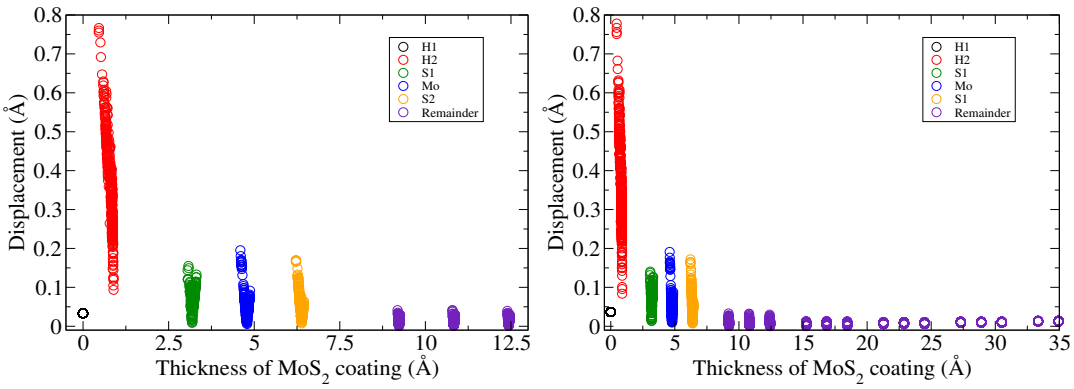

(a) Horizontal configuration for the thinnest coating.

(c) Horizontal configuration for the thickest coating, displaying the first 35 Å.

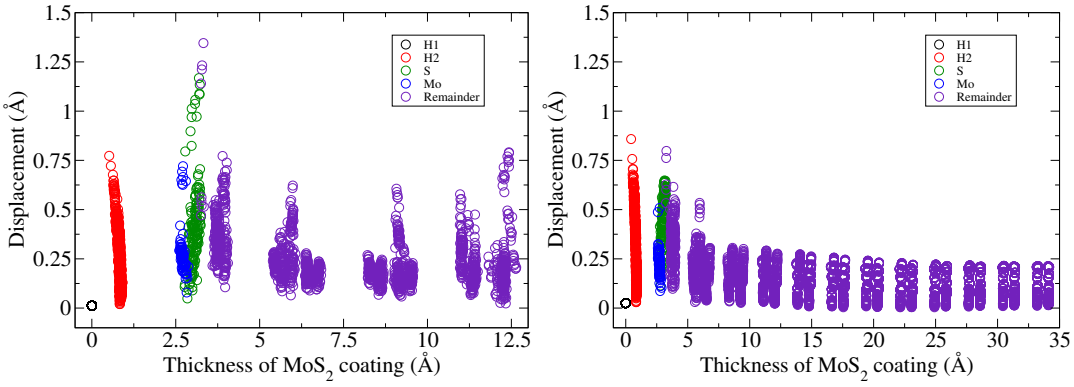

(b) Perpendicular configuration for the thinnest coating.

(d) Perpendicular configuration for the thickest coating, displaying the first 35 Å.

Figure 6.2: Atomic displacements with respect to the isolated subsystems.

molecules or MoS_2 layers. In general, it was found that the origin of the inversion of the stability from a horizontal to a perpendicular orientation, when increasing the coating thickness, can be traced back to local features such as structural distortions and changes in charge and energy of the atoms at the interface. This is confirmed in Figs. 6.2-6.4, where these quantities are compared for the two limiting cases (thinnest and thickest coatings). Regarding the atomic displacements, we found that most of the distortions are accommodated by the hydrogen atoms facing the interface, as displayed in Figs. 6.2 (a-d). In Figs. 6.1 (d-g), we present histograms for both configurations based on the change in charge or energy per atom. These histograms are derived from the simulations where the thickest coating was considered. Looking at the redistribution of charges, several observations were made. In the case of horizontally oriented MoS_2 (Fig. 6.1-d), it was found that the hydrogen sur-

face facing the coating had a net positive charge, resulting in a polarization of the H_2 molecules. Besides, charge polarization also occurred in the first MoS_2 layer. Here, the sulfurs facing the interface were negatively charged, whereas the molybdenum atoms had a net positive charge. This observation is in agreement with the difference in electronegativity for each type of atom. Finally, no significant effect of the coating thickness on the charge redistribution was found, as is confirmed by Figs. 6.3 (a-b).

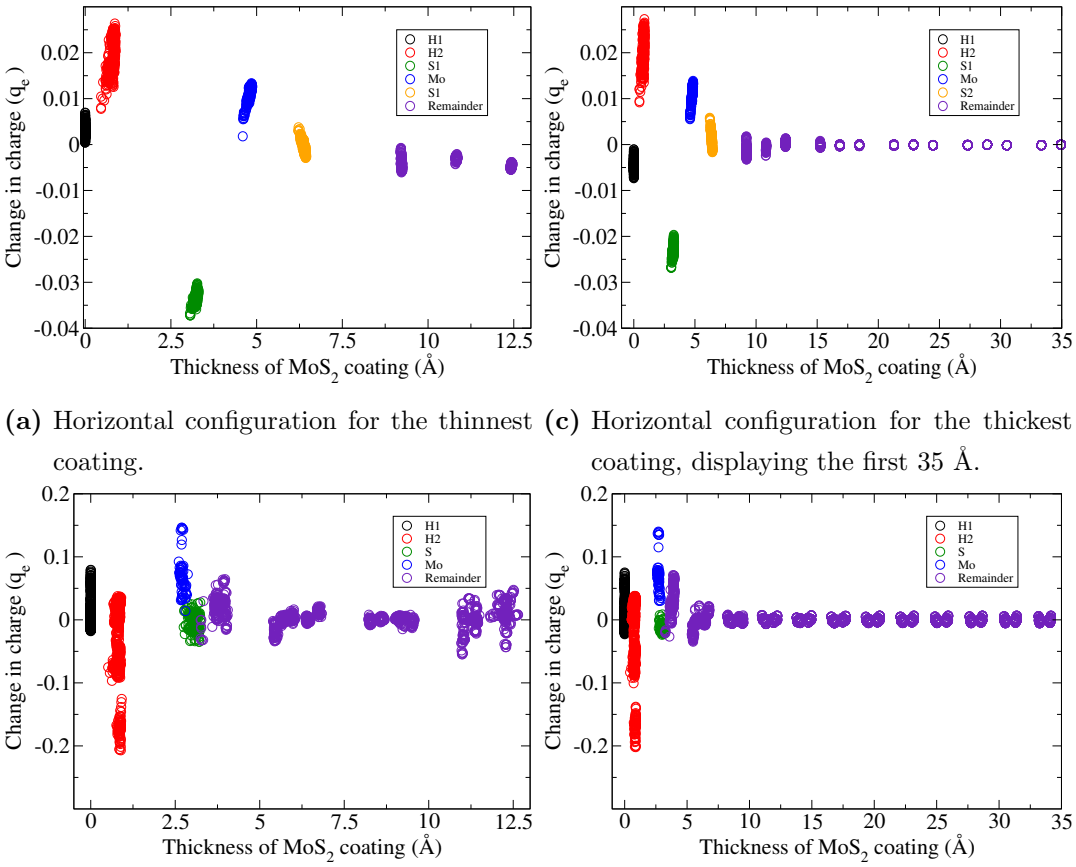

(a) Horizontal configuration for the thinnest coating.

(c) Horizontal configuration for the thickest coating, displaying the first 35 Å.

(b) Perpendicular configuration for the thinnest coating.

(d) Perpendicular configuration for the thickest coating, displaying the first 35 Å.

Figure 6.3: Change in charge per atom with respect to the isolated subsystem.

In perpendicularly oriented coatings, the charge redistribution is more complex (see Fig. 6.1-e). We found that the hydrogen atoms facing sulfur atoms had a more positive charge. In contrast, the sulfur atoms became more negatively charged, similar to the observations of the horizontal configuration. Conversely, the hydrogen atoms facing molybdenum atoms carried a negative charge, while molybdenum atoms became more positively charged. Further-

more, the thickness of the coating did not seem to alter the results significantly, as can been seen in Figs. 6.3 (c-d).

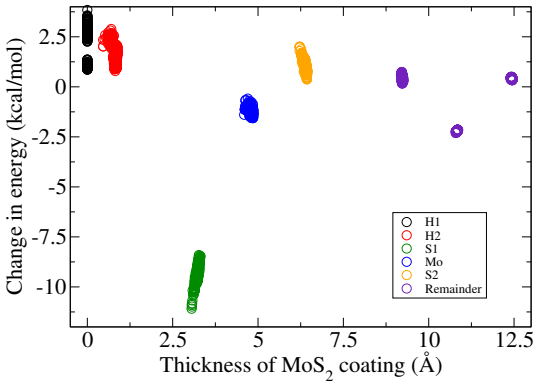

(a) Horizontal configuration for the thinnest coating.

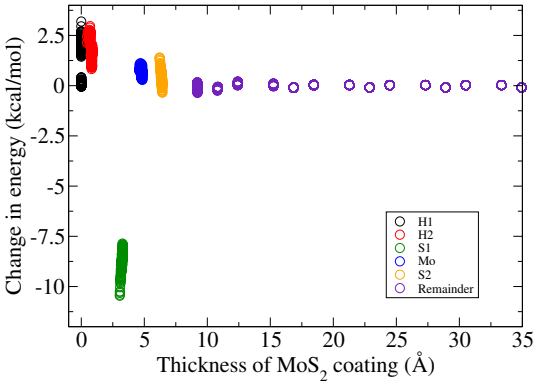

(c) Horizontal configuration for the thickest coating, displaying the first 35 Å.

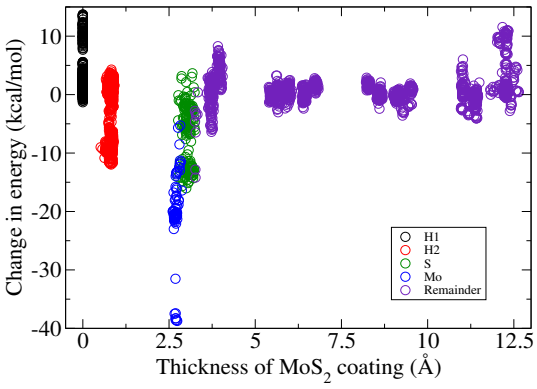

(b) Perpendicular configuration for the thinnest coating.

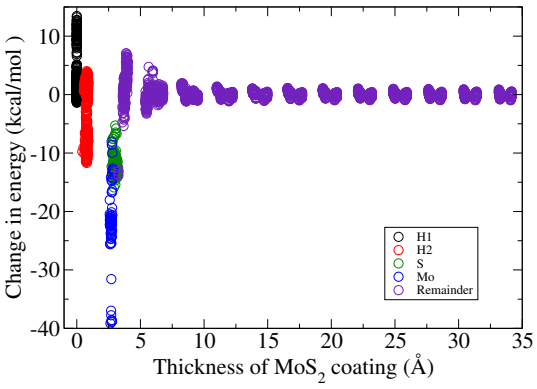

(d) Perpendicular configuration for the thickest coating, displaying the first 35 Å.

Figure 6.4: Change in energy per atom with respect to the isolated subsystems.

Next, we considered the change in energy per atom. First of all, in both configurations, the coating thickness did not alter the behavior observed at the interface (see Fig. 6.4). For the horizontal case (see Fig. 6.1-f), a slight destabilization of the hydrogen atoms was observed, accompanied by a robust stabilization of the sulfur atoms facing them. This picture further confirms that the interaction-induced distortions are indeed accommodated on the hydrogen atoms. For the perpendicular case (see Fig. 6.1-g), it was found that it is mainly the outer hydrogen layer that is destabilized, while the interface hydrogen layer brings a stabilizing contribution. Finally, the behavior of the MoS_2 coating leads to an overall stabilization of the structure, dominated by the molybdenum atoms. In this regard, and generally speaking,

the stabilizing effect was quantitatively more effective by a factor of 4 in the perpendicular orientation compared to the horizontal one.

The results presented above reveal a relation between the MoS_2 coating thickness and the relative orientation above a diamond substrate, which is in line with the experimental results mentioned above. This study is a perfect example of scientific power when experimental and computational techniques are combined. Firstly, we found a shortcut to overcome the unavailability of the current FFs by simplifying the system under study. Secondly, our results contributed to the characterization of the stacking orientation of the system through structural deformation and charge polarization. In principle, our analysis is general and can be used for other systems.

I was a contributing author of this work and carried out the computational conceptualization, computational data production and subsequent analysis, and preparing of the results for publication. All results have been given to the corresponding author and the manuscript is in preparation.

7

Conclusions

In this thesis, we have investigated the tribological behavior of solid lubricants by employing computational modeling. The main goal of this research effort was to obtain new insights into the fundamental understanding of the frictional properties of MoS_2 at the nanoscale. Moreover, we aimed to elucidate the different channels of energy dissipation present when changing the intrinsic and/or external properties of the systems considered. Such investigations are significant as they contribute directly to a general understanding of friction and rationalize experimental observations. Additionally, considering the enormous potential of solid lubricants on the one hand but their limited industrial implementation on the other, validates any quest in this direction.

To realize this aim, three main projects and three side projects were realized. The first main project (Chap. 3) consisted of a study on the structural frictional properties of pure MoS_2. This project aimed to determine if

superlubricity can be achieved through mechanisms other than incommensurability. More precisely, we studied the effect of load and sliding direction on the frictional forces of commensurate bilayer MoS_2 by performing non-equilibrium MD simulations. We observed frictional anisotropy based on a relation between the sliding direction and the type of frictional behavior. In doing so, we have shown for the first time that superlubricity can also be achieved by sliding with commensurate contacts.

The second main project (Chap. 4) consisted of an investigation into the rotational energetic behavior of a bilayer heterostructure of MoS_2 and graphene. The goal of this project was to relate the energetic landscape to the rotational mismatch angles between the layers. We performed MM energy minimizations with an in-house optimized FF based on DFT results. Our results showed a relation between the relative mismatch angle and the energy profile. We explained our observations as an interplay between the local deformation of the layers and flexural phonons. The energetic behavior of this system was found to go hand-in-hand with an out-of-plane rippling of the layers, which matched the periodicity of the Moiré pattern. Through this work, a new perspective was brought to seemingly contradictory experimental results. Moreover, our findings could serve as guidance for the future design of twistronics devices. Finally, the limits of epitaxy theory were revealed when applied to this system due to the complex three-atom layered structure of MoS_2.

The third main project (Chap. 5) consisted of an investigation of the effects of water contamination on the tribological behavior of pseudo-bulk MoS_2. Here, we wanted to gain insights into how the frictional properties of MoS_2 are quantitatively affected by the presence of water during sliding, and to determine if there is a relation to the type of H-bond water network. This was achieved by modeling the effect of load and sliding velocity on the frictional properties of a six-layered commensurate MoS_2 structure during sliding in the presence of water via non-equilibrium MD. In general, it was found that a thin layer of water forms and that the orientation of the H-bond network is related to the frictional behavior. Moreover, it was concluded that water could act both as a contaminant and a lubricant. On the one hand, these

outcomes enhanced the understanding of the frictional mechanisms at play for solid lubricants in the presence of water. On the other, they provided a general starting point for the design of nanoscale devices in ambient conditions.

The first side project (Chap. 6) studied the conformational behavior of MoS_2 on top of a diamond surface. This project aimed to provide an atomistic explanation of the different structural orientations found during an experimental study on the optoelectronic properties of this specific structure. By performing MM energy minimizations, we studied the energetic behavior of various coating thicknesses and orientations of MoS_2 atop diamond. Our results supported the experimental findings and explained the conformational behavior of MoS_2 coatings through local distortions and redistribution of charges – information that is not directly accessible via experiments.

The final two side projects, which are not discussed in this thesis because only minor contributions were made, can be found in Appxs. D and E. One consists of a large viewpoint on atomic-scale design protocols. Here, our contribution consisted of a review and outlook on the principles behind electricity generation through tribology, e.g., by triboelectric nanogenerators. This viewpoint concluded that to realize the true potential of functional nanomaterials and their application in industry, the scientific community should focus on a synergy between theory (atomistic simulations) and experiment (advanced AFM techniques). The other relates to a study on the frictional properties and edge pinning effects within MoS_2 and graphene, and MoS_2 and boron nitride heterostructures. Here, the importance of interface steps and edges in determining the frictional behavior in large lattice mismatch heterojunctions was confirmed by MD simulations.

To conclude, the works presented in this thesis have actively contributed to the general understanding of the different friction mechanisms at play during sliding, for various internal and external conditions, of MoS_2 and solid lubricants in general. Furthermore, the robustness of using computational simulations to complement experimental results has once more been highlighted. These insights have been disseminated at international conferences, which provided the opportunity to translate feedback from world-renowned tribologists

into improvements and refinements of some fundamental concepts that underpin this work, alongside establishing strong research collaborations for future endeavors. As a result, this thesis can facilitate the next step towards making the large-scale industrial implementation of solid lubricants feasible.

The outcomes presented here also hint at where the focus should be in future works. We have seen that MD simulations are capable of providing a wealth of information on the processes determining nanoscale friction. However, we have also been confronted by their limitations. Firstly, reliable FFs are not readily available. Here, machine learning algorithms may offer a workaround in providing a systematic way of extending the library of FFs. Also, including the concept of aging into the FFs could enormously benefit the accuracy of the outcomes. Secondly, the mismatch between the timescales of nanoscale experiments and MD results impedes a one-to-one comparison and prevents tracing back to the fundamental origin of nanoscale stick-slip dynamics. The development of more coarse-grained methods could prove to be a valuable approach.

Finally, developing a framework to generalize the observations made for specific solid lubricants, both at the nanoscale and macroscale, could enormously benefit the search for novel 2D materials and increase the pace of industrial implementation. This, in combination with ever-increasing computational power, means one can only dream of the possibilities that might be available in the coming decades.

If I have seen farther than others, it is because I was standing on the shoulders of giants.

Sir Isaac Newton

8

List of Publications

In this chapter, the publications that have been produced during the period 2017-2021 are listed. This list is divided into projects that are directly related to this thesis and those that are not. All works have been published in impacted, peer-reviewed journals. Where I am not the main author of the work, the paper is listed under the subcategory of 'contributing author'.

8.1 Published Works within the Scope of this Thesis

Main Author

[1] V.E.P. Claerbout, T. Polcar, and P. Nicolini. "Superlubricity achieved for commensurate sliding: MoS_2 frictional anisotropy in silico". In: *Computational Materials Science* 163 (2019), pp. 17-23. DOI: 10.1016/j.commatsci.2019.03.019.

[2] A. Silva, V.E.P. Claerbout, T. Polcar, D. Kramer, and P. Nicolini. "Exploring the Stability of Twisted van der Waals Heterostructures". In: *ACS Applied Materials & Interfaces* 12 (2020), pp. 45214-45221. DOI: 10.1021/acsami.0c13971.

8.2 Submitted Works within the Scope of this Thesis

Main Author

[·] V.E.P. Claerbout, T. Polcar, and P. Nicolini. "Exploring nanoscale lubrication mechanisms of multilayer MoS_2 during sliding: the effect of humidity". Submitted to: *Frontiers in Chemistry*.

Contributing Author

[·] M. Liao, P. Nicolini, et al. "Ultra-low friction and edge pinning effect between large lattice mismatch van der Waals heterostructure interfaces". Submitted to: *Nature Materials*.

8.3 Published Works outside the Scope of this Thesis

Contributing Author

[3] F. Belviso, V.E.P. Claerbout, et al. "Viewpoint: Atomic-Scale Design Protocols toward Energy, Electronic, Catalysis, and Sensing Applications". In: *Inorganic Chemistry* 58 (2019), pp. 14939-14980. DOI: 10.1021/acs.inorgchem.9b01785.

[4] E. Matoušková, E. Bignon, et al. "Impact of the Nucleosome Histone Core on the Structure and Dynamics of DNA-Containing Pyrimidine–Pyrimidone (6–4) Photoproduct". In: *Journal of Chemical Theory and Computation* 16 (2020), pp. 5972–5981. DOI: 10.1021/acs.jctc.0c00593.

[5] E. Bignon, V.E.P. Claerbout, et al. "Nucleosomal embedding reshapes the dynamics of abasic sites". In: *Scientific Reports* 10 (2020), pp. 17314. DOI: 10.1038/s41598-020-73997-y.

Bibliography

[1] K. Holmberg and A. Erdemir. "Influence of tribology on global energy consumption, costs and emissions". In: *Friction* 5 (2017), pp. 263–284. DOI: 10.1007/s40544-017-0183-5.

[2] D. Dowson. *History of Tribology, 2nd Edition*. London: Longman, 1979.

[3] R. M. Mortier, M. F. Fox, and S. T. Orszulik. *Chemistry and Technology of Lubricants, 3rd Edition*. Dordrecht Heildelberg London New York: Springer, 2010.

[4] H. E. Sliney. "Solid Lubricants". In: *NASA Technical Memorandum* (1991).

[5] D. Berman, A. Erdemir, and A. V. Sumant. "Graphene: a new emerging lubricant". In: *Materials Today* 17 (2014), pp. 31–42. DOI: 10.1016/j.mattod.2013.12.003.

[6] W. Choi et al. "Recent development of two-dimensional transition metal dichalcogenides and their applications". In: *Materials Today* 20 (2017), pp. 116–130. DOI: 10.1016/j.mattod.2016.10.002.

[7] H. P. Jost. *Lubrication (tribology), education and research; a report on the present position and industry's needs*. UK: H.M. Stationery Office, 1966.

[8] G. Amontons. "De la resistance causée dans les machines". In: *Memoires de l'Academie Royale A* (1699), pp. 251–282.

[9] C. A. Coulomb. "Théorie des machines simples en ayant égard au frottement de leurs parties et à la roideur des cordages". In: *Mémoires de mathématique et de physique* (1785), pp. 161–342.

[10] C. S. Gillmor. *Coulomb and the Evolution of Physics and Engineering in Eighteenth-Century France*. Princeton: Princeton University Press, 1971.

[11] S. Yu. Krylov and J. W. M. Frenken. "The physics of atomic-scale friction: Basic considerations and open questions". In: *Physica Status Solidi B* 251 (2014), pp. 711–736. DOI: 10.1002/pssb.201350154.

[12] A. I. Vakis et al. "Modeling and simulation in tribology across scales: An overview". In: *Tribology International* 125 (2018), pp. 169–199. DOI: 10.1016/j.triboint.2018.02.005.

[13] J. Gao et al. "Frictional Forces and Amontons' Law: From the Molecular to the Macroscopic Scale". In: *Journal of Physical Chemistry B* 108 (2004), pp. 3410–3425. DOI: 10.1021/jp0363621.

[14] E. Riedo et al. "Interaction Potential and Hopping Dynamics Governing Sliding Friction". In: *Physical Review Letters* 91 (2003), p. 084502. DOI: 10.1103/PhysRevLett.91.084502.

[15] A. Smolyanitsky. "Effects of thermal rippling on the frictional properties of free-standing graphene". In: *RSC Advances* 5 (2015), pp. 29179–29184. DOI: 10.1039/c5ra01581b.

[16] A. Vanossi et al. "Colloquium: Modeling friction: From nanoscale to mesoscale". In: *Reviews of Modern Physics* 85 (2013), pp. 529–552. DOI: 10.1103/RevModPhys.85.529.

[17] X. Zeng et al. "Dependence of the friction strengthening of graphene on velocity". In: *Nanoscale* 10 (2018), pp. 1855–1864. DOI: 10.1039/c7nr07517k.

[18] J. J. Mazo et al. "Time Strengthening of Crystal Nanocontacts". In: *Physical Review Letters* 118 (2017), p. 246101. DOI: 10.1103/PhysRevLett.118.246101.

[19] B. Luan and M. O. Robbins. "The breakdown of continuum models for mechanical contacts". In: *Nature* 435 (2005), pp. 929–932. DOI: 10.1038/nature03700.

[20] Y. Mo, K. T. Turner, and I. Szlufarska. "Friction laws at the nanoscale". In: *Nature* 457 (2009), pp. 1116–1119. DOI: 10.1038/nature07748.

[21] V. E. P. Claerbout, T. Polcar, and P. Nicolini. "Superlubricity achieved for commensurate sliding: MoS_2 frictional anisotropy *in silico*". In: *Computational Materials Science* 163 (2019), pp. 17–23. DOI: 10.1016/j.commatsci.2019.03.019.

[22] K. Miura and S. Kamiya. "Observation of the Amontons-Coulomb law on the nanoscale: Frictional forces between MoS_2 flakes and MoS_2 surfaces". In: *Europhysics Letters* 58 (2002), pp. 610–615. DOI: 10.1209/epl/i2002-00439-9.

[23] F. P. Bowden and D. Tabor. *The Friction and Lubrication of Solids*. UK: Oxford University Press, 1950.

[24] G. Binnig, C. F. Quate, and Ch. Gerber. "Atomic Force Microscope". In: *Physical Review Letters* 56 (1986), pp. 930–933. DOI: 10.1103/PhysRevLett.56.930.

[25] C. M. Mate et al. "Atomic-Scale Friction of a Tungsten Tip on a Graphite Surface". In: *Physical Review Letters* 59 (1987), p. 1942. DOI: 10.1007/978-94-011-1812-5_35.

[26] E. Gnecco et al. "Friction experiments on the nanometre scale". In: *Journal of Physics: Condensed Matter* 13 (2001), R619–R642. DOI: 10.1088/0953-8984/13/31/202.

[27] V. L. Popov and J. A. T. Gray. "Prandtl-Tomlinson model: History and applications in friction, plasticity, and nanotechnologies". In: *Zeitschrift für Angewandte Mathematik und Mechanik* 92 (2012), pp. 683–708. DOI: 10.1002/zamm.201200097.

[28] L. Prandtl. "Ein Gedankenmodell zur kinetischen Theorie der festen Körper". In: *Zeitschrift für Angewandte Mathematik und Mechanik* 8 (1928), pp. 85–106. DOI: 10.1002/zamm.19280080202.

[29] G. A. Tomlinson. "CVI. A molecular theory of friction". In: *The London, Edinburgh, and Dublin Philosophical Magazine and Journal of Science* 7 (1929), pp. 905–939. DOI: 10.1080/14786440608564819.

[30] N. Manini et al. "Friction and nonlinear dynamics". In: *Journal of Physics: Condensed Matter* 28 (2016), p. 293001. DOI: 10.1088/0953-8984/28/29/293001.

[31] O. Hod et al. "Structural superlubricity and ultralow friction across the length scales". In: *Nature* 563 (2018), pp. 485–492. DOI: 10.1038/s41586-018-0704-z.

[32] T. W. Scharf and S. V. Prasad. "Solid lubricants: a review". In: *Journal of Materials Science* 48 (2013), pp. 511–531. DOI: 10.1007/s10853-012-7038-2.

[33] S. Zhang et al. "Tribology of two-dimensional materials: From mechanisms to modulating strategies". In: *Materials Today* 26 (2019), pp. 67–86. DOI: 10.1016/j.mattod.2018.12.002.

[34] W. Zhai and K. Zhou. "Nanomaterials in Superlubricity". In: *Advanced Functional Materials* 29 (2019), p. 1806395. DOI: 10.1002/adfm.201806395.

[35] A. Erdemir. *Solid Lubricants and Self-lubricating Films*. Florida: CRC Press Boca Raton, 2001.

[36] E. W. Roberts. "Thin solid lubricant films in space". In: *Tribology International* 23 (1990), pp. 95–104. DOI: 10.1016/0301-679X(90)90042-N.

[37] W. M. van Spengen, V. Turq, and J. W. M. Frenken. "The description of friction of silicon MEMS with surface roughness: virtues and limitations of a stochastic Prandtl–Tomlinson model and the simulation of vibration-induced friction reduction". In: *Beilstein Journal of Nanotechnology* 1 (2010), pp. 163–171. DOI: 10.3762/bjnano.1.20.

[38] C. R. Woods et al. "Macroscopic self-reorientation of interacting two-dimensional crystals". In: *Nature Communications* 7 (2016), p. 10800. DOI: 10.1038/ncomms10800.

[39] M. E. Bell and J. H. Findlay. "Molybdenite as a New Lubricant". In: *Physical Review* 59 (1941), pp. 922–927.

[40] C. Donnet and A. Erdemir. "Solid lubricant coatings: recent developments and future trends". In: *Tribology Letters* 17 (2004), pp. 389–397. DOI: 10.1023/B:TRIL.0000044487.32514.1d.

[41] J. C. J. Bart, E. Gucciardi, and S. Cavallaro. *Biolubricants: Science and technology*. Oxford: Woodhead, 2013.

[42] M. Evaristo, T. Polcar, and A. Cavaleiro. "Tribological behaviour of C-alloyed transition metal dichalcogenides (TMD) coatings in different environments". In: *International Journal of Mechanics and Materials in Design* 4 (2008), pp. 137–143. DOI: 10.1007/s10999-007-9034-2.

[43] G. Levita, P. Restuccia, and M. C. Righi. "Graphene and MoS_2 interacting with water: A comparison by *ab initio* calculations". In: *Carbon* 107 (2016), pp. 878–884. DOI: 10.1016/j.carbon.2016.06.072.

[44] H. S. Khare and D. L. Burris. "The Effects of Environmental Water and Oxygen on the Temperature-Dependent Friction of Sputtered Molybdenum Disulfide". In: *Tribology Letters* 52 (2013), pp. 485–493. DOI: 10.1007/s11249-013-0233-8.

[45] J. K. G. Panitz et al. "The tribological properties of MoS_2 coatings in vacuum, low relative humidity, and high relative humidity environments". In: *Journal of Vacuum Science & Technology A* 6 (1988), pp. 1166–1170. DOI: 10.1116/1.575669.

[46] M. Chhowalla and G. A. J. Amaratunga. "Thin films of fullerene-like MoS_2 nanoparticles with ultra-low friction and wear". In: *Nature* 407 (2000), pp. 164–167. DOI: 10.1038/35025020.

[47] M. Chhowalla et al. "The chemistry of two-dimensional layered transition metal dichlacogenide nanosheets". In: *Nature Chemistry* 5 (2013), pp. 263–275. DOI: 10.1038/NCHEM.1589.

[48] S. Manzeli et al. "2D transition metal dichalcogenides". In: *Nature Review Materials* 2 (2017), pp. 1–15. DOI: 10.1038/natrevmats.2017.33.

[49] A. V. Kolobov and J. Tominaga. *Two-Dimensional Transition-Metal Dichalcogenides*. Switzerland: Springer, 2016.

[50] M.-H. Kang et al. “2.04 - Structure and Chemistry of 2D Materials”. In: *Comprehensive Nanoscience and Nanotechnology (Second Edition)* 2 (2019), pp. 55–90. DOI: 10.1016/B978-0-12-803581-8.10507-7.

[51] B. Irving, P. Nicolini, and T. Polcar. “On the lubricity of transition metal dichalcogenides: an *ab initio* study”. In: *Nanoscale* 9 (2017), pp. 5597–5607. DOI: 10.1039/c7nr00925a.

[52] R. G. Dickinson and L. Pauling. “THE CRYSTAL STRUCTURE OF MOLYBDENITE”. In: *Journal of the American Chemical Society* 45 (1923), pp. 1466–1471. DOI: 10.1021/ja01659a020.

[53] X. Li and H. Zhu. “Two-dimensional MoS_2: Properties, preparation, and applications”. In: *Journal of Materiomics* 1 (2015), pp. 33–44. DOI: 10.1016/j.jmat.2015.03.003.

[54] M. R. Vazirisereshk et al. “Solid Lubrication with MoS_2: A Review”. In: *Lubricants* 7 (2019). DOI: 10.3390/lubricants7070057.

[55] W.L. Bragg. *An introduction to Crystal Analysis*. London: G. Bell and Son, Ltd., 1928, p. 64.

[56] H. Li et al. “Superlubricity between MoS_2 Monolayers”. In: *Advanced Materials* 29 (2017), p. 1701474. DOI: 10.1002/adma.201701474.

[57] J. M. Martin et al. “Superlubricity of molybdenum disulphide”. In: *Physical Review B* 48 (1993), pp. 10583–10588. DOI: 10.1103/PhysRevB.48.10583.

[58] C. Lee et al. “Frictional Characteristics of Atomically Thin Sheets”. In: *Science* 328 (2010), pp. 76–80. DOI: 10.1126/science.1184167.

[59] T. Onodera et al. “A Computational Chemistry Study on Friction of h-MoS_2. Part II. Friction Anisotropy”. In: *Journal of Physical Chemistry B* 114 (2010), pp. 15832–15838. DOI: 10.1021/jp1064775.

[60] M. R. Vazirisereshk et al. “Origin of Nanoscale Friction Contrast between Supported Graphene, MoS_2, and a Graphene/MoS_2 Heterostructure”. In: *Nano Letters* 19 (2019), pp. 5496–5505. DOI: 10.1021/acs.nanolett.9b02035.

[61] T. Arif et al. "Understanding the independent and interdependent role of water and oxidation on the tribology of ultrathin molybdenum disulfide (MoS_2)". In: *Advanced Materials Interfaces* 6 (2019), p. 1901246. DOI: 10.1002/admi.201901246.

[62] X. Zhao and S. S. Perry. "The Role of Water in Modifying Friction within MoS_2 Sliding Interfaces". In: *ACS Applied Materials and Interfaces* 2 (2010), pp. 1444–1448. DOI: 10.1021/am100090t.

[63] G. Levita and M. C. Righi. "Effects of Water Intercalation and Tribochemistry on MoS_2 Lubricity: An Ab Initio Molecular Dynamics Investigation". In: *ChemPhysChem* 18 (2017), pp. 1475–1480. DOI: 10.1002/cphc.201601143.

[64] T. Kubart et al. "Temperature dependence of tribological properties of MoS_2 and $MoSe_2$ coatings". In: *Surface & Coatings Technology* 193 (2005), pp. 230–233. DOI: 10.1016/j.surfcoat.2004.08.146.

[65] O. Acikgoz and M. Z. Baykara. "Speed dependence of friction on single-layer and bulk MoS_2 measured by atomic force microscopy". In: *Applied Physics Letters* 116 (2020), p. 071603. DOI: 10.1063/1.5142712.

[66] D. D. L. Chung. "Review Graphite". In: *Journal of Materials Science* 37 (2002), pp. 1475–1489. DOI: 10.1023/A:1014915307738.

[67] P. Trucano and R. Chen. "Structure of graphite by neutron diffraction". In: *Nature* 258 (1975), pp. 136–137. DOI: 10.1038/258136a0.

[68] Y. Baskin and L. Meyer. "Lattice Constants of Graphite at Low Temperatures". In: *Physical Review* 100 (1955), p. 544. DOI: 10.1103/PhysRev.100.544.

[69] K. Hasz et al. "Experiments and simulations of the humidity dependence of friction between nanoasperities and graphite: The role of interfacial contact quality". In: *Physical Review Materials* 2 (2018), p. 126001. DOI: 10.1103/PhysRevMaterials.2.126001.

[70] K. S. Novoselov et al. "Electric Field Effect in Atomically Thin Carbon Films". In: *Science* 306 (2004), pp. 666–669. DOI: 10.1126/science.1102896.

[71] K. P. Loh et al. “The chemistry of graphene”. In: *Journal of Materials Chemistry* 20 (2010), pp. 2277–2289. DOI: 10.1039/b920539j.

[72] K. S. Novoselov et al. “2D materials and van der Waals heterostructures”. In: *Science* 353 (2016), aac9439. DOI: 10.1126/science.aac9439.

[73] M. Xu et al. “Graphene-Like Two-Dimensional Materials”. In: *Chemical Reviews* 113 (2013), pp. 3766–3798. DOI: 10.1021/cr300263a.

[74] L. A. Ponomarenko et al. “Tunable metal–insulator transition in double-layer graphene heterostructures”. In: *Nature Physics* 7 (2011), pp. 958–961. DOI: 10.1038/NPHYS2114.

[75] A. K. Geim and I. V. Grigorieva. “Van der Waals heterostructures”. In: *Nature* 499 (2013), pp. 419–425. DOI: 10.1038/nature12385.

[76] J. M. Martin and A. Erdemir. “Superlubricity: Friction’s vanishing act”. In: *Physics Today* 71 (2018), pp. 40–46. DOI: 10.1063/PT.3.3897.

[77] M. Dienwiebel et al. “Superlubricity of Graphite”. In: *Physical Review Letters* 92 (2004), p. 126101. DOI: 10.1103/PhysRevLett.92.126101.

[78] Y. Cao et al. “Unconventional superconductivity in magic-angle graphene superlattices”. In: *Nature* 556 (2018), pp. 43–50. DOI: 10.1038/nature26160.

[79] R. Ribeiro-Palau et al. “Twistable electronics with dynamically rotatable heterostructures”. In: *Science* 361 (2018), pp. 690–693. DOI: 10.1126/science.aat6981.

[80] W. Jin et al. “Tuning the electronic structure of monolayer graphene/MoS_2 van der Waals heterostructures via interlayer twist”. In: *Physical Review B* 92 (2015), 210409R. DOI: 10.1103/PhysRevB.92.201409.

[81] L. Wang et al. “Superlubricity of a graphene/MoS_2 heterostructure: a combined experimental and DFT study”. In: *Nanoscale* 9 (2017), pp. 10846–10853. DOI: 10.1039/c7nr01451a.

[82] M. Peyrard and S. Aubry. “Critical behaviour at the transition by breaking of analyticity in the discrete Frenkel-Kontorova model”. In: *Journal of Physics C: Solid State Physics* 16 (1983), pp. 1593–1608. DOI: 10.1088/0022-3719/16/9/005.

[83] J. B. Sokoloff. "Theory of energy dissipation in sliding crystal surfaces". In: *Physical Review B* 42 (1990), pp. 760–765. DOI: 10.1103/PhysRevB.42.760.

[84] K. Shinjo and M. Hirano. "Dynamics of friction: superlubric state". In: *Surface Science* 283 (1993), pp. 473–478. DOI: 10.1016/0039-6028(93)91022-H.

[85] M. Hirano and K. Shinjo. "Superlubricity and frictional anisotropy". In: *Wear* 168 (1993), pp. 121–125. DOI: 10.1016/0043-1648(93)90207-3.

[86] M. Hirano et al. "Anisotropy of Frictional Forces in Muscovite Mica". In: *Physical Review Letters* 67 (1991), pp. 2642–2645. DOI: 10.1103/PhysRevLett.67.2642.

[87] M. Z. Baykara, M. R. Vazirisereshk, and A. Martini. "Emerging superlubricity: A review of the state of the art and perspectives on future research". In: *Applied Physics Reviews* 5 (2018), p. 041102. DOI: 10.1063/1.5051445.

[88] Z. Liu et al. "Observation of Microscale Superlubricity in Graphite". In: *Physical Review Letters* 108 (2012), p. 205503. DOI: 10.1103/PhysRevLett.108.205503.

[89] I. Leven et al. "Robust Superlubricity in Graphene/h-BN Heterojunctions". In: *Journal of Physical Chemistry Letters* 4 (2013), pp. 115–120. DOI: 10.1021/jz301758c.

[90] D. Berman et al. "Macroscale superlubricity enabled by graphene nanoscroll formation". In: *Science* 348 (2015), pp. 1118–1122. DOI: 10.1126/science.1262024.

[91] X. Feng et al. "Superlubric Sliding of Graphene Nanoflakes on Graphene". In: *ACS Nano* 7 (2013), pp. 1718–1724. DOI: 10.1021/nn305722d.

[92] S.-W. Liu et al. "Robust microscale superlubricity under high contact pressure enabled by graphene-coated microsphere". In: *Nature Communications* 8 (2017), pp. 1–8. DOI: 10.1038/ncomms14029.

[93] P. Atkins and R. Friedman. *Molecular Quantum Mechanics*. New York, USA: Oxford University Press Inc., 2011.

[94] H. Shull and G. G. Hall. "Atomic Units". In: *Nature* 184 (1959), pp. 1559–1560. DOI: 10.1038/1841559a0.

[95] W. Kohn. "Nobel Lecture: Electronic structure of matter-wave functions and density functionals". In: *Reviews of Modern Physics* 71 (1999), pp. 1253–1266. DOI: 10.1103/RevModPhys.71.1253.

[96] P. Hohenberg and W. Kohn. "Inhomogeneous Electron Gas". In: *Physical Review* 136 (1964), B864–B871. DOI: 10.1103/PhysRev.136.B864.

[97] W. Kohn and L. J. Sham. "Self-Consistent Equations Including Exchange and Correlation Effects". In: *Physical Review* 140 (1965), A1133–A1138. DOI: 10.1103/PhysRev.140.A1133.

[98] M. E. Tuckerman. *Statistical Mechanics: Theory and Molecular Simulation*. UK: Oxford University Press, 2016.

[99] N. Wakabayashi, H. G. Smith, and R. M. Nicklow. "Lattice dynamics of hexagonal MoS_2 studied by neutron scattering". In: *Physical Review B* 12 (1975), pp. 659–663. DOI: 10.1103/PhysRevB.12.659.

[100] J.-W. Jiang. "Parametrization of Stillinger–Weber potential based on valence force field model: application to single-layer MoS_2 and black phosphorus". In: *Nanotechnology* 26 (2015), p. 315706. DOI: 10.1088/0957-4484/26/31/315706.

[101] D. Frenkel and B. Smit. *Understanding Molecular Simulation: From Algorithms to Applications*. San Diego, USA: Academic Press, 2002.

[102] V. Sresht et al. "Quantitative Modeling of MoS_2-Solvent Interfaces: Predicting Contact Angles and Exfoliation Performance using Molecular Dynamics". In: *Journal of Physical Chemistry C* 121 (2017), pp. 9022–9031. DOI: 10.1021/acs.jpcc.7b00484.

[103] F. Paesani et al. "An accurate and simple quantum model for liquid water". In: *Journal of Chemical Physics* 125 (2006), p. 184507. DOI: 10.1063/1.2386157.

[104] G. Levita et al. "Sliding Properties of MoS_2 Layers: Load and Interlayer Orientation Effects". In: *Journal of Physical Chemistry C* 118 (2014), pp. 13809–13816. DOI: 10.1021/jp4098099.

[105] A. Ostadhossein et al. "ReaxFF Reactive Force-Field Study of Molybdenum Disulfide (MoS_2)". In: *Journal of Physical Chemistry Letters* 8 (2017), pp. 631–640. DOI: 10.1021/acs.jpclett.6b02902.

[106] Z. Ding et al. "Interfacial thermal conductance in graphene/MoS_2 heterostructures". In: *Carbon* 96 (2016), pp. 888–896. DOI: 10.1016/j.carbon.2015.10.046.

[107] F. H. Stillinger and T. A. Weber. "Computer simulation of local order in condensed phases of silicon". In: *Physical Review B* 31 (1985), pp. 5262–5271. DOI: 10.1103/PhysRevB.31.5262.

[108] J.-W. Jiang, H. S. Park, and T. Rabczuk. "Molecular Dynamics Simulations of Single-Layer Molybdenum Disulphide (MoS_2): Stillinger-Weber Parametrization, Mechanical Properties, and Thermal Conductivity". In: *Journal of Applied Physics* 114 (2013), p. 064307. DOI: 10.1063/1.4818414.

[109] D. W. Brenner et al. "A second-generation reactive empirical bond order (REBO) potential energy expression for hydrocarbons". In: *Journal of Physics: Condensed Matter* 14 (2002), pp. 783–802. DOI: 10.1088/0953-8984/14/4/312.

[110] A. C. T. van Duin et al. "ReaxFF: A Reactive Force Field for Hydrocarbons". In: *Journal of Physical Chemistry A* 105 (2001), pp. 9396–9409. DOI: 10.1021/jp004368u.

[111] B. Schönfeld, J. J. Huang, and S. C. Moss. "Anisotropic mean-square displacements (MSD) in single-crystals of 2H- and 3R-MoS_2". In: *Acta Crystallographica Section B* B39 (1983), pp. 404–407. DOI: 10.1107/S0108768183002645.

[112] P. Nicolini and T. Polcar. "A comparison of empirical potentials for sliding simulations of MoS_2". In: *Computational Materials Science* 115 (2016), pp. 158–169. DOI: 10.1016/j.commatsci.2016.01.013.

[113] S. Plimpton. "Fast Parallel Algorithms for Short-Range Molecular Dynamics". In: *Journal of Computational Physics* 117 (1995), pp. 1–19. DOI: 10.1006/jcph.1995.1039.

[114] T. Schneider and E. Stoll. "Molecular-dynamics study of a three-dimensional one-component model for distortive phase transitions". In: *Physical Review B* 17 (1978), pp. 1302–1322. DOI: 10.1103/PhysRevB.17.1302.

[115] G. J. Martyna, D. J. Tobias, and M. L. Klein. "Constant pressure molecular dynamics algorithms". In: *Journal of Chemical Physics* 101 (1994), pp. 4177–4189. DOI: 10.1063/1.467468.

[116] M. Parrinello and A. Rahman. "Polymorphic transitions in single crystals: A new molecular dynamics method". In: *Journal of Applied Physics* 52 (1981), pp. 7182–7190. DOI: 10.1063/1.328693.

[117] M. E. Tuckerman et al. "A Liouville-operator derived measure-preserving integrator for molecular dynamics simulations in the isothermal–isobaric ensemble". In: *Journal of Physics A: Mathematical and General* 39 (2006), pp. 5629–5651. DOI: 10.1088/0305-4470/39/19/S18.

[118] W. Shinoda, M. Shiga, and M. Mikami. "Rapid estimation of elastic constants by molecular dynamics simulation under constant stress". In: *Physical Review B* 69 (2004), p. 134103. DOI: 10.1103/PhysRevB.69.134103.

[119] B. Efron and R. J. Tibshirani. *An Introduction to the Bootstrap*. Florida, USA: Chapman & Hall/CRC, 1998.

[120] S. Srinivasan and G. Balasubramanian. "Reduced Thermal Transport in the Graphene/MoS_2/Graphene Heterostructure: A Comparison with Freestanding Monolayers". In: *Langmuir* 34 (2018), pp. 3326–3335. DOI: 10.1021/acs.langmuir.7b03974.

[121] F. Gong et al. "Enhanced Electrochemical and Thermal Transport Properties of Graphene/MoS_2 Heterostructures for Energy Storage: Insights from Multiscale Modeling". In: *ACS Applied Materials and Interfaces* 10 (2018), pp. 14614–14621. DOI: 10.1021/acsami.7b19582.

[122] Y. Ma et al. "Graphene adhesion on MoS_2 monolayer: An *ab initio* study". In: *Nanoscale* 9 (2011), pp. 3883–3887. DOI: 10.1039/C1NR10577A.

[123] Z. Wang, Q. Chen, and J. Wang. "Electronic Structure of Twisted Bilayers of Graphene/MoS_2 and MoS_2/MoS_2". In: *Journal of Physical Chemistry C* 119 (2015), pp. 4752–4758. DOI: 10.1021/jp507751p.

[124] X. Liu et al. "Rotationally Commensurate Growth of MoS_2 on Epitaxial Graphene". In: *ACS Nano* 10 (2016), pp. 1067–1075. DOI: 10.1021/acsnano.5b06398.

[125] Y. Shi et al. "van der Waals Epitaxy of MoS_2 Layers Using Graphene As Growth Templates". In: *Nano Letters* 12 (2012), pp. 2784–2791. DOI: 10.1021/nl204562j.

[126] C.-I Lu et al. "Graphite edge controlled registration of monolayer MoS_2 crystal orientation". In: *Applied Physics Letters* 106 (2015), p. 181904. DOI: 10.1063/1.4919923.

[127] A. D. Novaco and J. P. McTague. "Orientational Epitaxy-the Orientational Ordering of Incommensurate Structures". In: *Physical Review Letters* 38 (1977), pp. 1286–1289. DOI: 10.1103/PhysRevLett.38.1286.

[128] J. P. McTague and A. D. Novaco. "Substrate-induced strain and orientational ordering in adsorbed monolayers". In: *Physical Review B* 19 (1979), pp. 5299–5306. DOI: 10.1103/PhysRevB.19.5299.

[129] J. A. Nelder and R. Mead. "A Simplex Method for Function Minimization". In: *The Computer Journal* 7 (1965), pp. 308–313. DOI: 10.1093/comjnl/7.4.308.

[130] T. E. Oliphant. *SciPy: Open source scientific tools for Python*. 2007. DOI: 10.1109/MCSE.2007.58. URL: http://www.scipy.org/.

[131] A. Silva et al. "Exploring the Stability of Twisted van der Waals Heterostructures". In: *ACS Applied Materials and Interfaces* 12 (2020), pp. 45214–45221. DOI: 10.1021/acsami.0c13971.

[132] G. J. Dudder et al. "Environmental Effects on the Tribology and Microstructure of MoS_2-Sb_2O_3-C Films". In: *Tribology Letters* 42 (2011), pp. 203–213. DOI: 10.1007/s11249-011-9764-z.

[133] H. S. Khare and D. L. Burris. "Surface and Subsurface Contributions of Oxidation and Moisture to Room Temperature Friction of Molybdenum Disulfide". In: *Tribology Letters* 53 (2014), pp. 329–336. DOI: 10.1007/s11249-013-0273-0.

[134] J. F. Curry et al. "Impact of Microstructure on MoS_2 Oxidation and Friction". In: *ACS Applied Materials and Interfaces* 9 (2017), pp. 28019–28026. DOI: 10.1021/acsami.7b06917.

[135] M. Tagawa et al. "Space environmental effects on MoS_2 and diamond-like carbon lubricating films: Atomic oxygen-induced erosion and its effects on tribological properties". In: *Surface & Coatings Technology* 202 (2007), pp. 1003–1010. DOI: 10.1016/j.surfcoat.2007.07.069.

[136] P. Bampoulis et al. "Hydrophobic Ice Confined between Graphene and MoS". In: *Journal of Physical Chemistry C* 120 (2016), pp. 27079–27084. DOI: 10.1021/acs.jpcc.6b09812.

[137] Y. Jung et al. "Metal Seed Layer Thickness-Induced Transistion From Vertical to Horizontal Growth of MoS_2 and WS_2". In: *Nano Letters* 14 (2014), pp. 6842–6849. DOI: 10.1021/nl502570f.

[138] C. Stern et al. "Growth Mechanisms and Electronic Properties of Vertically Aligned MoS_2". In: *Scientific Reports* 8 (2018), p. 16480. DOI: 10.1038/s41598-018-34222-z.

[139] H. Li et al. "Synthesis and characterization of vertically standing MoS_2 nanosheets". In: *Scientific Reports* 6 (2016), p. 21171. DOI: 10.1038/srep21171.

[140] D. Kong et al. "Synthesis of MoS_2 and $MoSe_2$ Films with Vertically Aligned Layers". In: *Nano Letters* 13 (2013), pp. 1341–1347. DOI: 10.1021/nl400258t.

[141] K. Chenoweth, A. C. T. van Duin, and W. A. Goddard. "ReaxFF Reactive Force Field for Molecular Dynamics Simulations of Hydrocarbon Oxidation". In: *Journal of Physical Chemistry A* 112 (2008), pp. 1040–1053. DOI: 10.1021/jp709896w.

[142] J. Zemann. "Crystal structures, 2nd edition. Vol. 1 by R. W. G. Wyckoff". In: *Acta Crystallographica* 18.1 (1965), pp. 139–139. DOI: 10.1107/S0365110X65000361.

[143] R. T. Downs and M. Hall-Wallace. "The American Mineralogist crystal structure database". In: *American Mineralogist* 88.1 (2003), pp. 247–250.

[144] G. Bergerhoff and I. D. Brown. "Crystallographic Databases". In: *International Union of Crystallography* (1987).

[145] F. Belviso et al. "Viewpoint: Atomic-Scale Design Protocols toward Energy, Electronic, Catalysis, and Sensing Applications". In: *Inorganic Chemistry* 58.22 (2019), pp. 14939–14980. DOI: acs.inorgchem.9b01785.

A

SI. Pure MoS_2

Supporting Information of

"Superlubricity achieved for commensurate sliding: MoS_2 frictional anistropy *in silico*

Victor E. P. Claerbout
Department of Control Engineering, Faculty of Electrical Engineering, Czech Technical University, Karlovo náměstí 13, 121 35, Prague 2, Czech Republic. E-mail: claervic@fel.cvut.cz

Tomas Polcar
Department of Control Engineering, Faculty of Electrical Engineering, Czech Technical University, Karlovo náměstí 13, 121 35, Prague 2, Czech Republic
National Centre for Advanced Tribology (nCATS), University of Southampton, Highfield Campus (7/4083), SO17 1BJ Southampton, United Kingdom

Paolo Nicolini
Department of Control Engineering, Faculty of Electrical Engineering, Czech Technical University, Karlovo náměstí 13, 121 35, Prague 2, Czech Republic. E-mail: nicolpao@fel.cvut.cz

The Bootstrap method

The Bootstrap method is a random sampling approach with replacement. Given a certain reference data set, one randomly selects data points from the reference data set (allowing the multiple selection of a data point) until an equal number of data points as present in the reference set is collected. In our case, the reference set was the instantaneous force. Next, the average of the randomly sampled set is calculated and this process is repeated 2000 times. Finally, one calculates the average and the standard deviation of the averages found for every set. In the present study, we calculated five bootstrap averages per sliding conditions, due to the fact that we simulated five independent trajectories. We then considered these as independent values and we calculated the final average and standard deviation.

Selected sliding MD trajectories

Projections of MD trajectories in the *xy*-plane of the S2' COM superimposed on the static potential energy surface at zero load, given per unit MoS_2, for all sliding angles.

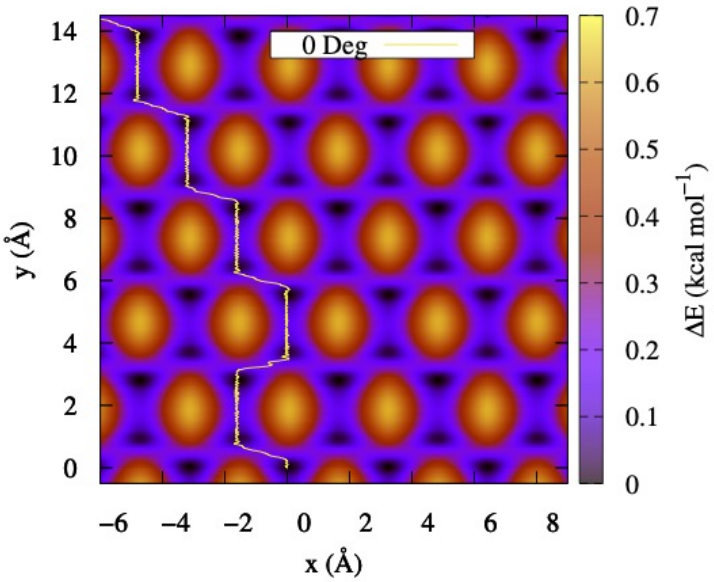

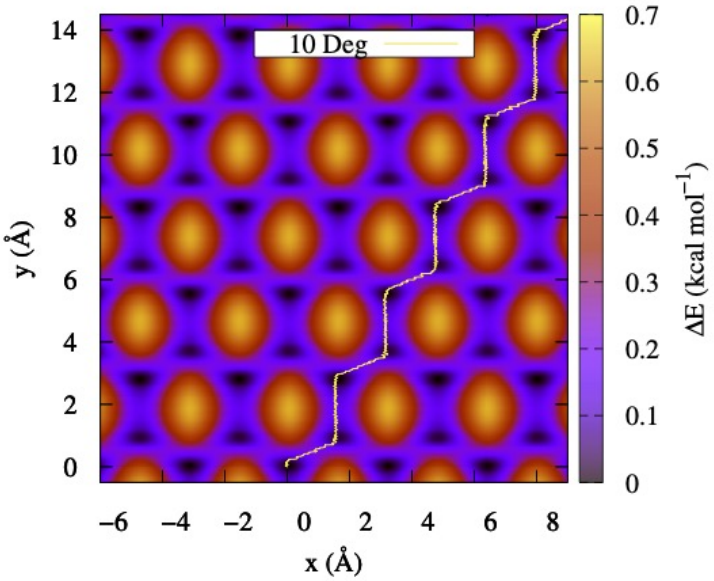
10 Deg
y (Å)
x (Å)
ΔE (kcal mol^{-1})
14
12
10
8
6
4
2
0
−6
−4
−2
0
2
4
6
8
0.7
0.6
0.5
0.4
0.3
0.2
0.1
0

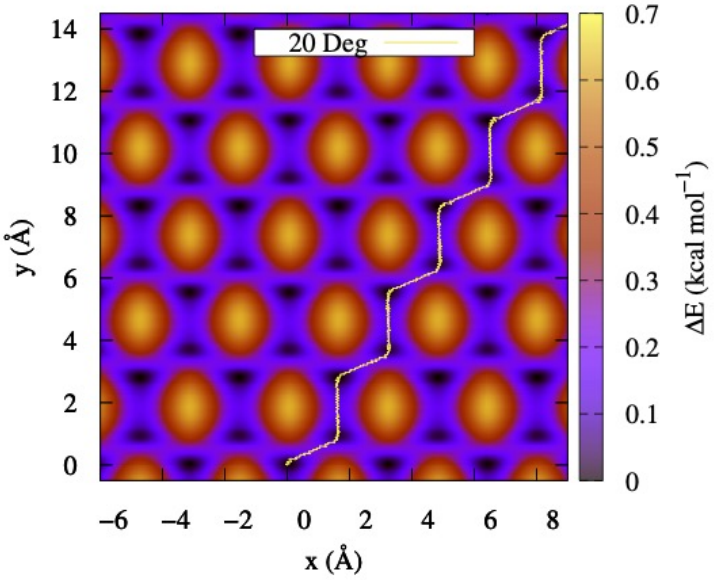
20 Deg
y (Å)
x (Å)
ΔE (kcal mol^{-1})
14
12
10
8
6
4
2
0
−6
−4
−2
0
2
4
6
8
0.7
0.6
0.5
0.4
0.3
0.2
0.1
0

3

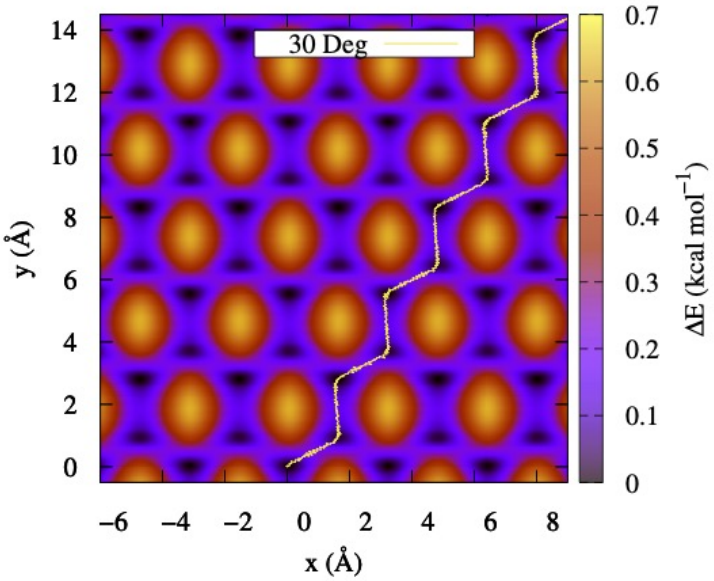
30 Deg
y (Å)
x (Å)
ΔE (kcal mol^{-1})
14
12
10
8
6
4
2
0
−6
−4
−2
0
2
4
6
8
0.7
0.6
0.5
0.4
0.3
0.2
0.1
0

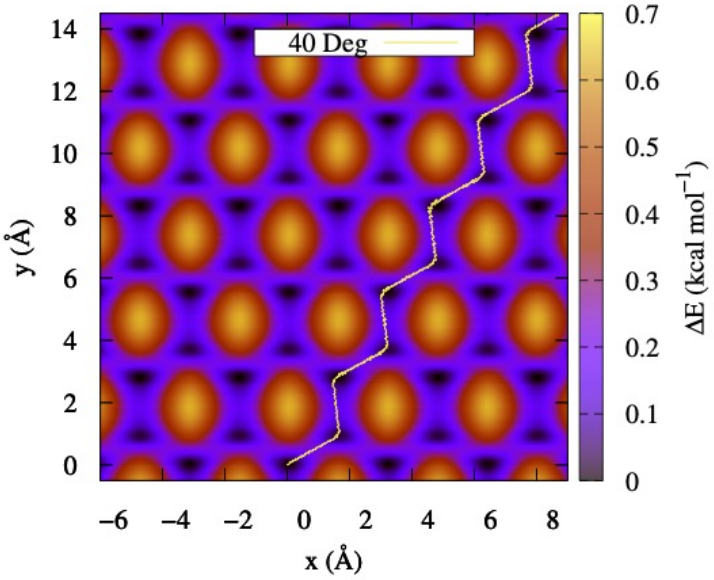
40 Deg
y (Å)
x (Å)
ΔE (kcal mol^{-1})
14
12
10
8
6
4
2
0
−6
−4
−2
0
2
4
6
8
0.7
0.6
0.5
0.4
0.3
0.2
0.1
0

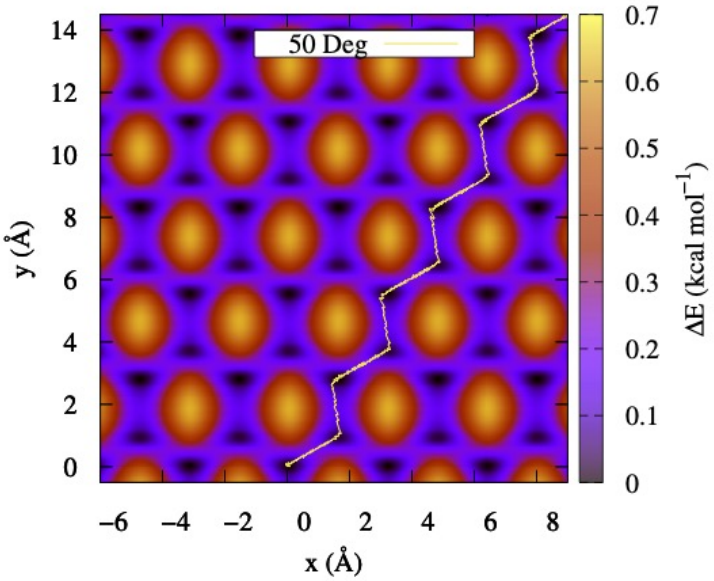
50 Deg
y (Å)
x (Å)
ΔE (kcal mol^{-1})
14
12
10
8
6
4
2
0
−6
−4
−2
0
2
4
6
8
0.7
0.6
0.5
0.4
0.3
0.2
0.1
0

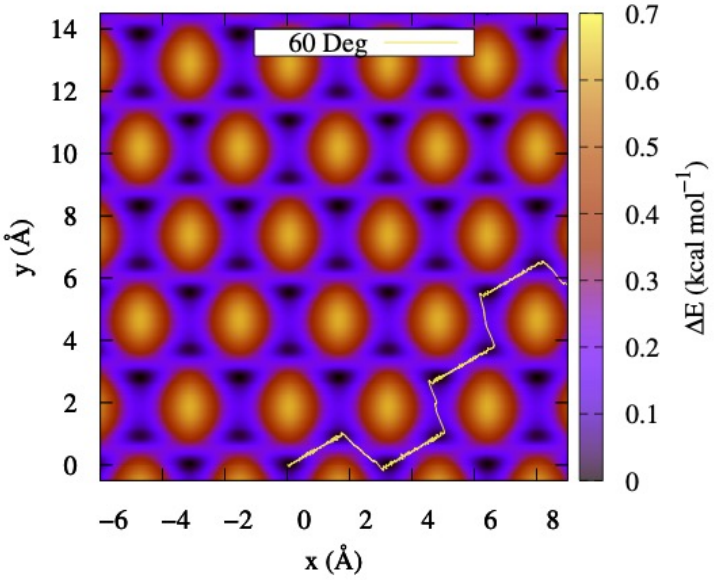
60 Deg
y (Å)
x (Å)
ΔE (kcal mol^{-1})
14
12
10
8
6
4
2
0
−6
−4
−2
0
2
4
6
8
0.7
0.6
0.5
0.4
0.3
0.2
0.1
0

B

SI. MoS_2 & Graphene

Supporting Information for Exploring the Stability of Twisted van der Waals Heterostructures

Andrea Silva,[*,†,‡] Victor E.P. Claerbout,[*,¶] Tomas Polcar,[†,¶] Denis Kramer,[†,§] and Paolo Nicolini[¶]

†*Engineering Materials, University of Southampton, Southampton SO17 1BJ, U.K.*

‡*national Centre for Advanced Tribology Study at University of Southampton, Southampton SO17 1BJ, U.K*

¶*Department of Control Engineering, Faculty of Electrical Engineering, Czech Technical University in Prague, Technicka 2, Prague 6, 16627, Czech Republic*

§*Mechanical Engineering, Helmut Schmidt University, Hamburg, Germany*

E-mail: a.silva@soton.ac.uk; claervic@fel.cvut.cz

In the following, we present in more details the methods and technical details used in this work. In the first section, we describe the protocol used to obtain the supercells of the heterostructures. We also provide a table with the parameters of all structures used in this study. In the second section, we explain the protocol used to refine the force field parameters, including the updated parameters. In the third section, we prove that the enhancement of the LJ parameters does not alter the actual physics of the problem. In the fourth section, we discuss the phonon dispersion and how we extracted from it the quantities required as input for the NM approximation. In the fifth section, we further investigate the limits of the NM theory by modelling a constrained system midway between pure NM assumptions and a fully free bilayer. Finally, in the sixth section, we present a benchmark of the force fields used.

1 Supercells for twisted lattices

Here, we explain the procedure used to obtain the twisted lattice supercells. Let l_a and l_b be the spacing of the Bravais lattices of layer a and layer b, respectively and $\hat{\mathbf{a}}_1 = \left(\begin{smallmatrix}1\\0\end{smallmatrix}\right)$ be one of the primitive versors of the first lattice, aligned with the x axis; the lattice with the desired periodicity is generated by a primitive vector, $\mathbf{a}_1 = l_\mathrm{a}\hat{\mathbf{a}}_1$. The matrix representing the discrete rotational symmetry of the lattice by an angle $\Omega = \pi/3$ is:

$$\underline{\underline{R}}_\Omega = \begin{pmatrix} \cos\pi/3 & -\sin\pi/3 \\ \sin\pi/3 & \cos\pi/3 \end{pmatrix} = \begin{pmatrix} 1/2 & -\sqrt{3}/3 \\ \sqrt{3}/3 & 1/2 \end{pmatrix} \tag{S.1}$$

thus, the second versor defining the lattice is $\hat{\mathbf{a}}_2 = \underline{\underline{R}}_\Omega \hat{\mathbf{a}}_1$. Since the second lattice, b, has the same symmetry but it is rotated with respect to the first one by an angle θ, versors defining it are $(\hat{\mathbf{b}}_1, \hat{\mathbf{b}}_2) = (\underline{\underline{R}}_\theta \hat{\mathbf{a}}_1,\ \underline{\underline{R}}_\Omega \underline{\underline{R}}_\theta \hat{\mathbf{a}}_1)$, where

$$\underline{\underline{R}}_\theta = \begin{pmatrix} \cos\theta & -\sin\theta \\ \sin\theta & \cos\theta \end{pmatrix} \tag{S.2}$$

describes the misalignment between the lattices. A heterostructure supercell will be compatible with both periodicities if the individual lattice cells match exactly at the edges, in other words, if the following matching condition is satisfied

$$l_\mathrm{a}(n_1\hat{\mathbf{a}}_1 + n_2\hat{\mathbf{a}}_2) = l_\mathrm{b}(m_1\hat{\mathbf{b}}_1 + m_2\hat{\mathbf{b}}_2), \tag{S.3}$$

where n_1, n_2, m_1, m_2 represent the repetition along the corresponding versor of the unit cell of the first and second lattice, respectively. An overview of the matching condition is given in Figure S1. This condition can be rewritten with a matrix formalism to:

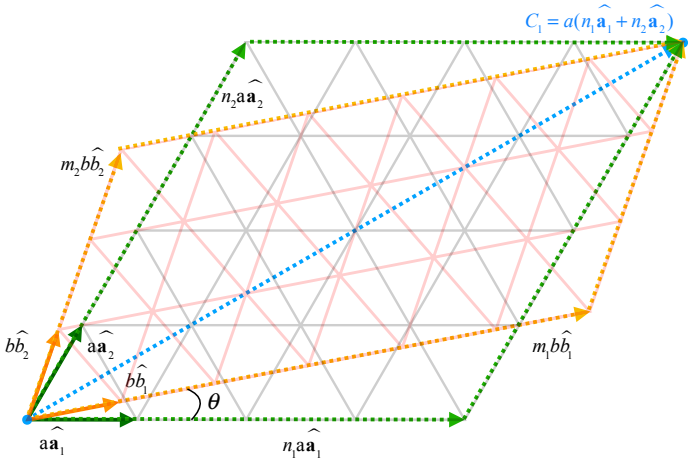

Figure S1: Graphical overview of the matching condition in Eq. (S.3) for unit cells with different lattice constants a and b at imposed angles θ. Colored arrows refer to primitive, repeated and supercell lattices, as indicated by the labels. The low-opacity lines connect the points of the Bravais lattice described by the primitive vectors.

$$\frac{l_\mathrm{a}}{l_\mathrm{b}}(n_1\hat{\mathbf{a}}_1 + n_2\underline{\underline{R}}_\Omega \cdot \hat{\mathbf{a}}_1) = m_1\underline{\underline{R}}_\theta \cdot \hat{\mathbf{a}}_1 + m_2\underline{\underline{R}}_\Omega \cdot \underline{\underline{R}}_\theta \cdot \hat{\mathbf{a}}_1$$

$$\rho \begin{pmatrix} \mathbb{I} & \underline{\underline{R}}_\Omega \end{pmatrix} \cdot \begin{pmatrix} n_1 \\ n_2 \end{pmatrix} = \begin{pmatrix} \mathbb{I} & \underline{\underline{R}}_\Omega \end{pmatrix} \cdot \begin{pmatrix} m_1 \\ m_2 \end{pmatrix} \cdot \underline{\underline{R}}_\theta \tag{S.4}$$

where $\mathbb{I}$ is the identity matrix, we used the definition of the lattice vectors, introduced the mismatch ratio $\rho = l_\mathrm{a}/l_\mathrm{b}$, grouped the matrices and the indexes in vectors and simplified $\hat{\mathbf{a}}_1$ from both sides.

Although the mismatch ratio of a system is fixed by the equilibrium values of the lattice parameters, it would be impractical to approximate a real number using integers, as the size of the supercells would easily exceed our computational capabilities. Instead, we follow instead the inverse procedure: given the four indexes $\{m_i, n_i\}_{i=1,2}$, we can invert the system and find the mismatch ratio ρ and the misalignment angle θ that satisfy the matching condition of Eq. (S.3). This means that $\{m_i, n_i\}_{i=1,2}$ are now fixed parameters of Eq. (S.3), while ρ is a variable, along with θ. Next, we find an expression for ρ and θ in terms of $\{m_i, n_i\}_{i=1,2}$ that satisfies Eq. (S.3). In the following paragraph, we address the problem of selecting sets of indices, whose corresponding ρ is close enough the real value fixed by the system ρ_0. We solve the equation Eq. (S.4) for the matrix $\underline{\underline{R}}_\theta$ and for ρ under the constraint that $\underline{\underline{R}}_\theta$ is a rotation matrix, namely:

$$\begin{cases} \underline{\underline{R}}_\theta = \rho \left(m_1\mathbb{I} + m_2\underline{\underline{R}}_\Omega \right)^{-1} \begin{pmatrix} \mathbb{I} & \underline{\underline{R}}_\Omega \end{pmatrix} \cdot \begin{pmatrix} n_1 \\ n_2 \end{pmatrix} \\ \det \underline{\underline{R}}_\theta = 1. \end{cases} \tag{S.5}$$

The first line in Eq. (S.5) is readily solved by

$$\begin{aligned}\underline{\underline{R}}_\theta &= \frac{\rho}{N_\mathrm{b}}\begin{pmatrix} m_1n_1 + m_2n_2 + 1/2(m_1n_2 + m_2n_1) & -\sqrt{3}/2(m_1n_2 - m_2n_1) \\ \sqrt{3}/2(m_1n_2 - m_2n_1) & m_1n_1 + m_2n_2 + 1/2(m_1n_2 + m_2n_1)\end{pmatrix} \\ &= \frac{\rho}{N_\mathrm{b}}\underline{\underline{A}}, \end{aligned} \tag{S.6}$$

where $N_\mathrm{b} = m_1^2 + m_2^2 + m_1m_2$ is the number of Bravais lattice points in the b lattice[1] and $\underline{\underline{A}}$, implicitly defined in the last step, is shorthand for the matrix of known coefficients. Substituting Eq. (S.6) into the second line of Eq. (S.5) yields an expression for ρ: $\det \underline{\underline{R}}_\theta = \frac{\rho^2}{N_\mathrm{b}^2}\det \underline{\underline{A}} = 1$. Substituting this back into Eq. (S.6) gives us the solution of (ρ, θ) of Eq. (S.3) at chosen $\{m_i, n_i\}_{i=1,2}$:

$$\begin{cases} \rho &= \frac{N_\mathrm{b}}{\sqrt{\det \underline{\underline{A}}}} \\ \theta &= (\underline{\underline{R}}_\theta)_{11} = \arccos\left(\frac{1}{\sqrt{\det \underline{\underline{A}}}}A_{11}\right) \end{cases} \tag{S.7}$$

Finally, the first vector of the supercell is given by one of the members of the equality in Eq. (S.3) and the second is obtained by symmetry, i.e.,

$$\mathbf{C_1} = l_\mathrm{a}(n_1\hat{\mathbf{a}}_1 + n_2\hat{\mathbf{a}}_2) \tag{S.8}$$

$$\mathbf{C_2} = \underline{\underline{R}}_\Omega \cdot \mathbf{C_1} = -l_\mathrm{a}n_1\hat{\mathbf{a}}_1 + l_\mathrm{a}(n_1 + n_2)\hat{\mathbf{a}}_2. \tag{S.9}$$

In order to obtain a system with the desired misalignment θ, and a ρ that is an acceptable approximation of the equilibrium mismatch ρ_0, we consider all combinations of integers $n_i,\ m_i$ within the range $(-200, 200)$ and select the supercells which satisfy $\theta \in [0°, 60°]$ and $|\Delta\rho| = |\rho - \rho_0| \leq 1 \times 10^{-7}$. We then bin the resulting supercells with a spacing of $\Delta\theta = 0.01°$ and select the cell with the fewest Bravais points within each bin. Note that this procedure does not guarantee that the resulting supercells will be evenly spaced with respect to the

[1] An equivalent relation holds for the other lattice $N_\mathrm{a} = n_1^2 + n_2^2 + n_1n_2$

mismatch angle.

The indices defining the supercells used in this work for the MoS_2/G heterostructures are reported in Table S1, along with the misalignment angle, $\rho - \rho_0$, and the number of atoms in each layer. For this system, $\rho_0 = l_G/l_{MoS_2} = 2.460\,187\,8\,\text{Å}/3.093\,682\,7\,\text{Å} = 0.7952295$, and the number of atoms in each lattice is given by the number of Bravais lattice points multiplied by the number of atoms in the crystal basis, i.e. $N_{tot} = N_{Bravais} \cdot n_{basis}$ with n_{basis} is equal to 2 and 3 for G and MoS_2, respectively. In creating the supercell, the strain ϵ due to the approximated mismatch ρ is applied to MoS_2. The residual strains for different values of the tolerance $\Delta\rho = \rho - \rho_0$ are reported in Figure S2.

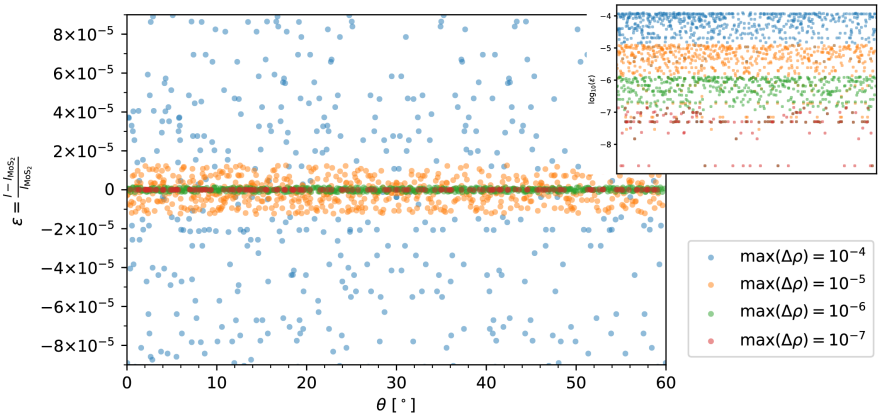

Figure S2: Strain applied to the MoS_2 lattice versus angle imposed to the supercell according to Eq. (S.7) for different values of tolerance. The tolerance value used in the work is $\Delta\rho \leq 1 \times 10^{-7}$. The lattice spacing is obtained as $l = l_G/\rho$, where ρ is the solution of the Eq. (S.7). The inset in the upper right corner reports the logarithm of the absolute value of the strain ϵ .

$\theta[°]$	n_1	n_2	m_1	m_2	$\rho - \rho_0$	N_G	N_{MoS_2}
0.23	**-135**	**-104**	**-108**	**-82**	**9.8e-08**	**86162**	**81732**
0.58	-192	61	-153	50	8.1e-08	57744	54774
0.79	-184	-41	-148	-30	9.8e-08	86162	81732
1.01	-113	-182	-86	-148	-6.2e-08	132916	126081

1.24	-176	-59	-137	-51	4.3e-09	89682	85071
1.39	-109	39	-87	33	-5.7e-08	18300	17361
1.60	-141	-128	-107	-107	2.6e-08	108626	103038
2.11	-138	-99	-104	-85	-2.2e-08	85012	80640
2.88	-184	-41	-140	-42	9.8e-08	86162	81732
3.05	-118	12	-96	15	9e-08	25302	24000
3.21	-182	-113	-134	-102	-6.2e-08	132916	126081
4.17	-184	33	-142	15	8.1e-08	57744	54774
4.93	-191	-48	-140	-55	3.5e-08	95904	90972
5.30	-192	61	-155	62	8.1e-08	57744	54774
5.34	-185	63	-149	63	4.6e-08	53076	50349
5.95	-164	-41	-118	-50	1.5e-08	70600	66969
6.23	-164	-115	-110	-113	6.2e-08	117960	111894
6.64	-123	-185	-71	-169	-8.8e-08	144216	136800
6.75	-164	-145	-154	-89	4.4e-08	143402	136029
7.18	-152	-99	-140	-55	3.5e-08	95906	90972
7.94	-172	169	-146	122	-8.3e-08	58152	55164
8.14	-118	12	-99	24	9e-08	25302	24000
8.42	-163	-125	-156	-68	-9.6e-08	125136	118704
8.64	-145	145	-104	124	1.2e-08	42048	39885
8.75	-138	-99	-85	-104	-2.2e-08	85012	80640
9.01	-184	33	-153	50	8.1e-08	57744	54774
9.04	-176	-59	-117	-76	4.3e-09	89682	85071
9.69	-172	169	-122	146	-8.3e-08	58152	55161
9.75	**-181**	**-95**	**-113**	**-110**	**6.2e-08**	**117960**	**111894**
10.25	-169	-174	-90	-178	7e-08	176484	167409
10.64	-181	-95	-110	-113	6.2e-08	117960	111894

10.81	-164	-145	-89	-154	4.4e-08	143402	136029
11.22	-174	-169	-90	-178	7e-08	176484	167409
11.37	-170	71	-130	31	-4.5e-08	43740	41493
12.17	-113	-182	-134	-102	-6.2e-08	132916	126081
12.27	-185	63	-138	19	4.6e-08	53076	50349
12.60	-192	61	-142	15	8.1e-08	57744	54774
12.99	-135	-104	-140	-42	9.8e-08	86162	81732
13.65	-118	12	-81	-15	9e-08	25302	24000
13.73	-184	33	-155	62	8.1e-08	57744	54774
14.52	-144	-98	-150	-31	1.7e-10	88904	84333
15.20	-184	33	-127	-15	8.1e-08	57744	54774
15.53	-185	63	-149	86	4.6e-08	53076	50349
15.63	-184	-41	-108	-82	9.8e-08	86162	81732
16.39	-182	-113	-86	-148	-6.2e-08	132916	126081
16.66	-135	-104	-148	-30	9.8e-08	86162	81732
17.14	-163	-125	-68	-156	-9.6e-08	125136	118704
17.26	-109	39	-87	54	-5.7e-08	18300	17358
18.47	-192	61	-155	93	8.1e-08	57744	54774
18.74	-118	12	-75	-24	9e-08	25302	24000
18.91	-41	-184	30	-178	9.8e-08	86162	81729
19.89	**-185**	**-123**	**-71**	**-169**	**-8.8e-08**	**144216**	**136800**
20.15	-184	-23	-101	-79	-7.1e-08	77232	73263
20.95	-187	-101	-75	-153	-5.7e-08	128114	121527
21.08	-152	-99	-55	-140	3.5e-08	95906	90972
21.47	-182	-23	-173	48	-8.3e-08	75678	71784
21.55	-135	-104	-42	-140	9.8e-08	86162	81732
22.24	-170	71	-130	99	-4.5e-08	43740	41493

22.58	-184	-41	-182	42	9.8e-08	86162	81732
23.03	-176	-59	-76	-117	4.3e-09	89682	85071
23.20	-192	61	-153	103	8.1e-08	57744	54774
23.63	-192	61	-127	-15	8.1e-08	57744	54774
24.25	-148	-132	-185	-15	-4.9e-08	117728	111675
24.67	-184	-41	-82	-108	9.8e-08	86162	81732
25.00	-113	-182	-174	-52	-6.2e-08	132916	126081
25.23	-135	-104	-30	-148	9.8e-08	86162	81732
26.82	-191	-48	-195	55	3.5e-08	95904	90972
26.86	-185	63	-119	-19	4.6e-08	53076	50349
27.05	-144	-98	-31	-150	1.7e-10	88904	84333
27.74	-164	-41	-168	50	1.5e-08	70600	66969
28.03	-148	-132	-15	-185	-4.9e-08	117728	111675
28.22	-184	-23	-79	-101	-7.1e-08	77232	73263
28.37	-184	33	-103	-50	8.1e-08	57744	54774
29.17	**-176**	**-59**	**-188**	**51**	**4.3e-09**	**89682**	**85071**
30.83	-176	-59	-51	-137	4.3e-09	89682	85071
31.63	-184	33	-153	103	8.1e-08	57744	54774
31.78	-23	-184	79	-180	-7.1e-08	77232	73260
31.97	-148	-132	-200	15	-4.9e-08	117728	111675
32.26	-164	-41	-50	-118	1.5e-08	70600	66969
32.95	-144	-98	-181	31	1.7e-10	88904	84333
33.14	-185	63	-138	119	4.6e-08	53076	50349
34.77	-104	-135	30	-178	9.8e-08	86162	81729
35.33	-41	-184	82	-190	9.8e-08	86162	81729
35.75	-148	-132	15	-200	-4.9e-08	117728	111675
36.37	-192	61	-142	127	8.1e-08	57744	54774

36.80	-192	61	-103	-50	8.1e-08	57744	54774
36.97	-59	-176	76	-193	4.3e-09	89682	85068
37.42	-184	-41	-42	-140	9.8e-08	86162	81732
37.76	-170	71	-99	-31	-4.5e-08	43740	41493
38.45	-135	-104	-182	42	9.8e-08	86162	81732
38.53	-23	-182	-125	-48	-8.3e-08	75678	71784
38.92	-152	-99	-195	55	3.5e-08	95906	90972
39.85	-23	-184	101	-180	-7.1e-08	77232	73260
41.09	-184	-41	-30	-148	9.8e-08	86162	81732
41.26	-118	12	-99	75	9e-08	25302	24000
41.53	-192	61	-93	-62	8.1e-08	57744	54774
42.74	-109	39	-54	-33	-5.7e-08	18300	17361
43.34	-135	-104	30	-178	9.8e-08	86162	81729
44.37	-41	-184	108	-190	9.8e-08	86162	81729
44.47	-185	63	-86	-63	4.6e-08	53076	50349
44.80	-184	33	-142	127	8.1e-08	57744	54774
45.48	-144	-98	31	-181	1.7e-10	88904	84333
46.27	-184	33	-62	-93	8.1e-08	57744	54774
46.35	-118	12	-96	81	9e-08	25302	24000
47.01	-135	-104	42	-182	9.8e-08	86162	81732
47.40	-192	61	-127	142	8.1e-08	57744	54774
47.73	-185	63	-119	138	4.6e-08	53076	50349
48.63	-170	71	-99	130	-4.5e-08	43740	41493
50.31	-172	169	-146	24	-8.3e-08	58152	55164
50.99	-184	33	-50	-103	8.1e-08	57744	54774
51.20	-104	-135	82	-190	9.8e-08	86162	81729
51.25	-138	-99	-189	85	-2.2e-08	85012	80640

51.36	-145	145	-124	20	1.2e-08	42048	39885
51.86	-118	12	-24	-75	9e-08	25302	24000
52.06	-172	169	-24	146	-8.3e-08	58152	55161
52.82	-152	-99	55	-195	3.5e-08	95906	90972
54.05	-164	-41	-168	118	1.5e-08	70600	66969
54.66	-185	63	-63	-86	4.6e-08	53076	50349
55.07	-191	-48	-195	140	3.5e-08	95904	90972
55.83	-184	33	-127	142	8.1e-08	57744	54774
56.95	-118	12	-15	-81	9e-08	25302	24000
57.12	-184	-41	-182	140	9.8e-08	86162	81732
57.89	-138	-99	-189	104	-2.2e-08	85012	80640
58.61	-109	39	-33	-54	-5.7e-08	18300	17358
58.76	-176	-59	-188	137	4.3e-09	89682	85071
59.21	-184	-41	30	-178	9.8e-08	86162	81729
59.42	-192	61	-50	-103	8.1e-08	57744	54774
59.77	-135	-104	82	-190	9.8e-08	86162	81729

Table S1: Parameters of the rotated supercells used in this work. The lines relative to the four misaligned geometries shown in Figure 5 in the main text are highlighted in bold font.

2 Force Field refinement

As part of this study, we refined the LJ coupling parameters for the heterostructure of MoS_2 and G. As a starting point, we took the parameters provided in Ref.[1] However, our preliminary results revealed some significant discrepancies, both quantitatively as well as qualitatively, with the results obtained via accurate DFT calculations. This motivated us to perform a recalibration of the parameters.

In order to do so, we applied the Simplex algorithm[2] as implemented in SciPy.[3] This

algorithm samples the N-dimensional (N=number of LJ parameters) phase space using a convex polygon. This algorithm acts on the following objective function:

$$\chi^2[f_{\mathrm{L}}] = \frac{1}{W}\int_0^{\infty} |f_{\mathrm{DFT}}(r) - f_L(r)|^2 w(r)\mathrm{d}r \tag{S.10}$$

$$\approx \frac{1}{W}\sum_{r_i}^{r_{\mathrm{cut}}} |f_{\mathrm{DFT}}(r_i) - f_L(r_i)|^2 w(r_i), \tag{S.11}$$

where $r_{\mathrm{cut}} = 14.5\,\text{Å}$, beyond the LJ potential cutoff in LAMMPS and enough to consider negligible the LJ interactions in VASP. The function f_{DFT} is the reference, in our case the Lennard-Jones binding energy profile from DFT, whereas f_{L} is the same binding energy profile computed with LAMMPS using the current ϵ and σ. We used the weight function $w(r) = \exp[-(\frac{r-r_0}{\zeta})^2]$ to ensure that the most relevant part, the minimum of the Lennard-Jones at $r_0 = 4.94\,\text{Å}$ and its directs surroundings, are represented correctly. The amplitude of the relevant interval around the minimum is tuned with the ζ parameter. Both the reference energy profile and the one from LAMMPS are obtained by fixing the interlayer distance between G and MoS_2. In our case we fixed the carbon atoms and the outermost sulfur atoms in the z direction. The heterostructure itself results from a 4x4 MoS_2 unit cell repetition and a 5x5 G unit cell repetition, in which the residual strain of 2.6% is applied to MoS_2. The results of this optimization can be found in Table S2 and Figure S3.

Table S2: Optimized LJ parameters for the interlayer interaction between G and MoS_2.

Optimized LJ Parameters			
Atoms	ϵ [meV]	σ [Å]	ζ [Å]
C-S	1.64	3.640	0.30
C-Mo	4.55	4.391	0.30

3 LJ enhancement

The LJ-coupling between the layers of MoS_2 and G was enhanced during the constraint simulations as mentioned in the main text. This was done because the strain posed on the

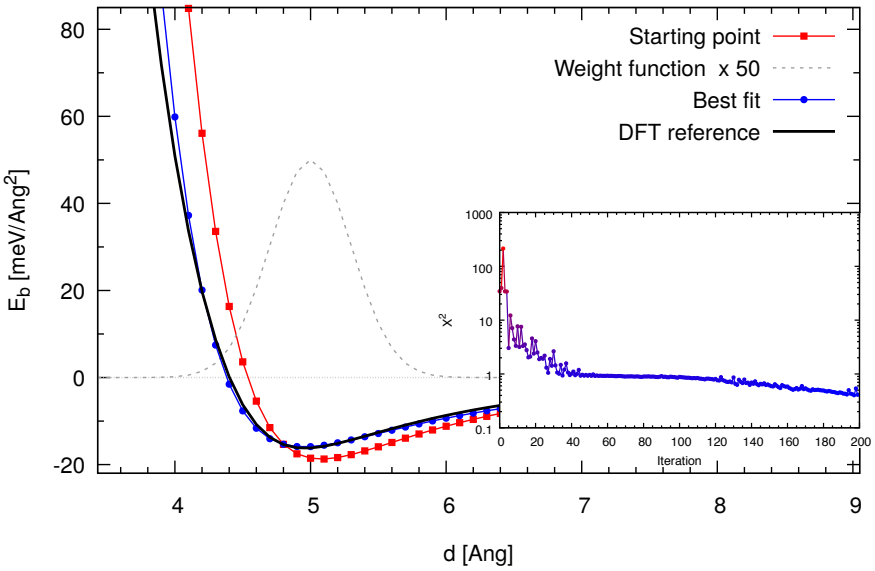

Figure S3: Refining of LJ-parameters. Binding energies (normalized by the cell area) versus the interlayer distance in $\mathring{A}$. The black line is the reference binding energy obtained through DFT, whereas the red and the blue line are the starting and final binding energies obtained through LAMMPS, respectively. The dashed line represents the weight function around the energy minimum enhanced by a factor of 50, as guide for the eye. The inset shows the objective function χ^2 versus the number of the iterations of the optimization algorithm.

MoS_2 lattice, in order to create a supercell suitable for the application of PBC, results in a noise significantly affecting the energy profile upon rotating the lattices. In Figure S4, we report the underlying energy profile $E(\theta)$ for different values of the scaling factor f in $\epsilon' = f\epsilon$. From Figure S4, it can be seen that this computational trick does not alter the physics, but purely amplifies the energy trends that otherwise get progressively hidden by the noise. Figure S5 reports the scaling relation at $\theta = 30°$, showing an almost quadratic behaviour. In order to make comparison between Fig. 1 and Fig. 2 in the main text easier, we scaled back the value computed at $\epsilon'_{LJ} = 100\epsilon_{LJ}$ according to $E^{100}(30°)/E^{1}(30°) = 1751.57$. In other words, both the minima and maxima remain located at the same angle, however, their absolute energy value is scaled according to the LJ-coupling.

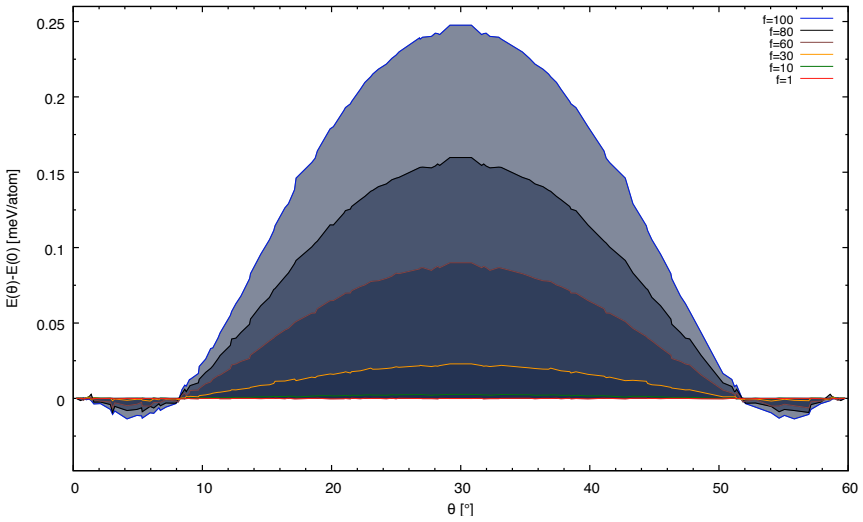

Figure S4: Enhancement of the LJ-coupling. The plot reports the energy $E(\theta)$ in meV/atom versus angle θ for rigid MoS_2 and soft G for increasing values of LJ coupling f, as reported in the legend.

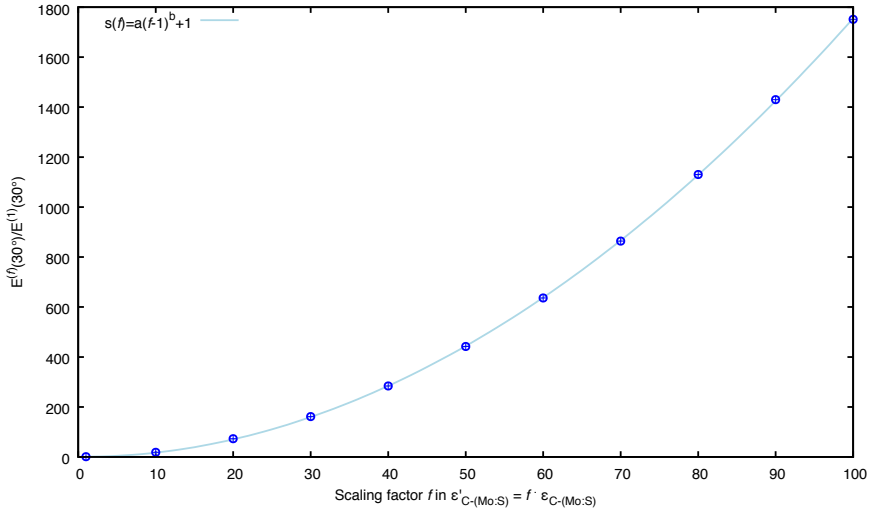

Figure S5: Scaling relation between the maximum energy ratio and the LJ coupling parameter ϵ. Blue circles represent the energy at $\theta = 30°$ computed at a given enhancement factor f, with respect to $f = 1$, versus the scaling factor f. The light-blue line shows the fitted power law reported in the legend with parameters $a = 0.217837$ and $b = 1.9572$.

4 Phonon dispersion and sound velocity

Figure S6 reports the phonon band structure along the path $\Gamma \to M \to K \to \Gamma$ of G and MoS_2, panels (a) and (b) respectively. These figures allow us to compare phonon dispersion computed from quantum forces, at the DFT level, and from classical forces. We focus on the acoustic modes first. Quantum and classical dispersion are in good agreement around Γ, the center of the Brillouin zone; this means that the long wavelength distortions at the base of NM theory are well-described by the classical force fields. As we move to the edge of the cell, towards shorter distortions, the two dispersions start to deviate. For example, the splitting of quantum-computed transverse and longitudinal branches observed at M point in G is shifted to a different k in the classical results. Similar observations can be made for the region around K and for the MoS_2 phonon bands. The general trend is that the classical treatment underestimates the energy of acoustic branches and overestimates

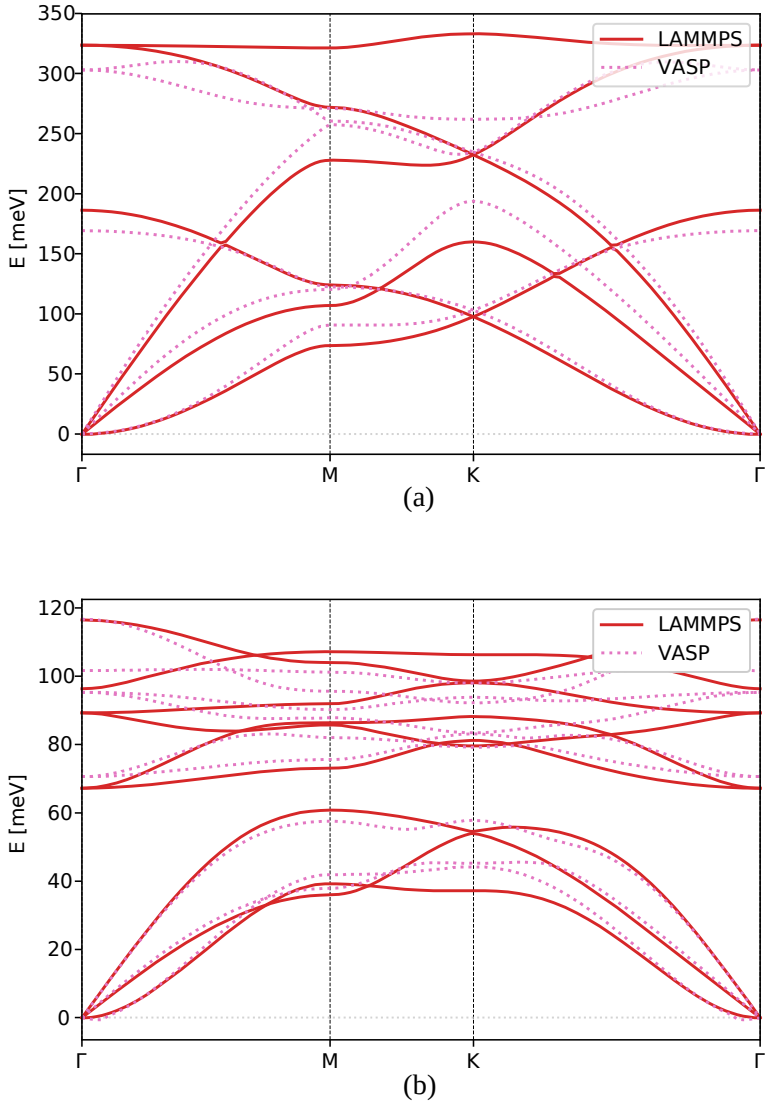

Figure S6: Phonon band structure of (a) G and (b) MoS_2 computed with LAMMPS (solid lines) and VASP (dashed lines). The y axis reports the phonon energy, while the x axis marks the distance from the origin along the path $\Gamma \to M \to K \to \Gamma$.

the optical ones. However, strong quantitative agreement is not needed for the qualitative statements developed in the main text and, in order to obtain the sound velocity needed as input of the NM theory, only an accurate description around the Γ point is required.

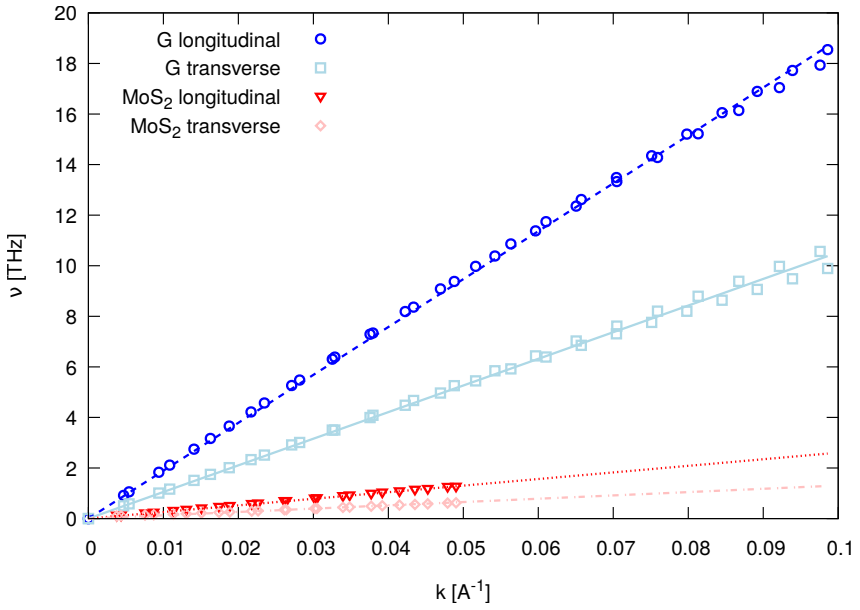

Figure S7: Sound velocity fit from the phonon dispersion in G (shades-of-blue symbols) and MoS_2 monolayer (shades-of-red symbols). The y axis reports the frequency ν in THz and the x axis the distance from Γ in $Å^{-1}$. The color-matching lines report the linear fit of that branch, i.e. $\nu_i = v_i k$.

As explained in the main text, the NM theory describes the distortion of a 2D layer due to interaction with a rigid substrate in terms of long wavelength phonons. The theory yields analytical predictions in the limit of linear dispersion $\omega_i(k) = v_i k$, where $i = \mathrm{L}, \mathrm{T}$ labels either the transverse (T) or longitudinal (L) branch and v_i is the speed of sound of the corresponding branch i. This is defined as the slope of the phonon dispersion near Γ: $v_i = \frac{\partial \omega(k)}{\partial k}\Big|_\Gamma$. Figure S7 shows the longitudinal and transverse branches close to Γ of G and MoS_2. The plot also shows the linear fits obtained from the points, including their fitted

slopes representing the sound velocities, as reported in Table S3. This leads to the values

Table S3: Sound velocity of transverse and longitudinal phonon branches in G and monolayer MoS_2 extracted from Figure S7. The uncertainty arises from the linear fitting procedure.

Material	v_L[km/s]	v_T[km/s]
G	18.9403 ± 0.0005	10.5298 ± 0.0005
MoS_2	0.2608 ± 0.0005	0.131 ± 0.002

$\delta_{\mathrm{G}} = 2.235$ and $\delta_{\mathrm{MoS_2}} = 2.968$ used to evaluate Eq. 4 in the main text.

5 NM approximation limits

We discuss the difference behaviour between the pure NM theory reported the main text (see Figure 2 in the main text) and free 2D system. More specifically, we consider a bilayer MoS_2/G where atoms are free to move in the xy plane but the z coordinate of each atom is frozen. This corresponds to lifting the rigid substrate assumption of the NM theory, while enforcing a constant interlayer distance. Figure S8 reports on the results for this case. The NM theory does not cover this scenario, as here none of the two layers is rigid. As a result, the two layers can mutually influence and distort each other, reaching configurations not included in the NM model. A minimum at $\theta \approx 8°$ is clearly visible, midway between the two rigid substrate approximations. This means that the physics described in the NM theory still applies to this case, even though the model does not describe the mutual interaction between the layers and does not provide a prediction for the the minimum-energy angle. The behaviour of the system is thus qualitatively different from the h-BN/G heterostructures studied by Guerra et al.[4] In that case the NM theory was found to explain quantitatively the energetics of the rigid and z-frozen scenario, i.e. blue and red lines in Figure S8, but removing the rigid substrate constraint changed the behavior qualitatively: the non-zero minimum-energy angle predicted by NM disappeared from the energy profile of the system. From this observation, we can conclude that in our system, comprising of 2D and 3D ML, when the assumption of a rigid substrate is relaxed, a non-zero minimum angle dominates

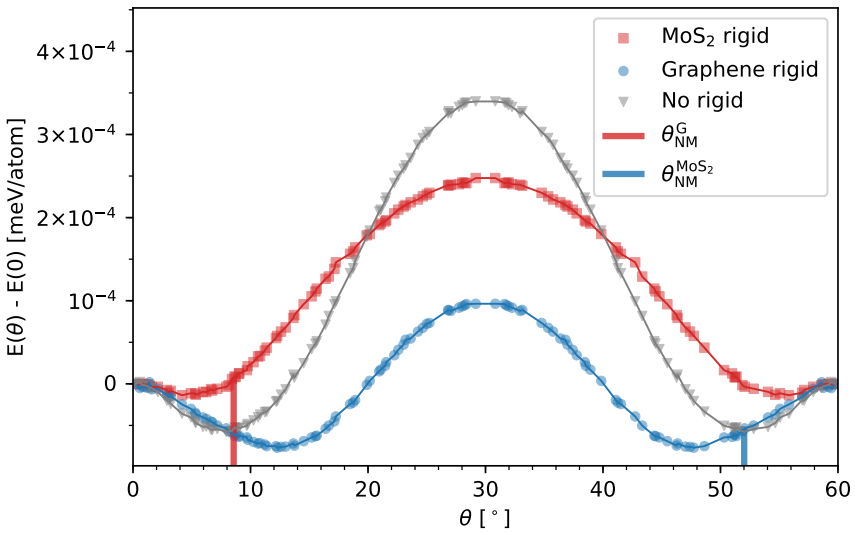

Figure S8: Energy per atom $E(\theta)$, in meV/atom, as a function of the imposed angle θ in degrees for different 2D models: red squares refer to flexible G on top of rigid MoS_2; blue circles refer to flexible MoS_2 on top of rigid G. Gray triangles refer to flexible MoS_2 on top of flexible G. The reference value of the energy scale is set by $E(0)$ and the values have been corrected according to the initial LJ enhancement. Red and blue segments mark the minimum angle predicted by the NM theory for the first and second case, respectively.

the energy landscape and, thus, the NM argument still describes the physics of the system.

6 Force Field Benchmark

In this section, we present a benchmark of the force fields used in this study compared to experimental results and first principle calculations.

Table S4: Structural parameters obtained by authors using the SW model for MoS_2, the REBO model for graphene together with reference data from X-ray diffraction experiments and density functional theory (DFT) calculations. The DFT results were obtained using the following previously mentioned computational details.

	SW	REBO	DFT	Experimental
Lattice constant graphene(Å)	-	2.4602	2.4668	2.4589,[5] 2.464(2)[6]
Lattice constant MoS_2 (Å)	3.0937	-	3.1901	3.15,[7] 3.1625[8]
C-C bond distance (Å)	-	1.4204	1.4242	-
Mo-S bond distance (Å)	2.3920	-	2.4112	-

7 Magnitude of the out-of-plane displacements

In this section we compared the out-of-plane displacements of G layer with the MoS_2 one. The thickness of a ML is defined as $\tau(\theta) = z_{\max} - z_{\min}$ in the relaxed geometry. In the case of MoS_2 since it comprises 3 atomic layers, the analysis has been carried out on the separate components: bottom S layer, Mo layer and top S layer, as reported in Figure S9. The bottom S layer of MoS_2, being the closest to G, shows the larger displacements and shows an opposite trend compared to G. This is due to the fact that the less convenient it becomes for G do modulate, the more important is the contribution from the MoS_2 modulation; albeit still small if compared to the G signal. The Mo layer shows an appreciable modulation only after $\theta = 20°$, when G starts to flatten. Finally, the top S layer, furthest from the interface with G, remains essentially flat throughout the spectrum and the small fluctuations can be regarded as numerical noise.

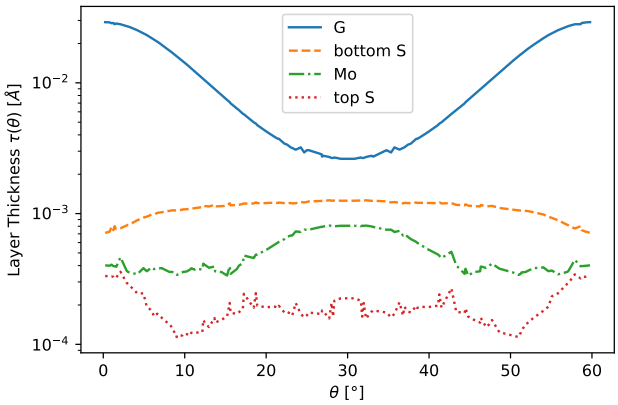

Figure S9: Thickness of the atomic layers as a function of the mismatch angle. The y axis is reported in logarithmic scale for better comparison.

The total variations Δ between all values θ are reported in Table S5. The last column reports the variations with respect to the one occurring in G (Δ_G): the modulation in MoS_2 is at least 2 orders of magnitude less than in G, thus supporting our claim that the structural distortion representing the leading order in lowering the energy occurs in the G layer only.

Table S5: Minimum and maximum thickness across θ. Variation of thickness $\Delta = \max_\theta(\tau) - \min_\theta(\tau)$. Variation relative to the one occurring in G.

Atom layer	$\min_\theta(\tau)$ [Å]	$\max_\theta(\tau)$ [Å]	Δ [Å]	Δ/Δ_G
G	0.0026	0.0291	0.0265	1
Bottom S	0.0007	0.0013	0.0006	0.021
Mo	0.0003	0.0008	0.0005	0.018
Top s	0.0001	0.0004	0.0002	0.009

References

(1) Ding, Z.; Pei, Q. X.; Jiang, J. W.; Huang, W.; Zhang, Y. W. Interfacial Thermal Conductance in Graphene/MoS_2 Heterostructures. *Carbon* **2016**, *96*, 888–896.

(2) Nelder, J. A.; Mead, R. A Simplex Method for Function Minimization. *The Computer Journal* **1965**, *7*, 308–313.

(3) Oliphant, T. E. SciPy: Open Source Scientific Tools for Python. 2007; `http://www.scipy.org/`.

(4) Guerra, R.; van Wijk, M.; Vanossi, A.; Fasolino, A.; Tosatti, E. Graphene on h-BN: to Align or Not to Align? *Nanoscale* **2017**, *9*, 8799–8804.

(5) Baskin, Y.; Meyer, L. Lattice Constants of Graphite at Low Temperatures. *Physical Review* **1955**, *100*, 544.

(6) Trucano, P.; Chen, R. Structure of Graphite by Neutron Diffraction. *Nature* **1975**, *258*, 136–137.

(7) Wakabayashi, N.; Smith, H. G.; Nicklow, R. M. Lattice Dynamics of Hexagonal MoS_2 Studied by Neutron Scattering. *Physical Review B* **1975**, *12*, 659–663.

(8) Py, M. A.; Haering, R. R. Structural Destabilization Induced by Lithium Intercalation in MoS_2 and Related Compounds. *Canadian Journal of Physics* **1983**, *61*, 76–84.

C

SI. MoS_2 & Water

frontiers

Supplementary Material

1 INTRODUCTION

In the Supplementary Information we address more details regarding the techniques and methods used. Firstly, we present a benchmark of the force field. Secondly, we describe the bootstrap method. Thirdly, we present the results of the ideal water network used as a reference in the main text.

2 BENCHMARK

The force field used to perform the classical molecular dynamics simulations was developed by Srehst *et al.*(Sresht et al., 2017). Here, we will present a benchmark by means of comparison with density functional theory (DFT) (Ref. (Levita et al., 2014)) and experimental data (Ref. (Schönfeld et al., 1983)). Table S1 presents the most relevant structural parameters, comparing the different methods. A more elaborate description of the parameters can be found in Ref. (Nicolini and Polcar, 2016).

	MD	Experimental	DFT
Lateral lattice constant (Å)	3.1741	3.161	3.198
Perpendicular lattice constant (Å)	12.409	12.295	12.454
Mo-S distance (Å)	2.397	2.366	2.425
Mo-S-Mo (ϕ) angle (°)	82.910	83.816	82.504
S-Mo-S (θ) angle (°)	82.910	83.816	82.504
S-Mo-S (ψ) angle (°)	80.284	79.064	80.829
S-Mo-S (ω) angle (°)	135.057	134.634	135.247

Table S1. Structural parameters obtained via the Sresht *et al.* force field (MD) (Sresht et al., 2017) compared to DFT (Levita et al., 2014) and experimental data (Schönfeld et al., 1983).

3 BOOTSTRAP METHOD

To obtain the average frictional force from the instantaneous frictional forces experienced while sliding the top layer, we resorted to the random sampling bootstrap method. This method works as follows. First, starting from the original dataset, one generates a new set (with the same number of data points) by randomly selecting points from the original set. During this step, the order of the data may change and some data points may be present multiple times, while others may be missing completely. Next, the average over the new data set is calculated. Finally, the process is repeated 2000 times, after which the final average and the standard deviation are calculated.

4 IDEAL WATER NETWORK

Here, we present the outcomes for the ideal parallel and antiparallel water networks. We performed two additional MD simulations of 100 ps with the same parameters reported in the main text. Here, no MoS_2 was present (i.e., we simulated the water network only). Moreover, the water layers were fixed in the z-direction to mimic 2D confinement. Although no sliding happened in these simulations, the black arrows indicate the sliding direction as in Fig. 4 of the main text. Please refer to the main text for the discussion of the outcomes.

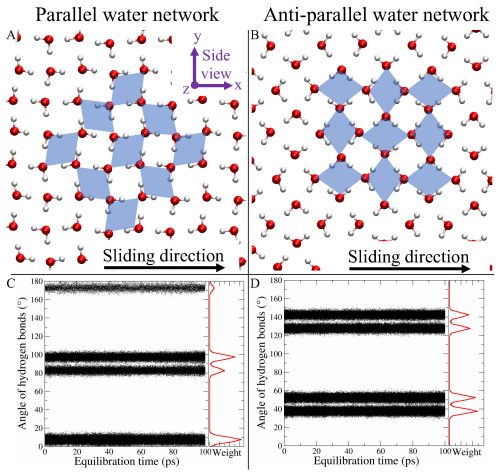

Figure S1. Top view representation of the ideal parallel (panel A) and anti-parallel (panel B) water network. The blue diamond serve as guide for the eye in distinguishing the pcd configuration. The bottom row (panel C-D) represents the angles of all the hydrogen bonds for every time step with respect to the x-axis, in red the corresponding histograms are depicted. Figure obtained with VMD (Humphrey et al., 1996).

REFERENCES

Humphrey, W., Dalke, A., and Schulten, K. (1996). Vmd: Visual molecular dynamics. *Journal of Molecular Graphics* 14, 33–38. doi:https://doi.org/10.1016/0263-7855(96)00018-5

Levita, G., Cavaleiro, A., Molinari, E., Polcar, T., and Righi, M. (2014). Sliding properties of MoS_2 layers: Load and interlayer orientation effects. *The Journal of Physical Chemistry C* 118, 13809–13816. doi:10.1021/jp4098099

Nicolini, P. and Polcar, T. (2016). A comparison of empirical potentials for sliding simulations of MoS_2. *Computational Materials Science* 115, 158–169. doi:10.1016/j.commatsci.2016.01.013

Schönfeld, B., Huang, J. J., and Moss, S. C. (1983). Anisotropic mean-square displacements (msd) in single-crystals of 2H- and 3R-MoS_2. *Acta Crystallographica Section B* B39, 404–407. doi:10.1107/S0108768183002645

Sresht, V., Rajan, A. G., Bordes, E., Strano, M. S., Pádua, A. A., and Blankschtein, D. (2017). Quantitative modeling of MoS_2–solvent interfaces: Predicting contact angles and exfoliation performance using molecular dynamics. *The Journal of Physical Chemistry C* 121, 9022–9031. doi:10.1021/acs.jpcc.7b00484

D

Viewpoint

I was a co-author of this work and was, together with my supervisor Dr. Paolo Nicolini and another Ph.D. student from our group Florian Belviso, responsible for Section 13 'TRIBOLOGY AS A NOVEL FIELD FOR ELECTRICITY GENERATION'. All results of this study have been published in the Computational Materials Science journal [145]. This is an impacted journal, which had an impact factor of 4.825 in 2019 and belongs to the quartile category Q1 in the field of inorganic and nuclear chemistry. A copy of the manuscript is attached below.

Inorganic Chemistry
Viewpoint
Cite This: Inorg. Chem. 2019, 58, 14939−14980
pubs.acs.org/IC

Viewpoint: Atomic-Scale Design Protocols toward Energy, Electronic, Catalysis, and Sensing Applications

Florian Belviso,[†] Victor E. P. Claerbout,[†] Aleix Comas-Vives,[‡] Naresh S. Dalal,[§,∥] Feng-Ren Fan,[⊥] Alessio Filippetti,[#] Vincenzo Fiorentini,[#] Lucas Foppa,[▽] Cesare Franchini,[○,◆] Benjamin Geisler,[⊕] Luca M. Ghiringhelli,[⊗] Axel Groß,[◑,◐] Shunbo Hu,[◒] Jorge Íñiguez,[◓,◔] Steven Kaai Kauwe,[◪] Janice L. Musfeldt,[◪] Paolo Nicolini,[†] Rossitza Pentcheva,[⊕] Tomas Polcar,[†] Wei Ren,[◒] Fabio Ricci,[⬡] Francesco Ricci,[⬢] Huseyin Sener Sen,[†] Jonathan Michael Skelton,[⬠] Taylor D. Sparks,[◪] Alessandro Stroppa,[◭] Andrea Urru,[#,◀] Matthias Vandichel,[⊖,⊙] Paolo Vavassori,[◨,▶] Hua Wu,[⊥,◧] Ke Yang,[⊥] Hong Jian Zhao,[◒,⬒] Danilo Puggioni,[*,⬓] Remedios Cortese,[*,◹] and Antonio Cammarata[*,†]

[†]Department of Control Engineering, Czech Technical University in Prague, Technicka 2, 16627 Prague 6, Czech Republic
[‡]Department of Chemistry, Universitat Autònoma de Barcelona, 08193 Cerdanyola del Vallès, Catalonia, Spain
[§]National High Magnet Field Lab, Tallahassee, Florida 32310, United States
[∥]Department of Chemistry & Biochemistry, Florida State University, Tallahassee, Florida 32306, United States
[⊥]Laboratory for Computational Physical Sciences (MOE), State Key Laboratory of Surface Physics, and Department of Physics, Fudan University, Shanghai 200433, China
[#]Department of Physics at University of Cagliari, and CNR-IOM, UOS Cagliari, Cittadella Universitaria, I-09042 Monserrato (CA), Italy
[▽]Department of Chemistry and Applied Biosciences, ETH Zürich, Vladimir-Prelog-Weg 1-5, CH-8093 Zürich, Switzerland
[○]Faculty of Physics and Center for Computational Materials Science, University of Vienna, Sensengasse 8, A-1090 Vienna, Austria
[◆]Dipartimento di Fisica e Astronomia, Università di Bologna, Bologna 40127, Italy
[⊕]Department of Physics and Center for Nanointegration (CENIDE), Universität Duisburg-Essen, Lotharstr. 1, Duisburg 47057, Germany
[⊗]Fritz-Haber-Institut der Max-Planck-Gesellschaft, Berlin-Dahlem 14195, Germany
[◑]Electrochemical Energy Storage, Helmholtz Institut Ulm, Ulm 89069, Germany
[◐]Institute of Theoretical Chemistry, Ulm University, Ulm 89069, Germany
[◒]Department of Physics, Materials Genome Institute, and International Center of Quantum and Molecular Structures, Shanghai University, 99 Shangda Road, Shanghai 200444, China
[◓]Materials Research and Technology Department, Luxembourg Institute of Science and Technology, Avenue des Hauts-Fourneaux 5, L-4362 Esch/Alzette, Luxembourg
[⊖]Department of Chemical Sciences and Bernal Institute, Limerick University, Limerick, Ireland
[⊙]Department of Chemistry and Material Science and Department of Applied Physics, Aalto University, Espoo 02150, Finland
[◨]CIC nanoGUNE, San Sebastian E-20018, Spain
[◧]Collaborative Innovation Center of Advanced Microstructures, Nanjing 210093, China
[⬒]Physics Department and Institute for Engineering, University of Arkansas, Fayetteville, Arkansas 72701,United States
[⬓]Department of Materials Science and Engineering, Northwestern University, 2220 Campus Drive, Evanston, Illinois 60208, United States
[◹]Department of Physics and Chemistry, Università degli Studi di Palermo, Viale delle Scienze ed. 17, Palermo 90128, Italy
[◹]Physics and Materials Research Unit, University of Luxembourg, Rue du Brill 41, Belvaux L-4422, Luxembourg
[◪]Materials Science & Engineering Department, University of Utah, 122 Central Campus Drive, Salt Lake City, Utah 84112, United States
[◪]Department of Chemistry, University of Tennessee, Knoxville, Tennessee 37996, United States
[⬡]Physique Theorique des Materiaux, Universite de Liege, Sart-Tilman B-4000, Belgium
[⬢]Institute of Condensed Matter and Nanosciences, Universite Catholique de Louvain, Chemin des Etoiles 8, Louvain-la-Neuve B-1348, Belgium
[⬠]Department of Chemistry, University of Manchester, Oxford Road, Manchester M13 9PL, United Kingdom
[◭]CNR-SPIN, Department of Physical Sciences and Chemistry, Universita degli Studi dell'Aquila, Via Vetoio, Coppito (AQ) 67010, Italy
[▶]IKERBASQUE, Basque Foundation for Science, Bilbao 48013, Spain

Received: June 20, 2019
Published: October 31, 2019

DOI: 10.1021/acs.inorgchem.9b01785
Inorg. Chem. 2019, 58, 14939−14980

Inorganic Chemistry Viewpoint

ABSTRACT: Nanostructured materials are essential building blocks for the fabrication of new devices for energy harvesting/storage, sensing, catalysis, magnetic, and optoelectronic applications. However, because of the increase of technological needs, it is essential to identify new functional materials and improve the properties of existing ones. The objective of this Viewpoint is to examine the state of the art of atomic-scale simulative and experimental protocols aimed to the design of novel functional nanostructured materials, and to present new perspectives in the relative fields. This is the result of the debates of Symposium I "Atomic-scale design protocols towards energy, electronic, catalysis, and sensing applications", which took place within the 2018 European Materials Research Society fall meeting.

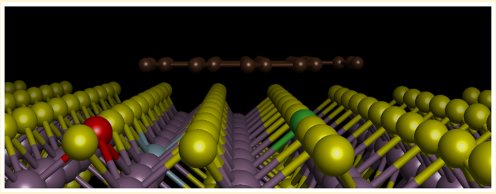

1. INTRODUCTION

Modern technology has a huge impact on our everyday life. For example, nowadays a vast number of tasks can be performed with a couple of clicks. Functional materials, that is, materials exhibiting adaptive capabilities to external stimuli,[1] form the basis for a wide range of technologies. Their societal impact is tantamount in energy harvesting/storage, sensing, catalysis, magnetic, and optoelectronic applications.

During the last years, intensive research activities have been devoted to the synthesis and characterization of nanomaterials. The discovery of novel materials with desirable properties, however, requires that we understand the atomic structural principles governing the functional response. In this perspective, the Symposium I "Atomic-scale design protocols towards energy, electronic, catalysis, and sensing applications", which took place within the 2018 European Materials Research Society fall meeting, focused on the recent developments of design strategies for smart materials. Here, the outcomes of the Symposium's debates are reported.

This Viewpoint first focuses on general technical aspects of performing first-principles calculations, on creating integrated data infrastructures and extracting useful information from them, and on issues related to machine learning techniques. Materials and processes for energy conversion through catalysis and hazards in energy storage in batteries are then addressed. A broad range of functional materials is covered in the remaining sections of this Viewpoint, from molecular solids and metallic multilayer composites, oxide thermoelectrics, and "ferroelectric" metals to hybrid organic−inorganic perovskites and triboelectric materials. These examples illustrate the challenges in understanding and improving functional materials, but they also demonstrate the progress that has been made on an atomistic level by advanced techniques, both in theoretical and experimental studies. Particular emphasis has been put on synergistic investigations involving experimentals, materials informatics, and computational approaches, which can provide the fundamental understanding of these materials as well as new insights necessary to guide and accelerate the search of materials with targeted functionalities.

2. PREDICTING THE BAND GAP OF COMPLEX MATERIALS: COMPUTATIONAL METHODS AND PROCEDURES

The prediction and interpretation of materials properties requires the combination of advanced theoretical models and accurate numerical schemes. For decades, density functional theory (DFT)[2,3] has been the primary method to estimate the ground-state properties of materials, and it still represents a common methodological scheme for studying a wide variety of physical phenomena, including those reviewed in the present Viewpoint. Despite its great success, DFT has some limitations arising from the approximation used to construct the exchange and correlation functionals that hinders its performance. An archetypal shortcoming of DFT is the calculation of the band gap, a property of fundamental importance and crucial for all practical applications, including energy, electronic, catalysis, and sensing applications, which are the main focus of this work and will be elaborated and discussed more extensively in the following sections. A variety of quantum-mechanical methods has been proposed to cure this problem, including local corrections inspired by the Hubbard-based models[4] (e.g., DFT +U and self-interaction corrected schemes), hybrid functionals

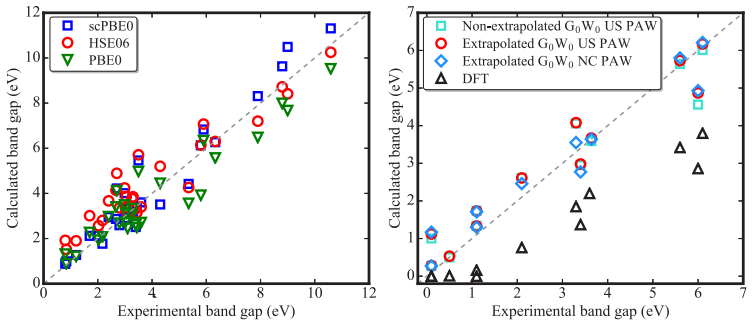

Figure 1. Comparison between calculated and experiment band gaps. (a) Hybrid functionals for a data set including 30 semiconductors and (b) GW applied to a perovskite data set including 3d, 4d, and 5d transition metals. Adapted from refs 10 and 12.

DOI: 10.1021/acs.inorgchem.9b01785
Inorg. Chem. 2019, 58, 14939−14980

(e.g., see refs 5−7), quasiparticle approaches[8] (GW), and, for what concern the optical excitations, the Bethe-Salpeter equation (BSE).[9]

2.1. scPBE0 Hybrid Functional. A promising compromise between the computational cost and the accuracy of the calculated band gap value is represented by hybrid functionals. Figure 1 shows a selection of hybrid functional band gaps computed for a wide set of insulating and semiconducting materials.[10] Despite the research effort made so far, further investigation is still needed to improve the prediction of the band gap value, which mainly relies on mixing parameters at the basis of the hybrid energy functional formulation. As an example, the procedure to carry one scPBE0[10] calculation is here concisely described, which is one of the last members of the hybrid family.

The scPBE0 hybrid energy functional is based on the self-consistent evaluation of the mixing parameter α, which controls the amount of HF exchange.[10] is the This is done by means of an iterative calculation of the static dielectric constant using the perturbation expansion after discretization (PEAD) method.[11] Specifically, one starts the self-consistent loop by using the standard mixing $\alpha_{in} = 0.25$. At the end of this iteration the output mixing α_{out} is determined as the inverse of the mean value of the diagonal elements of the dielectric function evaluated by PEAD; that is, $\alpha_{out} = 1/\bar{\varepsilon}_{\infty}$, where ε_{∞} is the ion-clamped static dielectric tensor. This new value of α is then used to start a new iteration. The self-consistent procedure stops when $\alpha_{out} - \alpha_{in}$ is smaller than the desired accuracy (usually $\sim 10^{-2}$).

The results obtained by fixed-α (PBE0 and HSE03) and self-consistent (scPBE0) hybrids (Figure 1 show that scPBE0 performs better for band gaps smaller than ∼8 eV, whereas for larger gaps PBE0 appears to be a better choice. The nonempirical extension of range-separated hybrids, in which not only the mixing parameters α but also the screening length (typically labeled μ in HSE-like hybrids), represents a possible route for improvement. Following this idea, a new class of nonempirical hybrid functionals based on a model dielectric function has been recently proposed that indeed predicts accurately band gaps for both narrow- and wide-gap semiconductor.[13] The next level of theory, which allows the computation of quasiparticle energies and guarantees an improved prediction of band gaps, is the GW method.[8]

2.2. GW Method. The GW method is probably the most accurate approach presently available for condensed matter physics calculations. Alternative advanced methodologies have been developed in other sectors, for example, quantum-chemistry methods, such as Møller−Plesset perturbation and coupled cluster theories,[14] which are however still computationally too demanding when applied to complex extended systems. The essence of the GW scheme is the inclusion of the self-energy, defined as $\Sigma = iGW$ (where G is the single particle Green's function, and W is the screened Coulomb interaction), in the generalized Kohn−Sham equations. Regrettably enough, despite its success, the proper use of the GW method is not well-established from a technical point of view, yielding to nonconverged solutions. In fact, the convergence criteria requires a summation over many empty states (N) and a sufficiently dense k-points mesh resulting in large computational cost and memory requirements. However, two different routes can be followed to obtained converged results:[12]

1. *Basis-set extrapolation.* The core aspect of this scheme is to extrapolate the quasi-particle (QP) energies obtained using a finite-basis-set to the infinite-basis-set limit through the formulawhere $E(N_k,N)$ is the calculated QP energies with N_k **k**-points and N bands, $E(N_k, N_\infty)$ is the corresponding extrapolated ($N \rightarrow \infty$) QP energies, and the variables n_k and N_k indicate the number of **k**-points in the small and large **k**-point mesh, respectively.

2. *Conventional scheme.* This method attempts to converge the QP energies with respect to a set of three parameters: number of bands, energy cutoff for the

$$E_{\infty}(N_k, N_{\infty}) \approx \underbrace{E_{\infty}(n_k, N_{\infty}) \overbrace{- E(n_k, N)}^{\Delta_k(N)} + E(N_k, N)}_{\Delta_N(n_k)} \quad (1)$$

plane wave expansion for the orbitals E_{pw}, and the number of **k**-points.

An important aspect to consider when performing GW calculations is the choice of the pseudopotential. Even though accurate results can be also obtained with ultrasoft pseudopotentials, it is recommended, when possible, to adopt norm-conserving pseudopotentials. Following the above consideration one can achieve a remarkably good fundamental band gap for a wide set of transition metal perovskites, as shown in Figure 1.

An additional ambiguity, which is often a source of confusion, is the difference between fundamental electronic gap, that is, the energy difference between the lowest unoccupied state and the highest occupied one, and the optical gap, which includes electron−hole interaction and is lower than the fundamental electronic gap by an amount that is typically referred to as excitonic energy.[15] Excitonic effects, not included in the GW scheme, can be accounted for by using the Bethe-Salpeter equation, in which the response function is computed from the Dyson-like equation.[16]

2.3. BSE Calculations. The procedure to conduct BSE calculations consists of four steps:[17]

1. Standard self-consistent DFT calculations. If the DFT ground state turns out to be metallic it is necessary to add a small U or a scissor operator (only in this step).

2. Additional DFT step to compute the one-electron wave functions and eigenenergies of all virtual orbitals evaluated by an exact diagonalization.

3. G_0W_0 runs to compute the QP energies and static screened interaction W, and

4. BSE run (typically in the Tamm-Dancoff approximation[18]) to compute the frequency-dependent macroscopic dielectric function

$$\varepsilon(\omega) = 1 - \lim_{q \rightarrow 0} V(\mathbf{q}) \sum_{\Lambda} \left(\frac{1}{\omega - \Omega_{\Lambda} + i\eta} - \frac{1}{\omega + \Omega_{\Lambda} - i\eta} \right) \times \left\{ \sum_{\mathbf{k}} \omega_{\mathbf{k}} \sum_{v,c} \langle \psi_{c\mathbf{k}} | e^{i\mathbf{q}\cdot\mathbf{r}} | \psi_{v\mathbf{k}} \rangle X^{\Lambda}_{cv\mathbf{k}} \right\} \times \{c.\ c.\ \} \quad (2)$$

with the oscillator strengths S_{Λ} associated with the optical transitions defined by

DOI: 10.1021/acs.inorgchem.9b01785
Inorg. Chem. 2019, 58, 14939−14980

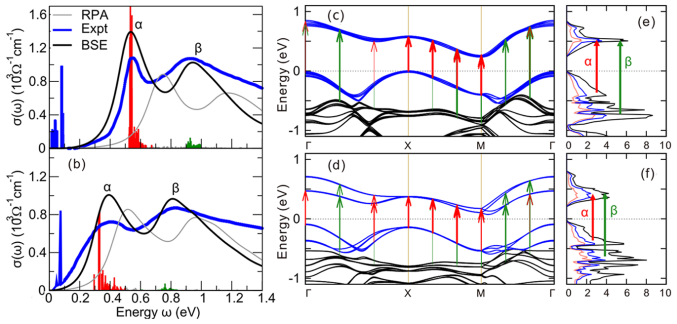

Figure 2. Experimental and calculated optical conductivity spectra $\sigma(\omega)$ of (a) Sr_2IrO_4 and (b) $Sr_3Ir_2O_7$. The gray vertical lines represent the oscillator strength whose contributions to α and β peaks are highlighted in red and blue colors, respectively. (c, d) *GW* band structure. (e, f) *GW* total density of states. The red and blue arrows in (c, d) represent the dominant interband transitions for the α and β peaks, respectively. The width of the arrows denotes the normalized amplitude of BSE eigenvectors $|X^{\Lambda}_{cv\mathbf{k}}|$. Adapted from ref 17.

$$S_{\Lambda} = \mathbf{Tr}\left[\left\{\sum_{\mathbf{k}} w_{\mathbf{k}} \sum_{v,c} \langle \psi_{c\mathbf{k}} | e^{i\mathbf{q}\cdot\mathbf{r}} | \psi_{v\mathbf{k}} \rangle X^{\Lambda}_{cv\mathbf{k}}\right\} \times \{c.\ c.\ \}\right] \tag{3}$$

In the last two equations, Ω_{Λ} and X^{Λ} are BSE eigenvalues and eigenvectors, respectively, V is the bare interaction, η is a positive infinitesimal, and $w_{\mathbf{k}}$ are the k-point weights, while $\psi_{v\mathbf{k}}$ and $\psi_{c\mathbf{k}}$ refer to occupied and unoccupied DFT(+U) wave functions, respectively.

With these prescriptions, excellent optical properties are obtained for the challenging spin−orbit coupled Dirac-Mott properties of Sr_2IrO_4 and $Sr_3Ir_2O_7$,[17] as shown in Figure 2. Note that step 3 is rather expensive and does not scale favorably with the number of k points. Considering that the calculation of BSE spectra requires many k points to reach a good level of convergence, it can be useful to adopt an analytical treatment of the screening as input in the BSE run (step 4):

$$\varepsilon^{-1}_{\mathbf{G},\mathbf{G}}(\mathbf{q}) = \varepsilon_{\infty}^{-1} + (1 - \varepsilon_{\infty}^{-1})\left[1 - \exp\left(-\frac{|\mathbf{q} + \mathbf{G}|^2}{4\lambda^2}\right)\right] \tag{4}$$

where ε_{∞} is the static ion-clamped dielectric function in the long-wave limit, and the screening length parameter λ is derived by fitting the screening ε^{-1} at small wave vectors with respect to $|\mathbf{q} + \mathbf{G}|$ with $\mathbf{q}$ and $\mathbf{G}$ being the wave vector and lattice vector of the reciprocal cell, respectively.[17]

2.4. Outlook. In conclusion, a set of state-of-the-art first-principles schemes have been briefly scrutinized; these are capable to deliver a good estimation of band gaps, not only for standard semiconductors but also for complex oxides with different electronic configurations, magnetic orderings, structural characteristics, and spin−orbit coupling strength. These methods, in particular, GW and BSE, are computationally very demanding, and much care must be taken in setting up the computational protocol. As future challenges, it would be desirable and useful (i) to find common standards for the automation of these complex sequences of simulations (streamline workflows), (ii) to build a high-quality beyond-DFT materials database ("Quantum Materials Repository") and, possibly, (iii) to envision smart ways to accelerate the calculations without loss of accuracy (machine learning techniques). This would facilitate a paradigmatic shift in the materials modeling community from massively DFT-based calculations to beyond-DFT schemes, which would be beneficial for the quality and accuracy of the results and therefore for the prediction and understanding of material-specific functionalities.

3. DATA-DRIVEN MATERIALS SCIENCE: BUILDING MAPS OF MATERIALS PROPERTIES

3.1. Descriptors in Materials Science. High-performance computing (HPC) is used for the search and design of novel functional materials with improved functionalities. According to the Springer Materials database,[19] ∼250 000 inorganic materials, including stable and metastable phases, are known to exist. Unfortunately, even somewhat basic properties—such as elastic constants, electrical and thermal conductivity, and similar—are systematically known only for very few of them. Computational high-throughput initiatives like Materials Project,[20] AFLOW,[21] and OQMD[22] have collected information on hundreds of thousands of possible materials and made them available in open-access databases. However, while electronic structure calculations provide a wealth of information, the majority of these data are not efficiently used.

Recently, a manifesto[23] on how scientific data should be handled has been proposed: It goes under the acronym FAIR, which stands for findable, accessible, interoperable, and reusable/repurposable. The recently established Novel Materials Discovery (NOMAD) Laboratory[24,25] already complies to the FAIR principles. This is made possible by the NOMAD Repository & Archive, as of end of 2018 containing more than 50 000 000 open-access single-point calculations of millions of different chemical compositions and atomic structures, mainly bulk materials. These include also calculations from the above-mentioned databases and more. For all the calculations, original input and output files are stored in the Repository, and a code-independent representation of all calculations' data is accessible in the Archive, thanks to a remapping of the raw data into a hierarchical metadata framework.[24]

It is easy to realize that the number of possible stable and metastable materials is to all practical purposes infinite. This suggests that novel functional materials with superior properties for any conceivable application should exist but are not yet known. High-throughput scanning of the compositional and

DOI: 10.1021/acs.inorgchem.9b01785
Inorg. Chem. 2019, 58, 14939−14980

structural materials space may not be an efficient approach when used with accurate electronic-structure methods, because the latter are computationally demanding in terms of CPU/GPU hours.

A promising alternative approach is to construct models almost as accurate as reliable electronic-structure methods but running at a fraction of the cost by means of learning algorithms. This is the realm of artificial intelligence or (big-)data analytics that is data mining, machine/statistical learning, deep learning, compressed sensing, and others. In the past 10 years, more and more such approaches have been developed and applied to the wealth of materials-science data.[26−37] The first blind-test, crowd-sourced competition for the machine learning of properties from materials-science data—the NOMAD 2018 Kaggle competition[38]—has been a recent turning point toward widespread acceptance of good-practice protocols in data-driven materials science. Besides, it confirmed (Gaussian) kernel methods or, alternatively, the similar Gaussian-process regression, artificial neural networks, and tree-regression methods as the most popular and versatile artificial-intelligence approaches.[38]

In all the cited works, the crucial step is the identification of *descriptors* that capture the underlying mechanism of a given material's property or function and are the numerical input for the machine-learning model. The descriptors are carefully designed by the researcher, via imposing known physical symmetries and constraints. Alternatively, the descriptors can be learned from the data; more precisely, the best descriptors can be identified among a possibly immense set of candidates by exploiting a signal-analysis technique known as compressed-sensing (CS).[38]

3.2. Compressed Sensing. The compressed sensing (CS) approach reconstructs a high-quality "signal", starting from a sparse set of "observations".[40,41] Mathematically, given a set of samples measured incoherently ($\boldsymbol{P}$) CS finds the sparse solution ($\boldsymbol{c}$) of an undetermined system of linear equations $\boldsymbol{Dc} = \boldsymbol{P}$, where $\boldsymbol{D}$ is the *sensing matrix* with the number of columns much larger than the number of rows. The recasting of CS into materials-science challenges[39,42] starts from a set of materials (m_i) with observable properties listed in vector $\boldsymbol{P}_i$ and a possibly immense list of test features d_j, which form the features space. The projection of each i-material into the j-feature is the i,j component of the sensing matrix $\boldsymbol{D}$. The sparse solution of $\arg\min_{\boldsymbol{c}} (\|\boldsymbol{P} - \boldsymbol{Dc}\|_2^2 + \lambda\|\boldsymbol{c}\|_0)$, where $\|\boldsymbol{c}\|_0$ is the improper norm of $\boldsymbol{c}$ (i.e., its number of nonzero components), gives the optimum Ω-dimensional descriptor, that is, the set of features "singled out" by the Ω nonzero components of the solution vector $\boldsymbol{c}$. The first term in the minimized expression is a familiar mean square error, as in least-squares regression; the second term is known as regularization. In this case, a "penalty" is paid for every nonzero component of $\boldsymbol{c}$. Effectively, CS performs a *dimensionality reduction* from the large input features space to the selected low-dimensional descriptor. Differently from most dimensionality-reduction schemes,[43] CS provides an "inspectable" solution, in the sense that the components of the selected descriptor are among the input features.

The sure independence screening and sparsifying operator (SISSO)[44] is a recently developed CS-based method, designed for identifying low-dimensional descriptors for material properties. It is an iterative scheme that combines the sure independence screening scheme (SIS)[45] for dimensionality reduction of huge features space and the sparsifying operators (SO) for finding sparse solutions. SISSO improves the results over the conventional CS methods, such as the linear absolute shrinkage and selection operator (LASSO)[39,42,46] and greedy algorithms,[47,48] when features are correlated, and can efficiently manage immense features spaces.

For applying SISSO, a feature space Φ_q is constructed by starting from a set of primary features and a set of unary and binary operators, such as +, −, exp, $\sqrt{}$, etc. The features are then iteratively combined with the operators, where at each iteration each feature, or pair of features, is exhaustively combined with each unary/binary operator, with the constraint that sums and differences are taken only among homogeneous quantities. The index q in Φ_q counts how many such iterations were performed. The primary features are typically *atomic properties* (e.g., ionization potential, radius of s or p valence orbital, etc.) and *compounds properties* (e.g., formation energy of dimers, volume of the unit cell in a given crystal structure, average coordination, ...)[44]. Φ_q contains features in terms of mathematical expressions; when the values of the features are determined for each material m_i, the matrix $\boldsymbol{D}$ is constructed. The *atomic properties* are repurposable and therefore can be used for many descriptors and model learning. For easier reference and reusability, the atomic features used in this work and other related works[39,42,44,49] can be accessed online at the NOMAD Analytics Toolkit: https://analytics-toolkit.nomad-coe.eu.[50] A tutorial[51] shows how to access these quantities and use them in a python notebook.

Next, a sketch of the SISSO approach for one important class of problems in materials science will follow: constructing materials-properties maps. Then, one application of the method is shown.

3.3. SISSO for Building Materials-Properties Maps. A materials-property map (Figure 3) is a low-dimensional representation of the materials space, where each material is represented by means of a convenient descriptor. The components of the descriptor are the coordinates in the low-dimensional representation, such that all materials sharing a certain property (e.g., being metal or topological insulator) are located in the same convex hull. In a useful map, hulls containing materials with exclusive properties (e.g., metals vs insulators) do not overlap.

The mathematical formulation of SISSO for classification[44] substitutes a measure of overlap between convex hulls to the usual mean square error adopted in continuous problems.[44] For a property with M categories, the norm for classification is defined as

$$\hat{\boldsymbol{c}} = \arg\min_{\boldsymbol{c}} \left(\sum_{I=1}^{M-1} \sum_{J=I+1}^{M} O_{IJ}(\boldsymbol{D}, \boldsymbol{c}) + \lambda \|\boldsymbol{c}\|_0 \right) \tag{5}$$

where $O_{IJ}(\boldsymbol{D}, \boldsymbol{c})$ is the number of data in the overlap region between the I and J domains, $\boldsymbol{c}$ is a vector with 0 or 1 elements, so that a feature k (the kth column of $\boldsymbol{D}$) is selected (deselected) when $c_k = 1(0)$, and λ is a parameter controlling the number of nonzero elements in $\boldsymbol{c}$. O_{IJ} depends on $(\boldsymbol{D}, \boldsymbol{c})$ in the sense that the nonzero values of $\boldsymbol{c}$ select features from $\boldsymbol{D}$ that determine the coordinates of the data and the shape of the convex hulls.

The SISSO algorithm provides an efficient solution to eq 5 also when the number of columns of $\boldsymbol{D}$ (size of the features space) is immense.[44] SISSO has been successfully applied to identify descriptors for relevant materials-science properties.[44,52,49,53] As a showcase application of SISSO, we

DOI: 10.1021/acs.inorgchem.9b01785
Inorg. Chem. 2019, 58, 14939−14980

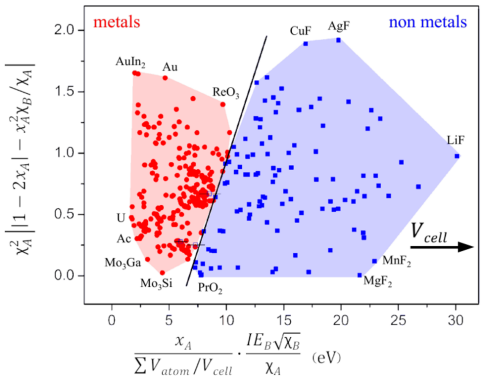

Figure 3. Material-property map for the metal/nonmetal classification (see ref 44 for the data and a more detailed discussions). The axes are the components of the descriptor, as found by SISSO, by imposing that materials classified as metal are represented in a (convex) region that does not overlap with the region containing materials classified as nonmetals. In the descriptor, x is the atomic fraction, IE is the ionization energy, χ is the electronegativity, V_{atom} is the volume of a sphere with radius equal to the covalent radius of the element, and V_{cell} is the volume of the unit cell of the considered material.[44] The red circles/blue squares are the training metal/nonmetal materials.

summarize here the recently introduced new descriptor for the prediction of stable ABX_3 perovskites.[49]

3.3.1. Stability Prediction of ABX_3 Perovskites. Perovskite materials possess exceptional properties for a variety of applications such as electrocatalysis, proton conduction, ferroelectrics, battery materials, as well as photovoltaics and optoelectronics.[54−59] ABX_3 perovskite crystal structures are defined as a network of corner-sharing BX_6 octahedra surrounding a larger A-site cation ($r_A > r_B$).

While the A and B cations can span the periodic table, the X anion is typically a chalcogen or halogen. Distortions from the cubic structure can arise from size-mismatch of the cations and anion, which results in additional perovskite structures and nonperovskite structures. The B cation can also be replaced by two different ions resulting in a double perovskite with chemical formula $A_2B'B''X_6$.

Predicting the stability of ABX_3 and $A_2B'B''X_6$ compounds remains a longstanding challenge for the discovery of new functional materials. Most of the approaches that address this challenge are computationally demanding, limiting their use to a small set of materials.[60−63] Conversely, descriptor-based approaches enable high-throughput screening applications, because they provide rapid estimates of material properties.[64] A notable example of "human-learned" descriptor is the Goldschmidt tolerance factor[65]

$$t = \frac{r_A + r_X}{\sqrt{2}(r_B + r_X)} \tag{6}$$

introduced in 1926 and since then used extensively to predict the stability of ABX_3 perovskites based only on the ionic radii (r_i) of each ion ($i = A, B, X$). The prediction accuracy of t is not very high, especially for compounds containing heavier halides.[66] Considering a data set of 576 ABX_3 experimentally characterized material compositions,[67−69] the overall prediction accuracy of t is 74%. Using the same 576 ABX_3 materials, Bartel et al.[49] set up SISSO by starting from r_i and the oxidation numbers (ν_i). Note that, in eq 6, ν_i are implicitly used to determine r_i. Out of a constructed feature space of 3×10^9 features (up to the third iteration of feature/operator combination), the following one-dimensional (1D) descriptor was identified:

$$\tau = \frac{r_X}{r_B} - \nu_A\left(\nu_A - \frac{r_A/r_B}{\ln r_A/r_B}\right) \tag{7}$$

This new tolerance factor (τ) shows a prediction accuracy of 94% and nearly uniform performance across the five anions evaluated ($X = O^{2-}$, F^-, Cl^-, Br^-, I^-). Like t, τ requires only the chemical composition, allowing the tolerance factor to be agnostic to the many structures that are considered perovskites. In addition, τ provides a monotonic estimate of the probability that a material is stable in the perovskite structure (Figure 4). The accurate and probabilistic nature of τ, as well as its generalizability over a broad range of ABX_3 and $A_2B'B''X_6$ perovskites [with $r_B = (r_{B'} + r_{B''})/2$ in eq 7] allows for new physical insights into the stability of the perovskite structure. As a direct result, Bartel et al. report the prediction of 23 314 new double-perovskite oxides and halides.[49]

The equations found by SISSO are not then necessarily unique, and all components of the descriptors may change at each added dimension. This reflects the approximate nature of the equations and the unavoidable relationships among

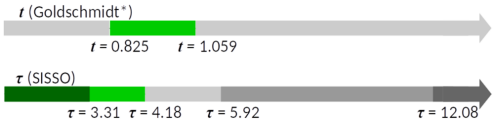

Figure 4. 1D maps for Goldschmidt t vs the newly proposed τ for perovskite-stability prediction. The green (gray) areas are the domains of predicted stability (instability) of perovskites. The boundaries of Goldschmidt's t were trained via a decision-tree classifier over the same data set used for SISSO, hence, the asterisk. In the case of τ, the darker green and gray areas are regions of 100% prediction accuracy. So, if for a material τ is smaller than 3.31 or larger than 12.08, its classification is certain. At $\tau = 4.18$, the predicted probability that a material is a perovskite is 50%, and the probability to be perovskite smoothly decreases from left to right.

features. In words, one or more primary features may be accurately described by nonlinear functions of a subset of the remaining features. It is also noted that the mathematical constraints imposed in order to obtain the minimally overlapping convex hulls are very flexible but not complete; that is, the found descriptor → property relationship is intrinsically approximate.

3.4. The NOMAD Analytics Toolkit. Artificial intelligence approaches like SISSO are promising tools that could become part of the modern materials scientist's set of skills. In this respect, it is fundamental for any researcher adopting such methods to share not only the data used for training the algorithms but also the (implemented) learning algorithm themselves. This has both educational/tutorial purposes and the merit of improving scientific reproducibility. Besides maintaining a large (and growing) Repository & Archive, the NOMAD Laboratory also provides the infrastructure to share data-analytic tools, in terms of python (or other languages)

DOI: 10.1021/acs.inorgchem.9b01785
Inorg. Chem. 2019, 58, 14939−14980

notebooks. By logging in at https://analytics-toolkit.nomad-coe.eu, users can find tutorial notebooks, for instance, introducing the CS method and allowing for the reproduction of published results such as those presented in refs 35, 39, 42, 44, 49, 52, and more.

3.5. Outlook. Compressed-sensing-based descriptor identification is a promising approach for the artificial-intelligence-assisted determination of maps of materials properties. In particular, SISSO is a powerful tool for the identification of descriptors starting from a huge number of candidates. However, this approach is currently limited to scalar features. This seems to be not a severe limitation in cases where the chemical composition of a material corresponds to a well-defined structure, including crystal symmetry and atomic arrangement. In this case, suitable descriptors depending on properties of free atoms are readily found. When polymorphism is present, the atomic (local) environment appears to be a necessary input, but currently the approach described in this section lacks a systematic strategy to construct environment-dependent features of increasing complexity, to be used as candidates in the feature space.

4. IDENTIFYING ERROR IN MACHINE LEARNING MODELS

The design of new materials has long relied on DFT, molecular dynamics, phase field calculations, and more. While these approaches are very useful, they are also costly in terms of computational resources and time, limiting their utility. In the past decade, we have seen a surge in interest in applying machine learning (ML) techniques to help address these challenges.[70−72] For example, fewer computations need to be performed if an ML algorithm is able to prescreen compounds of interest.[73,74]

Despite increasingly broad acceptance of ML in the discovery of new materials, there remain common and often valid criticisms,[75] which include:

(i) Necessity of data. Is there sufficient data in the literature, and how do we organize it in a way that is useful?
(ii) ML algorithms are a black box. As such they lack the ability to provide physical insight from a mechanistic perspective.
(iii) Suspicions about the ability to extrapolate beyond the training data.
(iv) We often do not consider the error, or uncertainty, associated with model predictions.
(v) Reported error does not represent the actual ability to predict targets due to overfitting.
(vi) Given relatively recent adoption of data science into material science, there remain numerous instances of bad data practices.

The ML community has begun to identify and address these issues in a number of ways.[76,77] Next, a tool to allow materials research practitioners to leverage their chemical knowledge to identify model error is explored.

4.1. An Interactive Tool to Visualize Model Error and Chemistry. The error identification in ML is accomplished by providing an interactive tool to visualize error and chemistry. In our experience, materials researchers want to rely on their own chemical intuition as they address the following questions:

(a) Do I have enough data for meaningful learning?
(b) Do my data provide the required diversity to predict across a variety of chemistries?
(c) Is my data set skewed toward certain types of chemistry?
(d) Is my model error artificially low due to overfitting?

At the heart of these questions are two key problems: (i) understanding the error associated with sparse representation of chemical classes, and (ii) recognizing the extent of chemical clustering and how clustering may effect performance. As we seek to understand the role of chemistry in model error, it is best described with a model system.

Consider this preliminary tool[78] built using a model that predicts experimental band gap. The model was trained on 2483 compounds where experimental band gap was known, and the details of the model are reported elsewhere.[79] The first thing that this tool provides is a periodic table (Figure 5), where elemental prevalence in the data set is visualized using a heat map. Sorting the data by elements allows us to not only express elemental prevalence but also demonstrate the error versus number of entries. The overall model may look acceptable, but on closer investigation one can see that certain classes sufferer from systematic error.

Figure 6a provides evidence whether the error in these classes could be reduced by obtaining additional entries in this class. In other words, additional data from compounds containing these elements should be gathered to improve

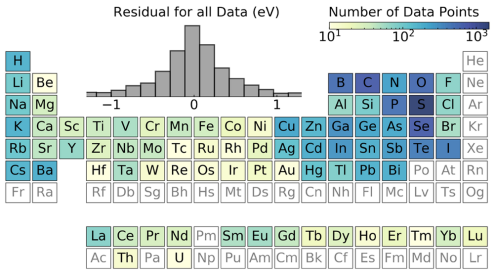

Figure 5. Interactive periodic table allows for quick and efficient exploration of chemical space. The tool is described in detail in ref 78. Such tool will also be generalizable for any machine learning model where chemistries are being explored, not just for bandgap.

accuracy. This same periodic table could be toggled to have the heat map represent the absolute error for compounds containing each element. Moreover, hovering over and clicking on individual elements could then provide element-specific information.

In Figure 6b the distribution of residual values for vanadium are shown. It is also possible to display information regarding the average band gap, the variance in band gap, the percent error, or even things like feature values. Extending this approach to include AND/OR logic (formula contains: O, F, and/or Al) is also possible and would allow for a more nuanced analysis. For example, the residual error associated with hydroxides or fluorooxides can be considered as opposed to the broader class of oxides. This allows users to visualize if the error is a function of trends from the periodic table—which chemists already know and understand such as bonding, electronegativity, size, screening, etc.

Interacting with the periodic table to select elements can also allow for a better analysis of residual plots. The current practice of examining outliers that contribute large errors could instead be replaced by examining whole classes of materials at a

DOI: 10.1021/acs.inorgchem.9b01785
Inorg. Chem. 2019, 58, 14939−14980

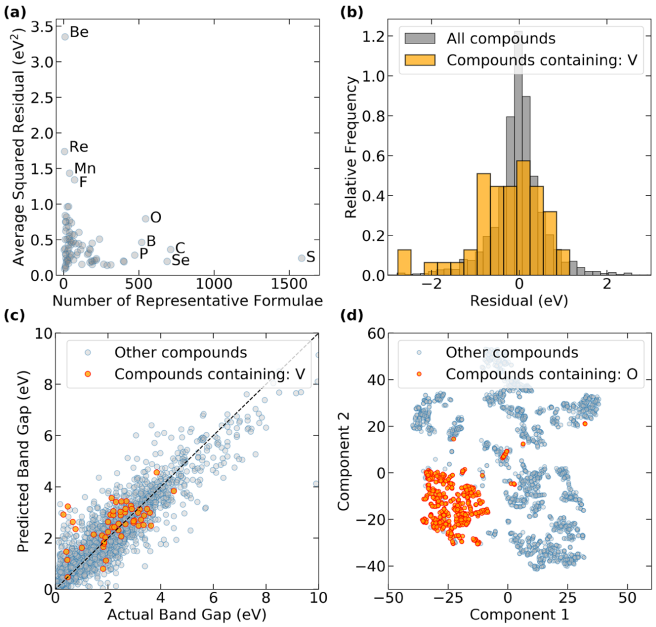

Figure 6. (a) Error decreases as more representative data become available. (b) Residual values allow to explore whether there are patterns in the error associated with compounds containing specific elements. (c) The actual vs predicted values for all experimental band gap values. Compounds containing vanadium highlighted in orange. (d) Extreme example of grouping for compounds containing oxygen on the t-SNE.

time and seeing where their error lies compared to the average model residual error. This can be seen in Figure 6c, where the actual versus predicted band gap of compounds containing vanadium is shown in orange color, while the remaining compounds are shown in blue. This visualization allows a user to easily observe an overprediction trend in this class of materials. This observation is confirmed when the residual error histogram for vanadium versus all compounds is compared in Figure 6b. Furthermore, selecting elements from an interactive periodic table can also provide information about clustering. The dimensionality reduction technique, t-distributed stochastic neighbor embedding (t-SNE),[80] has been used to cluster data together, but determining whether clusters are grouped by chemistry is not straightforward.[81] Users will have to test point-by-point as they seek to establish chemical trends in the clusters.

Visualization of compounds containing specific elements allows for easy identification of which clusters belong to specific chemistries and which chemistries do not cluster. An example is shown in Figure 6d, where the t-SNE plot clearly shows clustering, and one cluster is identified as primarily containing oxides. Is it possible to anticipate that future ML by materials researchers will utilize information from elemental t-SNE diagrams as they select cross-validation training sets to prevent overfitting due to interpolation in overly similar data sets.[81]

4.2. Outlook. As researchers embrace the philosophy of data-driven science, we expect great progress to be made in the materials front. In particular, open-source projects revolving around sharing of materials data could revolutionize how we think about the field of materials science and engineering. Within this paradigm, the training and sharing of ML-based tools has already become popular for the purpose of predicting materials properties. Although this is an exciting prospect, we should be cautious that the data and modeling efforts give appropriate answers. In particular, the types of materials included in these modeling efforts are often skewed toward specific chemistries. This can lead to a systematic error that is otherwise not accounted for in the reported model accuracies. The increased use of data visualization techniques will allow us to probe these models from a domain-driven perspective. Using both materials knowledge and data visualization techniques, we can provide researchers with a strong intuitive feel for how a model performs while also providing a way to visualize and identify common problems that occur in the modeling process.

5. ACCELERATED AB INITIO MOLECULAR DYNAMICS APPLIED TO THE SIMULATION OF HETEROGENEOUS CATALYSIS

The experimental identification of intermediates and surface sites under reaction conditions is challenging. To this purpose, computational approaches based on quantum-chemical calculations have become a fundamental tool to understand reaction mechanisms and investigate active surface sites in heterogeneous catalysis.[82,83] The establishment of DFT as an efficient method to solve the electronic structure problem[84] combined with the development of high-performance computing facilities has fostered the investigation of reaction mechanisms occurring on the solid surfaces.

DOI: 10.1021/acs.inorgchem.9b01785
Inorg. Chem. 2019, 58, 14939−14980

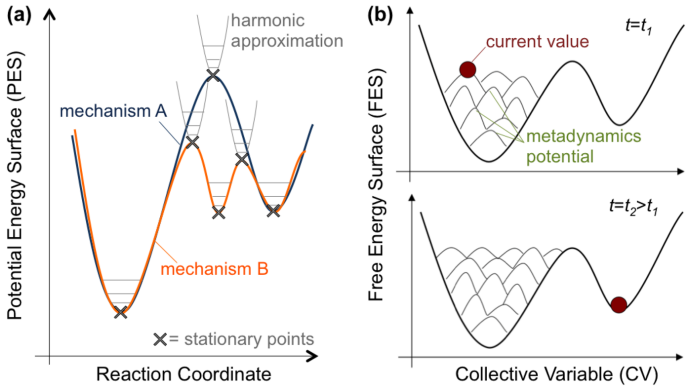

Figure 7. (a) Common approach to evaluate surface reaction mechanisms by DFT calculations: focus on locally harmonic stationary points of PESs corresponding to mechanisms assumed beforehand. (b) AIMD/MetaD approach for reaction mechanism exploration. The history-dependent potential (represented by the Gaussian hills on the FESs in (b)) forces the system to escape from local minima on the FES defined by a set of CVs as the simulation proceeds in time (e.g., t_1 and t_2 shown in (b)).

The evaluation of reaction mechanisms on surfaces based on DFT calculations (Figure 7a) generally consists of (i) the postulation of possible pathways, that is, sequences of bond-forming and -breaking elementary steps that transform reactants into products; (ii) the geometry optimization of selected initial guesses, locating stationary points of the potential energy surfaces (PESs) and calculating the (electronic) energy of minima and transition states along each postulated reaction pathway (at 0 K); and (iii) the estimation of entropic contributions via partition functions, often assuming that the stationary points of the PES are locally harmonic.[85] These procedures allow to obtain the free energy surfaces (FESs) at the reaction temperature. These FESs are then used to discuss the relevance of the different possible reaction mechanisms. In spite of the popularity of such an approach, two severe shortcomings may be associated with it. First, the surface of the catalyst can be highly covered by chemisorbed species under reaction conditions (formation of adlayers), for instance, during the industrially relevant Fischer–Tropsch synthesis and the methanation reactions, among other reactions.[86] For these cases, the energies of reaction intermediates and transition states can be influenced by complex adsorbate–adsorbate interactions. Second, the evaluation of adsorbate entropy by the harmonic oscillator model may be oversimplified when anharmonic,[87−89] translational/rotational,[90−94] or configurational[95] degrees of freedom are relevant for the evaluation of the free energy of minima and transition states. Aside from the above-mentioned standard approaches, it is worth mentioning a recent computational method, namely, *Normal-Modes Transition Approximation*, which rephrases the search of transition paths in terms of eigendisplacements of the dynamical matrix of the system.[96] Such method allows to identify possible reaction paths from the only knowledge of the phonon modes of the stable geometry, showing how to control reaction barriers through a fine-tuning of the eigenfrequencies of the system.

In this section, modeling approaches to evaluate reaction mechanisms in heterogeneous catalysis are based on molecular dynamics (MD). This technique has recently emerged as a promising alternative to overcome the limitations of the PES-based approaches.[97,99]

5.1. Ab Initio Molecular Dynamics. Ab initio molecular dynamics (AIMD)[100,101] is the molecular dynamics method of choice for the study of reaction mechanisms in catalysis. The electronic structure is explicitly included (e.g., at DFT level), allowing the description of bond-breaking and -forming events. During MD simulations, starting from a given initial structure, nuclei positions and velocities are evolved in time subjected to determined thermodynamic boundary conditions. The collection of visited states at finite temperatures (trajectory) can then be used for the calculation of free energy differences. Compared to the common evaluation of discrete points of PESs, the free energies obtained from MD simulations include additional contributions that are fundamental to overcome the limitations of modeling surface reactions on adlayers. The calculation is performed on a large number of configurations explored during the simulation at finite temperature—and not only on selected geometry-optimized structures at 0 K—which increases the chances of capturing relevant adsorbate–adsorbate interactions that affect the energetics of surface reaction mechanisms. Furthermore, the free energy is not calculated using a posteriori correction to the PES, but it is instead obtained on-the-fly during the simulation. This means that the partition functions simultaneously include translational, rotational, and (anharmonic) vibrational degrees of freedom. Despite such benefits, the evaluation of free energy differences by AIMD is computationally demanding. In particular, surface reactions involving energy barriers much higher than thermal energy require relatively long trajectories resulting in prohibitive calculations. This problem can be avoided by coupling the AIMD with the Metadynamics (MetaD) technique.[99,102−106]

5.2. Metadynamics. MetaD consists of the exploration of the phase space using a reduced configurational space defined by a set of selected reaction coordinates, called collective variables (CVs). At regular time intervals during the AIMD simulation, a history-dependent potential (e.g., Gaussian functions) is applied forcing the system to escape from (local) already explored minima on the reduced phase space

DOI: 10.1021/acs.inorgchem.9b01785
Inorg. Chem. 2019, 58, 14939−14980

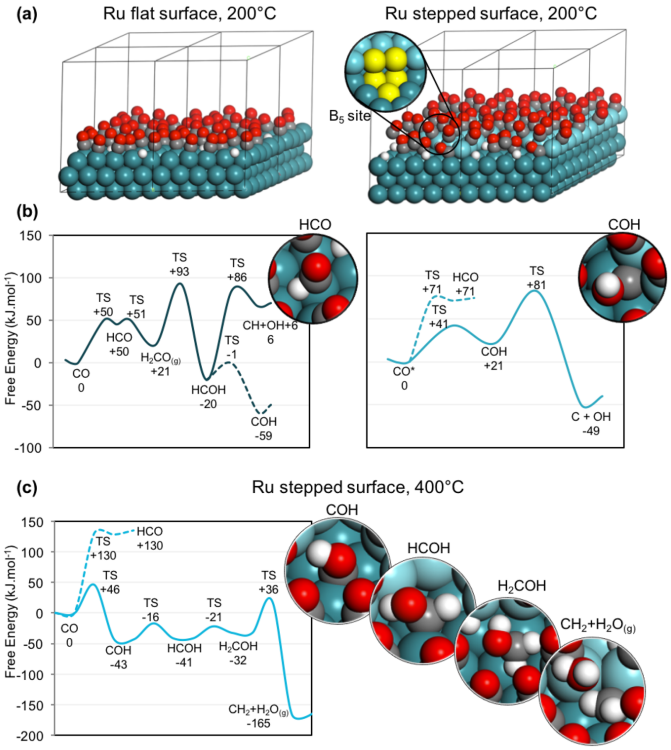

Figure 8. (a) CO activation at Fischer−Tropsch reaction conditions (200 °C) modeled by AIMD/MetaD simulations: Ru flat and stepped model surfaces (containing step-edge sites shown in the inset) covered with CO/H adlayers and (b) FESs for observed mechanisms: HCO vs COH intermediates on the flat and stepped surfaces, respectively (shown in the insets). (c) CO activation at methanation reaction conditions (400 °C) modeled by AIMD/MetaD simulations: FES for mechanism identified on the stepped Ru surface involving multiple hydrogen transfers and water elimination (reaction intermediates shown in the insets). Ru, C, O, and H atoms are shown in blue, gray, red, and white, respectively. The Ru atoms of the top layer in the Ru stepped surface are shown in lighter blue. The simulation cell is shown in black (a 2 × 2 supercell is represented). (a, b) Adapted from ref 97; (c) adapted from ref 99.

(Figure 7b). For sufficiently large simulation times, the applied MetaD potential approximates the FES, and the meta-trajectory follows the minimum free energy pathway. The use of MetaD therefore replaces the need to postulate, beforehand, the detailed sequence of elementary steps. The combination of AIMD with MetaD has been used to unravel the mechanisms of catalytic processes on molecular systems[107] as well as on oxide-supported clusters and metal surfaces.[97,108−110]

5.3. A Case Study: The Fischer−Tropsch Synthesis. The Fischer−Tropsch synthesis (see eq 8) with $n > 1$, which converts syngas (CO/H_2 mixture) to hydrocarbons, is an example of complex reaction taking place at high adsorbate coverage, whose mechanistic understanding has benefited from the use of AIMD (in this case Born−Oppenheimer MD[100,101]) coupled with MetaD simulations at 200 °C.[97,98] By using ruthenium flat and stepped surface models covered with coadsorbed CO and H species (Figure 8a), the effect of adlayer on the favored reaction mechanisms and the active sites for CO activation, the highly debated key step of the reaction, was addressed.

$$n\mathrm{CO} + (2n+1)\mathrm{H_2} \leftrightarrows \mathrm{C}_n\mathrm{H}_{(2n+2)} + n\mathrm{H_2O}$$
$$\Delta H^{\circ}_{298} = -167\ \mathrm{kJ/mol} \quad (8)$$

AIMD/MetaD simulations were performed by using a set of three CVs, namely, C−O distance, C−H coordination number, and O−H coordination number. The simulations allowed to capture, simultaneously, several mechanisms involving zero or several hydrogen transfer steps to both C and O ends of the adsorbed CO molecule, in any order, before the actual elementary step of C−O cleavage. It was found that the CO activation mechanism via the formyl intermediate (HCO) is the most likely one on the flat surfaces (Figure 8b), in line with previous proposals.[111] Conversely, in the case of the stepped surface, hydrogen-assisted routes via the COH intermediate are the most favored ones (Figure 8b).[112] This is because adsorbed H preferentially bound to step-edges can be easily transferred to carbon monoxide O end at high coverages. The comparison of the reaction intermediates stability calculated by the evaluation of discrete points of the PES and the AIMD/MetaD approach reveals that the dynamic effects are hardly

DOI: 10.1021/acs.inorgchem.9b01785
Inorg. Chem. 2019, 58, 14939−14980

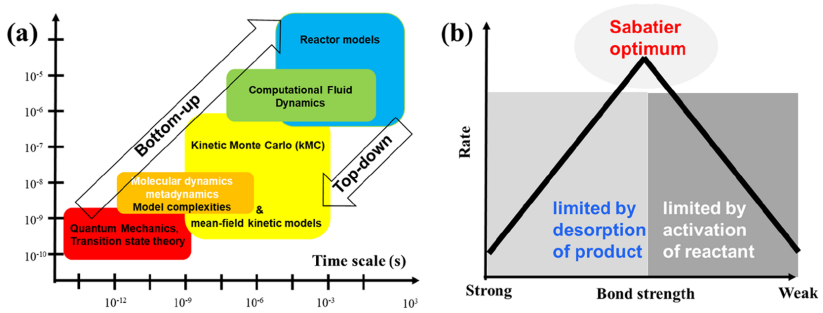

Figure 9. (a) Top-down and bottom-up catalyst development/length and time scales. (b) Sabatier principle, which states that there is an optimum "bond strength" defining the best catalyst for a given reaction (partially based on refs 120 and 147).

captured by the static approach, due to complex adsorbate−adsorbate interactions.

The methanation reaction on ruthenium (eq 8, with n = 1) was also studied, using the same models and methodology at a higher temperature (400 °C).[99] The simulations revealed that, in the presence of step-edges, an unusual low-energy mechanism, involving four hydrogen transfer steps and the simultaneous C−O cleavage with the formation of CH_2 species and H_2O, is available on the stepped surface (Figure 8c). This mechanism is entropy-driven, since the C−O bond activation step involves the formation of a water molecule, which readily desorbs from the surface. These results reveal how valuable can be the AIMD/MetaD approach in capturing entropy-driven mechanisms at higher temperatures. Despite the use of MetaD to accelerate the AIMD simulation, the computational effort needed for such simulations, which need the evaluation of the electronic structure at each time step of the MD run, is still high, and some of the limitations of the approach are associated with it. If on one hand the MetaD potential allows crossing of energy barriers, on the other hand the simulation time scale (in the order of ps) is not long enough to allow equilibrating of gas-phase species with the surface. This means that the coverage is fixed during the simulations and needs to be carefully determined beforehand via, for instance, ab initio thermodynamics.[113] The accuracy of FESs calculated by MetaD[103,114] depends on the shape of the biasing potential (Gaussian hill height and width) as well as on the frequency at which it is applied; there is thus a compromise between the accuracy and the length of the simulated time. Larger hill width and height applied more frequently, for instance, will enable quicker exploration of the free energy landscape but will also smear out the details of the FESs and increase the error of the simulation. Another limitation of the MetaD technique is related to the choice of CVs, since mechanisms that are not described by the chosen set cannot be accessed.

5.4. Outlook. The application of the AIMD/MetaD techniques to catalytic processes, occurring on the materials surface, shows its potential to unravel favorable reaction mechanisms in heterogeneous catalysis. Such techniques result to be particularly useful in the case of reactions that occur at high coverages, where adsorbate−adsorbate interactions modulate the preferred pathways. Nevertheless, the high cost of the simulations is still a drawback. The recent development of accurate and less resource-consuming representation of the PES by statistical methods[115] represents a promising alternative to overcome such limitation, which could enable the systematic analysis of reaction networks in heterogeneous catalysis by AIMD simulations.

6. PREDICTIVE DESCRIPTION OF CATALYTIC SYSTEMS USING MICROKINETIC MODELING

Ab initio-derived free energy landscapes embedded within kinetic and Monte Carlo models[116−130] are a recent evolution necessary to bridge the gaps between theory and experiment in catalytic systems modeling (Figure 9a). This gap can either be bridged in a top-down fashion, using parameter fitting and regression analysis, or in a bottom-up fashion, using ab initio data.[120,131]

Within the bottom-up approach, temperature and pressure gaps can be sufficiently bridged by the embedding of a computational reaction network (computational reaction kinetics) within kinetic model and/or Monte Carlo models. However, it remains challenging to make a realistic atomistic model, which should be representative enough for the studied catalyst.

Recently, ab initio-based kinetic and Monte Carlo models have demonstrated their usefulness to get insights into reaction mechanisms onto various catalyst models, such as metal nanoparticles,[132] periodic metal surfaces,[124,125,129] as well as oxides,[126,127] and even metal-oxide interfaces.[123,128,130] The computational catalyst development has frequently used simplified reaction networks by exploitation of scaling relations. These have been known in various subfields of chemistry for several decades as Brønsted relations, Evans−Polanyi relations,[133,134] and Hammett equations.[135] The computational prediction of qualitative structure−activity relationships or QSARs facilitates the development of more active new catalysts. Within the last two decades, Nørskøv and co-workers have focused on the application of DFT on metal surfaces to identify computational activity descriptors.[136−140] Plotting the logarithm of the turnover frequency in function of one or more descriptors allows the construction of one- or multidimensional "volcano-plots" (Figure 9b). A famous example of a descriptor is the N_2 dissociation energy (EN-N) in case of the NH_3 synthesis.[138,139] Besides numerous examples of energy descriptors, for example,[138,139,141,142] there are other frequently used descriptors, such as the d-band center.[136,143,144] The d-band center can, for example, be employed to rank metals for their CO dissociation potential.[145,146] By constructing scaling relations and embed-

DOI: 10.1021/acs.inorgchem.9b01785
Inorg. Chem. 2019, 58, 14939−14980

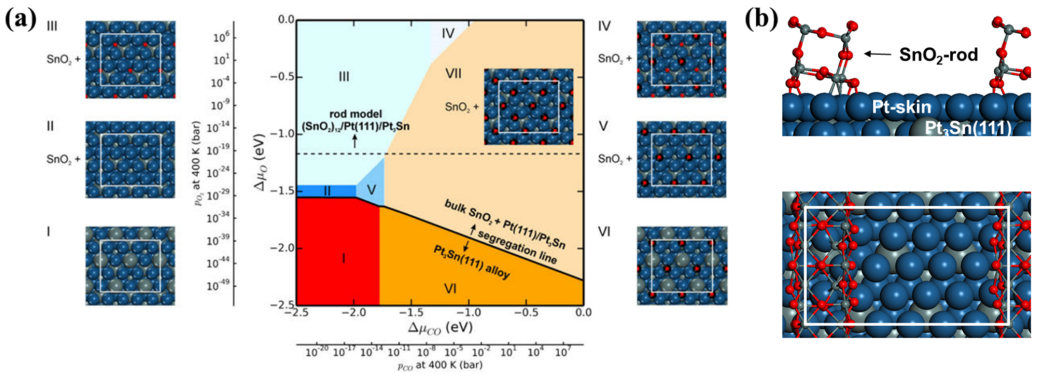

Figure 10. (a) Thermodynamic phase diagram showing the preferred phase [lowest difference in surface energy with respect to $Pt_3Sn(111)$] as a function of differences in chemical potential ($\Delta\mu_i$) for CO and O_2. The solid black line indicates segregation from a $Pt_3Sn(111)$ surface to Pt/$Pt_3Sn(111)$ and bulk SnO_2. Structural models for the phases I–VII are shown. (b) The dotted line shows the conditions, when the formation of the rod model becomes thermodynamically preferred. The surface cells are indicated by white rectangles. Atomic color codes: C in black, O in red, Sn in green, and Pt in blue (based on ref 123).

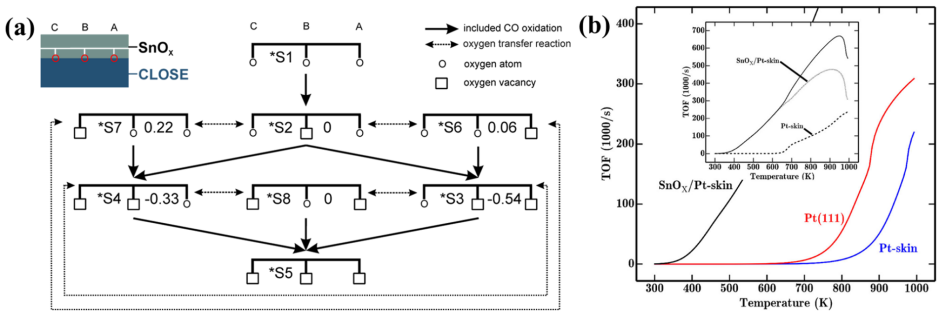

Figure 11. (a) Considered reactions for the SnO_X/metal interface model or SnO_X/Pt(111)/Pt_3Sn model within the mean-field microkinetic model. The energy differences between SnO_X-states with the same number of oxygen atoms are given in electronvolts (displayed green). (b) Comparison of the TOF for Pt(111), Pt(111)/Pt_3Sn, and SnO_X/Pt(111)/Pt_3Sn (inset). Different contributions to the total TOF for SnO_X/Pt(111)/Pt_3Sn. The partial pressures for CO and O_2 are 11.0 and 21.4 mbar, respectively (On the basis of ref 123).

ding these within ab initio Micro-Kinetic Models (MKM), it is possible to map the catalytic activity onto a 1D or two-dimensional (2D) descriptor space and obtain activity and selectivity maps.[140] The resulting activity maps can be viewed as a quantitative implementation of the classical Sabatier principle.[147] This screening approach is applied frequently to metal surfaces,[147,148] and it allows the selection of optimal metal alloys.

The computational screening approaches that exploit scaling relations between activation energies and reaction energies are also dependent on (i) the reaction mechanism and (ii) the atomistic model.[136−139,149] Furthermore, the simplified scaling approach still lacks complexity and is unable to describe possible catalytic interface effects and support effects, confinement effects, etc. In most cases adsorbate−adsorbate interactions on metallic systems and adsorbate pairing effects on oxides are also neglected when scaling relations are constructed. This explains why most state-of-the-art kinetic models cannot predict catalyst activities and selectivities reliably. It is thus clear that existing microkinetic models can be improved by the addition of more complexities.

6.1. Embedding Complexities within the Microkinetic Modeling on Interface Catalysts: The Case Study of CO Oxidation on PtSn. Sometimes it happens that the classical reaction route can be circumvented by another reaction route, for example, a route taking place at a catalytic interface. Then, the computational description of interfaces becomes important, since the presence of interfaces creates new reaction mechanisms.

In recent years, a variety of atomistic models and/or computational reaction pathways have been presented describing reactions onto catalytic interfaces, for example, for CO_2 conversions[128,130,150−154] and CO oxidation.[123,155−162] While the reaction networks are studied in detail on these interface catalysts, they are frequently not included within microkinetic models, and even for developed existing ab initio kinetic models[123,128,130] there is still room to implement more complexities.

DOI: 10.1021/acs.inorgchem.9b01785
Inorg. Chem. 2019, 58, 14939−14980

For CO oxidation on PtSn nanoparticles, the low-temperature CO oxidation activity arises from the presence of a SnO_X/Pt interface.[123] The idea that SnO_X/Pt interfaces were responsible for the catalytic activity was postulated initially by the renowned Somorjai group in 2014.[163] The likelihood to form such SnO_2/Pt interfaces can be studied via ab initio thermodynamics, by ranking different studied phases according to their most stable surface energy in function of the chemical potential ($\Delta\mu_i$) for CO and O_2 (Figure 10).

As chemical potentials are functions of temperature and pressure, it is possible to plot the corresponding pressure axis for each temperature, for example, at 400 K (Figure 10a). At regular operating conditions for CO oxidation, that is, pO_2 and pCO > 0.01 bar, the segregated system of a Pt-skin and SnO_2-bulk is thermodynamically more feasible compared to the bare alloy phase. However, a more likely situation is presented in Figure 10, where a bulklike SnO_2 rod is formed that is 0.72 eV/SnO_2 higher in energy compared to bulk SnO_2,[123] the dotted line in Figure 10. Different sites can be present at a SnO_2/Pt-skin interface. Therefore, a representative number of interface sites should be evaluated and included within kinetic and Monte Carlo models.

For the SnO_2 rod (Figure 10b), a reaction scheme can be constructed based on the three different possibilities into which oxygen can react with CO (A, B, and C in Figure 11a). This results in a network containing eight different states of the rod (*Si, where i is the state, Figure 11a), which can be embedded as a microkinetic model with 23 elementary reactions, accounting for regeneration steps as well as transfer steps between states of the rod with the same number of oxygen atoms.[123]

This microkinetic model for CO oxidation at the chosen SnO_2/Pt interface can then be compared with a model for CO oxidation on Pt(111) (Figure 11b). The cocatalytic role of a SnO_2 rim is clearly manifested in an enhanced activity at low temperatures. Furthermore, the interface is even found to solely contribute to the CO oxidation rate below 600 K. To make this kinetical model for CO oxidation work, several complexities need to be included: coverage-dependent adsorption energies and CO oxidation barriers. Moreover, for a mean-field microkinetic model, also a realistic determination of a representative site distribution is required (SnO_2: 12.6%, interface: 15.7%, metal: 71.7%) as well as diffusion possibilities for CO from metal to near (SnO_X/Pt interface)-sites.

6.2. Outlook. Within computational catalysis, there is a trend to validate whether the catalytic model systems are representative at operating conditions based on ab initio thermodynamics. The reaction network is closely related to the type of active sites, and the coupling of various routes within microkinetic models allows to distinguish which routes are more feasible based on rate control analysis, which is a promising technique to evaluate microkinetic and Monte Carlo methods.[164−167] The technique allows to extract the rate-controlling reaction mechanisms, that is, those that contribute most to the turnover frequency.[123,130]

The computational determination of the apparent activation barrier and reaction orders for a given reaction condition remains necessary to achieve a good comparison with the experimentally measured activation barriers and reaction orders.[126] Nevertheless, the type of active sites can vary a lot, especially within model systems describing interfaces, which means that a representative distribution of sites needs to be investigated before a correct activity picture can be constructed.

Catalyst changes during a catalytic run remain hard to describe. No models can yet describe the adsorbate restructuring of metal nanoparticles upon adsorption. Nevertheless, kinetic Monte Carlo methods have been successfully implemented to describe the aggregation of different catalyst particles as a function of temperature.[168] However, it remains a major challenge for the future to describe the restructuring based on adsorbates. For CO oxidation on metal nanoparticles, this restructuring during reaction could include a coordination number and coverage-dependent scaling of adsorption energies and barriers, as successfully implemented for nanoparticles of different shapes.[132] Summarizing, bridging the pressure and temperature gaps becomes feasible via using ab initio microkinetic models or Monte Carlo models, and implementing catalyst dynamics to bridge the materials gaps remains a major challenge for the future.

7. ATOMIC DESIGN PRINCIPLE FOR SAFER BATTERY MATERIALS

One of the main concerns with respect to high-energy batteries is safety. Li-ion batteries exhibit so-called dendrite growth[169] that can lead to short-circuits and to subsequent battery fires.[170,171] The process of dendrite growth is rather complex,[171] and the reasons for its occurrence are not fully understood yet. Interestingly, while Na-ion batteries also show dendrite growth,[172] Mg-ion batteries do not.[173] Unfortunately, existing models for dendrite growth are typically not element-specific and, therefore, are not able to explain why Li and Na exhibit dendrite growth but Mg does not.

7.1. The Dendrite Growth Problem. Growth processes require mass transport, and recently it was suggested that there might be a correlation between the height of diffusion barriers of Li, Na, and Mg and their tendency toward dendrite growth.[174] Indeed, DFT electronic structure calculations found that Mg has a diffusion barrier on its most stable surface termination that is 1 order of magnitude smaller than the corresponding diffusion barriers of Li and Na.[174] On the basis of these results, it was argued that low diffusion barriers lead to a high mobility of the deposited metal atoms so that they can easily attach to existing step edges and lead to the growth of smooth surfaces. In contrast, high diffusion barriers lead to immobile surface atoms, which are the origin of rough surfaces.

Concerning the growth environment of dendrites, it was found in Li deposition experiments that the formation of needles occurs both in an electrochemical environment as well as under vacuum conditions.[175] This indicates that the growth of Li dendrites is an inherent property of lithium itself. Moreover, it is important to note that, for the growth of smooth surfaces also the diffusion barrier across step edges, the so-called Ehrlich-Schwöbel barrier,[176,177] is critical. When metal atoms are deposited on top of an existing island, two-dimensional growth will only result if the atoms are easily able to propagate to the lower terrace. Now, the transfer from the upper to the lower terrace across the step is typically hindered by rather large barriers, as the diffusing atom has to propagate through an energetically very unfavorable low-coordinated configuration. This is illustrated in the upper right panel of Figure 12, which indicates that the diffusion process across the step in the so-called hopping mode is hindered by a large barrier.

DOI: 10.1021/acs.inorgchem.9b01785
Inorg. Chem. 2019, 58, 14939−14980

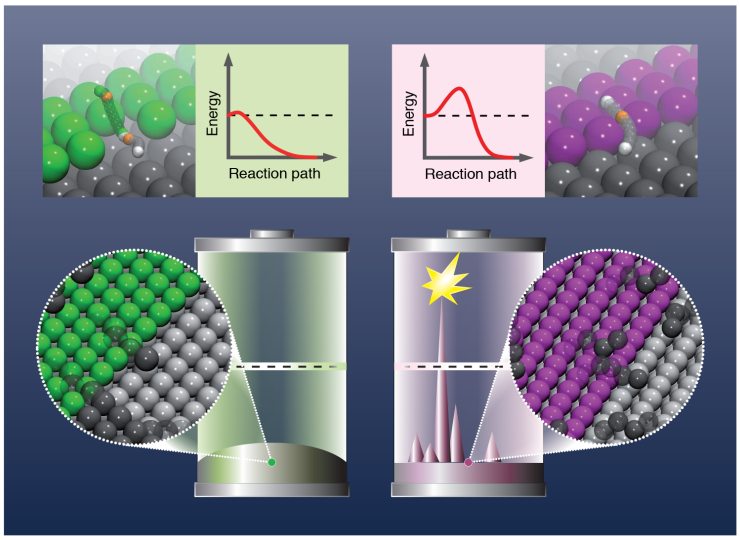

Figure 12. Illustration of the relation between diffusion barriers across step edges and the tendency toward dendrite growth in batteries. The two upper panels depict diffusion paths from the upper to the lower terrace, whereas the two lower panels illustrate the consequences of the diffusion barriers on the growth mode of the deposited metal atoms. (right panels) If diffusion from the upper to the lower terrace occurs in the hopping mode, large barriers result. Thus, the deposited metal atoms tend to stay on upper terraces and islands, leading to rough surfaces and eventually dendrite growth. (left panels) Diffusion across the step in the exchange mode is usually associated with small barriers. Thus, deposited metal atoms can easily move to the lower terraces leading to the growth of smooth flat surfaces thus prohibiting dendrite growth.

In a recent DFT study, diffusion barriers of Li, Na, and Mg across steps, as illustrated in the upper panels of Figure 12, were considered.[178] Furthermore, the study was extended to the diffusion of zinc and aluminum, which correspond to promising beyond-Li battery systems.[179−181] On the one hand, these calculations confirmed the previous findings, showing that the Li and Na body-centered cubic (bcc) metals also exhibit relatively large barriers for diffusion across steps. On the other hand, on the hexagonal close-packed (hcp) metal Mg, propagation across steps is facilitated through the exchange mechanism,[182] which is illustrated in the upper left panel of Figure 12. Instead of hopping from the upper terrace to the lower terrace across the step through a low-coordinated configuration, as shown in the upper right panel of Figure 12, the adatom from the upper terrace pushes a step atom away from the step onto the lower terrace thereby replacing it. Although in this mechanism two atoms have to move, they maintain a high coordination number along the minimum energy path making it energetically favorable. The lower panels of Figure 12 illustrate the consequences of these two different mechanisms. On the one hand, if the barriers to propagate from an upper terrace to a lower terrace are large, then atoms deposited on upper terraces or islands will remain there, which will lead to rough surfaces. These could then act as nuclei for the dendrite growth, which can cause short-circuits in the batteries and thus battery fires, as indicated in the right panels of Figure 12. If, on the other hand, the diffusion barrier to propagate to the lower terrace are rather small, then atoms deposited on the upper terraces will easily leave these upper terraces, attach to the step edges at the lower terrace, and thus lead to the growth of smooth surfaces, as illustrated in the left panels of Figure 12.

Diffusion on aluminum and zinc, whose most favorable surface terminations like Mg correspond to densely packed hexagonal structures, is also only hindered by rather small barriers. However, it is well-known that the growth of dendrites in Zn-based batteries is a serious issue.[183] Thus, on the one hand, it seems that there is an inconsistency between Al and Mg on the one side and Zn on the other side, as far as the correlation between the height of the diffusion barriers and the tendency toward dendrite growth is concerned. On the other hand, it has been shown that, in fact, the conversion of Zn to ZnO during battery discharge is critical for the occurrence of dendrites in Zn-air batteries.[180,181] Typical Zn anodes are made of loosely connected Zn powder and polymer binder. Upon discharge, resistive ZnO forms between the particles interrupting the interparticle conductivity, which has been proposed to lead to dendrite formation.[180] Zn dendrite growth can in fact been suppressed, if the Zn anode is kept metallic by using a spongelike Zn anode with interconnected continuous Zn domains.[180,181] This indicates that dendrite growth is caused by the formation of ZnO needles, that is, by the loss of metallic properties. Consequently, it does not correspond to an inherent property of Zn, as also suggested by the calculations presented above. Thus, from the theoretical considerations together with the experimental observations, a design principle for dendrite-free metal anodes can be derived, as illustrated in Figure 12. It will help to select a metal with low self-diffusion barriers, thus preventing the dendrite growth, and to maintain the metallic properties during charging and discharging.[178]

DOI: 10.1021/acs.inorgchem.9b01785
Inorg. Chem. 2019, 58, 14939−14980

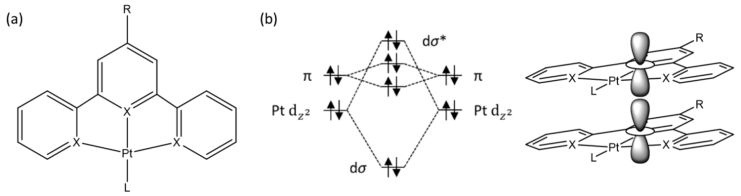

Figure 13. (a) Structure of a general Pt(II)-"pincer" complex, where the symbol X may represent N^C^N, N^N^C, or C^N^C depending on the chosen ligand skeleton. (b) Vertical stacking through supramolecular assembly or in the solid state leads to overlap of the Pt d_{z^2} orbitals, producing a new metal−metal dσ* orbital higher in energy than the pincer-based π orbitals.

7.2. Outlook. Note that, in the study described above,[178] no full theory of dendrite growth was presented. Rather a correlation has been found between a property of the considered material, the height of self-diffusion barriers, and an observable related to this material, namely, its tendency toward dendrite growth. Hence the height of the diffusion barriers can be used as a descriptor for possible dendrite growth. The concept of descriptors has been discussed in detail in Section 3 of this work. There it was shown how descriptors can be learned from gathered data of materials in a machine learning approach. Here the descriptor has been rather proposed based on physical reasoning. Independent of how the descriptor has been identified, it represents a very powerful tool for improving materials properties. A very first selection of promising materials does not need to be based on a full study of its desired properties but rather on whether the materials value of the descriptor for the desired property falls in the desired range. Furthermore, it also provides a design principle for materials with the desired properties. In the case of dendrite growth in batteries considered here, the results presented above suggest that diffusion of metal atoms deposited on the electrode should be kept facile.

Still it should be kept in mind that here no simulations of dendrite growth have been reported. Note that also for Mg the formation of dendrites during electrodeposition has been observed,[184] although it is typically assumed that Mg does not exhibit dendrite growth.[173] Hence further theoretical studies are required to clarify the connection between self-diffusion properties and the tendency toward dendrite growth,[185] taking the electrochemical environment at the interface between electrode and electrolyte more realistically into account.[186]

8. RESPONSIVE MOLECULAR SOLIDS

Molecular solids are an attractive prospect for low-to-medium temperature device applications,[187−189] because molecular design can access virtually limitless chemical diversity and can tap into the large body of knowledge on synthetic routes, structure−property relationships, supramolecular assembly and crystal engineering to match the properties to the application. Many molecular materials are amenable to solution processing, providing flexibility for incorporating them into device structures, and can meet increasingly important practical concerns such as being nontoxic and prepared by environmentally friendly chemical processes from earth-abundant elements and sustainable chemical feedstocks.

Quantum-chemical modeling has long been instrumental to understanding structure−property relationships in molecules, and advances in techniques for modeling periodic systems and the capabilities of high-performance computing (HPC) have led to an explosion in theoretical screening studies on inorganic solids.[190] The generally larger and lower-symmetry crystal structures formed by molecular solids pose a bigger challenge, but capabilities are rising to meet demand. As we will see, modeling studies play an increasingly valuable role in understanding the link between the molecular species, solid-state structure, and physical properties of functional molecular solids, and they are particularly powerful when combined with state-of-the-art experimental techniques.

Two example classes of responsive molecular solids are reviewed here, with a particular focus on highlighting the interplay between experiment and theory that has led to a fundamental understanding of their behavior and properties.

8.1. Vapochromism in Pt-"Pincer" Complexes. Cyclometalated square-planar Pt(II) complexes based around tridentate "pincer" ligands (Figure 13a) are widely studied for their tunable luminescence[191−193] and have applications as organic light-emitting diode (OLED) emitters and biological imaging agents.[187−194]

Stacking of the planar molecules through supramolecular assembly in solution or in the solid state causes the occupied Pt d_{z^2} orbitals to interact, producing a frontier molecular orbital (MO) above the π MOs on the aromatic ligand (Figure 13b).[189] This results in strong metal−metal ligand charge-transfer (MMLCT) optical absorptions that in the solid state are highly sensitive to the crystal packing.[195] The stacking also produces channels allowing small molecules to diffuse into the crystal and interact with functional groups, either on the pincer scaffold or the ancillary ligand at the fourth Pt coordination site,[196−198] which modulates the energies of the frontier orbitals, widens or narrows the energy gap, and shifts the onset of absorption.[196]

There are several examples in the literature of pincer complexes exhibiting vapochromic responses to small-molecule analytes. [PtCl{$C_6H_2(CH_2NMe_2)_2$-2,6-OH-4}] undergoes a reversible solid-state reaction with SO_2 gas on the time scale of minutes, which is accompanied by a change from colorless to orange.[199] [Pt(Me_2bzimpy)Cl]Cl·$2H_2O$ (Me_2bzimpy = 2,6-bis(1-methylbenzimidazol-2-yl)pyridine) changes from yellow to red on exposure to methanol, chloroform, ethanol, and acetonitrile, while the corresponding PF_6^- salt shows a selective color change from yellow to violet when exposed to acetonitrile.[195] A similar response is also shown by the dimethylformamide (DMF) solvate [Pt(Me_2bzimpy)Cl](PF_6)·DMF.[200]

Recently, a new vapochromic system was identified based on the 1,3-di(2-pyridyl)benzene (N^C^N) pincer skeleton with R = C(O)OMe and L = CN^-.[196] Quantum-chemical calculations were used to screen potential ancillary ligands, from which the

DOI: 10.1021/acs.inorgchem.9b01785
Inorg. Chem. 2019, 58, 14939−14980

cyanide complex (Figure 14a) was selected based on (1) a high-energy Pt d_{z^2} orbital, placing the solid-state MMLCT band within the visible spectrum (Figure 13b), and (2) the high polarity and potential to form strong hydrogen bonds to guest molecules in the crystal structure. Microcrystalline thin films coated on glass or impregnated flexible polymer films showed selective subsecond responses to dry gases, water, and methanol, changing between a yellow empty structure, a red hydrate, and a blue methanolic form (Figure 14b).

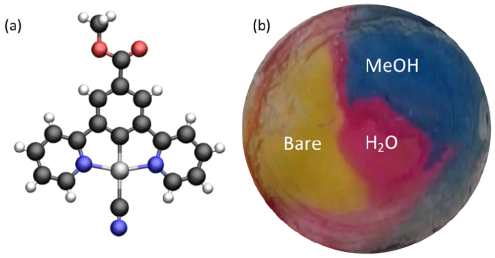

Figure 14. (a) Molecular structure of the Pt complex reported in ref 196, taken from the X-ray structure without guest molecules (CCDC: GEJTOH). (b) Image of a microcrystalline thin film of the compound showing the desolvated ("bare") yellow form and the vapochromic responses to H_2O (red) and MeOH (blue).

With synchrotron radiation, high-quality single-crystal X-ray structures of the dry (yellow) form and the hydrate and methanol solvate (red/blue) were obtained, allowing the electronic structures to be modeled. The calculations confirmed the conceptual picture in Figure 13, with the highest-occupied crystal orbitals (HOCOs) being degenerate chains of antiphase Pt d_{z^2} MOs and the lowest-unoccupied crystal orbitals (LUCOs) being pincer-based π MOs supporting strong MMLCT absorptions. By comparing the empty and solvated crystal structures, it was shown that the different patterns of H-bonding between the solvents and ancillary CN ligand changed the Pt−Pt distances and the offset between the Pt centers, modulating the degree of orbital overlap and the resulting HOCO energy. The calculations also revealed secondary interactions between LUCOs which led to a further cooperative reduction in the gap and red-shifted absorption with increasing overlap.

This study highlights the role of modeling both at the molecular-design phase and in understanding the links between solid-state structure and properties, and it also illustrates the strong synergy between experiment and theory.

8.2. Photoactivated Linkage Isomerization. Linkage isomers are coordination complexes where one or more ligands display several distinct binding modes to the metal centers.

Reports of linkage isomerism date at least as far back as the 1900s, when the color difference between the yellow and red forms of the Co complex $[Co(NH_3)_5(NO_2)]Cl_2$ was explained by the nitrite (NO_2^-) ligand coordinating to the metal through either N or O (Figure 15a). ^{18}O-Labeling experiments showed that the ONO-coordinated isomer was a kinetic product and converted to the more stable NO_2 isomer via an intramolecular rearrangement.[201] By using spectroscopic techniques, it was also shown that the isomerization occurs both in solution and in the solid state.[202] The isomerization between both forms can also be effected photochemically by irradiating at an appropriate wavelength.[203]

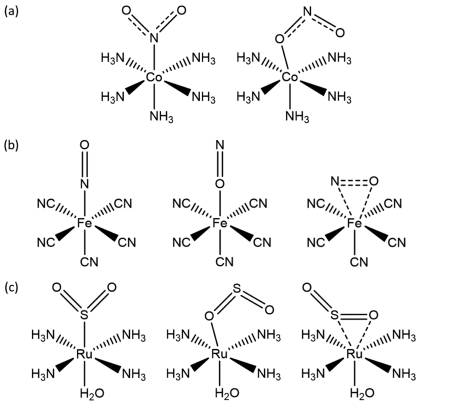

Figure 15. Examples of linkage-isomer complexes: (a) NO_2 binding modes in $[Co(NH_3)_5(NO_2)]^{2+}$; (b) NO binding modes in $[Fe(CN)_5(NO)]^{2-}$ (nitroprusside); and (c) SO_2 binding modes in $[Ru(NH_3)_4(H_2O)(SO_2)]^{2+}$.

Photoswitchable materials are of interest for a number of applications. The photoexcitation in $[Nd(dmf)_4(H_2O)_3(\mu\text{-}CN)Fe(CN)_5]\cdot H_2O$ is accompanied by a change in magnetic susceptibility, raising the possibility of optically switched and magnetically read molecular data storage.[204] Photochromic materials have also been investigated for data storage and have a wide range of other potential uses including as optical switches and photocontrolled catalysts.[205] More recently, a linkage-isomer system was identified where the photoactivated isomerization induces rotation of a neighboring benzene ring, thus acting as a transducer between solar energy and mechanical motion.[206]

In the solid state, linkage isomerism results in the movement of whole atoms and typically proceeds without loss of crystallinity, allowing the process to be followed with single-crystal X-ray diffraction. Pioneering "photocrystallography" experiments conducted by Coppens et al.,[207] in which single crystals were irradiated in situ on the diffractometer and the fractional occupations of the ground and metastable isomer(s) refined from the data, conclusively identified three NO binding modes in sodium nitroprusside $Na_2[Fe(CN)_5(NO)]\cdot 2H_2O$ (SNP; Figure 15b), and the technique has remained of huge importance to the field since then.[208]

Following the seminal work on SNP, several families of organometallic linkage isomers have been identified and characterized, including systems based on nitrite (NO_2^-),[209−211] sulfur dioxide (SO_2; Figure 15c),[206,212,213] and (di)nitrogen (N_2) ligands.[214] Key material parameters are the speed and extent of the photoconversion and the thermal stability of the metastable state. Earlier studies focused on maximizing photoconversion, and in 2009 Warren et al. demonstrated 100% conversion in $[Ni(dppe)(NO_2)Cl]$ (dppe = 1,2-bis(diphenylphosphino)ethane) by using the bulky dppe ligand to engineer a large "reaction cavity" to facilitate the isomerization.[215] More recently, attention has turned to increasing the so-called metastable limit—the temperature above which spontaneous decay of the metastable

DOI: 10.1021/acs.inorgchem.9b01785
Inorg. Chem. 2019, 58, 14939−14980

state can be observed—toward room temperature, with a view to eventual device applications, and a limit of 240 K was recently achieved with $[Pd(Bu_4dien)(NO_2)]BPh_4$ (Bu_4dien = *N*,*N*,*N*′,*N*′-tetrabutyldiethylenetriamine, BPh_4 = tetraphenylborate).[216]

Computational modeling is regularly employed alongside experimental measurements on linkage isomers to study the energetics of the isomerization and to identify possible conversion pathways and the associated activation energies.[217,218] A recent study on the $[Ni(Et_4dien)(\eta^2\text{-O,ON})(\eta^1\text{-}NO_2)]$ linkage-isomer complex used time-dependent density-functional theory (TD-DFT) to examine the photochemical conversion between the ground-state NO_2 and metastable-state ONO binding modes.[217] Redistribution of electron density, due to low-lying metal-to-ligand charge-transfer (MLCT) absorption bands, was found to populate antibonding states and reduce the activation barrier to isomerization. However, as this particular system also shows thermal isomerization, which was studied using molecular-dynamics simulations,[217] it is also possible that strong vibronic coupling could promote isomerization by leaving the system in a vibrational "hot" ground state after de-excitation.

Another area where modeling plays an important role is in studying the isomerization kinetics. Improvements in X-ray sources and detector technology, particularly at synchrotron facilities, have made it feasible to probe the kinetics of the forward (excitation) and reverse (decay) isomerization processes with time-resolved X-ray diffraction experiments.[208,219] At low temperatures, the metastable isomer is sufficiently long-lived that the sample can be cooled, photoexcited, and warmed, and the decay can be monitored by collecting sequential single-crystal data sets. A similar procedure can be followed for the ground → metastable excitation by interspersing light pulses with data collections at temperatures below the metastable limit. At higher temperatures, the balance of excitation and decay leads to a temperature-dependent steady-state population of the metastable isomer, which can be probed by collecting structures while the sample is under continuous illumination. One could also envisage using synchrotron radiation and fast detectors to perform pump−probe X-ray diffraction experiments, although such experiments have so far been confined to measurements of carefully chosen Bragg reflections rather than complete data sets.[220]

It is typically found that the population of the metastable state $\alpha_{MS}(t)$ during excitation and decay follows Johnson-Mehl-Avrami-Kolmogorov (JMAK) kinetics:

$$\alpha_{MS} = \alpha_{MS}^{\infty} + (\alpha_{MS}^{0} - \alpha_{MS}^{\infty})e^{-kt^{n}} \tag{9}$$

where α_{MS}^{0} and α_{MS}^{∞} are the initial and final metastable state populations, respectively, k is the rate constant, and n is the Avrami exponent, which is usually close to integer and related to the dimensionality of the growth of the incipient phase by $D = 1 - n$ (i.e., $n = 4$ implies three-dimensional (3D) growth, and $n = 1$ implies homogeneous conversion throughout the bulk with no cooperativity). It is further found that the decay rate is strongly temperature-dependent and follows an Arrhenius law with an activation energy E_A, that is

$$k(T) = Ae^{-E_A/RT} \tag{10}$$

where R is the gas constant, and the prefactor A relates to the attempt frequency and is assumed to be temperature-independent. By combining the JMAK and Arrhenius equations and assuming a 100% initial population of the metastable isomer (i.e., $\alpha_{MS}^{0} = 1$), an analytical expression for the half-life of the decay can be derived as[219]

$$t_{0.5}(T) = \left[-\frac{1}{A}\ln\left(\frac{1}{2}\right)e^{E_A/RT}\right]^{1/n} \tag{11}$$

Taking the $[Pd(Bu_4dien)NO_2]BPh_4$ linkage isomer studied in ref 219 as an example, the measured activation energy of 60 kJ mol^{-1} corresponds to half-lives from 10^5 s (>24 h) to 1 s over a temperature range from 200 to 300 K. The predictable variation of the metastable-state lifetime with temperature makes these systems very well-suited to the fundamental development of time-resolved spectroscopic methods that could then be adapted to other photoactive systems of interest such as photocatalysts.

8.3. Outlook. In this section, two classes of responsive materials have been discussed. Pt-pincer complexes show solid-state vapochromic responses to small-molecule analytes, and the solvent selectivity and color change can be controlled directly through the chemistry of the molecule and indirectly through the crystal packing in the solid state. Photoactivated linkage isomerism is a canonical example of a single-crystal-to-single-crystal phase transition, and the ability to study the isomerization using single-crystal X-ray diffraction and to control the lifetime of the metastable state with temperature provides the scope to develop novel time-resolved techniques for studying photochemical reactions in molecular solids.

Both examples demonstrate the utility of modeling at all stages of the material "lifecycle", from selecting an initial synthetic target to providing complementary insight into spectroscopic measurements and suggesting material modifications to optimize physical properties toward the intended application. Atomistic simulations using, for example, electronic-structure methods such as DFT are particularly powerful and are becoming increasingly commonplace, but more "phenomenological" modeling, such as using empirical rate laws fitted to experimental data to predict kinetics, remains an important complementary technique. As first-principles modeling and advanced spectroscopic techniques continue to become more widely available, tighter integration between theory and experiment will be a key factor in establishing new insights that will ultimately yield novel functional molecular materials with tunable properties to meet contemporary challenges.

9. MATERIALS FOR NUCLEAR REACTORS

The first electricity-generating nuclear power plant, with an experimental breeder reactor, began operation in 1951 in the United States; since then, a lot of effort has been spent toward improved efficiency and safety.[221−224] Most common challenges are the effects of radiation and temperature on the structural materials, which are key elements for containment of nuclear fuel and the fission products. During fission, α particles are emitted becoming helium particles by capturing electrons from the surrounding structural materials. Initially He radiation damage appears in the form of local defects; however, these defects quickly agglomerate and interact with the underlying structure causing undesired effects such as blistering.[225−227] Helium atoms can rapidly diffuse through interstitial sites even below the room temperature.[228] Usually, they form bubbles, which cause embrittlement within the material, resulting in

DOI: 10.1021/acs.inorgchem.9b01785
Inorg. Chem. 2019, 58, 14939−14980

degradation of its mechanical, thermal, and electronic properties. Several classes of structural materials have been proposed[229] to guarantee the successful operation, maintenance, and long life span of the reactor; nonetheless, defect-induced blistering and helium embrittlement are still issues to be handled.

9.1. Nanoscale Metallic Multilayer Composites. It has been known for decades that surfaces, grain boundaries, and interphase boundaries act as sinks for radiation-induced point defects and traps for He.[230] However, the detailed mechanisms at the level of the atomic structure of an interface, which enable a nanocomposite to be stable under high irradiation flux or high concentration of He, are only just started to be clarified through studies of model systems, where ion irradiation is integrated with atomistic modeling.[231] The emergence of new concepts using nanoscience in the design of bulk structural materials shows promise to provide the breakthroughs needed for future nuclear energy systems. In particular, the design and control of interfaces and complex defect structures could lead to self-healing materials with extremely low sensitivity to radiation damage. Such a concept has the potential to make radiation damage a much less critical factor in technical design and opens new horizons for nuclear energy sector.

Nanoscale metallic multilayer composites (NMMC), which contain many interfaces between different types of metals, represent a step-change in the design of nuclear materials, with the potential to overcome limitations of existing technologies. Recently, a promising heterophase interface design approach was proposed, where interfaces could be produced to act as efficient sinks for irradiation-induced vacancy-interstitial (Frenkel) pairs, leading to their enhanced recombination and thus restoring part of the material to its undamaged state.[232] Such concept has been illustrated using a Cu/Nb nanolayered system.[231,233−241]

A Cu/Nb multilayer composite is produced using magnetron sputtering technique and is shown in Figure 16a,b as an example. The combination of such interface with a multilaminate material design concept[231,232] has been shown to produce nanostructured materials exhibiting ultrahigh strengths (hardness ∼5−7 GPa for Cu/Nb) and enhanced radiation damage tolerance.[232,242−244] The unique ability of Cu/Nb interfaces to trap and recombine Frenkel pairs created during irradiation-induced collision cascades can be traced back to the unusual properties of interfacial point defects in Cu/Nb multilayer composites. One of the most noticeable differences between the behavior of such defects and the ones present in perfect crystalline environments of the corresponding element is the greatly reduced formation energy of interfacial point defects compared to the latter. For example, in the Cu/Nb system, vacancy formation energy drops from 1.3 to 0.3 eV for Cu and from 2.8 to 1.1 eV for Nb,[237,238] while in the Zr/Nb system, the same energy drops from 2.0 to 0.8 eV for Zr[245] as the vacancy migrates to the interface. Vacancies and interstitials that migrate to the Cu/Nb interfaces are effectively trapped there and undergo accelerated recombination due to the enhanced diffusivity and effective size of interfacial point defects.[232,233,240,241,246,247]

Unlike vacancies and interstitials, helium atoms cannot be annihilated via recombination, thus remaining as impurities within the material. Two prospective interfaces are mostly studied including irradiation testing: Cu/Nb[247−253] and Cu/W[254−257] both experimentally and computationally. In copper-based systems, relevant mechanisms governing the He

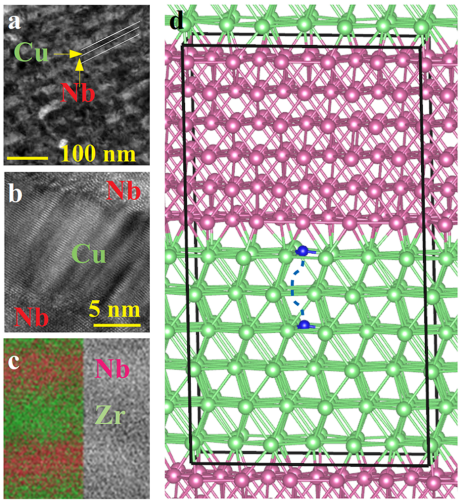

Figure 16. Various NMMCs produced using magnetron sputtering method (a) Cu/Nb, (b) Cu/Nb enlarged, (c) Zr/Nb systems. (d) The unit cell used in DFT calculations to model the system in (c): pink, green, and blue spheres represent Nb, Zr, and He atoms, respectively. The blue line represents the migration path of He atom (from right to left) toward the interface.

dynamics seem to be identified,[230] and the total amount of He atoms that can be trapped at the interface is obtainable by considering two key quantities: the misfit dislocation intersections (MDIs) density, which depends on geometrical and chemical parameters and finally identify the availability of nucleation sites, and the maximum number of He atoms that can be accommodated into a cavity preventing a "platelet-to-bubble" transition to occur. Furthermore, these systems also show promising properties in the sequestration and arrest of He bubble growth.[248,253] Structural analyses on implanted samples showed interfaces decorated by He bubbles thus underlying the key role also played by Cu/X interfaces. However, Cu exhibits significantly lower energy barrier with respect to X for vacancy formation (0.5 eV for Cu and 2.18 eV for W at the interface) and migration (vacancy migration barrier of 1.07 eV inside Cu and 1.79 eV inside W) in Cu/W multilayer system, and self-diffusion barrier (0.7 eV/atom for Cu and 1.2 eV/atom for Nb) in Cu/Nb multilayer system.[254,258] In combination with lower Cu homologous temperature, He bubbles formation occurs exclusively in Cu layers.[255] The unbalanced He bubbles distribution between constituent elements is accompanied by development of complex residual stress distributions in W layers and leads to the degradation of mechanical and functional properties already at ambient temperature. Moreover, in generation IV reactors, temperatures greater than 500 °C are expected; unfortunately, this strongly limits the use of copper, since temperature-driven recrystallization and crystal growth already occur at ∼300 °C.[259−261] On top of that, at high temperatures, functional properties (hardness, toughness) of Cu/Nb[262] and Cu/W[263] films drop significantly. Because of the issues mentioned above, although Cu/X is profoundly studied as a model material to understand the role of interfaces in radiation

DOI: 10.1021/acs.inorgchem.9b01785
Inorg. Chem. 2019, 58, 14939−14980

environments, its employment in nuclear industry would be rather limited. This appealed for the selection of other materials with suitable thermal and structural stability. It was evident that Cu is a weak point in the interface design; substitution of Cu by Zr could indeed represent the key solution allowing for a prompt introduction of this class of materials in the future of nuclear industry. Among various systems, the Zr/Nb one has been identified[245,255,264−267] as appropriate from mechanical and thermal stability point of view. Zr/Nb system outperforms mechanical properties of Cu/Nb and W/Cu above 300 °C; indeed Zr−Nb alloys are currently used in CANDU-type reactor.[268] Zr/Nb interfaces have recently been prepared[255,264−267] in a multilayer architecture using magnetron sputtering method (Figure 16c). The results indicate that the Zr/Nb system retains high hardness (reaching as high as 13 GPa) even at 400 °C and shows remarkable resistance to γ[266] and heavy Si ion[267] radiation. High interface-to-volume ratio due to small crystallites is expected to have exceptional positive effects on the self-healing properties of the materials subjected to radiation damage.

DFT calculations[245] indicate Zr/Nb multilayer systems retain most of the mechanical properties of their bulk forms, thus becoming promising candidates for nuclear applications. The electronic structure calculations further reveal that He atom prefers to sit at the low electron density region within the material. He atom is either trapped by a vacancy or is drawn to the Zr side of the interface, due to the charge transfer at the interface, which makes Zr side positively charged. The unit cell for this calculation and the migration path for He toward the interface is shown in Figure 16. Similarly, it is energetically favorable when the vacancy within the material is in the Zr side of the interface, so as to minimize the stress that is generated by the presence of the vacancy in the first place. Therefore, both He atom and the vacancy are drawn to the Zr side of the interface, although due to different reasons. To sum up, evolution of nuclear technology allows us today to harvest energy from nuclear reactions by means of nuclear power stations in a controlled and safe way. However, there are still problems related to the structural components of the reactors limiting the harvested energy and life span of the reactors themselves. Although many of these issues can be resolved through the use of proper materials, defect-induced blistering and He embrittlement have yet to be worked out. Recently proposed NMMCs can be a solution to these final problems.[231] So far, Zr/Nb multilayer composites appear to be a great candidate, but still further research is required.

9.2. Outlook. Several possible NMMCs can be designed. For example, Mg/Ti (hcp/hcp) interface, similar to Zr/Nb, could be an interesting candidate owing to the mutual immiscibility of the constituent elements, which may lead to high thermal and compositional stability.[269] The lattice mismatch and consequently misfit strain (∼8.6%) between Mg and Ti would give birth to a misfit dislocation network well acting as a sink for helium atoms. Moreover, the high mechanical stiffness-to-weight ratio makes this combination also particularly suitable where high specific strength is required.[270] Even if the He atoms are attracted to the interface, a way to prevent their accumulation and hence bubble formation must be identified.

It has been shown[245] that He atoms follow the lower electron density regions inside the material. Therefore, by manipulating the charge density within the material, it might be possible to lead He atoms out of the system, thus taking the He embrittlement part of the problem totally out of the picture.

10. NOVEL MECHANISMS FOR IMPROVED OXIDE THERMOELECTRICS EXPLORED FROM FIRST PRINCIPLES

Transition-metal oxides where electronic correlations play an important role[271,272] are an attractive materials class for thermoelectric applications. They exhibit a substantial chemical and thermal stability and are generally environmentally friendly. Considerable experimental and computational[273,274] effort aims at finding oxide thermoelectrics with improved performance, usually by maximizing the electronic contribution to the thermoelectric figure of merit $ZT = \sigma S^2 T/(\kappa_{el} + \kappa_{ph})$, namely, the electrical conductivity σ and the Seebeck coefficient S at temperature T. At the same time, electronic and lattice contributions to the thermal conductivity, κ_{el} and κ_{ph}, need to be as small as possible.

In bulk materials, *n*- and *p*-type thermoelectric response is commonly attained by doping,[275−277] a prominent example being La-doped $SrTiO_3$ (STO) single crystals,[278] or epitaxial films.[279,280] A different route is to utilize the impact of epitaxial strain on the electronic structure. Specifically, the delafossite $PtCoO_2$ exhibits a remarkable change in thermopower when varying from tensile to compressive strain.[281] This is related to a reconstruction of the Fermi surface topology, that is, a strain-induced shift of additional bands through the Fermi energy. An alternative strategy is to exploit heterostructuring and dimensional confinement,[282,283] a concept that is not only applied to oxides[284−292] but also used in Heusler/oxide magnetic tunnel junctions[293] or Heusler/metal hybrid systems.[294−296] This is based on the recent ability to grow transition-metal oxide superlattices (SLs) with atomic precision.[297−299]

Next, three different approaches to design thermoelectric properties are described, which go beyond the initial proposal by Hicks and Dresselhaus.[282] Such approaches rely on the insight that can be obtained from atomistic simulations within the framework of DFT combined with Boltzmann transport theory. The focus is on the correlated metal $LaNiO_3$ (LNO) heterostructured with the band insulators STO[290] or $LaAlO_3$ (LAO),[291,292] materials that can be grown epitaxially "cube-on-cube" in their natural perovskite ABO_3 structure,[300−304] as well as in the form of Ruddlesden−Popper/perovskite hybrid structures.[299,305,306] While LNO and STO result in polar interfaces, the LNO/LAO materials combination is nonpolar but, nonetheless, shows intriguing properties concerning confinement and strain. A discussion and an outlook on the influence of the phonon system close this section.

10.1. Impact of the Interface Polarity on the Thermoelectric Response. An efficient thermoelectric energy conversion requires both n- and p-type materials that are structurally and electronically compatible. It has been recently shown that this can be realized in oxide SLs by exploiting the interface polarity.[290] In particular, the mechanisms of electronic reconstruction at polar oxide interfaces[307,308] have attracted significant interest in the past decade.

In LNO/STO(001) SLs, variation of the stacking sequence at the interface generates different types of SLs, particularly an electron-doped one with n-type $(LaO)^+/(TiO_2)^0$ interfaces (IF-*n*), or a hole-doped one with $(NiO_2)^-/(SrO)^0$ interfaces (IF-*p*). The resulting stoichiometries for SLs with three layers of each material are $(LNO)_{3.5}/(STO)_{2.5}$ for the n-type SL and

DOI: 10.1021/acs.inorgchem.9b01785
Inorg. Chem. 2019, 58, 14939−14980

$(LNO)_{2.5}/(STO)_{3.5}$ for the p-type SL. Both structures are displayed in Figure 17a. DFT+U calculations show that the charge mismatch at the interfaces is exclusively accommodated in the nickelate region by shifting upward/downward the Fermi level for the SL with n-/p-type interfaces, while STO is rather a spectator. This is in sharp contrast to the much-studied LAO/STO(001) system, where the Ti 3d states are involved.[308,309] Transport calculations within Boltzmann theory show that the distinct band alignment between LNO and STO in the two stacking sequences leads to either n- or p-type thermoelectric response of the SL in cross-plane direction (Figure 17b). While in the n-type case the electronic transport involves tunneling through the insulating STO region, the particular position of the STO valence band maximum directly below the Fermi level in the p-type SL strongly boosts the thermoelectric response with a Seebeck coefficient of +135 μV/K at room temperature.

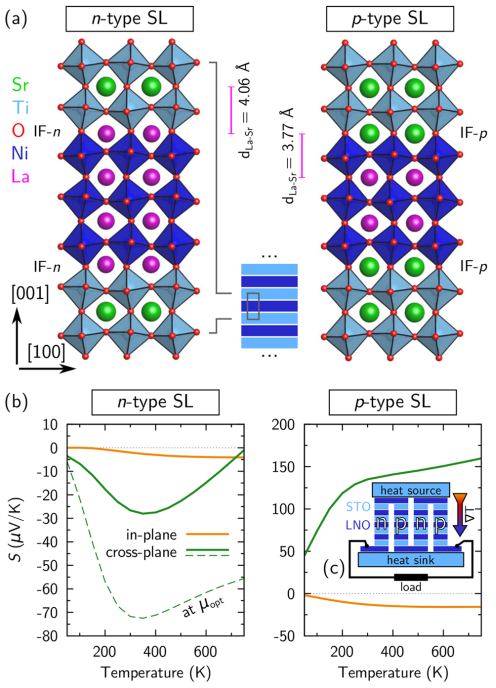

Figure 17. (a) Side views of the optimized geometry of LNO/STO(001) SLs with interfaces of opposite polarity (IF-n or IF-p) grown on STO. The La−Sr distance d_{La-Sr} across the interface acts as a fingerprint of the interface type, being elongated for an electron-doped SL and compressed for a hole-doped SL. In both cases, significant octahedral tilts are induced in the STO part. (b) Thermoelectric response of the SLs. The sign of the cross-plane Seebeck coefficient S is consistent with the polarity of the interfaces (negative/positive for n-/p-type). Additional doping (μ_{opt}, see ref 290) enhances the performance. (c) Illustration of a thermoelectric generator based on n- and p-type SL legs composed of the same materials combination (Adapted from ref 290).

We note that a related concept was proposed by Botana et al.[310] for CrN/MgO(111) SLs, which however differs in the strong charge mismatch at the interface (formal charge of the layers at the interface: $2^-/3^+$) that may drive the formation of compensating defects, and the fact that the voltage builds up perpendicular to the thermal gradient. Since polar interfaces occur also in many other systems, for instance, in group IV/III−V semiconductor heterostructures such as Ge/GaAs,[311] the outlined concept is not restricted to oxides but may be relevant for other classes of materials.

10.2. Epitaxial Strain as Control Parameter in a System with Confinement-Induced Metal-to-Insulator Transition. In doped bulk materials or epitaxial films,[278−280] the carrier concentration is used as control parameter to maximize the power factor PF = σS^2. The highest power factor is usually found in the intermediate regime between semiconducting and metallic behavior, which provides the best tradeoff between Seebeck coefficient (which reflects the transmission asymmetry near the chemical potential μ and thus benefits from the band gap in a semiconductor) and electrical conductivity (which is largest in a metal). In the following, it is shown that epitaxial strain can take on a similar role in artificial transition-metal oxides.

Nonpolar LNO/LAO(001) SLs are an intensely studied system.[300,304,312,313] In the ultrathin limit, epitaxial strain together with quantum confinement drive a metal-to-insulator transition in $(LNO)_1/(LAO)_1(001)$ SLs (Figure 18a).[291,312] The emerging band gap for tensile strain (~0.3 eV for a_{STO}) leads to a strong enhancement of the thermoelectric response, as one can infer from Figure 18. A particularly interesting aspect of this system is that the short-period SL design in the [001] direction (cross-plane) considerably improves the *in-plane* thermoelectric performance. Consequently, the in-plane power factor outperforms the cross-plane one due to the much higher in-plane conductivity. Comparing the conductivity obtained from DFT+U for $(LNO)_3/(LAO)_3(001)$ SLs with experiment,[304] the relaxation time at room temperature was estimated to be $\tau \approx 4$ fs. This results in in- and cross-plane Seebeck coefficients of ±600 μV/K and an in-plane power factor of 11 $\mu W/K^2$ cm at approximately room temperature, making the system comparable to some of the best-performing oxide systems such as La-doped STO[278−280] or layered cobaltates.[314] Further increase of the epitaxial strain (e.g., as induced by a $DyScO_3$ substrate) does not lead to an additional enhancement, but on the contrary it reduces the power factor again due to a decrease of the in-plane conductivity at the edges of the further increased band gap.[291]

Increasing the thickness of both constituents to three layers each in $(LNO)_3/(LAO)_3(001)$ SLs deteriorates the thermoelectric performance due to the two-dimensional metallic nature of the LNO region and the too-thick large-band-gap LAO spacer layer, irrespective of the epitaxial strain. This underlines the key role of quantum confinement.

It is then concluded that a significant enhancement of the thermoelectric properties can be obtained in oxide SLs such as $(LNO)_1/(LAO)_1(001)$ at the verge of a metal-to-insulator transition.

10.3. Transport Resonances Tuned by Strain Engineering of the Orbital Polarization. Above it has been discussed that n- and p-type thermoelectric response can be induced in polar oxide SLs by a selective design of the stacking sequence at the polar interfaces.[290] In the following, it is shown

DOI: 10.1021/acs.inorgchem.9b01785
Inorg. Chem. 2019, 58, 14939−14980

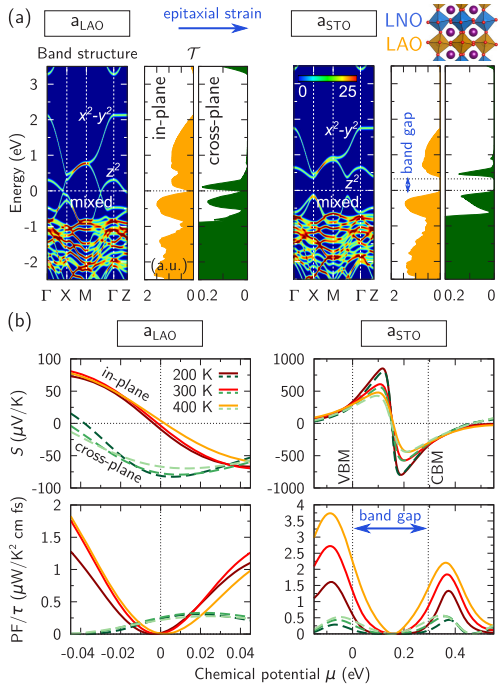

Figure 18. (a) In ultrathin $(LNO)_1/(LAO)_1(001)$ SLs, increasing the substrate lattice constant from a_{LAO} (compressive strain) to a_{STO} (tensile strain) drives a metal-to-insulator transition,[312] as one can see from the band structure diagrams and the corresponding transmission $\mathcal{T}$. (b) This is accompanied by a drastic enhancement of the thermoelectric response (Seebeck coefficient S and power factor PF), both in-plane and cross-plane. Further increase of strain was found to be counterproductive.[291] Adapted from ref 291.

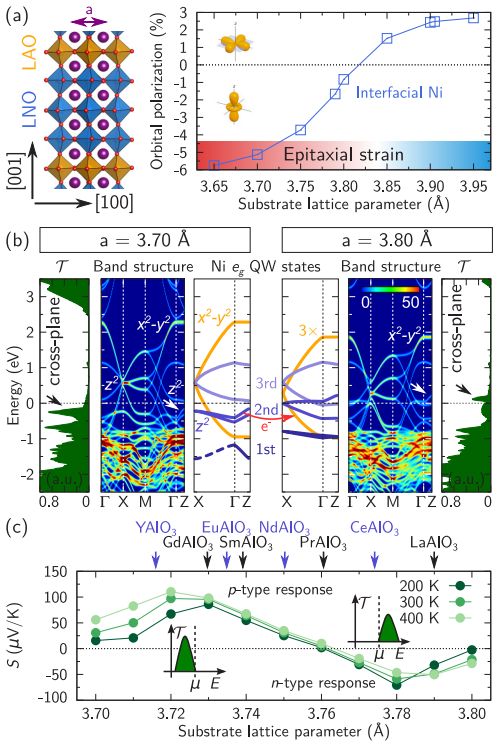

Figure 19. (a) Side view of the optimized geometry of a nonpolar $(LNO)_3/(LAO)_1(001)$ SL (a = 3.79 Å), together with the Ni e_g orbital polarization in the interfacial LNO layers as a function of the substrate lattice parameter a that varies from −6% (compressive strain, red shaded) to ca. +3% (tensile strain, blue shaded). (b) Confining three layers of LNO separated by a single LAO spacer layer leads to the formation of distinct QW states with Ni e_g character. Their relative occupation (and thus the orbital polarization) can be precisely tuned by epitaxial strain. In particular, resonances emerge in the cross-plane transmission $\mathcal{T}$ (black arrows) that are associated with the $3d_{z^2}$-derived QW states (white arrows) and can be shifted with respect to the Fermi energy by moderately varying the degree of strain. (c) With this strain engineering of the orbital polarization, considerable n- and p-type thermoelectric response can be achieved in the system. Exemplarily, some (rare-earth) aluminate substrates are marked. Adapted from ref 292.

that the same goal can be achieved in nonpolar SLs by strain engineering of the orbital polarization.[292]

Designing the thermoelectric response of a system necessitates quantum control over the asymmetry of its spectral transmission function $\mathcal{T}$ around the Fermi energy.[293,315] Mathematically, it has been shown decades ago that transport resonances are attractive for thermoelectric applications.[316] Nevertheless, the explicit use of these resonances has been limited to model studies.[317,318] To pursue this route, (i) a transmission function $\mathcal{T}$ exhibiting sharp resonances must be designed, and (ii) a mechanism that allows for a precise tuning of the transport resonances with respect to the Fermi energy is required.

This concept has been demonstrated on the basis of first-principles calculations in $(LNO)_3/(LAO)_1(001)$ SLs,[292] which are displayed in Figure 19. The confinement of three layers of LNO separated by a single LAO spacer layer induces the formation of distinct Ni $3d_{x^2-y^2}$- and $3d_{z^2}$-derived quantum well (QW) states, while at the same time permitting cross-plane electronic transport through the single LAO spacer layer. This leads to the emergence of sharp cross-plane $3d_{z^2}$-derived transport resonances (Figure 19b). Epitaxial strain strongly impacts the orbital polarization in this system and thus the relative energy and occupation of the $3d_{x^2-y^2}$- and $3d_{z^2}$-derived QW states (Figure 19a). Because of this charge redistribution mechanism, the $3d_{z^2}$-derived transport resonances can be shifted with high precision relative to the Fermi energy. Thereby, considerable n- and p-type thermoelectric response (ca. −60 to +100 μV/K at approximately room temperature) can be obtained in one and the same materials combination by moderately varying the control parameter epitaxial strain between −1.5 and −2.8% (Figure 19c). It has been shown that this concept is robust with respect to the formation of oxygen vacancies.[292]

This work exemplifies how the thermoelectric properties of oxide heterostructures can be controlled and optimized by varying layer thickness, quantum confinement, and epitaxial strain. Moreover, it manifests an application for the control of

DOI: 10.1021/acs.inorgchem.9b01785
Inorg. Chem. 2019, 58, 14939−14980

orbital polarization, which is intensively pursued in artificial transition-metal oxides.[312,319−322]

10.4. Outlook: The Role of Phonons. On the one hand, the focus of most theoretical studies lies on improving the electronic contribution to the thermoelectric figure of merit ZT, that is, optimizing conductivity σ and Seebeck coefficient S. On the other hand, the impact of phonons, which affect (i) the relaxation time τ and (ii) the lattice contribution to the thermal conductivity κ_{ph}, is often neglected. Both quantities can be obtained from first-principles: The relaxation times have been calculated very recently for bulk Si[323] and for elemental noble metals,[324] employing a combination of DFT and many-body perturbation theory. On the one hand, because of the high numerical demand, this approach has not been applied so far to more complex systems such as the oxide SLs discussed here. The thermal transport, on the other hand, has been calculated recently for bulk MgO by a complete solution of the linearized Boltzmann transport equation.[325] Larger systems such as Fe/MgO/Fe(001) magnetic tunnel junctions have been treated within a Green's function framework.[326]

Exploiting interface scattering of phonons by heterostructuring is a viable strategy to reduce the lattice thermal conductivity.[283,327−329] In SLs, the periodicity has a strong impact, and it has been demonstrated experimentally that at the crossover point between incoherent to coherent phonon scattering in oxide SLs the lattice thermal conductivity exhibits a minimum.[330] However, the parameters corresponding to this optimal point have to be determined in each specific case. High crystalline quality is beneficial for electronic properties, but simultaneously it can lead to coherent phonon heat conduction, and it has been shown for GaAs/AlAs(001) SLs that the thermal conductivity can even increase with the number of layer repeats.[331] In short-period SLs the thermal conductivity can exceed that of the constituent materials, as has been demonstrated for Si/Ge(001) SLs.[332] This highlights that further effort is required to explore the influence of heterostructuring on the phonon system from first principles.

11. POLAR, FERROELECTRIC, AND MULTIFERROIC METALS: THREE CASE STUDIES

Here, case studies of polar,[333] ferroelectric,[334] and multiferroic[335] metals are discussed, where polar symmetry—and in some cases, polarization itself, is actually realized in metals. The idea of ferroelectric metals harkens back to a suggestion by Anderson and Blount[336] that some metals may possess, or acquire, polar symmetry, that is, one compatible with the existence of electric polarization. Whether a polarization and attendant phenomena, would actually materialize as a consequence was left unspecified, and this is one of the issues being investigated, mostly theoretically so far.

It is appropriate to have a checklist for the definition of a ferroelectric metal: it should

(i) be a metal.

(ii) have polar symmetry.

(iii) have a measurable or computable zero-field polarization P.

(iv) optionally support a polarization-induced depolarizing electric field when cast in finite form (e.g., thin film), which would imply the actual switchability of P.

The last requirement is optional, because even bona fide ferroelectrics often do not satisfy it: a large polarization in a film causes a large depolarizing field, which destroys the polar distortion and, ultimately, the polarization itself.

11.1. Metascreening in Metalized Ferroelectrics. Polar metals should satisfy the (i) and (ii) requirements. A further distinction can be made between metals that are or can be rendered polar and polar insulators, which are made robustly metallic. Among the former, let us briefly mention $LiOsO_3$ and related composite systems, which stands out in both experiment and theory,[337−339] and the general guidelines laid out for their search.[340]

In this section, the mechanism that causes metalized ferroelectrics to conserve polar distortions, that is, to become polar metals, is discussed. Figure 20 shows the amplitude of the polar distortion as a function of free charge density of either sign, normalized to the value at zero added charge, for a limited selection of the materials discussed in ref 333. Evidently, all materials exhibit stable polar distortions as a function of charge density of both signs, except three of them whose distortion dies out at high n-type density.

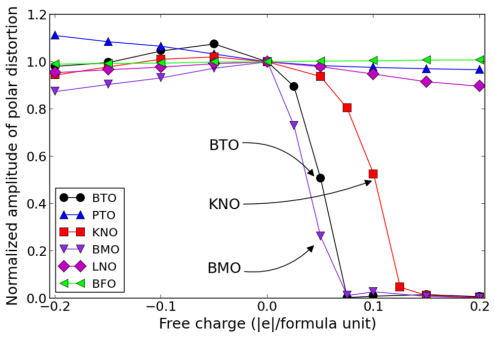

Figure 20. Normalized polar amplitude vs carrier density for a sample of metalized ferroelectrics. In the legend, $BaTiO_3$, $PbTiO_3$, $KNbO_3$, $BaMnO_3$, $LiNbO_3$, and $BaFeO_3$ compounds are represented by the element initials, respectively. For example, 0.1 |e|/formula unit are 1.5 × 10^{21} cm^{-3} in BTO. Figure adapted from ref 333.

$BaTiO_3$ (BTO) is an interesting case, as it allows to monitor the transition from polar to nonpolar phase. As detailed in ref 333, in an 80 Å long supercell of cubic BTO perturbed by a dipolar displacement of a plane of Ti atoms, it is found that free charge screens out long-range interactions over a typical length scale of less than 10 Å from the perturbation. Doping produces a concurrent short-range effect (referred as *metascreening*) that enhances the distorting forces on the atoms in the immediate vicinity of the perturbation; specifically, a lattice distortion near the perturbation accommodates the screening electrons or holes, and it is essentially indistinguishable from the original polar distortion in the undoped case.

To prove that this effect is not a consequence of incomplete screening but indeed due to short-range effects, one can calculate the stiffness constant for the soft ferroelectric mode $\mathcal{S} = \mathbf{s}^T \cdot \mathbf{F} \cdot \mathbf{s}$, with $\mathbf{F}$ the force constant matrix calculated at the Γ point and $\mathbf{s}$ the soft-mode eigenvector. Another stiffness $\mathcal{S}_{sr}$ is calculated, just the same way as $\mathcal{S}$, except that the force constants between neighboring Ti atoms are always those of

DOI: 10.1021/acs.inorgchem.9b01785
Inorg. Chem. 2019, 58, 14939−14980

the undoped case, independently of the doping level: the shortest-range interactions are thus frozen into the undoped configuration. On the one hand, as Figure 21 reports, $\mathcal{S}$ is negative for all free carrier densities up to ca. +0.05 |e|/formula unit, predicting a polar distortion in accordance with Figure 20; on the other hand, $\mathcal{S}_{sr}$ is always positive, corresponding to stability against polar distortion, except in the undoped case. This shows directly that the metascreening short-range forces are the key enabler of the survival of the distortion in the doped system.

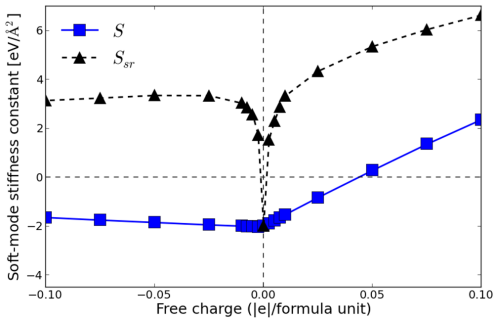

Figure 21. Force constants vs carrier density for metalized $BaTiO_3$. Negative values of the stiffness indicate the occurrence of a polar distortion, while positive values correspond to stability against polar distortion.

11.2. A Ferroelectric Metal. A proper ferroelectric metal obeying all the requirements in the checklist has been found[334] in a different, and so far unique in this respect, class of materials: the layered perovskites of the $A_nX_nO_{3n+2}$ class, which features prominently $n = 4$ ferroelectrics and multiferroics such as $La_2Ti_2O_7$ and $La_2Mn_2O_7$.[341] The $n = 5$ class is trivially metallic from electron counting with a density of $\sim 3 \times 10^{21}$ cm^{-3}, but the ferroelectric mechanism active in $n = 4$ materials[342] does not apply. Luckily, it turns out that $Bi_5Ti_5O_{17}$ (BTO-5517 below) has polar symmetry $Pm2_1n$, with polar axis equal to the stacking direction b, due to local chemical Bi−O dipoles (analogous to $BiFeO_3$), and, thus, BTO-5517 is a polar metal in agreement with points (i) and (ii).

The computability of zero-field polarization P, point (iii), is potentially contentious, because the Berry phase polarization[343] is ill-defined in its original form if the number of occupied bands change along the k integration direction (parallel to P itself), as expected in metallic conduction bands. The conduction bands in BTO-5517, however, are very flat along P (i.e., $k_\parallel$) direction; thus, for all numerical intents and purposes, the number of occupied bands will not change along $k_\parallel$, and a convergent P will be obtained as usual on a finite grid made up of string parallel to the P direction. To cure the unavoidable occasional crossings (the bands are not perfectly flat), P is calculated as the 2D average of a renormalized phase subject to a charge conservation constraint.[334] Physically, this corresponds to Fermi surface sections that are quasi-1D lines when projected on the $k_\perp$ plane (i.e., with zero measure in that plane, perpendicular to the integration direction) as is the case in BTO-5517 or to conduction charge that is strongly localized within the blocks and not very mobile. The latter view suggests to also estimate the polarization simply as the dipole of a single block. The modified Berry approach and the block-dipole approximation give similar values for the conduction band, ∼5 $\mu C/m^2$; summing up the dominant valence and ionic contributions, a large total $P = 35$ $\mu C/m^2$ is obtained, in the same league as ferroelectrics such as $BaTiO_3$.

To complete point (iii) and address point (iv) in the checklist, it is here demonstrated that the material can support a depolarizing field (i.e., the polarization can be switched). To this end, a BTO-5517 layer is cladded with the insulator $Ba_2Zr_2O_7$; this configuration is an open circuit with no current flow, which will instead occur if BTO-5517 is contacted directly. In Figure 22, showing the electrostatic potential difference of the polar and nonpolar superlattice, the metallic layer screens only partially the polarization-induced depolarizing field. The polarization will thus switch, as in ferroelectrics, upon application of a field exceeding the depolarizing field (i.e., the finite screening ability of the layer). The free-charge response in the finite system is limited by the small amount and localization of the mobile charges, and the screening ends

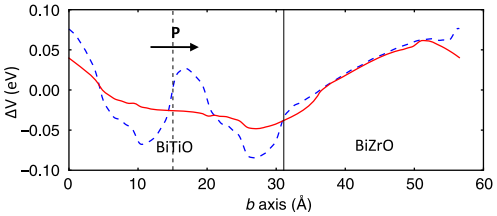

Figure 22. Potential difference of the polar and nonpolar BiTiO-5517/BiZrO-227 SL, exhibiting the sawtooth shape due to interface polarization charge. The two lines correspond to two different running-average filters. Figure adapted from ref 334.

up being incomplete; the multilayer is in effect a dielectric medium with finite low-frequency, low-wavevector dielectric function in agreement with recent results on sub-nanometer metal−air multilayers.[344]

Single-domain BTO-5517, not only polarized but also sustaining a polarization-generated depolarizing field, contradicts the usual assumption that a large polarization cannot survive its own depolarization field in a thin film.

In this respect, BTO-5517 is unlike other ferroelectrics precisely because of the self-screening mechanism that cancels in part the depolarizing field, while not destroying the chemically driven polar distortion. In this context, BTO-5517 behaves as a limiting case of hyper-ferroelectric,[345] and it might be dubbed a self-screened hyper-ferroelectric metal.

11.3. A Three-Order-Parameter Multiferroic Metal. Thinking along the same lines as for BTO-5517, a natural extension is to look[335] for possible multiferroicity in $Bi_5Mn_5O_{17}$ (BMO henceforth), where magnetism is expected due to Mn ions and metallicity. The result is partially analogous to BTO-5517, in that Bi−O dipoles again cause ionic polarization; the symmetry is the same as in BTO-5517, but the polar axis is now c, the (110)-like axis orthogonal to the stacking axis. The total polarization, calculated in the same way as before, is ∼5 $\mu C/cm^2$; the conduction contribution is minor, ∼0.05 $\mu C/cm^2$; the Fermi surface is indeed flat, sheetlike, and closely parallel to the c axis.

DOI: 10.1021/acs.inorgchem.9b01785
Inorg. Chem. 2019, 58, 14939−14980

As hinted above, due to the Mn ions interacting via double exchange, BMO is a ferromagnet with average moment 3.2 μ_B. In fact, it is a half-metallic ferromagnet, with a metallic majority spin channel and insulating minority (with a gap of ∼3 eV using self-interaction corrections). Interestingly, the polarization is nonzero in both spin channels and larger in the majority than the minority spin channel by roughly a 3 to 1 ratio.[346] A definite point of interest in the O-rich layered phase BMO is that, according to the calculations,[335] it is thermodynamically favored over the known $BiMnO_3$ normal perovskite phase in a sizable window of O chemical potential, favoring the synthesis of BMO unlike that of BTO-5517, which has not been achieved yet.

Demonstrating the existence of a depolarizing field in BMO is trickier than in BTO-5517, because there is no natural way of stacking BMO and an insulator along *c*. Eventually, cladding BMO with the n = 5 compound $BaLa_4Zr_5O_{17}$ (with a gap of ∼2 eV) ended up doing the trick. Again, as in the case of BTO-5517, there is a charge monopole at the metal−insulator interfaces and a residual field inside both the metal and the insulator. The screened-field energy density is much lower than the stabilization energy of the polar distortion (which is a bit larger than that of $BaTiO_3$, suggesting thermal stability up to at least 400 K), so the distortion is not affected by the depolarizing fields. Hence BMO checks all the boxes in the checklist and qualifies as a ferromagnetic ferroelectric metal.

Actually there is more to the story: BMO turns out to also have ferrotoroidic order; that is, its magnetic symmetry allows for a nonzero toroidal moment **T**, a polar vector that inverts under time reversal. The symmetry group is the only one such that **T**, **P**, and **M** are all mutually orthogonal, and since noncollinear magnetic calculations show that the magnetization **M** points along *a*, it eventually turns out that **T** ≈ **P** × **M** in this case. Both time reversal *and* inversion breaking are needed for a nonzero **T**, which implies that **T** would be nonzero even if **P** were suppressed by electronic screening, as long as the symmetry remains polar. Finally, magnetoelectric coupling also occurs in BMO; it happens to be off-diagonal (i.e., cross-field), and its value seems rather large.

11.4. Outlook. The just-discussed work on metalized ferroelectrics, especially layered perovskites, has revealed a wealth of unexpected effects. Among the open issues, the possible existence of energy-degenerate ferroelectric and antiferroelectric states, and the related (probably unusual, if not exotic) properties and dynamics of domain boundaries appear worth addressing, while waiting for experimental endeavor to prove predictions about metallic ferroelectricity in general.

12. ELECTRIC MAGNETO-OPTICAL PROPERTIES IN MULTIFUNCTIONAL HYBRID MATERIALS

Hybrid organic−inorganic perovskites (HOIPs) are similar to inorganic perovskites in terms of their ABX_3 topology, although the combination of organic and inorganic components provides for greater compositional flexibility.[347] In common perovskites,[348] A and B are cations, and X is an anion that is coordinated to B. The A atoms are normally larger than the B atoms, and the B cation is sixfold coordinated with the X atoms to form BX_6 octahedron (Figure 23). The resulting octahedra are corner-shared to form a three-dimensional framework in which the A site cations are located inside the framework cavities. In addition to their physical properties, many of their functionalities are controllable with external stimuli—for instance, magnetic field, pressure, electric field, and light.

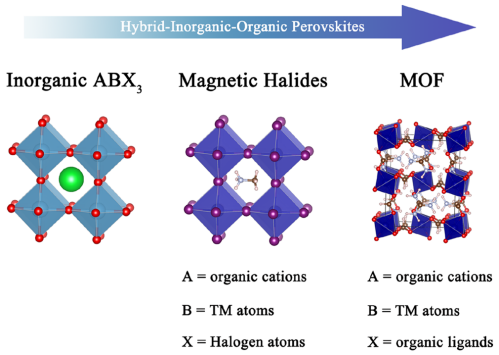

Figure 23. Starting from an inorganic ABX_3 perovskite: magnetic halides and metal−organic frameworks (TM: transition metal).

Hybrid organic−inorganic materials have emerging applications as multiferroics, photovoltaics, gas sensors, and transparent conductors.[347] HOIPs have a number of advantages compared to perovskite oxides. First and foremost, the A and/or X sites are occupied by organic cations and/or organic linkers, respectively (Figure 23).[349−351] At the same time, molecule-based HOIPs often have overall lower energy scales than their corresponding oxides. Quantum phase transitions—driven by magnetic field, pressure, and electric field—can thus occur at experimentally realizable conditions and be more easily controlled. These materials are also well-suited for the development of structure−property relations. For instance, the variations of the organic and inorganic components offer wide possibilities to create innovative and promising HOIPs in accordance with the generalized Goldschmidt tolerance factor.[352] This can serve as a guide for the rational design and synthesis of new HOIPs using compositions with desired functionalities and dimensionalities.[352,353] The metal−organic frameworks (MOFs) are a particularly interesting class of HOIPs (Figure 23). Here, the metal ions are linked together by organic bridging ligands, for example, carboxylate ligand ($HCOO^-$).[354] As a result, they have complex hydrogen-bonding networks that can be adjusted as a function of temperature. These materials display diverse properties including electrical, magnetic, catalytic, optical properties, multiferroic behavior, that is, coexistence of electric and magnetic ordering,[355−366] and magnetoelectric behavior,[355−366] that is, the coupling between the two long-range orderings. Like many other quantum materials, the MOFs are tunable in magnetic and electric fields.

Another emerging class of HOIPs is *hybrid halide perovskites* based on the semiconductive methylammonium (MA) lead halide $MAPbX_3$, where X = Cl, Br, I.[15,367−373] The replacement of the inorganic cation (A) by an isoelectronic organic moiety such as MA^+ $(CH_3NH_3)^+$ provides a unique way of tuning the chemical bonding and consequently also the optical and electronic response.[374−381]

The hybrid perovskite is a very versatile family of compounds with a large catalog of chemical components for the A and B sites.[353] For example, (i) for the A site: $(NH_2)_2CH^+$, $CH_3NH_3^+$, $NH_2NH_3^+$, $(CH_3)_2NH_2^+$, $CH_3CH_2NH_3^+$,

DOI: 10.1021/acs.inorgchem.9b01785
Inorg. Chem. 2019, 58, 14939−14980

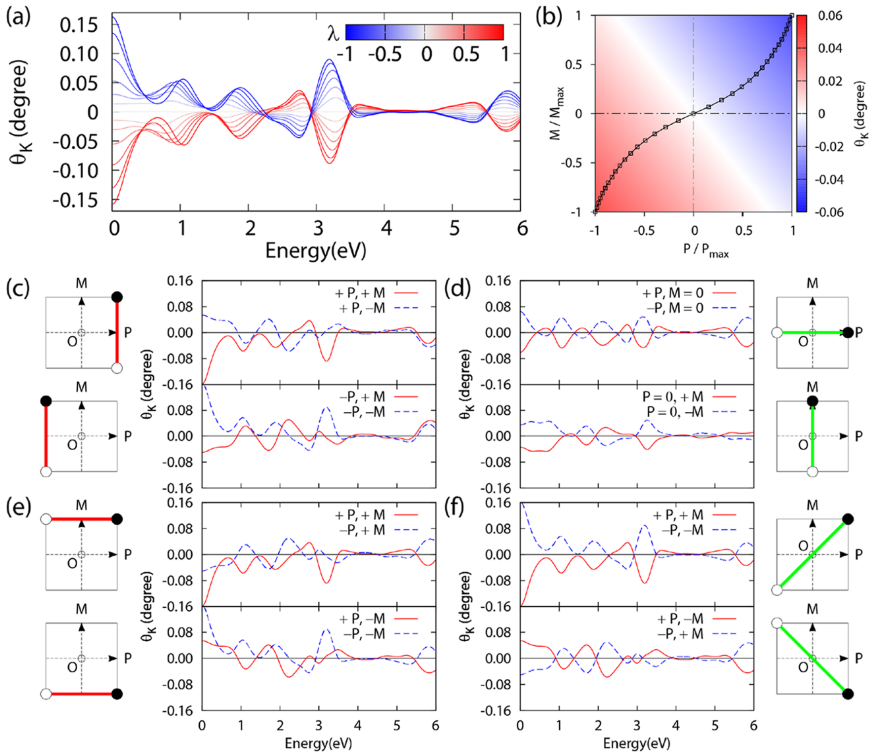

Figure 24. (a) θ_K as a function of the incident photon energy for different value of normalized amplitude of the polar distortion λ from −1 to +1. (b) Color scheme representation of different points in (P,M) space. Black curve represents the magneto-electric states, while the green line represents the locus of points with zero Kerr angle for the selected energy 3.8 eV. (c–f) Switching properties of the Kerr angle for different states in (P,M) space: green (red) lines connect states for which the Kerr angle does (not) switch.[392] The results are shown for the $[C(NH_2)_3]Cr(HCOO)_3$ MOF.

$C_3N_2H_5^+$, $C(NH_2)_3^+$, $(CH_2)_3NH_2^+$, $(CH_3)_3NH^+$, $(CH_3)_4N^+$;[352,353] (ii) for the B site: Cr^{2+}, Cu^{2+}, Fe^{2+}, Mn^{2+}, Co^{2+}, Ni^{2+};[352,353] and (iii) for X site: I^-, Br^-, Cl^-, CN^-, $HCOO^-$, N_3^-, $[N(CN)_2]^-$.

Moreover, the possibility to reduce the dimensionality by considering novel hybrid 2D materials appears an interesting direction to explore. For example, very recently, a novel magnetic 2D hybrid compound has been synthesized based on chromium-chloride-pyrazine, that is, $CrCl_2(pyrazine)_2$.[382−385] Organic molecules and magnetic metal ions can be used as molecular building blocks for synthesizing novel types of 2D materials exhibiting both electrical and magnetic properties, possibly cross-coupled to magneto-optical properties. Magnetic hybrid 2D materials are now at their infancy, and there is certainly room for new interesting physics to explore.

12.1. Symmetry Breaking and Physical Properties of Materials. *12.1.1. Multiferroicity and Magnetoelectricity.* Breaking of time-reversal (T) and inversion symmetry (I) leads to interesting changes in physical properties of crystals. If both symmetries are broken, the compound may have coexisting magnetic and ferroelectric order (multiferroicity).[386−388] It may happen that the two order parameters, that is, magnetization (M) and electric polarization (P), are coupled (magnetoelectricity)[386−388] with the possibility to tune the electric polarization by an external magnetic field and, vice versa, to tune the magnetization by an external electric field.[386−388] It is interesting to explore the unique effects of cross-coupling of ferroelectric and magnetic orders, which leads to the aforementioned multifunctional properties, on magneto-optical properties.[389−392]

12.1.2. Magneto-Optical Kerr Effect: Tunable and Switching Properties. The magneto-optical Kerr effect (MOKE) describes the change of linearly polarized light when reflected from the surface of a magnetic material. The change consists of two parts: a rotation of the polarization plane, the so-called *Kerr rotation* θ_K, and a phase difference between the electric field components perpendicular and parallel to the plane of the incident light, the so-called *Kerr ellipticity* η_K.[393] The Kerr rotation can be exploited to read suitably magnetic stored information by optical means in modern high-density data storage technology[394−397] or to probe the magnetic behavior of two-dimensional systems.[398]

The Kerr effect is described by the Kerr angle φ_K, a complex number defined as

DOI: 10.1021/acs.inorgchem.9b01785
Inorg. Chem. 2019, 58, 14939−14980

$$\varphi_K = \theta_K + i\eta_K = \frac{-\sigma_{xy}}{\sigma_{xx}\sqrt{1 + \left(\frac{4\pi}{\omega}\right)\sigma_{xx}}} \quad (12)$$

where the complex numbers σ_{xx} and σ_{xy} are the diagonal and the off-diagonal elements of the conductivity tensor, respectively.[399,400] Equation 12 is widely used in literature and is valid only in the polar geometry, for compounds with higher than threefold rotational symmetry.[399,400] The conductivity tensor can be calculated from the electronic structure of the solid, and, therefore, Kerr effect can be evaluated based on density functional theory.[400] In a system possessing inversion symmetry I, linear magneto-optical activity (Kerr effect) arises from breaking time reversal (T), like in a ferromagnet. If the system is anti-ferromagnetically ordered, the material is expected to be magneto-optical inactive. Despite this expectation, a multiferroic MOF has been recently found,[392] with chemical formula $[C(NH_2)_3]M[(HCOO)_3]$, where M = Cu^{2+} or Cr^{2+}, exhibiting magneto-optical activity even in its anti-ferromagnetic state. This result suggests that a magnetic compound may become magneto-optically active when the combined TI symmetry is broken.

If the system is invariant under T and I symmetry,[401−403] it does not have either magnetic or ferroelectric ordering. Breaking of T gives rise to magnetic ordering, while breaking of I is necessary for ferroelectricity. Breaking both T and I is necessary for a system to be multiferroic and/or magnetoelectric. When breaking the TI symmetry, the compound may be magneto-optical active.[401−404]

Moreover, in MOFs the Kerr angle can be tuned not only by M, as a common belief, but also by the ferroelectric polarization (P).[392] This raises the exciting possibility that the Kerr rotation angle could be controlled by M, P, or both—depending on the circumstances. This is an under-explored avenue for achieving the combination of functional behavior needed for logic and information storage in magnetic materials and nanostructures.

12.1.3. Switching Properties of Magneto-Optic Kerr Effect. As a proof of principle, a series of Kerr spectra calculations on a MOF compound showing ferroelectric and magnetic ordering have been performed.[392]

Figure 24a shows the variation of the Kerr rotation θ_K as a function of the incident photon energy (E) for different values of the normalized amplitude of the polar atomic distortion (λ). $\lambda = 0$ represents the paraelectric state (centrosymmetric), while $\lambda = \pm 1$ represents two ferroelectric states with opposite electric polarization. The parameter λ smoothly changes from −1 to +1 through zero, and it is codified by a color scheme from blue to red through white: by changing λ, θ_K changes continuously, and the switching occurs when λ changes sign. Since λ is proportional to P in the material, this leads to the interesting conclusion that *Kerr angle can be tuned by P and switches its sign when switching P*. These results have been derived in the case of a magnetoelectric compound:[392] one would naively expect that this ultimately recovers the standard case of $\theta_K \propto M$, since $P \propto M$. However, as shown below, calculations can be generalized by considering M and P as independent variables:

$$\theta_K = \alpha P + \beta M \quad (13)$$

θ_K can be expressed as linear function of both P and M as reported in eq 13. In Figure 24b, $\theta_K(P,M; E = 3.8\ \text{eV})$ is shown as a color code. The coordinates were normalized to P_{max} and M_{max}, respectively. For each point in (P,M) space, a color that corresponds to a well-defined value of the Kerr angle is associated. Figure 24b represents the following property by a color code in (P,M) space: $\theta_K(P,M; E) = -\theta_K(-P, -M; E)$, that is, θ_K can be switched only when both P and M change sign. This property is more general and can be extended to other ferroelectric and magnetic compounds—even in absence of a net magnetization.

In Figure 24c−f, simulations considering P and M as independent variables in the calculations are shown. According to eq 13, θ_K cannot be switched if only M or P is reversed when both M and P are different from zero. This is shown in Figure 24c,e: in (c) $+P$ (or $-P$) state is considered, and $+M$ switched to $-M$; in (e) $+M$ (or $-M$) state is considered, and $+P$ switched to $-P$. On the one hand, no switching occurs. On the other hand, when $M = 0$ (e.g., anti-ferromagnet), θ_K changes its sign when reversing P. This leads to the important result that θ_K can be tuned and reversed by P in ferroelectric antiferromagnets (see Figure 24d, upper panel). When $P = 0$ (e.g., nonpolar compound), θ_K can be tuned and reversed by M.[392] This would correspond to the standard case of a centrosymmetric ferromagnet (Figure 24d, lower panel). In general, *θ_K can be switched only when reversing both P and M* as shown in Figure 24f. Results can be summarized in the (P,M) space. Each couple of states considered in the panels (c−f) are shown as black and white circles in this space. The black and white circles are connected by a green or red line representing the switchability or nonswitchability of the Kerr angle between them. In summary, these results suggest that (i) the Kerr angle can be modified not only by M but also by P; (ii) θ_K changes its sign only when switching both P and M; (iii) it may be possible to tune and switch the Kerr angle in antiferromagnetic compounds; (iv) it could be possible to design novel memory devices, where the information is stored by the direction of the local ferroelectric domain, and the read-out is performed by exploiting the Kerr rotation depending on the direction of the dipole. On the basis of these predictions, it will certainly be interesting to explore the emerging class of hybrid organic−inorganic quantum materials with the potential of cross-coupling magnetic and electric order to the magneto-optical properties for active tunable photonics.

12.2. Outlook. It is important to design general principles from which material properties can be rationalized and qualitatively predicted, by focusing on the dimensionality, composition, and functional groups—by assessing their effects on the relevant properties such as P and M, which are expected to be cross-coupled to the MOKE in the materials outlined here. The Bilbao Crystallographic Server (BCS, http://www.cryst.ehu.es/) is useful for analyzing the magneto-optically activity (MTENSOR tool in BCS). The multilinear relation $\theta_K = \alpha P + \beta M$ requires (i) the evaluation of the two α, β parameters for a specific material, together with their dependence on the functional groups (A,B,X) of HOIPs[392] and (ii) understanding the microscopic mechanism of the switching properties of θ_K in terms of the underlying electronic structure, symmetry, and structural properties.[405] This will open new directions in magneto-optical Kerr engineering in complex functional materials in connection with antiferromagnetic spintronics[405−411] and topological quantum materials.[412−416]

DOI: 10.1021/acs.inorgchem.9b01785
Inorg. Chem. 2019, 58, 14939−14980

13. TRIBOLOGY AS A NOVEL FIELD FOR ELECTRICITY GENERATION

Tribology is defined as the study of interacting surfaces in relative motion.[417] It involves various and complex phenomena, such as friction, wear, and corrosion, and it has severe implications for energy saving. It has been estimated that ~23% of the world's total energy consumption originates from tribological contacts;[418] fortunately, several progresses have been achieved in the last decades regarding the comprehension and control of microscopic mechanisms related to friction, partly due to the advances made in simulation techniques.[419]

Despite the fact that one of the main goals of tribology is energy saving, an emerging topic is the conversion of friction into usable work. The importance of the latter becomes clear when considering the increasing demand of energy production in sustainable ways and is therefore discussed below. More specifically, the focus will now be on the production of energy through a clever control of the triboelectric effect.

In the past years, with the quick growth of electronic miniaturization, a remarkable number of novel devices (e.g., sensors, actuators, wireless transmitters) have been invented and introduced in many different fields, among which are health care, environmental and structural monitoring, the Internet of things, wireless transmission, security, and nanorobotics, among others.[420,421] These devices generally require only small-scale power (μW to mW)[422] and traditional approaches (i.e., batteries) but present several drawbacks, including the problematic implementation of wireless sensor networks with a huge number of distributed sensor nodes[423] or issues related to recycling.[421,424] This directly calls for the development of sustainable, maintenance-free and self-sufficient power generators that can ideally harvest energy from the environment and be integrated into such devices.

Almost every environment has an abundance of all sorts of energy: thermal, mechanical, solar, chemical, etc. Among these, mechanical vibrations may exist in most of the environments in which a power generator can be placed. Conventional power production is obtained through electromagnetic alternators based on Faraday's law of induction. However, these types of power generation technologies can only harvest high-frequency mechanical energies efficiently.[425] This means that a broad range of energy sources in the environment (e.g., water waves, human body motion, thermal vibrations) cannot be effectively exploited through conventional electromagnetic generators (EMGs).[422]

To effectively convert these different small-scale energies into an electrical output, Wang and Song proposed the first nanogenerator (NG) in 2006.[426] The idea behind this device was based on the piezoelectric effect (i.e., the accumulation of electric charge in response to an applied mechanical stress), and it was made of a zinc oxide nanowire array. A few years later, Wang and co-workers presented the first NG based on the triboelectric effect.[420] The triboelectric effect (or triboelectric charging) is a phenomenon that leads to the formation of charge separation between certain materials after they come into frictional contact. This effect is very common in everyday life and has been known for a long time (almost everybody has felt a small electrical shock after walking across a carpet and then touching a metallic surface). In general, both in scientific and in technological applications, this effect is considered to be negative.

The operation of triboelectric nanogenerators (TENGs) is based on triboelectrification and electrostatic induction, described by Maxwell's displacement current and change in surface polarization.[427] The power density of TENGs is related to the charge density produced in tribological conditions; this led researchers to investigate the role that bulk and surface structural composition and geometry have in the tribocharge formation, together with the related dynamic features. The distinct abilities for attracting electrons of the two triboelectric surfaces result in a transfer of electrostatic charges from one surface to the other. When one triboelectric layer is displaced, the movement of charges breaks the original electrostatic balance, resulting in a potential difference being built between the two electrodes. A current through an external load can then be driven by such potential difference to rebalance the electrostatic status. Therefore, under periodical mechanical triggering, an alternating current (AC) output can be obtained via the TENG, and its functionality is characterized by the voltage between the electrodes, the charge transferred between electrodes, and the relative displacement between triboelectric layers.

13.1. Available Setups for Triboelectric Nanogenerators. Currently, four different working modes have been identified:[422,423] vertical contact separation (CS), lateral sliding (LS), single electrode (SE), and freestanding triboelectric layer (FT).

All modes are schematically represented in Figure 25. CS-mode TENGs are triggered by the process of contact and separation of two triboelectric layers,[420] while TENGs operating in LS mode exploit the relative sliding between layers.[428] They basically differ in the kind of tribological contact exploited (vertical vs sliding). Both modes suffer from the common disadvantage that the triboelectric layers must be interconnected with an external circuit. Such a configuration might limit the application of TENGs, when one aims to harvest energy from free-moving objects. To solve this issue, SE- and FT-mode TENGs have been proposed, in which a tribolayer is simply replaced by an electrode.[429] In particular, the FT mode has been used for various high-output TENGs with record both in the maximum power output and energy conversion efficiency.[430]

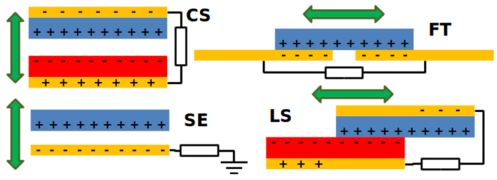

Figure 25. Four basic operation modes for TENGs: contact separation (CS), freestanding triboelectric-layer (FT), single electrode (SE), and lateral sliding (LS). Blue and red boxes represent the tribolayers, while electrodes are drawn in yellow.

The intensity of the triboelectric effect is ruled by the nature of the materials that come into contact. So far, polymers (which contain a naturally present dipole[422]) have been mostly used as tribolayers,[431] especially in implantable TENGs for biomedical applications.[432] Common examples of polymer materials are poly(dimethylsiloxane) (PDMS),[433] poly(tetrafluoroethylene),[428] poly(vinylidene fluoride),[431] fluori-

DOI: 10.1021/acs.inorgchem.9b01785
Inorg. Chem. 2019, 58, 14939−14980

nated ethylene propylene,[434] polyimide,[435] and lignin.[436] Typical values of output voltage and current density for such materials are in the order of 1−10 V and from 10^{-3} to 10^{-1} A·m^{-2}, respectively.[423] Recently, graphene has also been used as triboelectric material in TENGs, reporting values for output voltage and current of 5 V and 5×10^{-3} A·m^{-2}, respectively.[437] In addition to this, two-dimensional materials have also gained attention as triboactive candidates for TENGs.[422,437,438]

Nowadays, the choice of materials for novel TENG setups is made easier thanks to the availability of empirical lists of materials ordered by their capability of becoming tribocharged (the so-called *triboelectric series*).[439] Unfortunately, the studies on triboelectric series are sparse, and they do not provide an absolute assessment of the material performance. Making current triboelectric series both quantitative and more extended would be a welcomed progress. For achieving this aim, large-scale databases and computational resources (e.g., NOMAD[440] and AiiDA[441]) may be of crucial importance. Moreover, since the process of charge transfer in TENGs is an interfacial phenomenon, it is obvious that the characteristics of the surface are critical for the performance of the device. The effects on the signal output of the presence of impurities and/or oxides, the surface roughness, the geometry of the contact surfaces, or even the type of pretreatment during fabrication have already been highlighted.[442] This means that materials that are considered identical according to bulk analysis may display completely different microscopic surface properties. Attempts have already been made for enhancing the surface charge density by plasma[443] and laser treatment.[444]

By design, TENGs are meant to be used to harvest energy in various environments. It is therefore crucial to know the effect that the tribological conditions (e.g., contact pressure, temperature, sliding speed) can have on the TENG performance. For example, SE and FT modes can operate in open air and, thus, are subject to different pressures and atmosphere compositions. It was found that, under the same mechanical excitation, the generated charge of a PDMS-based TENG increased more than 20% when the relative humidity was decreased from 90% to 10% at ambient pressure. However, the interpretation of such an effect is not trivial, since a worsening of the performance is observed when the air pressure decreases from atmospheric pressure to 50 Torr in dry conditions.[445] In other studies, the influence of the temperature on the output performance of TENGs was investigated experimentally and supported by atomistic simulations.[446]

13.2. Triboelectric Nanogenerator Upscale. Recently, efforts have also been devoted to upscaling triboelectric nanogenerators, mainly by integrating single TENG units into a network. This was done to harvest low-frequency wave energy in oceans (the so-called blue energy), as a rich resource for large-scale clean-energy generation.[422,424,447] However, as mentioned before, harsh environmental conditions, such as humidity, have shown to significantly affect the performance of NGs.[448] One method that has proven to be promising is a hybrid approach in which conventional principles (i.e., EMGs) are combined with NGs, leading to the so-called *packaging*.[449] More specifically, in this approach the TENG is made waterproof by placing it within an isolating device, thus preventing any unwanted environmental interactions. Subsequently, an EMG is wrapped around, creating an indirect driving force on the mobile part of the TENG using its magnets. It has been shown that this approach can significantly improve the performance of TENGs.[447] First of all, this is because EMG and TENG operate in different frequency ranges, and, by combining both, one can significantly enlarge the working range.[449] Second, both vibrations and rotational motions can now be exploited for the generation of electricity. This is especially relevant for harvesting blue energy, which is characterized by a high irregularity and broad ranges of both frequencies and amplitudes. This novel design principle allows one to up-scale and go beyond the current efficiency of energy harvesting of these multivariate types of energies.[447]

13.3. Back to Nanoscale. A common issue of the above-mentioned TENGs is that frictional energy is converted into an AC output, which is unsuitable for large-impact applications such as light-emitting diodes, electronic watches, and mobile phones. Current rectification is achieved by a supplementary technological effort: switching circuits, combining TENGs with storage systems, rotating-disk configurations, or double-wheel designs have to be used to convert alternating to direct current (DC).[424] Moreover, the current density is limited due to the high impedance, if polymer-based systems are used.[450]

Recently, it has been shown that a DC current can be generated by direct sliding of a platinum-coated silicon AFM tip over a molybdenum disulfide thin film deposited on a substrate.[451] In addition, this setup also produced a maximum value of current density that is several orders of magnitude greater than the usually achievable range. In such a system, carrier flow is attributed to the direct electronic excitation at the interface followed by diffusion-drift conduction;[438] such excitation produces electron−hole pairs, triboluminescence, and exolectrons under tribological conditions.[452] However, no relation among the chemical composition of the frictional surfaces, the tribological conditions (i.e., temperature, normal load, and sliding velocity), and the current density and voltage have been clearly identified yet.

To conclude this section on TENGs, it is worth mentioning the Kelvin probe force microscopy (KPFM),[453] an experimental technique that can provide unique information about the tribocharging of materials at the nanoscale. Only recently researchers started to use this technique in combination with AFM for studying phenomena and properties related to the triboelectric effect.[454] However, it is expected that, in the coming years, the impact of this combination of techniques will bring significant contributions to the field. Another benefit of the KPFM/AFM approach is that the accessible time and size scales match very well with those available in classical molecular dynamics simulations.[455] Such computational tools are in fact suitable for interpreting experimental data, and especially for characterizing the effect of the tribological conditions and/or the nanostructure of the tribosurfaces. Despite the fact that classical tools can successfully simulate system sizes up to hundreds of thousands of atoms on the microsecond time scale, they cannot provide direct information about the electronic structure. However, hybrid (also called multiscale) approaches can be employed. For example, one can perform classical molecular dynamics simulations, to assess the tribological response of the material, and then use the configurations sampled in tribological conditions for a subsequent deeper analysis by means of ab initio techniques. Another promising tool is represented by the hybrid quantum mechanics/molecular mechanics (QM/MM) scheme, where the two levels of description are actually accessible at the same time within a single simulation.

13.4. Outlook. From the brief review given above, one can understand that, even though the computational tools for

DOI: 10.1021/acs.inorgchem.9b01785
Inorg. Chem. 2019, 58, 14939−14980

deepening our understanding of the phenomena are already in place, there is still a huge amount of work to be done. In particular, studies so far mainly dealt with polymer materials and the employment of nanostructures such as nanowires (the latter mostly for piezoelectric-based devices).[456] Moreover, the effect of the normal load on the TENG output performance has not yet been extensively studied.[457] The analysis of the hysteretic behavior of the output showed that a low contact force applied before a high one can enhance the charge transfer and consequently the performance of the device. This result is due to a dependence of the charge generation on the history of the forces applied, and such a phenomenon might be exploited to improve the operational performance of TENGs. Yet, the influence of ambient parameters such as humidity, temperature, and pressure on the hysteresis behavior needs to be further analyzed, if one wants to find ways to customize TENGs in various environments.

Important questions related to these aspects are still open. For example, how do tribological conditions affect the surface charge density, considered as the golden standard for assessing the overall performance of any NG?[448] Or how can the choice for certain materials improve durability but also reduce toxicity?

To sum up, we presented an emerging topic that directly links tribology and energy harvesting. It is expected that advances in this field will have a significant socioeconomic impact. Thanks to simulation approaches, we expect to see a vast enlargement of the list of materials used within the coming years. Because of their superior mechanical properties, inorganic materials are promising candidates for the selection of novel triboactive materials. This, in our opinion, is particularly likely to happen, considering the preliminary results already available in the literature.[437,438,451,458−463]

14. SUMMARY

The fast advance of the contemporary technology requires the improvement of existing materials and the discovery of new ones. In this perspective, nanostructured materials are the promising future for the creation of the next-generation technology. First-principle calculations are the basic starting point to obtain a good estimation of fundamental properties such as electronic configurations, magnetic orderings, structural characteristics, optical properties, and eventual coupling among these. Massive automation of such simulations would help to build a high-quality materials database to be exploited in "smart" systems (e.g., machine learning, neural networks), capable to identify existing or new materials with selected properties. However, a common standard that ensures the reliability of the results without loss of accuracy is still missing. The main effort to determine maps of materials properties (i.e., databases) is the identification of multiparameters descriptors. Despite SISSO being a valid engine to determine such descriptors, the approach is currently limited to scalar features, and the next step is to develop a systematic strategy to build environment-dependent features to be used as candidates in the feature space. Open-source projects that share materials data are the most effective means to obtain a rapid expansion of the databases. Machine-learning-based tools have already become popular for the purpose of predicting materials properties, thanks to the sharing paradigm. However, the quality of the database is crucial to obtain appropriate answers: unbalanced number of members in a family of materials could lead to systematic errors that must be accounted for. Data visualization techniques could help to identify such errors and guide the correction of the predicting model.

Besides high-throughput simulation machineries, massive ab initio molecular dynamics and meta-dynamics techniques are another efficient tool to explore and design material properties, especially when chemical reactions are to be taken into account. Nevertheless, the high cost of such kinds of simulations is still a drawback, and statistical methods like Monte Carlo-based ones represent a promising alternative to overcome such limitation. Another opportunity is the use of ad hoc descriptors, which can facilitate the characterization of specific processes and go at the same pace with the extension of existing theoretical frameworks or the development of new ones. This is the case of the specific applications discussed here such as the dendrite growth in batteries, vapochromic responses to small-molecule analytes, photoactivated linkage isomerism, prevention of He embrittlement in containment materials in nuclear reactors, thermoelectric figure of merit, metalized ferroelectrics, magneto-optical Kerr effect, and tribocharge generation. In these cases, the descriptors have been proposed based on physical reasoning rather than from statistical observations of gathered data.

From our perspective, atomistic simulations, automated modeling, and experimental techniques are rapidly developing and becoming more and more widely available. The mutual integration between theory and experiment turns out to be mandatory to significatively boost the advance of the scientific knowledge and to unveil new physical insights, which will ultimately lead to the design of novel functional materials with tunable properties meeting contemporary challenges.

AUTHOR INFORMATION

Corresponding Authors

*E-mail: danilo.puggioni@northwestern.edu. (D.P.)
*E-mail: remedios.cortese@unipa.it. (R.C.)
*E-mail: cammaant@fel.cvut.cz. (A.C.)

ORCID

Aleix Comas-Vives: 0000-0002-7002-1582
Naresh S. Dalal: 0000-0002-9996-6918
Alessio Filippetti: 0000-0002-9144-7005
Cesare Franchini: 0000-0002-7990-2984
Luca M. Ghiringhelli: 0000-0001-5099-3029
Axel Groß: 0000-0003-4037-7331
Shunbo Hu: 0000-0003-0472-0999
Janice L. Musfeldt: 0000-0002-6241-823X
Paolo Nicolini: 0000-0003-1324-7566
Rossitza Pentcheva: 0000-0002-4423-8980
Wei Ren: 0000-0001-7317-3867
Francesco Ricci: 0000-0002-2677-7227
Andrea Urru: 0000-0002-5602-3063
Paolo Vavassori: 0000-0002-4735-6640
Danilo Puggioni: 0000-0002-2128-4191
Remedios Cortese: 0000-0002-7232-8916
Antonio Cammarata: 0000-0002-5691-0682

Present Address

◀A.U.: International School for Advanced Studies (SISSA), Via Bonomea 265, 34136 Trieste, Italy.

Author Contributions

The present Viewpoint was written thanks to the contribution of all authors. Here in the following, the name of each section together with the initials of the authors contributing to it are

DOI: 10.1021/acs.inorgchem.9b01785
Inorg. Chem. 2019, 58, 14939−14980

reported for reader's convenience. "Predicting the band gap of complex materials: computational methods and procedures": C.F. "Data-driven materials science: building maps of materials properties": L.M.G. "Identifying error in machine learning models": T.D.S., K.K. "Accelerated ab initio molecular dynamics applied to the simulation of heterogeneous catalysis": L.F., A.C.-V. "Predictive description of catalytic systems using microkinetic modeling": M.V. "Atomic design principle for safer battery materials": A.G. "Responsive molecular solids": J.M.S. "Materials for nuclear reactors": T.P., H.S.S. "Novel mechanisms for improved oxide thermoelectrics explored from first-principles": B.G., R.P. "Polar, ferroelectric and multiferroic metals: three case studies": V.F., A.F., A.U., H.J.Z., J.I. "Electric Magneto-Optical properties in multi-functional hybrid materials": K.Y., F.F., S.H., W.R., F.R., P.V., J.M., N.D., H.W., A.S. "Tribology as a novel field for electricity generation": P.N., A.C., F.B., V.E.P.C. Finally, A.C., R.C., and D.P. conceptualized the work, composed the manuscript, and supervised the merging of all the contributions.

Notes

The authors declare no competing financial interest.

Biographies

Remedios Cortese collaborates with the University of Palermo and is part of the Group of Computational Chemistry of Palermo. She got degree in Chemistry and a Ph.D. in Chemical Science, both at the University of Palermo. Her scientific research is focused on the modellization, with DFT-based methods, of catalyzed reaction mechanisms concerning industrially relevant substrates.

Danilo Puggioni is an Assistant Research Professor in the Materials Science and Engineering Department at the Northwestern University. He holds a Laurea in Physics and a Ph.D. in Condensed Matter Physics, both from Università di Cagliari, Italy. Danilo joined the Northwestern University after completing postdoctoral work at Drexel University. Danilo uses first-principles theoretical techniques to understand the structural, electronic, magnetic, and optical properties of complex oxides.

After obtaining his Ph.D. in Physics at the Università degli Studi di Palermo (Italy), Antonio Cammarata moved to Philadelphia (U.S.) to work as a postdoctoral researcher at Drexel University. He then joined the Advanced Materials Group at the Department of Control Engineering of Czech Technical University in Prague (Czech Republic), where he is currently appointed as an Assistant Professor. His research interests include energy production in fuel cells, charge-ordering in perovskites, hybrid-improper ferroelectricity, nonlinear optically active materials, nanotribology, and electron−phonon and phonon−phonon coupling, among others.

■ ACKNOWLEDGMENTS

A.C., P.N., and H.S.S. acknowledge support of this work by the Czech Science Foundation (Project Nos. 17-24164Y, 16-11516Y, and 17-17921S), by Novel nanostructures for engineering applications No. CZ.02.1.01/0.0/0.0/16_026/0008396, and by The Ministry of Education, Youth and Sports from the Large Infrastructures for Research, Experimental Development and Innovations project "IT4Innovations National Supercomputing Center−LM2015070". The work of A.G. contributes to the research performed at Center for Electrochemical Energy Storage Ulm-Karlsruhe. J.M.S. is grateful to the UK Engineering and Physical Sciences Research Council for support (Grant Nos. EP/K004956/1 and EP/P007821/1) and to the Univ. of Manchester for the award of a Presidential Fellowship. Work at Tennessee (J.L.M.) is supported by NSF DMR-1707846. C.F. thanks P. Liu, J. He, and G. Kresse for the long-standing collaboration on the topic discussed in this contribution. This work was supported by the Austrian Science Fund (FWF) within the SFB ViCoM (Grant No. F41) and by the joint Indian Department of Science and Technology-FWF Project INDOX (I1490−N19). T.D.S. and S.K.K. gratefully acknowledge support from National Science Foundation through CAREER Award No. 1651668. D.P. was supported by the Army Research Office under W911NF-15-1-0017. The work of F.B. and V.E.P.C. has received funding from the European Union's Horizon 2020 research and innovation programme under Grant No. 721642: SOLUTION. L.M.G. acknowledges M. Scheffler, the main driving force behind all the works and activities presented in this contribution and all the people that contributed to the specific projects. For the SISSO development: R. Ouyang, E. Ahmetcik, and S. Curtarolo. For the perovskite classification: C. J. Bartel, C. Sutton, B. R. Goldsmith, and C. B. Musgrave. L.M.G. also acknowledges all the PIs that made the NOMAD Laboratory

DOI: 10.1021/acs.inorgchem.9b01785
Inorg. Chem. 2019, 58, 14939−14980

possible, besides M. Scheffler who is the coordinator of the Centre of Excellence: A. Rubio, R. Nieminen, F. Illas, D. Frenkel, C. Draxl, A. De Vita, K. Thygesen, K. Koski, S. Heinzel, J. M. Cela, D. Kranzlmüller, C. Clissman. The SISSO project has received funding from the European Union's Horizon 2020 research and innovation program (No. 676580: The NOMAD Laboratory—a European Center of Excellence and No. 740233: TEC 1p) and from the Berlin Big-Data Center (BBDC, No. 01IS14013E). B.G. and R.P. acknowledge funding by the German Research Foundation (Deutsche Forschungsgemeinschaft, DFG) within CRC/TRR 80, Project No. G8, and computing time at magnitUDE granted by the Center for Computational Sciences and Simulation of the Univ. of Duisburg-Essen (DFG Grant Nos. INST 20876/209-1 FUGG and No. INST 20876/243-1 FUGG). V.F. acknowledges support by Univ. di Cagliari, Fondazione di Sardegna, Regione Autonoma Sardegna via Progetto biennale di ateneo 2016 *Multiphysics approach to thermoelectricity*, and by CINECA via ISCRA grants. T.P. acknowledges support by the Centre for Advanced Photovoltaics (CZ.02.1.01/0.0/0.0/15_003/0000464). A.S. thanks the High End Foreign Expert program, Shanghai Eastern Scholar Chair Professor program, and Y. Qi for kind help in making the figures. P.V. acknowledges support from the Spanish Ministry of Economy, Industry and Competitiveness under the Maria de Maeztu Units of Excellence Programme—MDM-2016-0618. A.C.-V. acknowledges the financial support from the Spanish MEC and the European Social Fund (Grant RyC-2016-19930). L.F. thanks ETH Zurich (Research Grant ETH42 14-1) for financial support. A.F. thanks "Progetti biennali d'Ateneo Finanziati dalla Fondazione di Sardegna 2017" (project n. F71I17000170002), and Project PRIN 2017 "TOPSPIN", funded by Italian Ministry of University and Research. A.C., D.P., and R.C. thankfully acknowledge the DiFC of the University of Palermo for funding the "Atomic-scale design protocols towards energy, electronic, catalysis and sensing applications" Symposium of the EMRS 2018 Fall meeting.

REFERENCES

(1) Rogers, C.; Barker, D.; Jaeger, C. Introduction to Smart Materials and Structures, Proceedings of U.S. Army Research Office Workshop on *Smart Materials, Structures and Mathematical Issues*; Rogers, C. A., Ed.; Virginia Polytechnic Institute & State University. Technomic Publishing Co., Inc., September 15−16, 2016; pp 17−28.
(2) Hohenberg, P.; Kohn, W. Inhomogeneous Electron Gas. *Phys. Rev.* **1964**, *136*, B864.
(3) Kohn, W.; Sham, L. J. Self-Consistent Equations Including Exchange and Correlation Effects. *Phys. Rev.* **1965**, *140*, A1133.
(4) Hubbard, J.; Flowers, B. H. Electron correlations in narrow energy bands. *Proceedings of the Royal Society of London. Series A. Mathematical and Physical Sciences* **1963**, *276*, 238.
(5) Heyd, J.; Scuseria, G. E.; Ernzerhof, M. Hybrid functionals based on a screened Coulomb potential. *J. Chem. Phys.* **2003**, *118*, 8207−8215.
(6) Kim, K.; Jordan, K. D. Comparison of Density Functional and MP2 Calculations on the Water Monomer and Dimer. *J. Phys. Chem.* **1994**, *98*, 10089−10094.
(7) Stephens, P. J.; Devlin, F. J.; Chabalowski, C. F.; Frisch, M. J. Ab Initio Calculation of Vibrational Absorption and Circular Dichroism Spectra Using Density Functional Force Fields. *J. Phys. Chem.* **1994**, *98*, 11623−11627.
(8) Aryasetiawan, F.; Gunnarsson, O. The GW method. *Rep. Prog. Phys.* **1998**, *61*, 237.
(9) Salpeter, E. E.; Bethe, H. A. A Relativistic Equation for Bound-State Problems. *Phys. Rev.* **1951**, *84*, 1232.
(10) He, J.; Franchini, C. Assessing the performance of self-consistent hybrid functional for band gap calculation in oxide semiconductors. *J. Phys.: Condens. Matter* **2017**, *29*, 454004.
(11) Nunes, R. W.; Gonze, X. Berry-phase treatment of the homogeneous electric field perturbation in insulators. *Phys. Rev. B: Condens. Matter Mater. Phys.* **2001**, *63*, 155107.
(12) Ergönenc, Z.; Kim, B.; Liu, P.; Kresse, G.; Franchini, C. Converged GW quasiparticle energies for transition metal oxide perovskites. *Phys. Rev. Materials* **2018**, *2*, No. 024601.
(13) Chen, W.; Miceli, G.; Rignanese, G.-M.; Pasquarello, A. Nonempirical dielectricdependent hybrid functional with range separation for semiconductors and insulators. *Phys. Rev. Materials* **2018**, *2*, No. 073803.
(14) Grüneis, A. In *Handbook of Materials Modeling;* Andreoni, W., Yip, S., Eds.; Springer International Publishing, 2018; DOI: 10.1007/978-3-319-42913-7_90-2.
(15) Bokdam, M.; Sander, T.; Stroppa, A.; Picozzi, S.; Sarma, D.; Franchini, C.; Kresse, G. Role of polar phonons in the photo excited state of metal halide perovskites. *Sci. Rep.* **2016**, *6*, 28618.
(16) Sander, T.; Maggio, E.; Kresse, G. Beyond the Tamm-Dancoff approximation for extended systems using exact diagonalization. *Phys. Rev. B: Condens. Matter Mater. Phys.* **2015**, *92*, No. 045209.
(17) Liu, P.; Kim, B.; Chen, X.-Q.; Sarma, D. D.; Kresse, G.; Franchini, C. Relativistic GW+BSE study of the optical properties of Ruddlesden-Popper iridates. *Phys. Rev. Materials* **2018**, *2*, No. 075003.
(18) Hirata, S.; Head-Gordon, M. Time-dependent density functional theory within the Tamm−Dancoff approximation. *Chem. Phys. Lett.* **1999**, *314*, 291.
(19) https://materials.springer.com.
(20) Jain, A.; Hautier, G.; Moore, C. J.; Ong, S. P.; Fischer, C. C.; Mueller, T.; Persson, K. A.; Ceder, G. A high-throughput infrastructure for density functional theory calculations. *Comput. Mater. Sci.* **2011**, *50*, 2295−2310.
(21) Curtarolo, S.; Hart, G. L. W.; Setyawan, W.; Mehl, M. J.; Jahnátek, M.; Chepulskii, R. V.; Levy, O.; Morgan, D. *AFLOW: software for high-throughput calculation of material properties*, http://materials.duke.edu/aflow.html 2010.
(22) Saal, J. E.; Kirklin, S.; Aykol, M.; Meredig, B.; Wolverton, C. Materials Design and Discovery with High-Throughput Density Functional Theory: The Open Quantum Materials Database (OQMD). *JOM* **2013**, *65*, 1501−1509.
(23) Wilkinson, M. D.; et al. The FAIR Guiding Principles for scientific data management and stewardship. *Sci. Data* **2016**, *3*, 160018.
(24) Ghiringhelli, L. M.; Carbogno, C.; Levchenko, S.; Mohamed, F.; Huhs, G.; Lüders, M.; Oliveira, M.; Scheffler, M. Towards efficient data exchange and sharing for big-data driven materials science: metadata and data formats. *npj Computational Materials* **2017**, *3*, 46.
(25) Draxl, C.; Scheffler, M. NOMAD: The FAIR concept for big data-driven materials science. *MRS Bull.* **2018**, *43*, 676−682.
(26) Bartók, A.; Payne, M. C.; Kondor, R.; Csányi, G. Gaussian approximation potentials: The accuracy of quantum mechanics, without the electrons. *Phys. Rev. Lett.* **2010**, *104*, 136403.
(27) Behler, J. Atom-centered symmetry functions for constructing high-dimensional neural network potentials. *J. Chem. Phys.* **2011**, *134*, No. 074106.
(28) Carrete, J.; Mingo, N.; Wang, S.; Curtarolo, S. Nanograined Half-Heusler Semiconductors as Advanced Thermoelectrics: An Ab Initio High-Throughput Statistical Study. *Adv. Funct. Mater.* **2014**, *24*, 7427−7432.
(29) Rajan, K. Materials informatics: The materials "gene" and big data. *Annu. Rev. Mater. Res.* **2015**, *45*, 153−169.
(30) Mueller, T.; Kusne, A. G.; Ramprasad, R. *Reviews in Computational Chemistry;* John Wiley & Sons, Inc, 2016; pp 186−273.
(31) Kim, C.; Pilania, G.; Ramprasad, R. From organized high-throughput data to phenomenological theory using machine learning: the example of dielectric breakdown. *Chem. Mater.* **2016**, *28*, 1304−1311.

DOI: 10.1021/acs.inorgchem.9b01785
Inorg. Chem. 2019, 58, 14939−14980

(32) Faber, F. A.; Lindmaa, A.; von Lilienfeld, O. A.; Armiento, R. Machine Learning Energies of 2 Million Elpasolite (ABC_2D_6) Crystals. *Phys. Rev. Lett.* **2016**, *117*, 135502.
(33) Takahashi, K.; Tanaka, Y. Materials informatics: a journey towards material design and synthesis. *Dalton Trans.* **2016**, *45*, 10497−10499.
(34) Bartók, A.; De, S.; Poelking, C.; Bernstein, N.; Kermode, J.; Csányi, G.; Ceriotti, M. Machine learning unifies the modeling of materials and molecules. *Sci. Adv.* **2017**, *3*, 1701816.
(35) Goldsmith, B. R.; Boley, M.; Vreeken, J.; Scheffler, M.; Ghiringhelli, L. M. Uncovering structure-property relationships of materials by subgroup discovery. *New J. Phys.* **2017**, *19*, No. 013031.
(36) Pham, T. L.; Nguyen, N. D.; Nguyen, V. D.; Kino, H.; Miyake, T.; Dam, H. C. Learning structure-property relationship in crystalline materials: A study of lanthanide−transition metal alloys. *J. Chem. Phys.* **2018**, *148*, 204106.
(37) Ziletti, A.; Kumar, D.; Scheffler, M.; Ghiringhelli, L. M. Insightful classification of crystal structures using deep learning. *Nat. Commun.* **2018**, *9*, 2775.
(38) Sutton, C.; Ghiringhelli, L. M.; Yamamoto, T.; Lysogorskiy, Y.; Blumenthal, L.; Hammerschmidt, T.; Golebiowski, J.; Liu, X.; Ziletti, A.; Scheffler, M. NOMAD 2018 Kaggle Competition: Solving Materials Science Challenges Through Crowd Sourcing. *arXiv preprint arXiv:1812.00085*, 2018.
(39) Ghiringhelli, L. M.; Vybiral, J.; Levchenko, S. V.; Draxl, C.; Scheffler, M. Big data of materials science: Critical role of the descriptor. *Phys. Rev. Lett.* **2015**, *114*, 105503.
(40) Candès, E. J.; Wakin, M. B. An introduction to compressive sampling. *IEEE Signal Proc. Mag.* **2008**, *25*, 21−30.
(41) Nelson, L. J.; Hart, G. L. W.; Zhou, F.; Ozoliņš, V. Compressive sensing as a paradigm for building physics models. *Phys. Rev. B: Condens. Matter Mater. Phys.* **2013**, *87*, No. 035125.
(42) Ghiringhelli, L. M.; Vybiral, J.; Ahmetcik, E.; Ouyang, R.; Levchenko, S. V.; Draxl, C.; Scheffler, M. Learning physical descriptors for materials science by compressed sensing. *New J. Phys.* **2017**, *19*, No. 023017.
(43) Guyon, I.; Elisseeff, A. An introduction to variable and feature selection. *J. Mach. Learn. Res.* **2003**, *3*, 1157−1182.
(44) Ouyang, R.; Curtarolo, S.; Ahmetcik, E.; Scheffler, M.; Ghiringhelli, L. M. SISSO: A compressed-sensing method for identifying the best low-dimensional descriptor in an immensity of offered candidates. *Phys. Rev. Mater.* **2018**, *2*, No. 083802.
(45) Fan, J.; Lv, J. Sure independence screening for ultrahigh dimensional feature space. *J. R. Statist. Soc. B* **2008**, *70*, 849−911.
(46) Tibshirani, R. Regression shrinkage and selection via the lasso. *J. R. Statist. Soc. B* **1996**, *58*, 267−288.
(47) Tropp, J. A.; Gilbert, A. C. Signal recovery from random measurements via orthogonal matching pursuit. *IEEE Trans. Inf. Theory* **2007**, *53*, 4655−4666.
(48) Pati, Y. C.; Rezaiifar, R.; Krishnaprasad, P. S. *The Twenty-Seventh Asilomar Conference: Signals, Systems and Computers;* IEEE, 1993; Vol. *1*, pp 40−44.
(49) Bartel, C. J.; Sutton, C.; Goldsmith, B. R.; Ouyang, R.; Musgrave, C. B.; Ghiringhelli, L. M.; Scheffler, M. New tolerance factor to predict the stability of perovskite oxides and halides. *Science Advances* **2019**, *5*, No. eaav0693.
(50) Ghiringhelli, L. https://th.fhi-berlin.mpg.de/movies/?m=nomadbat, 2017.
(51) Regler, B. https://analytics-toolkit.nomad-coe.eu/tutorial-periodic-table, 2017.
(52) Acosta, C. M.; Ouyang, R.; Fazzio, A.; Scheffler, M.; Ghiringhelli, L. M.; Carbogno, C. Analysis of Topological Transitions in Two-dimensional Materials by Compressed Sensing. *arXiv:1805.10950* 2018.
(53) Bartel, C. J.; Millican, S. L.; Deml, A. M.; Rumptz, J. R.; Tumas, W.; Weimer, A. W.; Lany, S.; Stevanović, V.; Musgrave, C. B.; Holder, A. M. Physical descriptor for the Gibbs energy of inorganic crystalline solids and temperaturedependent materials chemistry. *Nat. Commun.* **2018**, *9*, 4168.
(54) Hwang, J.; Rao, R. R.; Giordano, L.; Katayama, Y.; Yu, Y.; Shao-Horn, Y. Perovskites in catalysis and electrocatalysis. *Science* **2017**, *358*, 751−756.
(55) Duan, C.; Tong, J.; Shang, M.; Nikodemski, S.; Sanders, M.; Ricote, S.; Almansoori, A.; O'Hayre, R. Readily processed protonic ceramic fuel cells with high performance at low temperatures. *Science* **2015**, *349*, 1321−1326.
(56) Cohen, R. E. Origin of ferroelectricity in perovskite oxides. *Nature* **1992**, *358*, 136−138.
(57) Yi, T.; Chen, W.; Cheng, L.; Bayliss, R. D.; Lin, F.; Plews, M. R.; Nordlund, D.; Doeff, M. M.; Persson, K. A.; Cabana, J. Investigating the Intercalation Chemistry of Alkali Ions in Fluoride Perovskites. *Chem. Mater.* **2017**, *29*, 1561−1568.
(58) Correa-Baena, J.-P.; Saliba, M.; Buonassisi, T.; Grätzel, M.; Abate, A.; Tress, W.; Hagfeldt, A. Promises and challenges of perovskite solar cells. *Science* **2017**, *358*, 739−744.
(59) Kovalenko, M. V.; Protesescu, L.; Bodnarchuk, M. I. Properties and potential optoelectronic applications of lead halide perovskite nanocrystals. *Science* **2017**, *358*, 745−750.
(60) Kirkpatrick, S.; Gelatt, C. D.; Vecchi, M. P. Optimization by simulated annealing. *Science* **1983**, *220*, 671−680.
(61) Doye, J. P.; Wales, D. J. Thermodynamics of global optimization. *Phys. Rev. Lett.* **1998**, *80*, 1357.
(62) Goedecker, S. Minima hopping: An efficient search method for the global minimum of the potential energy surface of complex molecular systems. *J. Chem. Phys.* **2004**, *120*, 9911−9917.
(63) Oganov, A. R.; Lyakhov, A. O.; Valle, M. How Evolutionary Crystal Structure Prediction Works−and Why. *Acc. Chem. Res.* **2011**, *44*, 227−237.
(64) Curtarolo, S.; Hart, G. L.; Nardelli, M. B.; Mingo, N.; Sanvito, S.; Levy, O. The high-throughput highway to computational materials design. *Nat. Mater.* **2013**, *12*, 191.
(65) Goldschmidt, V. M. Die gesetze der krystallochemie. *Naturwissenschaften* **1926**, *14*, 477−485.
(66) Li, W.; Wang, Z.; Deschler, F.; Gao, S.; Friend, R. H.; Cheetham, A. K. Chemically diverse and multifunctional hybrid organic−inorganic perovskites. *Nature Reviews Materials* **2017**, *2*, 16099.
(67) Zhang, H.; Li, N.; Li, K.; Xue, D. Structural stability and formability of ABO_3-type perovskitecompounds. *Acta Crystallogr., Sect. B: Struct. Sci.* **2007**, *63*, 812−818.
(68) Li, C.; Lu, X.; Ding, W.; Feng, L.; Gao, Y.; Guo, Z. Formability of ABX_3 (X = F, Cl, Br, I) Halide Perovskites. *Acta Crystallogr., Sect. B: Struct. Sci.* **2008**, *64*, 702−707.
(69) Travis, W.; Glover, E.; Bronstein, H.; Scanlon, D.; Palgrave, R. On the application of the tolerance factor to inorganic and hybrid halide perovskites: a revised system. *Chemical Science* **2016**, *7*, 4548−4556.
(70) Mansouri Tehrani, A.; Oliynyk, A.; Parry, M.; Rizvi, Z.; Couper, S.; Lin, F.; Miyagi, L.; Sparks, T.; Brgoch, J. Machine learning directed search for ultraincompressible, superhard materials. *J. Am. Chem. Soc.* **2018**, *140*, 9844−9853.
(71) Gaultois, M. W.; Oliynyk, A.; Mar, A.; Sparks, T.; Mulholland, G. J.; Meredig, B. Perspective: Web-based machine learning models forreal-times creening of thermoelectric materials properties. *APL Mater.* **2016**, *4*, No. 053213.
(72) Sparks, T.; Gaultois, M. W.; Oliynyk, A.; Brgoch, J.; Meredig, B. Data mining our way to the next generation of thermoelectrics. *Scr. Mater.* **2016**, *111*, 10−15.
(73) Kauwe, S.; Graser, J.; Vazquez, A.; Sparks, T. Machine learning prediction of heat capacity for solid inorganics. *Integrating Materials and Manufacturing Innovation* **2018**, *7*, 43−51.
(74) Graser, J.; Kauwe, S.; Sparks, T. Machine learning and energy minimization approaches for crystal structure predictions: A review and new horizons. *Chem. Mater.* **2018**, *30*, 3601−3612.
(75) Lemonick, S. Is machine learning overhyped? *Chem. Eng. News* **2018**, *96*, 16−20.

DOI: 10.1021/acs.inorgchem.9b01785
Inorg. Chem. 2019, 58, 14939−14980

(76) Seshadri, R.; Sparks, T. D. Perspective: Interactive material property databases through aggregation of literature data. *APL Mater.* **2016**, *4*, No. 053206.
(77) Michel, K.; Meredig, B. Beyond bulk single crystals: a data format for all materials structure-property-processing relationships. *MRS Bull.* **2016**, *41*, 617.
(78) Kauwe, S.; Yang, Y.; Sparks, T. VIsualization Tool for Atomic modeLs (VITAL): A simple visualization tool for materials predictions. *ChemRxiv* 2019, https://chemrxiv.org/s/cea9ca4196730fae1677.
(79) Kauwe, S. K.; Welker, T.; Sparks, T. D. Extracting Knowledge from DFT: Experimental Band Gap Predictions Through Ensemble Learning. *ChemRXiv* **2018**, DOI: 10.26434/chemrxiv.7236029.v1.
(80) Maaten, L.; Hinton, G. Visualizing data using t-SNE. *Journal of machine learning research* **2008**, *9*, 2579−2605.
(81) Meredig, B.; Antono, E.; Church, C.; Hutchinson, M.; Ling, J.; Paradiso, S.; Blaiszik, B.; Foster, I.; Gibbons, B.; Hattrick-Simpers, J.; Mehta, A.; Ward, L. Can machine learning identify the next high-temperature superconductor? Examining extrapolation performance for materials discovery. *Mol. Syst. Des. Eng.* **2018**, *3*, 819−825.
(82) Nørskov, J. K.; Bligaard, T.; Rossmeisl, J.; Christensen, C. H. Towards the computational design of solid catalysts. *Nat. Chem.* **2009**, *1*, 37.
(83) Nørskov, J. K.; Abild-Pedersen, F.; Studt, F.; Bligaard, T. Density functional theory in surface chemistry and catalysis. *Proc. Natl. Acad. Sci. U. S. A.* **2011**, *108*, 937−943.
(84) Michaelides, A.; Scheffler, M. *Surface and Interface Science;* John Wiley & Sons, Ltd, 2014; pp 13−72 DOI: 10.1002/9783527680535.ch2.
(85) Dumesic, J. *The Microkinetics of heterogeneous catalysis;* ACS professional reference book; American Chemical Society, 1993.
(86) Comas-Vives, A.; Furman, K.; Gajan, D.; Akatay, M. C.; Lesage, A.; Ribeiro, F. H.; Copéret, C. Predictive morphology, stoichiometry and structure of surface species in supported Ru nanoparticles under H_2 and CO atmospheres from combined experimental and DFT studies. *Phys. Chem. Chem. Phys.* **2016**, *18*, 1969−1979.
(87) Piccini, G.; Sauer, J. Effect of Anharmonicity on Adsorption Thermodynamics. *J. Chem. Theory Comput.* **2014**, *10*, 2479−2487.
(88) Piccini, G.; Alessio, M.; Sauer, J. Ab Initio Calculation of Rate Constants for Molecule−Surface Reactions with Chemical Accuracy. *Angew. Chem., Int. Ed.* **2016**, *55*, 5235−5237.
(89) Alessio, M.; Bischoff, F. A.; Sauer, J. Chemically accurate adsorption energies for methane and ethane monolayers on the MgO(001) surface. *Phys. Chem. Chem. Phys.* **2018**, *20*, 9760−9769.
(90) Li, H.; Paolucci, C.; Schneider, W. F. Zeolite Adsorption Free Energies from ab Initio Potentials of Mean Force. *J. Chem. Theory Comput.* **2018**, *14*, 929−938.
(91) Sprowl, L. H.; Campbell, C. T.; Árnadóttir, L. Hindered Translator and Hindered Rotor Models for Adsorbates: Partition Functions and Entropies. *J. Phys. Chem. C* **2016**, *120*, 9719−9731.
(92) Campbell, C. T.; Sprowl, L. H.; Árnadóttir, L. Equilibrium Constants and Rate Constants for Adsorbates: Two-Dimensional (2D) Ideal Gas, 2D Ideal Lattice Gas, and Ideal Hindered Translator Models. *J. Phys. Chem. C* **2016**, *120*, 10283−10297.
(93) Bajpai, A.; Mehta, P.; Frey, K.; Lehmer, A. M.; Schneider, W. F. Benchmark First Principles Calculations of Adsorbate Free Energies. *ACS Catal.* **2018**, *8*, 1945−1954.
(94) Jorgensen, M.; Grönbeck, H. Adsorbate Entropies with Complete Potential Energy Sampling in Microkinetic Modeling. *J. Phys. Chem. C* **2017**, *121*, 7199−7207.
(95) Sun, G.; Jiang, H. Ab initio molecular dynamics with enhanced sampling for surface reaction kinetics at finite temperatures: $CH_2 \rightleftharpoons CH + H$ on Ni(111) as a case study. *J. Chem. Phys.* **2015**, *143*, 234706.
(96) Cammarata, A.; Polcar, T. Overcoming nanoscale friction barriers in transition metal dichalcogenides. *Phys. Rev. B: Condens. Matter Mater. Phys.* **2017**, *96*, No. 085406.
(97) Foppa, L.; Iannuzzi, M.; Copéret, C.; Comas-Vives, A. Adlayer Dynamics Drives CO Activation in Ru-Catalyzed Fischer−Tropsch Synthesis. *ACS Catal.* **2018**, *8*, 6983−6992.
(98) Foppa, L.; Iannuzzi, M.; Copéret, C.; Comas-Vives, A. Facile Fischer−Tropsch Chain Growth from CH2 Monomers Enabled by the Dynamic CO Adlayer. *ACS Catal.* **2019**, *9*, 6571−6582.
(99) Foppa, L.; Iannuzzi, M.; Copéret, C.; Comas-Vives, A. CO methanation on ruthenium flat and stepped surfaces: Key role of H-transfers and entropy revealed by ab initio molecular dynamics. *J. Catal.* **2019**, *371*, 270−275.
(100) Marx, D.; Hutter, J. *Ab Initio Molecular Dynamics: Basic Theory and Advanced Methods;* Cambridge University Press, 2009.
(101) *Modern Methods and Algorithms of Quantum Chemistry: Proceedings;* NIC series; John-von-Neumann-Inst. for Computing, 2000.
(102) Laio, A.; Parrinello, M. Escaping free-energy minima. *Proc. Natl. Acad. Sci. U. S. A.* **2002**, *99*, 12562−12566.
(103) Laio, A.; Rodriguez-Fortea, A.; Gervasio, F. L.; Ceccarelli, M.; Parrinello, M. Assessing the Accuracy of Metadynamics. *J. Phys. Chem. B* **2005**, *109*, 6714−6721.
(104) Barducci, A.; Bonomi, M.; Parrinello, M. Metadynamics. *Wiley Interdisciplinary Reviews: Computational Molecular Science* **2011**, *1*, 826−843.
(105) Iannuzzi, M.; Laio, A.; Parrinello, M. Efficient Exploration of Reactive Potential Energy Surfaces Using Car-Parrinello Molecular Dynamics. *Phys. Rev. Lett.* **2003**, *90*, 238302.
(106) Ensing, B.; De Vivo, M.; Liu, Z.; Moore, P.; Klein, M. L. Metadynamics as a Tool for Exploring Free Energy Landscapes of Chemical Reactions. *Acc. Chem. Res.* **2006**, *39*, 73−81.
(107) Comas-Vives, A.; Stirling, A.; Lledós, A.; Ujaque, G. The Wacker Process: Inneror Outer-Sphere Nucleophilic Addition? New Insights from Ab Initio Molecular Dynamics. *Chem. - Eur. J.* **2010**, *16*, 8738−8747.
(108) Martínez-Suárez, L.; Siemer, N.; Frenzel, J.; Marx, D. Reaction Network of Methanol Synthesis over Cu/ZnO Nanocatalysts. *ACS Catal.* **2015**, *5*, 4201−4218.
(109) Cheng, T.; Xiao, H.; Goddard, W. A. Full atomistic reaction mechanism with kinetics for CO reduction on Cu(100) from ab initio molecular dynamics free-energy calculations at 298 K. *Proc. Natl. Acad. Sci. U. S. A.* **2017**, *114*, 1795−1800.
(110) Gurdal, Y.; Hutter, J.; Iannuzzi, M. Insight into (Co)Pyrphyrin Adsorption on Au(111): Effects of Herringbone Reconstruction and Dynamics of Metalation. *J. Phys. Chem. C* **2017**, *121*, 11416−11427.
(111) Loveless, B. T.; Buda, C.; Neurock, M.; Iglesia, E. CO Chemisorption and Dissociation at High Coverages during CO Hydrogenation on Ru Catalysts. *J. Am. Chem. Soc.* **2013**, *135*, 6107−6121.
(112) Ciobica, I. M.; van Santen, R. A. Carbon Monoxide Dissociation on Planar and Stepped Ru(0001) Surfaces. *J. Phys. Chem. B* **2003**, *107*, 3808−3812.
(113) Reuter, K.; Scheffler, M. Composition, structure, and stability of RuO_2(110) as a function of oxygen pressure. *Phys. Rev. B: Condens. Matter Mater. Phys.* **2001**, *65*, No. 035406.
(114) Micheletti, C.; Laio, A.; Parrinello, M. Reconstructing the Density of States by History-Dependent Metadynamics. *Phys. Rev. Lett.* **2004**, *92*, 170601.
(115) Behler, J. Perspective: Machine learning potentials for atomistic simulations. *J. Chem. Phys.* **2016**, *145*, 170901.
(116) James, A. D. *The Microkinetics of heterogeneous catalysis;* American Chemical Society: Washington, DC, 1993.
(117) Broadbelt, L. J.; Snurr, R. Q. Applications of molecular modeling in heterogeneous catalysis research. *Appl. Catal., A* **2000**, *200*, 23−46.
(118) Stoltze, P. Microkinetic simulation of catalytic reactions. *Prog. Surf. Sci.* **2000**, *65*, 65−150.
(119) Raimondeau, S.; Vlachos, D. G. Recent developments on multiscale, hierarchical modeling of chemical reactors. *Chem. Eng. J.* **2002**, *90*, 3−23.

DOI: 10.1021/acs.inorgchem.9b01785
Inorg. Chem. 2019, 58, 14939−14980

(120) Salciccioli, M.; Stamatakis, M.; Caratzoulas, S.; Vlachos, D. G. A review of multiscale modeling of metal-catalyzed reactions: Mechanism development for complexity and emergent behavior. *Chem. Eng. Sci.* **2011**, *66*, 4319−4355.
(121) Vlachos, D. G. Multiscale modeling for emergent behavior, complexity, and combinatorial explosion. *AIChE J.* **2012**, *58*, 1314−1325.
(122) Stamatakis, M.; Vlachos, D. G. Unraveling the Complexity of Catalytic Reactions via Kinetic Monte Carlo Simulation: Current Status and Frontiers. *ACS Catal.* **2012**, *2*, 2648−2663.
(123) Vandichel, M.; Moscu, A.; Gronbeck, H. Catalysis at the Rim: A Mechanism for Low Temperature CO Oxidation over Pt_3Sn. *ACS Catal.* **2017**, *7*, 7431−7441.
(124) Jorgensen, M.; Gronbeck, H. First-Principles Microkinetic Modeling of Methane Oxidation over Pd(100) and Pd(111). *ACS Catal.* **2016**, *6*, 6730−6738.
(125) Heard, C. J.; Siahrostami, S.; Gronbeck, H. Structural and Energetic Trends of Ethylene Hydrogenation over Transition Metal Surfaces. *J. Phys. Chem. C* **2016**, *120*, 995−1003.
(126) Bossche, M. V. d.; Gronbeck, H. Methane Oxidation over PdO(101) Revealed by First-Principles Kinetic Modeling. *J. Am. Chem. Soc.* **2015**, *137*, 12035−12044.
(127) Choksi, T.; Greeley, J. Partial Oxidation of Methanol on MoO_3 (010): A DFT and Microkinetic Study. *ACS Catal.* **2016**, *6*, 7260−7277.
(128) Hus, M.; Kopac, D.; Stefancic, N. S.; Jurkovic, D. L.; Dasireddy, V. D. B. C.; Likozar, B. Unravelling the mechanisms of CO_2 hydrogenation to methanol on Cu-based catalysts using first-principles multiscale modelling and experiments. *Catal. Sci. Technol.* **2017**, *7*, 5900−5913.
(129) Foppa, L.; Silaghi, M.-C.; Larmier, K.; Comas-Vives, A. Intrinsic reactivity of Ni, Pd and Pt surfaces in dry reforming and competitive reactions: Insights from first principles calculations and microkinetic modeling simulations. *J. Catal.* **2016**, *343*, 196−207.
(130) Foppa, L.; Margossian, T.; Kim, S. M.; Muller, C.; Copéret, C.; Larmier, K.; Comas-Vives, A. Contrasting the Role of Ni/Al_2O_3 Interfaces in Water−Gas Shift and Dry Reforming of Methane. *J. Am. Chem. Soc.* **2017**, *139*, 17128−17139.
(131) Borght, K.; Toch, K.; Galvita, V. V.; Thybaut, J. W.; Marin, G. B. Information-Driven Catalyst Design Based on High-Throughput Intrinsic Kinetics. *Catalysts* **2015**, *5*, 1948−1968.
(132) Jorgensen, M.; Gronbeck, H. The Site-Assembly Determines Catalytic Activity of Nanoparticles. *Angew. Chem., Int. Ed.* **2018**, *57*, 5086−5089.
(133) Bell, R. P. The Theory of Reactions Involving Proton Transfers. *Proceedings of the Royal Society of London A: Mathematical, Physical and Engineering Sciences* **1936**, *154*, 414−429.
(134) Evans, M. G.; Polanyi, M. Further considerations on the thermodynamics of chemical equilibria and reaction rates. *Trans. Faraday Soc.* **1936**, *32*, 1333−1360.
(135) Hammett, L. P.; Paul, M. A. The Relation between the Rates of Some Acid Catalyzed Reactions and the Acidity Function, H0. *J. Am. Chem. Soc.* **1934**, *56*, 830−832.
(136) Hammer, B.; Norskov, J. K. Why gold is the noblest of all the metals. *Nature* **1995**, *376*, 238.
(137) Liu, P.; Norskov, J. K. Ligand and ensemble effects in adsorption on alloy surfaces. *Phys. Chem. Chem. Phys.* **2001**, *3*, 3814−3818.
(138) Jacobsen, C. J. H.; Dahl, S.; Clausen, B. S.; Bahn, S.; Logadottir, A.; Norskov, J. K. Catalyst Design by Interpolation in the Periodic Table: Bimetallic Ammonia Synthesis Catalysts. *J. Am. Chem. Soc.* **2001**, *123*, 8404−8405.
(139) Norskov, J. K.; Bligaard, T.; Rossmeisl, J.; Christensen, C. H. Towards the computational design of solid catalysts. *Nat. Chem.* **2009**, *1*, 37−46.
(140) Medford, A. J.; Shi, C.; Hoffmann, M. J.; Lausche, A. C.; Fitzgibbon, S. R.; Bligaard, T.; Norskov, J. K. CatMAP: A Software Package for Descriptor-Based Microkinetic Mapping of Catalytic Trends. *Catal. Lett.* **2015**, *145*, 794−807.
(141) Stroppa, A.; Mittendorfer, F.; Andersen, J. N.; Parteder, G.; Allegretti, F.; Surnev, S.; Netzer, F. P. Adsorption and Dissociation of CO on Bare and Ni-Decorated Stepped Rh(553) Surfaces. *J. Phys. Chem. C* **2009**, *113*, 942−949.
(142) Schimka, L.; Harl, J.; Stroppa, A.; Gruneis, A.; Marsman, M.; Mittendorfer, F.; Kresse, G. Accurate surface and adsorption energies from many-body perturbation theory. *Nat. Mater.* **2010**, *9*, 741.
(143) Hammer, B.; Norskov, J. K. Electronic factors determining the reactivity of metal surfaces. *Surf. Sci.* **1995**, *343*, 211−220.
(144) Greeley, J.; Norskov, J. K. A general scheme for the estimation of oxygen binding energies on binary transition metal surface alloys. *Surf. Sci.* **2005**, *592*, 104−111.
(145) Stroppa, A.; Kresse, G. The shortcomings of semi-local and hybrid functionals: what we can learn from surface science studies. *New J. Phys.* **2008**, *10*, No. 063020.
(146) Stroppa, A.; Mittendorfer, F. Tuning the CO Dissociation Barriers by Low Dimensional Surface Alloys. *J. Phys. Chem. C* **2011**, *115*, 21320−21323.
(147) Medford, A. J.; Vojvodic, A.; Hummelshoj, J. S.; Voss, J.; Abild-Pedersen, F.; Studt, F.; Bligaard, T.; Nilsson, A.; Norskov, J. K. From the Sabatier principle to a predictive theory of transition-metal heterogeneous catalysis. *J. Catal.* **2015**, *328*, 36−42.
(148) Filot, I. A. W.; van Santen, R. A.; Hensen, E. J. M. The Optimally Performing Fischer−Tropsch Catalyst. *Angew. Chem., Int. Ed.* **2014**, *53*, 12746−12750.
(149) Busch, M.; Wodrich, M. D.; Corminboeuf, C. Linear scaling relationships and volcano plots in homogeneous catalysis - revisiting the Suzuki reaction. *Chemical Science* **2015**, *6*, 6754−6761.
(150) Rodriguez, J.; Graciani, J.; Evans, J.; Park, J.; Yang, F.; Stacchiola, D.; Senanayake, S.; Ma, S.; Pérez, M.; Liu, P.; Sanz, J.; Hrbek, J. Water-Gas Shift Reaction on a Highly Active Inverse CeOx/Cu(111) Catalyst: Unique Role of Ceria Nanoparticles. *Angew. Chem., Int. Ed.* **2009**, *48*, 8047−8050.
(151) Yang, F.; Graciani, J.; Evans, J.; Liu, P.; Hrbek, J.; Sanz, J. F.; Rodriguez, J. A. CO Oxidation on Inverse CeOx/Cu(111) Catalysts: High Catalytic Activity and Ceria-Promoted Dissociation of O2. *J. Am. Chem. Soc.* **2011**, *133*, 3444−3451.
(152) Schott, V.; Oberhofer, H.; Birkner, A.; Xu, M.; Wang, Y.; Muhler, M.; Reuter, K.; Wöll, C. Chemical Activity of Thin Oxide Layers: Strong Interactions with the Support Yield a New Thin-Film Phase of ZnO. *Angew. Chem., Int. Ed.* **2013**, *52*, 11925−11929.
(153) Kattel, S.; Yan, B.; Yang, Y.; Chen, J. G.; Liu, P. Optimizing Binding Energies of Key Intermediates for CO_2 Hydrogenation to Methanol over Oxide-Supported Copper. *J. Am. Chem. Soc.* **2016**, *138*, 12440−12450.
(154) Reichenbach, T.; Mondal, K.; Jager, M.; Vent-Schmidt, T.; Himmel, D.; Dybbert, V.; Bruix, A.; Krossing, I.; Walter, M.; Moseler, M. Ab initio study of CO_2 hydrogenation mechanisms on inverse ZnO/Cu catalysts. *J. Catal.* **2018**, *360*, 168−174.
(155) Huber, B.; Koskinen, P.; Hakkinen, H.; Moseler, M. Oxidation of magnesia-supported Pd-clusters leads to the ultimate limit of epitaxy with a catalytic function. *Nat. Mater.* **2006**, *5*, 44−47.
(156) Song, W. Y.; Su, Y. Q.; Hensen, E. J. M. A DFT Study of CO Oxidation at the Pd-CeO_2(110) Interface. *J. Phys. Chem. C* **2015**, *119*, 27505−27511.
(157) Vayssilov, G. N.; Lykhach, Y.; Migani, A.; Staudt, T.; Petrova, G. P.; Tsud, N.; Skala, T.; Bruix, A.; Illas, F.; Prince, K. C.; Matolin, V.; Neyman, K. M.; Libuda, J. Support nanostructure boosts oxygen transfer to catalytically active platinum nanoparticles. *Nat. Mater.* **2011**, *10*, 310−315.
(158) Kozlov, S. M.; Neyman, K. M. Effects of electron transfer in model catalysts composed of Pt nanoparticles on CeO2(111) surface. *J. Catal.* **2016**, *344*, 507−514.
(159) Sun, D.; Gu, X.-K.; Ouyang, R.; Su, H.-Y.; Fu, Q.; Bao, X.; Li, W.-X. Theoretical Study of the Role of a Metal−Cation Ensemble at the Oxide−Metal Boundary on CO Oxidation. *J. Phys. Chem. C* **2012**, *116*, 7491−7498.
(160) Pan, Q.; Weng, X.; Chen, M.; Giordano, L.; Pacchioni, G.; Noguera, C.; Goniakowski, J.; Shaikhutdinov, S.; Freund, H.-J.

DOI: 10.1021/acs.inorgchem.9b01785
Inorg. Chem. 2019, 58, 14939−14980

Enhanced CO Oxidation on the Oxide/Metal Interface: From Ultra-High Vacuum to Near-Atmospheric Pressures. *ChemCatChem* **2015**, *7*, 2620−2627.
(161) Vandichel, M.; Gronbeck, H. CO Oxidation at SnO_2/Pt_3Sn(111) Interfaces. *Top. Catal.* **2018**, *61*, 1458−1464.
(162) Vandichel, M.; Gronbeck, H. A dimer path for CO dissociation on PtSn. *Catal. Sci. Technol.* **2019**, *9*, 695.
(163) Michalak, W. D.; Krier, J. M.; Alayoglu, S.; Shin, J. Y.; An, K.; Komvopoulos, K.; Liu, Z.; Somorjai, G. A. CO oxidation on PtSn nanoparticle catalysts occurs at the interface of Pt and Sn oxide domains formed under reaction conditions. *J. Catal.* **2014**, *312*, 17−25.
(164) Campbell, C. T. The Degree of Rate Control: A Powerful Tool for Catalysis Research. *ACS Catal.* **2017**, *7*, 2770−2779.
(165) Stegelmann, C.; Andreasen, A.; Campbell, C. T. Degree of Rate Control: How Much the Energies of Intermediates and Transition States Control Rates. *J. Am. Chem. Soc.* **2009**, *131*, 8077−8082.
(166) Campbell, C. T. Micro- and macro-kinetics: their relationship in heterogeneous catalysis. *Top. Catal.* **1994**, *1*, 353−366.
(167) Jorgensen, M.; Gronbeck, H. Connection between macroscopic kinetic measurables and the degree of rate control. *Catal. Sci. Technol.* **2017**, *7*, 4034−4040.
(168) Dietze, E. M.; Abild-Pedersen, F.; Plessow, P. N. Comparison of Sintering by Particle Migration and Ripening through First-Principles-Based Simulations. *J. Phys. Chem. C* **2018**, *122*, 26563−26569.
(169) Groß, A. Fundamental Challenges for Modeling Electrochemical Energy Storage Systems at the Atomic Scale. *Top. Curr. Chem.* **2018**, *376*, 17.
(170) Xu, W.; Wang, J.; Ding, F.; Chen, X.; Nasybulin, E.; Zhang, Y.; Zhang, J.-G. Lithium metal anodes for rechargeable batteries. *Energy Environ. Sci.* **2014**, *7*, 513−537.
(171) Wu, F.; Yuan, Y.-X.; Cheng, X.-B.; Bai, Y.; Li, Y.; Wu, C.; Zhang, Q. Perspectives for restraining harsh lithium dendrite growth: Towards robust lithium metal anodes. *Energy Storage Mater.* **2018**, *15*, 148−170.
(172) Medenbach, L.; Bender, C. L.; Haas, R.; Mogwitz, B.; Pompe, C.; Adelhelm, P.; Schröder, D.; Janek, J. Origins of Dendrite Formation in Sodium−Oxygen Batteries and Possible Countermeasures. *Energy Technol.* **2017**, *5*, 2265−2274.
(173) Aurbach, D.; Cohen, Y.; Moshkovich, M. The Study of Reversible Magnesium Deposition by In Situ Scanning Tunneling Microscopy. *Electrochem. Solid-State Lett.* **2001**, *4*, A113.
(174) Jäckle, M.; Groß, A. Microscopic properties of lithium, sodium, and magnesium battery anode materials related to possible dendrite growth. *J. Chem. Phys.* **2014**, *141*, 174710.
(175) Steiger, J.; Richter, G.; Wenk, M.; Kramer, D.; Mönig, R. Comparison of the growth of lithium filaments and dendrites under different conditions. *Electrochem. Commun.* **2015**, *50*, 11−14.
(176) Ehrlich, G.; Hudda, F. G. Atomic view of surface self-diffusion: tungsten on tungsten. *J. Chem. Phys.* **1966**, *44*, 1039.
(177) Schwoebel, R. L.; Shipsey, E. J. Step motion on crystal surfaces. *J. Appl. Phys.* **1966**, *37*, 3682.
(178) Jäckle, M.; Helmbrecht, K.; Smits, M.; Stottmeister, D.; Groß, A. Self-diffusion barriers: possible descriptors for dendrite growth in batteries? *Energy Environ. Sci.* **2018**, *11*, 3400−3407.
(179) Elia, G. A.; Marquardt, K.; Hoeppner, K.; Fantini, S.; Lin, R.; Knipping, E.; Peters, W.; Drillet, J.-F.; Passerini, S.; Hahn, R. An Overview and Future Perspectives of Aluminum Batteries. *Adv. Mater.* **2016**, *28*, 7564−7579.
(180) Parker, J. F.; Chervin, C. N.; Nelson, E. S.; Rolison, D. R.; Long, J. W. Wiring zinc in three dimensions re-writes battery performance-dendrite-free cycling. *Energy Environ. Sci.* **2014**, *7*, 1117−1124.
(181) Parker, J. F.; Chervin, C. N.; Pala, I. R.; Machler, M.; Burz, M. F.; Long, J. W.; Rolison, D. R. Rechargeable nickel-3D zinc batteries: An energy-dense, safer alternative to lithium-ion. *Science* **2017**, *356*, 415−418.
(182) Lin, X.; Dasgupta, A.; Xie, F.; Schimmel, T.; Evers, F.; Groß, A. Exchange processes in the contact formation of Pb electrodes. *Electrochim. Acta* **2014**, *140*, 505−510.
(183) Wang, K.; Pei, P.; Ma, Z.; Chen, H.; Xu, H.; Chen, D.; Wang, X. Dendrite growth in the recharging process of Zinc−air batteries. *J. Mater. Chem. A* **2015**, *3*, 22648−22655.
(184) Davidson, R.; Verma, A.; Santos, D.; Hao, F.; Fincher, C.; Xiang, S.; Van Buskirk, J.; Xie, K.; Pharr, M.; Mukherjee, P.; Banerjee, S. Formation of Magnesium Dendrites during Electrodeposition. *ACS Energy Lett.* **2019**, *4*, 375−376.
(185) Gaissmaier, D.; Fantauzzi, D.; Jacob, T. First principles studies of self-diffusion processes on metallic lithium surfaces. *J. Chem. Phys.* **2019**, *150*, No. 041723.
(186) Magnussen, O. M.; Groß, A. Toward an Atomic-Scale Understanding of Electrochemical Interface Structure and Dynamics. *J. Am. Chem. Soc.* **2019**, *141*, 4777−4790.
(187) Xu, L.; Ho, C.-L.; Liu, L.; Wong, W.-Y. Molecular/polymeric metallaynes and related molecules: Solar cell materials and devices. *Coord. Chem. Rev.* **2018**, *373*, 233−257.
(188) Evans, R. C.; Douglas, P.; Winscom, C. J. Coordination complexes exhibiting room-temperature phosphorescence: Evaluation of their suitability as triplet emitters in organic light emitting diodes. *Coord. Chem. Rev.* **2006**, *250*, 2093−2126.
(189) Kato, M. Luminescent Platinum Complexes Having Sensing Functionalities. *Bull. Chem. Soc. Jpn.* **2007**, *80*, 287−294.
(190) Jain, A.; Ong, S. P.; Hautier, G.; Chen, W.; Richards, W. D.; Dacek, S.; Cholia, S.; Gunter, D.; Skinner, D.; Ceder, G.; Persson, K. A. Commentary: The Materials Project: A materials genome approach to accelerating materials innovation. *APL Mater.* **2013**, *1*, No. 011002.
(191) Williams, J. A. G.; Beeby, A.; Davies, E. S.; Weinstein, J. A.; Wilson, C. An Alternative Route to Highly Luminescent Platinum(II) Complexes: Cyclometalation with N^C^N-Coordinating Dipyridylbenzene Ligands. *Inorg. Chem.* **2003**, *42*, 8609−8611.
(192) Williams, J. A. G. The coordination chemistry of dipyridylbenzene: N-deficient terpyridine or panacea for brightly luminescent metal complexes? *Chem. Soc. Rev.* **2009**, *38*, 1783−1801.
(193) Fuertes, S.; Brayshaw, S. K.; Raithby, P. R.; Schiffers, S.; Warren, M. R. New C^N^C Bis-Cyclometalated Platinum(II) Complexes: Synthesis, Structures, and Photophysical Properties. *Organometallics* **2012**, *31*, 105−119.
(194) Botchway, S. W.; Charnley, M.; Haycock, J. W.; Parker, A. W.; Rochester, D. L.; Weinstein, J. A.; Williams, J. A. G. Time-resolved and two-photon emission imaging microscopy of live cells with inert platinum complexes. *Proc. Natl. Acad. Sci. U. S. A.* **2008**, *105*, 16071−16076.
(195) Grove, L. J.; Rennekamp, J. M.; Jude, H.; Connick, W. B. A New Class of Platinum(II) Vapochromic Salts. *J. Am. Chem. Soc.* **2004**, *126*, 1594−1595.
(196) Bryant, M. J.; et al. A rapidly-reversible absorptive and emissive vapochromic Pt(II) pincer-based chemical sensor. *Nat. Commun.* **2017**, *8*, 1800.
(197) Wadas, T. J.; Wang, Q.-M.; Kim, Y.-j.; Flaschenreim, C.; Blanton, T. N.; Eisenberg, R. Vapochromism and Its Structural Basis in a Luminescent Pt(II) Terpyridine−Nicotinamide Complex. *J. Am. Chem. Soc.* **2004**, *126*, 16841−16849.
(198) Kui, S. C. F.; Chui, S. S.-Y.; Che, C.-M.; Zhu, N. Structures, Photoluminescence, and Reversible Vapoluminescence Properties of Neutral Platinum(II) Complexes Containing Extended π-Conjugated Cyclometalated Ligands. *J. Am. Chem. Soc.* **2006**, *128*, 8297−8309.
(199) Albrecht, M.; Lutz, M.; Spek, A. L.; van Koten, G. Organoplatinum crystals for gastriggered switches. *Nature* **2000**, *406*, 970.
(200) Grove, L. J.; Oliver, A. G.; Krause, J. A.; Connick, W. B. Structure of a Crystalline Vapochromic Platinum(II) Salt. *Inorg. Chem.* **2008**, *47*, 1408−1410.
(201) Murmann, R. K.; Taube, H. The Mechanism of the Formation and Rearrangement of Nitritocobalt(III) Ammines1. *J. Am. Chem. Soc.* **1956**, *78*, 4886−4890.

DOI: 10.1021/acs.inorgchem.9b01785
Inorg. Chem. 2019, 58, 14939−14980

(202) Penland, R. B.; Lane, T. J.; Quagliano, J. V. Infrared Absorption Spectra of Inorganic Coördination Complexes. VII. Structural Isomerism of Nitro- and Nitritopentamminecobalt(III) Chlorides1a,b. *J. Am. Chem. Soc.* **1956**, *78*, 887−889.
(203) Adell, B. Die Geschwindigkeit der Rückwandlung von bestrahltem festem Nitropentamminkobalt(III) chlorid. *Zeitschrift für anorganische und allgemeine Chemie* **1955**, *279*, 219−224.
(204) Svendsen, H.; Overgaard, J.; Chevallier, M.; Collet, E.; Iversen, B. Photomagnetic Switching of the Complex $[Nd(dmf)_4(H_2O)_3(\mu\text{-}CN)Fe(CN)_5]\cdot H_2O$ Analyzed by Single-Crystal X-Ray Diffraction. *Angew. Chem.* **2009**, *121*, 2818−2821.
(205) Zhang, J.; Zou, Q.; Tian, H. Photochromic Materials: More Than Meets The Eye. *Adv. Mater.* **2013**, *25*, 378−399.
(206) Sylvester, S. O.; Cole, J. M. Solar-Powered Nanomechanical Transduction from Crystalline Molecular Rotors. *Adv. Mater.* **2013**, *25*, 3324−3328.
(207) Carducci, M. D.; Pressprich, M. R.; Coppens, P. Diffraction Studies of Photoexcited Crystals: Metastable Nitrosyl-Linkage Isomers of Sodium Nitroprusside. *J. Am. Chem. Soc.* **1997**, *119*, 2669−2678.
(208) Dynamic single-crystal diffraction studies using synchrotron radiation. *Coord. Chem. Rev.* **2014**, *277*−*278*, 69−79, , Following Chemical Structures using Synchrotron Radiation.
(209) Hatcher, L. E.; Christensen, J.; Hamilton, M. L.; Trincao, J.; Allan, D. R.; Warren, M. R.; Clarke, I. P.; Towrie, M.; Fuertes, D. S.; Wilson, C. C.; Woodall, C. H.; Raithby, P. R. Steady-State and Pseudo-Steady-State Photocrystallographic Studies on Linkage Isomers of $[Ni(Et_4dien)(\eta^2\text{-}O,ON)(\eta^1\text{-}NO_2)]$: Identification of a New Linkage Isomer. *Chem.−Eur. J.* **2014***20*, 3128−3134, .
(210) Warren, M. R.; Easun, T. L.; Brayshaw, S. K.; Deeth, R. J.; George, M. W.; Johnson, A. L.; Schiffers, S.; Teat, S. J.; Warren, A. J.; Warren, J. E.; Wilson, C. C.; Woodall, C. H.; Raithby, P. R. Solid-State Interconversions: Unique 100% Reversible Transformations between the Ground and Metastable States in Single-Crystals of a Series of Nickel(II) Nitro Complexes. *Chem.−Eur. J.*, **2014***205*468−5477, .
(211) Hatcher, L. E.; Bigos, E. J.; Bryant, M. J.; MacCready, E. M.; Robinson, T. P.; Saunders, L. K.; Thomas, L. H.; Beavers, C. M.; Teat, S. J.; Christensen, J.; Raithby, P. R. Thermal and photochemical control of nitro−nitrito linkage isomerism in singlecrystals of $[Ni(medpt)(NO_2)(\eta^2\text{-}ONO)]$. *CrystEngComm* **2014**, *16*, 8263−8271.
(212) Bowes, K. F.; Cole, J. M.; Husheer, S. L. G.; Raithby, P. R.; Savarese, T. L.; Sparkes, H. A.; Teat, S. J.; Warren, J. E. Photocrystallographic structure determination of a new geometric isomer of $[Ru(NH_3)4(H_2O)(\eta^1\text{-}OSO)][MeC_6H_4SO_3]_2$. *Chem. Commun.* **2006**, 2448−2450.
(213) Sylvester, S. O.; Cole, J. M. Quantifying Crystallographically Independent Optical Switching Dynamics in Ru SO2 Photoisomers via Lock-and-Key Crystalline Environment. *J. Phys. Chem. Lett.* **2013**, *4*, 3221−3226.
(214) Photo-Induced Linkage Isomerism of Transition Metal Nitrosyl and Dinitrogen Complexes Studied by Photocrystallographic Techniques. *Tetrahedron* **2000**, *56*, 6813−6820, .
(215) Warren, M.; Brayshaw, S.; Johnson, A.; Schiffers, S.; Raithby, P.; Easun, T.; George, M.; Warren, J.; Teat, S. Reversible 100% Linkage Isomerization in a Single-Crystal to Single-Crystal Transformation: Photocrystallographic Identification of the Metastable $[Ni(dppe)(\eta^1\text{-}ONO)Cl]$ Isomer. *Angew. Chem.*, **2009***1215*821−5824, .
(216) Hatcher, L. E. Raising the (metastable) bar: $100[Pd(Bu_4dien)(\eta^1\text{-}\underline{NO}_2)]^+$ approaches ambient temperature. *CrystEngComm* **2016**, *18*, 4180−4187.
(217) Skelton, J. M.; Crespo-Otero, R.; Hatcher, L. E.; Parker, S. C.; Raithby, P. R.; Walsh, A. Energetics, thermal isomerisation and photochemistry of the linkage-isomer system $[Ni(Et_4dien)(\eta^2\text{-}O,ON)(\eta^1\text{-}NO_2)]$. *CrystEngComm* **2015**, *17*, 383−394.
(218) Skelton, J. M.; Lora da Silva, E.; Crespo-Otero, R.; Hatcher, L. E.; Raithby, P. R.; Parker, S. C.; Walsh, A. Electronic excitations in molecular solids: bridging theory and experiment. *Faraday Discuss.* **2015**, *177*, 181−202.
(219) Hatcher, L. E.; Skelton, J. M.; Warren, M. R.; Stubbs, C.; da Silva, E. L.; Raithby, P. R. Monitoring photo-induced population dynamics in metastable linkage isomer crystals: a crystallographic kinetic study of $[Pd(Bu_4dien)NO_2]BPh_4$. *Phys. Chem. Chem. Phys.* **2018**, *20*, 5874−5886.
(220) Casaretto, N.; Schaniel, D.; Alle, P.; Wenger, E.; Parois, P.; Fournier, B.; Bendeif, E. E.; Palin, C.; Pillet, S. In-house time-resolved photocrystallography on the millisecond timescale using a gated X-ray hybrid pixel area detector. *Acta Crystallogr., Sect. B: Struct. Sci., Cryst. Eng. Mater.* **2017**, *73*, 696−707.
(221) Chater, J. A history of nuclear power. 2004. https://courses.engr.illinois.edu/npre470/sp2018/web/readings/James_Chater_History_nuclear.pdf
(222) IEA *World Energy Outlook 2018;* IEA: Paris, 2018, DOI: 10.1787/weo-2018-en.
(223) Goldberg, S. M.; Rosner, R. *Nuclear Reactors: Generation to Generation;* American Academy of Arts and Sciences, 2011.
(224) *GIF R&D Outlook for Generation IV Nuclear Energy Systems*; GIF, Aug 21, 2009. https://inis.iaea.org/collection/NCLCollectionStore/_Public/43/002/43002386.pdf
(225) Carpenter, G. J. C.; Watters, J. F. Vacancy precipitation in zirconium alloys. *Acta Metall.* **1973**, *21*, 1207−1214.
(226) Griffiths, M. A review of microstructure evolution in zirconium alloys during irradiation. *J. Nucl. Mater.* **1988**, *159*, 190−218.
(227) Onimus, F.; Béchade, J. L. In *Comprehensive Nuclear Materials;* Konings, R. J., Ed.; Elsevier: Oxford, UK, 2012; pp 1−31, DOI: 10.1016/B978-0-08-056033-5.00064-1.
(228) Becquart, C. S.; Domain, C. Migration Energy of He in W Revisited by Ab Initio Calculations. *Phys. Rev. Lett.* **2006**, *97*, 196402.
(229) Zinkle, S. In *Structural Materials for Generation IV Nuclear Reactors;* Yvon, P., Ed.; Woodhead Publishing, 2017; pp 569−594, DOI: 10.1016/B978-0-08-100906-2.00016-1.
(230) Beyerlein, I. J.; Demkowicz, M. J.; Misra, A.; Uberuaga, B. P. Defectinterface interactions. *Prog. Mater. Sci.* **2015**, *74*, 125−210.
(231) Demkowicz, M. J.; Misra, A.; Caro, A. The role of interface structure in controlling high helium concentrations. *Curr. Opin. Solid State Mater. Sci.* **2012**, *16*, 101−108.
(232) Bai, X.-M.; Voter, A. F.; Hoagland, R. G.; Nastasi, M.; Uberuaga, B. P. Efficient Annealing of Radiation Damage Near Grain Boundaries via Interstitial Emission. *Science* **2010**, *327*, 1631−1634.
(233) Demkowicz, M. J.; Hoagland, R. G.; Hirth, J. Interface Structure and Radiation Damage Resistance in Cu-Nb Multilayer Nanocomposite. *Phys. Rev. Lett.* **2008**, *100*, 136102.
(234) Saikia, U.; Sahariah, M. B.; González, C.; Pandey, R. Vacancy assisted He-interstitial clustering and their elemental interaction at fcc-bcc semicoherent metallic interface. *Sci. Rep.* **2018**, *8*, 3884.
(235) Kolluri, K.; Demkowicz, M. J. Formation, migration, and clustering of delocalized vacancies and interstitials at a solid-state semicoherent interface. *Phys. Rev. B: Condens. Matter Mater. Phys.* **2012**, *85*, DOI: 10.1103/PhysRevB.85.205416.
(236) Kolluri, K.; Liu, X.-Y.; Hoagland, R.; Demkowicz, M. Behavior of Vacancies and Interstitials at Semicoherent Interfaces. *JOM* **2013**, *65*, 374.
(237) González, C.; Iglesias, R.; Demkowicz, M. Point defect stability in a semicoherent metallic interface. *Phys. Rev. B: Condens. Matter Mater. Phys.* **2015**, *91*, No. 064103.
(238) Metsanurk, E.; Caro, A.; Tamm, A.; Aabloo, A.; Klintenberg, M. First-principles study of point defects at semicoherent interface. *Sci. Rep.* **2015**, *4*, DOI: 10.1038/srep07567.
(239) Metsanurk, E.; Tamm, A.; Aabloo, A.; Klintenberg, M.; Caro, A. Vacancies at the Cu−Nb semicoherent interface. *Modell. Simul. Mater. Sci. Eng.* **2017**, *25*, No. 025012.
(240) Demkowicz, M.; Thilly, L. Structure, shear resistance and interaction with point defects of interfaces in Cu−Nb nanocomposites synthesized by severe plastic deformation. *Acta Mater.* **2011**, *59*, 7744−7756.

DOI: 10.1021/acs.inorgchem.9b01785
Inorg. Chem. 2019, 58, 14939−14980

(241) Liu, X.-Y.; Uberuaga, B.; Demkowicz, M.; Germann, T.; Misra, A.; Nastasi, M. Mechanism for recombination of radiation-induced point defects at interphase boundaries. *Phys. Rev. B: Condens. Matter Mater. Phys.* **2012**, *85*, No. 012103.
(242) Snel, J.; Monclús, M. A.; Castillo-Rodríguez, M.; Mara, N.; Beyerlein, I. J.; Llorca, J.; Molina-Aldareguía, J. M. Deformation Mechanism Map of Cu/Nb Nanoscale Metallic Multilayers as a Function of Temperature and Layer Thickness. *JOM* **2017**, *69*, 2214−2226.
(243) Economy, D. R.; Schultz, B. M.; Kennedy, M. S. Impacts of accelerated aging on the mechanical properties of Cu−Nb nano-laminates. *J. Mater. Sci.* **2012**, *47*, 6986−6991.
(244) Zhang, J.; Zhang, P.; Zhang, X.; Wang, R.; Liu, G.; Zhang, G.; Sun, J. Mechanical properties of fcc/fcc Cu/Nb nanostructured multilayers. *Mater. Sci. Eng., A* **2012**, *545*, 118−122.
(245) Sen, H. S.; Polcar, T. Vacancy-interface-helium interaction in Zr-Nb multi-layer system: a first-principles study. *J. Nucl. Mater.*.**2019***518*11
(246) Demkowicz, M. J.; Hoagland, R. G.; Uberuaga, B. P.; Misra, A. Influence of interface sink strength on the reduction of radiation-induced defect concentrations and fluxes in materials with large interface area per unit volume. *Phys. Rev. B: Condens. Matter Mater. Phys.* **2011**, *84*, 104102.
(247) Li, N.; Demkowicz, M.; Mara, N. Microstructure Evolution and Mechanical Response of Nanolaminate Composites Irradiated with Helium at ElevatedTemperatures. *JOM* **2017**, *69*, 2206.
(248) Demkowicz, M. J.; Wang, Y. Q.; Hoagland, R. G.; Anderoglu, O. Mechanisms of He escape during implantation in CuNb multilayer composites. *Nucl. Instrum. Methods Phys. Res., Sect. B* **2007**, *261*, 524−528.
(249) Zhang, X.; Li, N.; Anderoglu, O.; Wang, H.; Swadener, J. G.; Höchbauer, T.; Misra, A.; Hoagland, R. G. Nanostructured Cu/Nb multilayers subjected to helium ion-irradiation. *Nucl. Instrum. Methods Phys. Res., Sect. B* **2007**, *261*, 1129−1132.
(250) Dunn, A.; McPhie, M.; Capolungo, L.; Martinez, E.; Cherkaoui, M. A rate theory study of helium bubble formation and retention in Cu−Nb nanocomposites. *J. Nucl. Mater.* **2013**, *435*, 141−152.
(251) Chen, D.; Li, N.; Yuryev, D.; Baldwin, J.; Wang, Y.; Demkowicz, M. Self-organization of helium precipitates into elongated channels within metal nanolayers. *Science Advances* **2017**, *3*, No. eaao2710.
(252) Bhattacharyya, D.; Demkowicz, M.; Wang, Y.-Q.; Baumer, R.; Nastasi, M.; Misra, A. A Transmission Electron Microscopy Study of the Effect of Interfaces on Bubble Formation in He-Implanted Cu-Nb Multilayers. *Microsc. Microanal.* **2012**, *18*, 152−161.
(253) Hattar, K.; Demkowicz, M.; Misra, A.; Robertson, I.; Hoagland, R. Arrest of He Bubble Growth in Cu-Nb Multilayer Nanocomposites. *Scr. Mater.* **2008**, *58*, 541−544.
(254) González, C.; Iglesias, R. Energetic analysis of He and monovacancies in Cu/W metallic interfaces. *Mater. Des.* **2016**, *91*, 171−179.
(255) Callisti, M.; Karlik, M.; Polcar, T. Bubbles formation in helium ion irradiated Cu/W multilayer nanocomposites: Effects on structure and mechanical properties. *J. Nucl. Mater.* **2016**, *473*, 18−27.
(256) Chen, S.; Liu, B.; Lin, L.; Jiao, G. Microstructural development and helium bubble formation in Cu/W(Re) nanometer multilayer films irradiated by He+ ion. *Nucl. Instrum. Methods Phys. Res., Sect. B* **2015**, *354*, 244−248 26th International Conference on Atomic Collisions in Solids. .
(257) Pacaud, J.; Jaouen, C.; Gladyszewski, G. Irradiation effects in Cu/W multilayers: Ion beam mixing and structural evolution. *J. Appl. Phys.* **1999**, *86*, 4847−4854.
(258) Nelasov, I. V.; Lipnitskii, A. G. The study of Cu/Nb interface diffusion using molecular dynamics simulation. *St. Petersburg Polytechnical University Journal: Physics and Mathematics* **2016**, *2*, 91−95.
(259) Woldt, E.; Jensen, D. J. Recrystallization kinetics in copper: Comparison between techniques. *Metall. Mater. Trans. A* **1995**, *26*, 1717−1724.
(260) Benchabane, G.; Boumerzoug, Z.; Thibon, I.; Gloriant, T. Recrystallization of pure copper investigated by calorimetry and microhardness. *Mater. Charact.* **2008**, *59*, 1425−1428.
(261) Monclús, M. A.; Zheng, S. J.; Mayeur, J. R.; Beyerlein, I. J.; Mara, N. A.; Polcar, T.; Llorca, J.; Molina-Aldareguía, J. M. Optimum high temperature strength of two-dimensional nanocomposites. *APL Mater.* **2013**, *1*, No. 052103.
(262) Primorac, M.-M.; Abad, M. D.; Hosemann, P.; Kreuzeder, M.; Maier, V.; Kiener, D. Elevated temperature mechanical properties of novel ultra-fine grained Cu−Nb composites. *Mater. Sci. Eng., A* **2015**, *625*, 296−302.
(263) Monclús, M. A.; Karlik, M.; Callisti, M.; Frutos, E.; LLorca, J.; Polcar, T.; Molina-Aldareguía, J. M. Microstructure and mechanical properties of physical vapor deposited Cu/W nanoscale multilayers: Influence of layer thickness and temperature. *Thin Solid Films* **2014**, *571*, 275−282 Multilayers 2013. .
(264) Monclús, M. A.; Callisti, M.; Polcar, T.; Yang, L. W.; Molina-Aldareguía, J. M.; LLorca, J. Effect of layer thickness on the mechanical behaviour of oxidationstrengthened Zr/Nb nanoscale multilayers. *J. Mater. Sci.* **2018**, *53*, 5860−5878.
(265) Callisti, M.; Polcar, T. Combined size and texture-dependent deformation and strengthening mechanisms in Zr/Nb nano-multilayers. *Acta Mater.* **2017**, *124*, 247−260.
(266) Callisti, M.; Lozano-Perez, S.; Polcar, T. Structural and mechanical properties of γ-irradiated Zr/Nb multilayer nano-composites. *Mater. Lett.* **2016**, *163*, 138−141.
(267) Callisti, M.; Karlik, M.; Polcar, T. Competing mechanisms on the strength of ion-irradiated Zr/Nb nanoscale multilayers: Interface strength versus radiation hardening. *Scr. Mater.* **2018**, *152*, 31−35.
(268) Rodgers, D.; Griffiths, M.; Bickel, G.; Buyers, A.; Coleman, C.; Nordin, H.; Lawrence, S. Performance of pressure tubes in CANDU reactors. *CNL Nuclear Review* **2016**, *5*, 1−15.
(269) Lu, Y.; Kotoka, R.; Ligda, J.; Cao, B.; Yarmolenko, S.; Schuster, B.; Wei, Q. The microstructure and mechanical behavior of Mg/Ti multilayers as a function of individual layer thickness. *Acta Mater.* **2014**, *63*, 216−231.
(270) Lu, Y.; Kotoka, R.; Ligda, J.; Cao, B.; Yarmolenko, S.; Schuster, B.; Wei, Q. The microstructure and mechanical behavior of Mg/Ti multilayers as a function of individual layer thickness. *Acta Mater.* **2014**, *63*, 216−231.
(271) He, J.; Liu, Y.; Funahashi, R. Oxide thermoelectrics: The challenges, progress, and outlook. *J. Mater. Res.* **2011**, *26*, 1762−1772.
(272) Hébert, S.; Maignan, A. In *Functional Oxides;* Bruce, D. W., O'Hare, D., Walton, R. I., Eds.; John Wiley & Sons, Ltd: Chichester, UK, 2010 DOI: 10.1002/9780470686072.ch4.
(273) Puggioni, D.; Rondinelli, J. M. Designing a robustly metallic noncenstrosymmetric ruthenate oxide with large thermopower anisotropy. *Nat. Commun.* **2014**, *5*, 3432.
(274) Gorai, P.; Stevanovic, V.; Toberer, E. Computationally guided discovery of thermoelectric materials. *Nat. Rev. Mater.* **2017**, *2*, 17053.
(275) Xing, G.; Sun, J.; Ong, K. P.; Fan, X.; Zheng, W.; Singh, D. J. Perspective: n-type oxide thermoelectrics via visual search strategies. *APL Mater.* **2016**, *4*, No. 053201.
(276) Garrity, K. F. First-principles search for n-type oxide, nitride, and sulfide thermoelectrics. *Phys. Rev. B: Condens. Matter Mater. Phys.* **2016**, *94*, No. 045122.
(277) Lamontagne, L. K.; Laurita, G.; Gaultois, M. W.; Knight, M.; Ghadbeigi, L.; Sparks, T. D.; Gruner, M. E.; Pentcheva, R.; Brown, C. M.; Seshadri, R. High Thermopower with Metallic Conductivity in p-Type Li-Substituted $PbPdO_2$. *Chem. Mater.* **2016**, *28*, 3367−3373.
(278) Okuda, T.; Nakanishi, K.; Miyasaka, S.; Tokura, Y. Large thermoelectric response of metallic perovskites: $Sr_{1-x}La_xTiO_3$($0 <\sim x <\sim 0.1$). *Phys. Rev. B: Condens. Matter Mater. Phys.* **2001**, *63*, 113104.
(279) Jalan, B.; Stemmer, S. Large Seebeck coefficients and thermoelectric power factor of La-doped $SrTiO_3$ thin films. *Appl. Phys. Lett.* **2010**, *97*, No. 042106.

DOI: 10.1021/acs.inorgchem.9b01785
Inorg. Chem. 2019, 58, 14939−14980

(280) Cain, T. A.; Kajdos, A. P.; Stemmer, S. La-doped $SrTiO_3$ films with large cryogenic thermoelectric power factors. *Appl. Phys. Lett.* **2013**, *102*, 182101.
(281) Gruner, M. E.; Eckern, U.; Pentcheva, R. Impact of strain-induced electronic topological transition on the thermoelectric properties of $PtCoO_2$ and $PdCoO_2$. *Phys. Rev. B: Condens. Matter Mater. Phys.* **2015**, *92*, 235140.
(282) Hicks, L. D.; Dresselhaus, M. S. Effect of quantum-well structures on the thermoelectric figure of merit. *Phys. Rev. B: Condens. Matter Mater. Phys.* **1993**, *47*, 12727−12731.
(283) Mao, J.; Liu, Z.; Ren, Z. Size effect in thermoelectric materials. *npj Quantum Mater.* **2016**, *1*, 16028.
(284) Ohta, H.; Kim, S.; Mune, Y.; Mizoguchi, T.; Nomura, K.; Ohta, S.; Nomura, T.; Nakanishi, Y.; Ikuhara, Y.; Hirano, M.; Hosono, H.; Koumoto, K. Giant thermoelectric Seebeck coefficient of two-dimensional electron gas in $SrTiO_3$. *Nat. Mater.* **2007**, *6*, 129.
(285) Filippetti, A.; Delugas, P.; Verstraete, M. J.; Pallecchi, I.; Gadaleta, A.; Marré, D.; Li, D. F.; Gariglio, S.; Fiorentini, V. Thermopower in oxide heterostructures: The importance of being multiple-band conductors. *Phys. Rev. B: Condens. Matter Mater. Phys.* **2012**, *86*, 195301.
(286) García-Fernández, P.; Verissimo-Alves, M.; Bilc, D. I.; Ghosez, P.; Junquera, J. First principles modeling of the thermoelectric properties of $SrTiO_3/SrRuO_3$ superlattices. *Phys. Rev. B: Condens. Matter Mater. Phys.* **2012**, *86*, No. 085305.
(287) Delugas, P.; Filippetti, A.; Verstraete, M. J.; Pallecchi, I.; Marré, D.; Fiorentini, V. Doping-induced dimensional crossover and thermopower burst in Nb-doped $SrTiO_3$ superlattices. *Phys. Rev. B: Condens. Matter Mater. Phys.* **2013**, *88*, No. 045310.
(288) Pallecchi, I.; Telesio, F.; Li, D.; Fête, A.; Gariglio, S.; Triscone, J.-M.; Filippetti, A.; Delugas, P.; Fiorentini, V.; Marré, D. Giant oscillating thermopower at oxide interfaces. *Nat. Commun.* **2015**, *6*, 6678.
(289) Bilc, D. I.; Floare, C. G.; Zârbo, L. P.; Garabagiu, S.; Lemal, S.; Ghosez, P. First Principles Modeling of $SrTiO_3$ Based Oxides for Thermoelectric Applications. *J. Phys. Chem. C* **2016**, *120*, 25678−25688.
(290) Geisler, B.; Blanca-Romero, A.; Pentcheva, R. Design of n- and p-type oxide thermoelectrics in $LaNiO_3/SrTiO_3(001)$ superlattices exploiting interface polarity. *Phys. Rev. B: Condens. Matter Mater. Phys.* **2017**, *95*, 125301.
(291) Geisler, B.; Pentcheva, R. Confinement- and strain-induced enhancement of thermoelectric properties in $LaNiO_3/LaAlO_3(001)$ superlattices. *Phys. Rev. Materials* **2018**, *2*, No. 055403.
(292) Geisler, B.; Pentcheva, R. Inducing n- and p-Type Thermoelectricity in Oxide Superlattices by Strain Tuning of Orbital-Selective Transport Resonances. *Phys. Rev. Appl.* **2019**, *11*, No. 044047.
(293) Geisler, B.; Kratzer, P. Spincaloric properties of epitaxial $Co_2MnSi/MgO/Co_2MnSi$ magnetic tunnel junctions. *Phys. Rev. B: Condens. Matter Mater. Phys.* **2015**, *92*, 144418.
(294) Geisler, B.; Kratzer, P.; Popescu, V. Interplay of growth mode and thermally induced spin accumulation in epitaxial $Al/Co_2TiSi/Al$ and $Al/Co_2TiGe/Al$ contacts. *Phys. Rev. B: Condens. Matter Mater. Phys.* **2014**, *89*, 184422.
(295) Comtesse, D.; Geisler, B.; Entel, P.; Kratzer, P.; Szunyogh, L. First-principles study of spin-dependent thermoelectric properties of half-metallic Heusler thin films between platinum leads. *Phys. Rev. B: Condens. Matter Mater. Phys.* **2014**, *89*, No. 094410.
(296) Popescu, V. Spin caloric transport from density-functional theory. *J. Phys. D: Appl. Phys.* **2019**, *52*, 073001.
(297) Middey, S.; Chakhalian, J.; Mahadevan, P.; Freeland, J.; Millis, A.; Sarma, D. Physics of Ultrathin Films and Heterostructures of Rare-Earth Nickelates. *Annu. Rev. Mater. Res.* **2016**, *46*, 305−334.
(298) Lorenz, M.; et al. The 2016 oxide electronic materials and oxide interfaces roadmap. *J. Phys. D: Appl. Phys.* **2016**, *49*, 433001.
(299) Wrobel, F.; Geisler, B.; Wang, Y.; Christiani, G.; Logvenov, G.; Bluschke, M.; Schierle, E.; van Aken, P. A.; Keimer, B.; Pentcheva, R.; Benckiser, E. Digital modulation of the nickel valence state in a cuprate-nickelate heterostructure. *Phys. Rev. Materials* **2018**, *2*, No. 035001.
(300) Liu, J.; Okamoto, S.; van Veenendaal, M.; Kareev, M.; Gray, B.; Ryan, P.; Freeland, J. W.; Chakhalian, J. Quantum confinement of Mott electrons in ultrathin $LaNiO_3/LaAlO_3$ superlattices. *Phys. Rev. B: Condens. Matter Mater. Phys.* **2011**, *83*, 161102.
(301) Son, J.; LeBeau, J. M.; Allen, S. J.; Stemmer, S. Conductivity enhancement of ultrathin $LaNiO_3$ films in superlattices. *Appl. Phys. Lett.* **2010**, *97*, 202109.
(302) Kaiser, A. M.; Gray, A. X.; Conti, G.; Son, J.; Greer, A.; Perona, A.; Rattanachata, A.; Saw, A. Y.; Bostwick, A.; Yang, S.; Yang, S.-H.; Gullikson, E. M.; Kortright, J. B.; Stemmer, S.; Fadley, C. S. Suppression of Near-Fermi Level Electronic States at the Interface in a $LaNiO_3/SrTiO_3$ Superlattice. *Phys. Rev. Lett.* **2011**, *107*, 116402.
(303) Hwang, J.; Son, J.; Zhang, J. Y.; Janotti, A.; Van de Walle, C. G.; Stemmer, S. Structural origins of the properties of rare earth nickelate superlattices. *Phys. Rev. B: Condens. Matter Mater. Phys.* **2013**, *87*, No. 060101.
(304) Wrobel, F.; Mark, A. F.; Christiani, G.; Sigle, W.; Habermeier, H.-U.; van Aken, P. A.; Logvenov, G.; Keimer, B.; Benckiser, E. Comparative study of $LaNiO_3/LaAlO_3$ heterostructures grown by pulsed laser deposition and oxide molecular beam epitaxy. *Appl. Phys. Lett.* **2017**, *110*, No. 041606.
(305) Kaya, P.; Gregori, G.; Baiutti, F.; Yordanov, P.; Suyolcu, Y. E.; Cristiani, G.; Wrobel, F.; Benckiser, E.; Keimer, B.; van Aken, P. A.; Habermeier, H.-U.; Logvenov, G.; Maier, J. High-Temperature Thermoelectricity in $LaNiO_3$-La_2CuO_4 Heterostructures. *ACS Appl. Mater. Interfaces* **2018**, *10*, 22786−22792.
(306) Pardo, V.; Botana, A. S.; Baldomir, D. Enhanced thermoelectric response of hole-doped $La_2NiO_{4+\delta}$ from ab initio calculations. *Phys. Rev. B: Condens. Matter Mater. Phys.* **2012**, *86*, 165114.
(307) Noguera, C. Polar oxide surfaces. *J. Phys.: Condens. Matter* **2000**, *12*, R367.
(308) Nakagawa, N.; Hwang, H. Y.; Muller, D. A. Why some interfaces cannot be sharp. *Nat. Mater.* **2006**, *5*, 204.
(309) Pentcheva, R.; Pickett, W. E. Charge localization or itineracy at $LaAlO_3/SrTiO_3$ interfaces: Hole polarons, oxygen vacancies, and mobile electrons. *Phys. Rev. B: Condens. Matter Mater. Phys.* **2006**, *74*, No. 035112.
(310) Botana, A. S.; Pardo, V.; Pickett, W. E. All-3d Electron-Hole Bilayers in CrN/MgO(111) Multilayers for Thermoelectric Applications. *Phys. Rev. Appl.* **2017**, *7*, No. 024002.
(311) Harrison, W. A.; Kraut, E. A.; Waldrop, J. R.; Grant, R. W. Polar heterojunction interfaces. *Phys. Rev. B: Condens. Matter Mater. Phys.* **1978**, *18*, 4402−4410.
(312) Blanca-Romero, A.; Pentcheva, R. Confinement-induced metal-to-insulator transition in strained $LaNiO_3/LaAlO_3$ superlattices. *Phys. Rev. B: Condens. Matter Mater. Phys.* **2011**, *84*, 195450.
(313) Freeland, J. W.; Liu, J.; Kareev, M.; Gray, B.; Kim, J. W.; Ryan, P.; Pentcheva, R.; Chakhalian, J. Orbital control in strained ultra-thin $LaNiO_3/LaAlO_3$ superlattices. *Europhys. Lett.* **2011**, *96*, 57004.
(314) Yordanov, P.; Wochner, P.; Ibrahimkutty, S.; Dietl, C.; Wrobel, F.; Felici, R.; Gregori, G.; Maier, J.; Keimer, B.; Habermeier, H.-U. Perovskite substrates boost the thermopower of cobaltate thin films at high temperatures. *Appl. Phys. Lett.* **2017**, *110*, 253101.
(315) Sivan, U.; Imry, Y. Multichannel Landauer formula for thermoelectric transport with application to thermopower near the mobility edge. *Phys. Rev. B: Condens. Matter Mater. Phys.* **1986**, *33*, 551−558.
(316) Mahan, G. D.; Sofo, J. O. The best thermoelectric. *Proc. Natl. Acad. Sci. U. S. A.* **1996**, *93*, 7436−7439.
(317) Nakpathomkun, N.; Xu, H. Q.; Linke, H. Thermoelectric efficiency at maximum power in low-dimensional systems. *Phys. Rev. B: Condens. Matter Mater. Phys.* **2010**, *82*, 235428.
(318) Jordan, A. N.; Sothmann, B.; Sánchez, R.; Büttiker, M. Powerful and efficient energy harvester with resonant-tunneling quantum dots. *Phys. Rev. B: Condens. Matter Mater. Phys.* **2013**, *87*, No. 075312.

DOI: 10.1021/acs.inorgchem.9b01785
Inorg. Chem. 2019, 58, 14939−14980

(319) Han, M. J.; Marianetti, C. A.; Millis, A. J. Chemical control of orbital polarization in artificially structured transition-metal oxides: La_2NiXO_6 (X = B, Al, Ga, In) from first principles. *Phys. Rev. B: Condens. Matter Mater. Phys.* **2010**, *82*, 134408.
(320) Wu, M.; et al. Strain and composition dependence of orbital polarization in nickeloxide superlattices. *Phys. Rev. B: Condens. Matter Mater. Phys.* **2013**, *88*, 125124.
(321) Doennig, D.; Pickett, W. E.; Pentcheva, R. Confinement-driven transitions between topological and Mott phases in $(LaNiO_3)_N/(LaAlO_3)_M(111)$ superlattices. *Phys. Rev. B: Condens. Matter Mater. Phys.* **2014**, *89*, 121110.
(322) Disa, A. S.; Kumah, D. P.; Malashevich, A.; Chen, H.; Arena, D. A.; Specht, E. D.; Ismail-Beigi, S.; Walker, F. J.; Ahn, C. H. Orbital Engineering in Symmetry Breaking Polar Heterostructures. *Phys. Rev. Lett.* **2015**, *114*, No. 026801.
(323) Bernardi, M.; Vigil-Fowler, D.; Lischner, J.; Neaton, J. B.; Louie, S. G. Ab Initio Study of Hot Carriers in the First Picosecond after Sunlight Absorption in Silicon. *Phys. Rev. Lett.* **2014**, *112*, 257402.
(324) Mustafa, J. I.; Bernardi, M.; Neaton, J. B.; Louie, S. G. Ab initio electronic relaxation times and transport in noble metals. *Phys. Rev. B: Condens. Matter Mater. Phys.* **2016**, *94*, 155105.
(325) Dekura, H.; Tsuchiya, T. Ab initio lattice thermal conductivity of MgO from a complete solution of the linearized Boltzmann transport equation. *Phys. Rev. B: Condens. Matter Mater. Phys.* **2017**, *95*, 184303.
(326) Zhang, J.; Bachman, M.; Czerner, M.; Heiliger, C. Thermal Transport and Non equilibrium Temperature Drop Across a Magnetic Tunnel Junction. *Phys. Rev. Lett.* **2015**, *115*, No. 037203.
(327) Mizuno, H.; Mossa, S.; Barrat, J.-L. Beating the amorphous limit in thermal conductivity by superlattices design. *Sci. Rep.* **2015**, *5*, 14116.
(328) O'Dwyer, C.; Chen, R.; He, J.-H.; Lee, J.; Razeeb, K. M. Scientific and Technical Challenges in Thermal Transport and Thermoelectric Materials and Devices. *ECS J. Solid State Sci. Technol.* **2017**, *6*, N3058.
(329) Katsufuji, T.; Saiki, T.; Okubo, S.; Katayama, Y.; Ueno, K. Thermal conductivity of $SrVO_3$−$SrTiO_3$ thin films: Evidence of intrinsic thermal resistance at the interface between oxide layers. *Phys. Rev. Materials* **2018**, *2*, No. 051002.
(330) Ravichandran, J.; et al. Crossover from incoherent to coherent phonon scattering in epitaxial oxide superlattices. *Nat. Mater.* **2014**, *13*, 168.
(331) Luckyanova, M. N.; Garg, J.; Esfarjani, K.; Jandl, A.; Bulsara, M. T.; Schmidt, A. J.; Minnich, A. J.; Chen, S.; Dresselhaus, M. S.; Ren, Z.; Fitzgerald, E. A.; Chen, G. Coherent Phonon Heat Conduction in Superlattices. *Science* **2012**, *338*, 936−939.
(332) Garg, J.; Bonini, N.; Marzari, N. High Thermal Conductivity in Short-Period Superlattices. *Nano Lett.* **2011**, *11*, 5135−5141.
(333) Zhao, H. J.; Filippetti, A.; Escorihuela-Sayalero, C.; Delugas, P.; Canadell, E.; Bellaiche, L.; Fiorentini, V.; Íñiguez, J. Meta-screening and permanence of polar distortion in metallized ferroelectrics. *Phys. Rev. B: Condens. Matter Mater. Phys.* **2018**, *97*, No. 054107.
(334) Filippetti, A.; Fiorentini, V.; Ricci, F.; Delugas, P.; Íñiguez, J. Prediction of a native ferroelectric metal. *Nat. Commun.* **2016**, *7*, 11211.
(335) Urru, A.; Filippetti, A.; Ricci, F.; Íñiguez, J.; Fiorentini, V. *to be published.*.
(336) Anderson, P. W.; Blount, E. I. Symmetry Considerations on Martensitic Transformations: "Ferroelectric" Metals? *Phys. Rev. Lett.* **1965**, *14*, 217−219.
(337) Padmanabhan, H.; Park, Y.; Puggioni, D.; Yuan, Y.; Cao, Y.; Gasparov, L.; Shi, Y.; Chakhalian, J.; Rondinelli, J. M.; Gopalan, V. Linear and nonlinear optical probe of the ferroelectric-like phase transition in a polar metal, $LiOsO_3$. *Appl. Phys. Lett.* **2018**, *113*, 122906.
(338) Puggioni, D.; Giovannetti, G.; Capone, M.; Rondinelli, J. M. Design of a Mott Multiferroic from a Nonmagnetic Polar Metal. *Phys. Rev. Lett.* **2015**, *115*, No. 087202.
(339) Puggioni, D.; Rondinelli, J. M. Designing a robustly metallic noncenstrosymmetric ruthenate oxide with large thermopower anisotropy. *Nat. Commun.* **2014**, *5*, 3432.
(340) Benedek, N. A.; Birol, T. "Ferroelectric" metals reexamined: fundamental mechanisms and design considerations for new materials. *J. Mater. Chem. C* **2016**, *4*, 4000−4015.
(341) Scarrozza, M.; Filippetti, A.; Fiorentini, V. Ferromagnetism and Orbital Order in a Topological Ferroelectric. *Phys. Rev. Lett.* **2012**, *109*, 217202.
(342) López-Pérez, J.; Íñiguez, J. Ab initio study of proper topological ferroelectricity in layered perovskite $La_2Ti_2O_7$. *Phys. Rev. B: Condens. Matter Mater. Phys.* **2011**, *84*, No. 075121.
(343) Vanderbilt, D. *Berry Phases in Electronic Structure Theory;* Cambridge University Press, 2018.
(344) Park, S. J.; Kim, T. Y.; Park, C.-H.; Kim, D.-S. Optical responses of a metal with sub-nm gaps. *Sci. Rep.* **2016**, *6*, 22981.
(345) Garrity, K. F.; Rabe, K. M.; Vanderbilt, D. Hyperferroelectrics: Proper Ferroelectrics with Persistent Polarization. *Phys. Rev. Lett.* **2014**, *112*, 127601.
(346) Puggioni, D.; Stroppa, A.; Rondinelli, J. M. Design of a polar half-metallic ferromagnet with accessible and enhanced electric polarization. *Phys. Rev. Materials* **2018**, *2*, 114403.
(347) Rao, C.; Cheetham, A.; Thirumurugan, A. Hybrid inorganic−organic materials: a new family in condensed matter physics. *J. Phys.: Condens. Matter* **2008**, *20*, No. 083202.
(348) Wenk, H.-R.; Bulakh, A. *Minerals: their constitution and origin;* Cambridge University Press, 2016.
(349) Jain, P.; Ramachandran, V.; Clark, R. J.; Zhou, H. D.; Toby, B. H.; Dalal, N. S.; Kroto, H. W.; Cheetham, A. K. Multiferroic behavior associated with an order−disorder hydrogen bonding transition in metal-organic frameworks (MOFs) with the perovskite ABX_3 architecture. *J. Am. Chem. Soc.* **2009**, *131*, 13625−13627.
(350) Besara, T.; Jain, P.; Dalal, N. S.; Kuhns, P. L.; Reyes, A. P.; Kroto, H. W.; Cheetham, A. K. Mechanism of the order−disorder phase transition, and glassy behavior in the metal-organic framework $[(CH_3)_2NH_2]$ $Zn(HCOO)_3$. *Proc. Natl. Acad. Sci. U. S. A.* **2011**, *108*, 6828.
(351) Ramesh, R. Materials science: Emerging routes to multiferroics. *Nature* **2009**, *461*, 1218.
(352) Kieslich, G.; Sun, S.; Cheetham, A. K. An extended tolerance factor approach for organic−inorganic perovskites. *Chemical science* **2015**, *6*, 3430−3433.
(353) Kieslich, G.; Sun, S.; Cheetham, A. K. Solid-state principles applied to organic−inorganic perovskites: new tricks for an old dog. *Chemical Science* **2014**, *5*, 4712−4715.
(354) Hu, K.-L.; Kurmoo, M.; Wang, Z.; Gao, S. Metal−Organic Perovskites: Synthesis, Structures, and Magnetic Properties of $[C(NH_2)_3][MII(HCOO)_3]$(M = Mn, Fe, Co, Ni, Cu, and Zn; $C(NH_2)_3$ = Guanidinium). *Chem.−Eur. J.* **2009**, *15*, 12050−12064.
(355) Stroppa, A.; Jain, P.; Barone, P.; Marsman, M.; Perez-Mato, J. M.; Cheetham, A. K.; Kroto, H. W.; Picozzi, S. Electric control of magnetization and interplay between orbital ordering and ferroelectricity in a multiferroic metal−organic framework. *Angew. Chem., Int. Ed.* **2011**, *50*, 5847−5850.
(356) Ghosh, S.; Di Sante, D.; Stroppa, A. Strain tuning of ferroelectric polarization in hybrid organic inorganic perovskite compounds. *J. Phys. Chem. Lett.* **2015**, *6*, 4553−4559.
(357) Stroppa, A.; Barone, P.; Jain, P.; Perez-Mato, J. M.; Picozzi, S. Hybrid Improper Ferroelectricity in a Multiferroic and Magnetoelectric Metal-Organic Framework. *Adv. Mater.* **2013**, *25*, 2284−2290.
(358) Tian, Y.; Stroppa, A.; Chai, Y.; Yan, L.; Wang, S.; Barone, P.; Picozzi, S.; Sun, Y. Cross coupling between electric and magnetic orders in a multiferroic metal-organic framework. *Sci. Rep.* **2015**, *4*, 6062.
(359) Stroppa, A.; Di Sante, D.; Barone, P.; Bokdam, M.; Kresse, G.; Franchini, C.; Whangbo, M.-H.; Picozzi, S. Tunable ferroelectric

DOI: 10.1021/acs.inorgchem.9b01785
Inorg. Chem. 2019, 58, 14939−14980

polarization and its interplay with spin−orbit coupling in tin iodide perovskites. *Nat. Commun.* **2014**, *5*, 5900.
(360) Di Sante, D.; Stroppa, A.; Jain, P.; Picozzi, S. Tuning the ferroelectric polarization in a multiferroic metal−organic framework. *J. Am. Chem. Soc.* **2013**, *135*, 18126−18130.
(361) Mazzuca, L.; Cañadillas-Delgado, L.; Rodríguez-Velamazán, J. A.; Fabelo, O.; Scarrozza, M.; Stroppa, A.; Picozzi, S.; Zhao, J.-P.; Bu, X.-H.; Rodríguez-Carvajal, J. Magnetic structures of heterometallic M (II)−M (III) formate compounds. *Inorg. Chem.* **2017**, *56*, 197−207.
(362) Kamminga, M. E.; Stroppa, A.; Picozzi, S.; Chislov, M.; Zvereva, I. A.; Baas, J.; Meetsma, A.; Blake, G. R.; Palstra, T. T. Polar Nature of $(CH_3NH_3)_3Bi_2I_9$ Perovskite-Like Hybrids. *Inorg. Chem.* **2017**, *56*, 33−41.
(363) Gómez-Aguirre, L.; Pato-Doldán, B.; Stroppa, A.; Yang, L.; Frauenheim, T.; Mira, J.; Yáñez-Vilar, S.; Artiaga, R.; Castro-García, S.; Sánchez-Andújar, M.; Señaris Rodríguez, M. Coexistence of Three Ferroic Orders in the Multiferroic Compound $[(CH_3)_4N][Mn(N_3)_3]$ with Perovskite-Like Structure. *Chem.−Eur. J.* **2016**, *22*, 7863−7870.
(364) Ptak, M.; Mączka, M.; Gągor, A.; Sieradzki, A.; Stroppa, A.; Di Sante, D.; PerezMato, J. M.; Macalik, L. Experimental and theoretical studies of structural phase transition in a novel polar perovskite-like $[C_2H_5\ NH_3][Na_{0.5}Fe_{0.5}(HCOO)_3]$ formate. *Dalton transactions* **2016**, *45*, 2574−2583.
(365) Zhao, W.-P.; Shi, C.; Stroppa, A.; Di Sante, D.; Cimpoesu, F.; Zhang, W. LonePair-Electron-Driven Ionic Displacements in a Ferroelectric Metal-Organic Hybrid. *Inorg. Chem.* **2016**, *55*, 10337−10342.
(366) Gómez-Aguirre, L.; Pato-Doldán, B.; Stroppa, A.; Yáñez-Vilar, S.; Bayarjargal, L.; Winkler, B.; Castro-García, S.; Mira, J.; Sánchez-Andújar, M.; Señarís-Rodríguez, M. Room-temperature polar order in $[NH_4][Cd(HCOO)_3]$-a hybrid inorganic-organic compound with a unique perovskite architecture. *Inorg. Chem.* **2015**, *54*, 2109−2116.
(367) Stroppa, A.; Quarti, C.; De Angelis, F.; Picozzi, S. Ferroelectric polarization of $CH_3NH_3PbI_3$: a detailed study based on density functional theory and symmetry mode analysis. *J. Phys. Chem. Lett.* **2015**, *6*, 2223−2231.
(368) Tian, Y.; Stroppa, A.; Chai, Y.-S.; Barone, P.; Perez-Mato, M.; Picozzi, S.; Sun, Y. High-temperature ferroelectricity and strong magnetoelectric effects in a hybrid organic−inorganic perovskite framework. *Phys. Status Solidi RRL* **2015**, *9*, 62−67.
(369) Lee, C.; Hong, J.; Stroppa, A.; Whangbo, M.-H.; Shim, J. H. Organic−inorganic hybrid perovskites ABI_3 (A = $CH_3\ NH_3$, $NH_2\ CHNH_2$; B = Sn, Pb) as potential thermoelectric materials: a density functional evaluation. *RSC Adv.* **2015**, *5*, 78701−78707.
(370) Lee, M. M.; Teuscher, J.; Miyasaka, T.; Murakami, T. N.; Snaith, H. J. Efficient hybrid solarcells based on meso-superstructured organometal halide perovskites. *Science* **2012**, *338*, 1228604.
(371) Kim, H.-S.; Lee, C.-R.; Im, J.-H.; Lee, K.-B.; Moehl, T.; Marchioro, A.; Moon, S. J.; Humphry-Baker, R.; Yum, J.-H.; Moser, J. E.; Grätzel, M.; Park, N.-G. Lead Iodide Perovskite Sensitized All-Solid-State Submicron Thin Film Mesoscopic Solar Cell with Efficiency Exceeding 9%. *Sci. Rep.* **2012**, *2*, 591.
(372) Docampo, P.; Ball, J. M.; Darwich, M.; Eperon, G. E.; Snaith, H. J. Efficient organometal trihalide perovskite planar-heterojunction solar cells on flexible polymer substrates. *Nat. Commun.* **2013**, *4*, 2761.
(373) Burschka, J.; Pellet, N.; Moon, S.-J.; Humphry-Baker, R.; Gao, P.; Nazeeruddin, M. K.; Grätzel, M. Sequential deposition as a route to high-performance perovskite-sensitized solar cells. *Nature* **2013**, *499*, 316.
(374) Liu, M.; Johnston, M. B.; Snaith, H. J. Efficient planar heterojunction perovskite solar cells by vapour deposition. *Nature* **2013**, *501*, 395.
(375) Liu, D.; Kelly, T. L. Perovskite solar cells with a planar heterojunction structure prepared using room-temperature solution processing techniques. *Nat. Photonics* **2014**, *8*, 133.
(376) Malinkiewicz, O.; Yella, A.; Lee, Y. H.; Espallargas, G. M.; Graetzel, M.; Nazeeruddin, M. K.; Bolink, H. J. Perovskite solar cells employing organic charge-transport layers. *Nat. Photonics* **2014**, *8*, 128.
(377) Mei, A.; Li, X.; Liu, L.; Ku, Z.; Liu, T.; Rong, Y.; Xu, M.; Hu, M.; Chen, J.; Yang, Y.; Grätzel, M.; Han, H. A hole-conductor−free,fullyprintablemesoscopicperovskitesolar cell with high stability. *Science* **2014**, *345*, 295−298.
(378) Green, M. A.; Ho-Baillie, A.; Snaith, H. J. The emergence of perovskite solar cells. *Nat. Photonics* **2014**, *8*, 506.
(379) Bellitto, C.; Bauer, E. M.; Righini, G. Organic−inorganic hybrids: from magnetic perovskite metal (II) halides to multifunctional metal (II) phosphonates. *Coord. Chem. Rev.* **2015**, *289*, 123−136.
(380) Náfrádi, B.; Szirmai, P.; Spina, M.; Lee, H.; Yazyev, O.; Arakcheeva, A.; Chernyshov, D.; Gibert, M.; Forró, L.; Horváth, E. Optically switched magnetism in photovoltaic perovskite CH_3NH_3 (Mn:Pb)I_3. *Nat. Commun.* **2016**, *7*, 13406.
(381) Ping, Y.; Zhang, J. Z. Spin-optotronic Properties of Organometal Halide Perovskites. *J. Phys. Chem. Lett.* **2018**, *9*, 6103−6111.
(382) Gong, C.; Li, L.; Li, Z.; Ji, H.; Stern, A.; Xia, Y.; Cao, T.; Bao, W.; Wang, C.; Wang, Y.; Qiu, Z. Q.; Cava, R. J.; Louie, S. G.; Xia, J.; Zhang, X. Discovery of intrinsic ferromagnetism in two-dimensional van der Waals crystals. *Nature* **2017**, *546*, 265.
(383) Huang, B.; Clark, G.; Navarro-Moratalla, E.; Klein, D. R.; Cheng, R.; Seyler, K. L.; Zhong, D.; Schmidgall, E.; McGuire, M. A.; Cobden, D. H.; Yao, W.; Xiao, D.; JarilloHerrero, P.; Xu, X. Layer-dependent ferromagnetism in a van der Waals crystal down to the monolayer limit. *Nature* **2017**, *546*, 270.
(384) Huang, B.; Zhang, J.-Y.; Huang, R.-K.; Chen, M.-K.; Xue, W.; Zhang, W.-X.; Zeng, M.-H.; Chen, X.-M. Spin-reorientation-induced magnetodielectric coupling effects in two layered perovskite magnets. *Chemical Science* **2018**, *9*, 7413−7418.
(385) Pedersen, K. S.; et al. Formation of the layered conductive magnet $CrCl_2(pyrazine)_2$ through redox-active coordination chemistry. *Nat. Chem.* **2018**, *10*, 1056−1061.
(386) Fiebig, M.; Lottermoser, T.; Meier, D.; Trassin, M. The evolution of multiferroics. *Nature Reviews Materials* **2016**, *1*, 16046.
(387) Dong, S.; Liu, J.-M.; Cheong, S.-W.; Ren, Z. Multiferroic materials and magnetoelectric physics: symmetry, entanglement, excitation, and topology. *Adv. Phys.* **2015**, *64*, 519−626.
(388) Eerenstein, W.; Mathur, N.; Scott, J. F. Multiferroic and magnetoelectric materials. *Nature* **2006**, *442*, 759.
(389) Dadoenkova, Y. S.; Lyubchanskii, I. L.; Lee, Y.; Rasing, T. Electric field controlled magneto-optical kerr effect at light reflection from an electro-optic/magneto-optic bilayer. *IEEE Trans. Magn.* **2011**, *47*, 1623−1626.
(390) Prati, E. Propagation in Gyroelectromagnetic Guiding Systems. *Journal of Electromagnetic Waves and Applications* **2003**, *17*, 1177−1196.
(391) Brown, W., Jr; Shtrikman, S.; Treves, D. Possibility of visual observation of antiferromagnetic domains. *J. Appl. Phys.* **1963**, *34*, 1233−1234.
(392) Fan, F.-R.; Wu, H.; Nabok, D.; Hu, S.; Ren, W.; Draxl, C.; Stroppa, A. ElectricMagneto-Optical Kerr Effect in a Hybrid Organic−Inorganic Perovskite. *J. Am. Chem. Soc.* **2017**, *139*, 12883−12886.
(393) Kerr, J. XLIII. On rotation of the plane of polarization by reflection from the pole of a magnet. *London, Edinburgh, and Dublin Philosophical Magazine and Journal of Science* **1877**, *3*, 321−343.
(394) Buschow, K. v.; Van Engen, P.; Jongebreur, R. Magneto-optical properties of metallic ferromagnetic materials. *J. Magn. Magn. Mater.* **1983**, *38*, 1−22.
(395) Mansuripur, M. *The physical principles of magneto-optical recording;* Cambridge University Press, 1998.
(396) Mee, C. D.; Daniel, E. D. *Magnetic Recording Technology;* McGraw-Hill: New York, 1987; Vol. *1*, pp 323−324.
(397) Waser, R.; Keller, H.; Erb, U. *Nanoelectronics and information technology: Advanced electronic materials and novel devices;* John Wiley & Sons, Inc., 2004.

DOI: 10.1021/acs.inorgchem.9b01785
Inorg. Chem. 2019, 58, 14939−14980

(398) Schmidt, F.; Rave, W.; Hubert, A. Enhancement of magneto-optical domain observation by digital image processing. *IEEE Trans. Magn.* **1985**, *21*, 1596−1598.
(399) Stroppa, A.; Picozzi, S.; Continenza, A.; Kim, M.; Freeman, A. J. Magneto-optical properties of (Ga, Mn) As: An ab initio determination. *Phys. Rev. B: Condens. Matter Mater. Phys.* **2008**, *77*, No. 035208.
(400) Feng, W.; Guo, G.-Y.; Zhou, J.; Yao, Y.; Niu, Q. Large magneto-optical Kerr effect in noncollinear antiferromagnets Mn_3X (X = Rh, Ir, Pt). *Phys. Rev. B: Condens. Matter Mater. Phys.* **2015**, *92*, 144426.
(401) Sivadas, N.; Okamoto, S.; Xiao, D. Gate-controllable magneto-optic Kerr effect in layered collinear antiferromagnets. *Phys. Rev. Lett.* **2016**, *117*, 267203.
(402) Sangalli, D.; Marini, A.; Debernardi, A. Pseudopotential-based first-principles approach to the magneto-optical Kerr effect: From metals to the inclusion of local fields and excitonic effects. *Phys. Rev. B: Condens. Matter Mater. Phys.* **2012**, *86*, 125139.
(403) Eremenko, V. V.; Kharchenko, N.; Litvinenko, Y. G.; Naumenko, V. *Magneto-optics and Spectroscopy of Antiferromagnets*; Springer Science & Business Media, 2012.
(404) Jungwirth, T.; Marti, X.; Wadley, P.; Wunderlich, J. Antiferromagnetic spintronics. *Nat. Nanotechnol.* **2016**, *11*, 231.
(405) Baltz, V.; Manchon, A.; Tsoi, M.; Moriyama, T.; Ono, T.; Tserkovnyak, Y. Antiferromagnetic spintronics. *Rev. Mod. Phys.* **2018**, *90*, No. 015005.
(406) Jungwirth, T.; Sinova, J.; Manchon, A.; Marti, X.; Wunderlich, J.; Felser, C. The multiple directions of antiferromagnetic spintronics. *Nat. Phys.* **2018**, *14*, 200.
(407) Šmejkal, L.; Mokrousov, Y.; Yan, B.; MacDonald, A. H. Topological antiferromagnetic spintronics. *Nat. Phys.* **2018**, *14*, 1.
(408) Bodnar, S. Y.; Šmejkal, L.; Turek, I.; Jungwirth, T.; Gomonay, O.; Sinova, J.; Sapozhnik, A.; Elmers, H.-J.; Kläui, M.; Jourdan, M. Writing and reading antiferromagnetic Mn_2Au by Néel spin-orbit torques and large anisotropic magnetoresistance. *Nat. Commun.* **2018**, *9*, 348.
(409) Němec, P.; Fiebig, M.; Kampfrath, T.; Kimel, A. V. Antiferromagnetic opto-spintronics. *Nat. Phys.* **2018**, *1*, 229.
(410) Wadley, P.; et al. Electrical switching of an antiferromagnet. *Science* **2016**, *351*, 587−590.
(411) Godinho, J.; Reichlova, H.; Kriegner, D.; Novak, V.; Olejnik, K.; Kaspar, Z.; Soban, Z.; Wadley, P.; Campion, R. P.; Otxoa, R. M.; Roy, P. E.; Zelezny, J.; Jungwirth, T.; Wunderlich, J. Electrically induced and detected Néel vector reversal in a collinear antiferromagnet. *Nat. Commun.* **2018**, *9*, DOI: 10.1038/s41467-018-07092-2.
(412) Haldane, F. D. M. Nobel lecture: Topological quantum matter. *Rev. Mod. Phys.* **2017**, *89*, No. 040502.
(413) DC, M.; Grassi, R.; Chen, J.-Y.; Jamali, M.; Reifsnyder Hickey, D.; Zhang, D.; Zhao, Z.; Li, H.; Quarterman, P.; Lv, Y.; Li, M.; Manchon, A.; Mkhoyan, K. A.; Low, T.; Wang, J.-P. Room-temperature high spin-orbit torque due to quantum confinement in sputtered $Bi_xSe_{(1-x)}$ films. *Nat. Mater.* **2018**, *17*, 800−807.
(414) Li, P.; Wu, W.; Wen, Y.; Zhang, C.; Zhang, J.; Zhang, S.; Yu, Z.; Yang, S. A.; Manchon, A.; Zhang, X.-x. Spin-momentum locking and spin-orbit torques in magnetic nano-heterojunctions composed of Weyl semimetal WTe_2. *Nat. Commun.* **2018**, *9*, 3990.
(415) Xing, W.; Chen, Y.; Odenthal, P. M.; Zhang, X.; Yuan, W.; Su, T.; Song, Q.; Wang, T.; Zhong, J.; Jia, S.; Xie, X. C.; Li, Y.; Han, W. Electric field effect in multilayer $Cr_2Ge_2Te_6$: a ferromagnetic 2D material. *2D Mater.* **2017**, *4*, No. 024009.
(416) Higo, T.; et al. Large magneto-optical Kerr effect and imaging of magnetic octupole domains in an antiferromagnetic metal. *Nat. Photonics* **2018**, *12*, 73−78.
(417) Hutchings, I.; Shipway, P. *Tribology*, 2nd ed.; Butterworth-Heinemann, 2017; DOI: 10.1016/B978-0-08-100910-9.00001-5.
(418) Holmberg, K.; Erdemir, A. Influence of tribology on global energy consumption, costs and emissions. *Friction* **2017**, *5*, 263−284.
(419) Vakis, A.; et al. Modeling and Simulation in Tribology Across Scales: an Overview. *Tribol. Int.* **2018**, *125*, 169−199.
(420) Wang, Z. Self-Powered Nanosensors and Nanosystems. *Adv. Mater.* **2012**, *24*, 280.
(421) Hinchet, R.; Seung, W.; Kim, S.-W. Recent Progress on Flexible Triboelectric Nanogenerators for Self-Powered Electronics. *ChemSusChem* **2015**, *8*, 2327.
(422) Zi, Y.; Wang, Z. Nanogenerators: An Emerging Technology towards Nanoenergy. *APL Mater.* **2017**, *5*, 74103.
(423) Khan, U.; Hinchet, R.; Ryu, H.; Kim, S.-W. Research Update: Nanogenerators for self-powered autonomous wireless sensors. *APL Mater.* **2017**, *5*, No. 073803.
(424) Wang, Z. Triboelectric Nanogenerators as New Energy Technology for Self-Powered Systems and as Active Mechanical and Chemical Sensors. *ACS Nano* **2013**, *7*, 9533.
(425) Zi, Y.; Guo, H.; Wen, Z.; Yeh, M.-H.; Hu, C.; Wang, Z. Harvesting Low-Frequency (<5 Hz) Irregular Mechanical Energy: A Possible Killer Application of Triboelectric Nanogenerator. *ACS Nano* **2016**, *10*, 4797.
(426) Wang, Z.; Song, J. Piezoelectric Nanogenerators Based on Zinc Oxide Nanowire Arrays. *Science* **2006**, *312*, 242.
(427) Wang, Z. On Maxwell's displacement current for energy and sensors: the origin of nanogenerators. *Mater. Today* **2017**, *20*, 74.
(428) Wang, S.; Lin, L.; Xie, Y.; Jing, Q.; Niu, S.; Wang, Z. Sliding-Triboelectric Nanogenerators Based on In-Plane Charge-Separation Mechanism. *Nano Lett.* **2013**, *13*, 2226.
(429) Yang, Y.; Zhang, H.; Chen, J.; Jing, Q.; Zhou, Y.; Wen, X.; Wang, Z. Single-Electrode Based Sliding Triboelectric Nanogenerator for Self-Powered Displacement Vector Sensor System. *ACS Nano* **2013**, *7*, 7342.
(430) Xie, Y.; Wang, S.; Niu, S.; Lin, L.; Jing, Q.; Yang, J.; Wu, Z.; Wang, Z. Grating Structured Freestanding Triboelectric-Layer Nanogenerator for Harvesting Mechanical Energy at 85% Total Conversion Efficiency. *Adv. Mater.* **2014**, *26*, 6599.
(431) Lee, J.; Ye, B.; Baik, J. Research Update: Recent progress in the development of effective dielectrics for high-output triboelectric nanogenerator. *APL Mater.* **2017**, *5*, No. 073802.
(432) Li, J.; Wang, X. Research Update: Materials design of implantable nanogenerators for biomechanical energy harvesting. *APL Mater.* **2017**, *5*, No. 073801.
(433) Fan, F.-R.; Lin, L.; Zhu, G.; Wu, W.; Zhang, R.; Wang, Z. Transparent Triboelectric Nanogenerators and Self-Powered Pressure Sensors Based on Micropatterned Plastic Films. *Nano Lett.* **2012**, *12*, 3109.
(434) Bai, P.; Zhu, G.; Jing, Q.; Yang, J.; Chen, J.; Su, Y.; Ma, J.; Zhang, G.; Wang, Z. Membrane-Based Self-Powered Triboelectric Sensors for Pressure Change Detection and Its Uses in Security Surveillance and Healthcare Monitoring. *Adv. Funct. Mater.* **2014**, *24*, 5807.
(435) Lin, L.; Wang, S.; Xie, Y.; Jing, Q.; Niu, S.; Hu, Y.; Wang, Z. Segmentally Structured Disk Triboelectric Nanogenerator for Harvesting Rotational Mechanical Energy. *Nano Lett.* **2013**, *13*, 2916.
(436) Bao, Y.; Wang, R.; Lu, Y.; Wu, W. Lignin biopolymer based triboelectric nanogenerators. *APL Mater.* **2017**, *5*, No. 074109.
(437) Kim, S.; Gupta, M.; Lee, K.; Sohn, A.; Kim, T.; Shin, K.-S.; Kim, D.; Kim, S.; Lee, K.; Shin, H.-J.; Kim, D.-W.; Kim, S.-W. Transparent Flexible Graphene Triboelectric Nanogenerators. *Adv. Mater.* **2014**, *26*, 3918.
(438) Liu, J.; Goswami, A.; Jiang, K.; Khan, F.; Kim, S.; McGee, R.; Li, Z.; Hu, Z.; Lee, J.; Thundat, T. Direct-current triboelectricity generation by a sliding Schottky nanocontact on MoS_2 multilayers. *Nat. Nanotechnol.* **2018**, *13*, 112.
(439) Diaz, A. F.; Felix-Navarro, R. M. A semi-quantitative tribo-electric series for polymeric materials: the influence of chemical structure and properties. *J. Electrost.* **2004**, *62*, 277.
(440) The NOMAD Laboratory−A European Centre of Excellence. https://nomadrepository.eu/. Online; accessed Aug 27, 2019.

DOI: 10.1021/acs.inorgchem.9b01785
Inorg. Chem. 2019, 58, 14939−14980

(441) Pizzi, G.; Cepellotti, A.; Sabatini, R.; Marzari, N.; Kozinsky, B. AiiDA: automated interactive infrastructure and database for computational science. *Comput. Mater. Sci.* **2016**, *111*, 218−230.
(442) Castle, G. Contact charging between insulators. *J. Electrost.* **1997**, *40*−*41*, 13−20.
(443) Cheng, G.-G.; Jiang, S.-Y.; Li, K.; Zhang, Z.-Q.; Wang, Y.; Yuan, N.-Y.; Ding, J.-N.; Zhang, W. Effect of argon plasma treatment on the output perfomance of triboelectric nanogenerator. *Appl. Surf. Sci.* **2017**, *412*, 350−356.
(444) Kim, D.; Tcho, I.-W.; Jin, I.; Park, S.-J.; Jeon, S.-B.; Kim, W.-G.; Cho, H.-S.; Lee, H. S.; Jeoung, S.; Choi, Y.-K. Direct-laser-patterned friction layer for the output enhancement of a triboelectric nanogenerator. *Nano Energy* **2017**, *35*, 379−386.
(445) Nguyen, V.; Yang, R. Effect of humidity and pressure on the triboelectric nanogenerator. *Nano Energy* **2013**, *2*, 604−608.
(446) Lu, C.; Han, C.; Gu, G.; Chen, J.; Yang, Z.; Jiang, T.; He, C.; Wang, Z. Temperature Effect on Performance of Triboelectric Nanogenerator. *Adv. Eng. Mater.* **2017**, *19*, 1700275.
(447) Wen, Z.; Guo, H.; Zi, Y.; Yeh, M.-H.; Wang, X.; Deng, J.; Wang, J.; Li, S.; Hu, C.; Zhu, L.; Wang, Z. L. Harvesting Broad Frequency Band Blue Energy by a Triboelectric-Electromagnetic Hybrid Nanogenerator. *ACS Nano* **2016**, *10*, 6526.
(448) Wang, Z. Triboelectric nanogenerators as new energy technology and self-powered sensors−principles, problems and perspectives. *Faraday Discuss.* **2014**, *176*, 447−458.
(449) Guo, H.; Wen, Z.; Zi, Y.; Yeh, M.-H.; Wang, J.; Zhu, L.; Hu, C.; Wang, Z. A Water-Proof Triboelectric-Electromagnetic Hybrid Generator for Energy Harvesting in Harsh Environments. *Adv. Energy Mater.* **2016**, *6*, 1501593.
(450) Zhu, G.; Lin, Z.-H.; Jing, Q.; Bai, P.; Pan, C.; Yang, Y.; Zhou, Y.; Wang, Z. Toward Large-Scale Energy Harvesting by a Nanoparticle-Enhanced Triboelectric Nanogenerator. *Nano Lett.* **2013**, *13*, 847.
(451) Goswami, A.; Dhandaria, P.; Pal, S.; McGee, R.; Khan, F.; Antić, Ž.; Gaikwad, R.; Prashanthi, K.; Thundat, T. Effect of interface on mid-infrared photothermal response of MoS_2 thin film grown by pulsed laser deposition. *Nano Res.* **2017**, *10*, 3571.
(452) Park, J.; Salmeron, M. Fundamental Aspects of Energy Dissipation in Friction. *Chem. Rev.* **2014**, *114*, 677−711.
(453) Nonnenmacher, M.; O'Boyle, M.; Wickramasinghe, H. Kelvin probe force microscopy. *Appl. Phys. Lett.* **1991**, *58*, 2921−2923.
(454) Wang, H.; Huang, C.-C.; Polcar, T. Controllable Tunneling Triboelectrification of Two-Dimensional Chemical Vapor Deposited MoS_2. *Sci. Rep.* **2019**, *9*, 334.
(455) Drolle, E.; Bennett, W.; Hammond, K.; Lyman, E.; Karttunen, M.; Leonenko, Z. Molecular dynamics simulations and Kelvin probe force microscopy to study of cholesterol-induced electrostatic nanodomains in complex lipid mixtures. *Soft Matter* **2017**, *13*, 355−362.
(456) Korir, K.; Cicero, G.; Catellani, A. Piezoelectric properties of zinc oxide nanowires: an ab initio study. *Nanotechnology* **2013**, *24*, 475401−475406.
(457) Seol, M.-L.; Han, J.-W.; Moon, D.-I.; Meyyappan, M. Hysteretic behavior of contact force response in triboelectric nanogenerator. *Nano Energy* **2017**, *32*, 408−413.
(458) Cammarata, A.; Polcar, T. Electro-vibrational coupling effects on "intrinsic friction" in transition metal dichalcogenides. *RSC Adv.* **2015**, *5*, 106809.
(459) Cammarata, A.; Polcar, T. Tailoring Nanoscale Friction in MX_2 Transition Metal Dichalcogenides. *Inorg. Chem.* **2015**, *54*, 5739.
(460) Cammarata, A.; Polcar, T. Layering effects on low frequency modes in n-layered MX_2 transition metal dichalcogenides. *Phys. Chem. Chem. Phys.* **2016**, *18*, 4807.
(461) Cammarata, A.; Polcar, T. Vibrational contributions to intrinsic friction in charged transition metal dichalcogenides. *Nanoscale* **2017**, *9*, 11488.
(462) Irving, B.; Nicolini, P.; Polcar, T. On the lubricity of transition metal dichalcogenides: an ab initio study. *Nanoscale* **2017**, *9*, 5597.
(463) Cammarata, A.; Nicolini, P.; Simonovic, K.; Ukraintsev, E.; Polcar, T. Atomic-scale design of friction and energy dissipation. *Phys. Rev. B: Condens. Matter Mater. Phys.* **2019**, *99*, No. 094309.

DOI: 10.1021/acs.inorgchem.9b01785
Inorg. Chem. 2019, 58, 14939−14980

E

Joint Study AFM & MD

I was a co-author of this work and contributed to the conceptualization of the computational setup. Moreover, our parametrization of the LJ parameters, as reported on in Chap. 4, was used. All results of this study have been submitted to the Nature Materials journal. This is an impacted journal, which had an impact factor of 38.663 in 2019 and belongs to the quartile category Q1 in the field of physical chemistry, materials science, applied physics, and condensed matter physics. A copy of the submitted manuscript is attached below.

Ultra-low friction and edge pinning effect between large lattice mismatch van der Waals heterostructure interfaces

Mengzhou Liao[1,2], Paolo Nicolini[2], Luojun Du[1,3], Jiahao Yuan[1,4], Shuopei Wang[1,9,a], Hua Yu[1,4], Jiang Tang[1,4], Peng Cheng[5], Kenji Watanabe[6], Takashi Taniguchi[6], Lin Gu[1,4], Victor E. P. Claerbout[2], Andrea Silva[7], Denis Kramer[7, 8], Tomas Polcar[2, 7], Rong Yang[1, 9,a], Dongxia Shi[1,4,9] and Guangyu Zhang[1,4,9,a*]

[1] *Beijing National Laboratory for Condensed Matter Physics and Institute of Physics, Chinese Academy of Sciences, Beijing 100190, China*

[2] *Department of Control Engineering, Faculty of Electrical Engineering, Czech Technical University in Prague, Technicka 2, 16627 Prague 6, Czech Republic*

[3] *Department of Electronics and Nanoengineering, Aalto University, Tietotie 3, FI-02150, Finland*

[4] *School of Physical Sciences, University of Chinese Academy of Sciences, Beijing 100190, China*

[5] *Oxford Instruments (Shanghai) Co. Limited, Shanghai 201109, China*

[6] *National Institute for Materials Science, 1-1 Namiki, Tsukuba 305-0044, Japan*

[7] *National Centre for Advanced Tribology Study at University of Southampton, Southampton SO171BJ, United Kingdom*

[8] *Faculty of Mechanical Engineering, Helmut Schmidt University, 22043, Hamburg, Germany*

[9] *Beijing Key Laboratory for Nanomaterials and Nanodevices, Beijing 100190, China*

[a] *Songshan Lake Materials Laboratory, Dongguan, Guangdong 523808, China*

* Corresponding author. E-mail: gyzhang@iphy.ac.cn (G.Z.)

Abstract

Two-dimensional heterostructures are excellent platforms to realize twist-angle independent ultra-low friction due to their weak interlayer van der Waals interactions and natural lattice mismatch. However, for finite-size interfaces, the effect of domain edges on the friction process remains unclear. Here, we report on the superlubricity phenomenon and the edge pinning effect at MoS_2/graphite and

MoS_2/h-BN van der Waals heterostructure interfaces. We find that friction coefficients of these heterostructures are below 10^{-6}. Molecular dynamics simulations corroborate experiments highlighting the contribution of edges and interface steps to friction forces. Our experiments and simulations provide more information on the sliding mechanism of finite low-dimensional structures, which is vital to understand the friction process of laminar solid lubricants.

Introduction

Friction causes massive energy dissipation and mechanical abrasion between machine component parts in the world every year (costing approximately 119 EJ)[1,2]. Understanding the mechanism of the frictional processes and searching for an optimum material combination, ideally providing a near frictionless state, are thus essential. The concept of superlubricity was proposed by K. Shinjo and M. Hirano in the 1990s[3], which describes the phenomenon of vanishing friction between two contact surfaces (also known as structural lubricity later). Superlubricity has been widely found in van der Waals (vdW) materials, as their crystalline structures are kept together by weak vdW forces[4]. However, superlubricity in two dimensional (2D) homostructures shows a strong twist-angle dependence[5-7]. Layers prefer to rotate and lock in the commensurate state when sliding occurs, leading to the disappearance of superlubricity[6,8]. vdW heterojunctions may reduce the commensuration problem since the lattice mismatch between the two contact materials will come into play. Micro-scale superlubricity has been uncovered in the graphene/hexagonal boron nitride (h-BN) heterostructure with a significant reduction of twist-angle dependence[9-13]. However, the twist-angle dependence is still present in graphene/h-BN heterostructure, perhaps due to the small lattice mismatch. Thus, it is crucial to explore the lattice mismatch influence on the superlubricity of 2D heterostructures. Furthermore, the effect of widespread domain edges and interface steps on the superlubricity of the finite-size 2D interfaces may prevent superlubricity.

In this work, we characterized 2D heterojunction interfaces with different lattice mismatches: molybdenum disulfide (MoS_2) /graphite, MoS_2/h-BN, and graphene/h-BN by Lateral Force Atomic Force Microscope (LF-AFM). Our results show that the coefficient of friction of the large lattice mismatch MoS_2/graphite and MoS_2/h-BN heterojunction interfaces is below 10^{-6}, and the twist-angle dependence is suppressed.

We demonstrate that the friction forces of these two heterojunctions are dominated by pinned edges or substrate step effects rather than resistance to interface sliding, from e.g. potential energy corrugation. For comparison, interface sliding resistance dominates the friction process in sliding of small lattice mismatch graphene/h-BN. Classical molecular dynamics (MD) simulations indicate that atoms near the edges of the flake play a distinctive role during the sliding dynamics, presenting enhanced out-of-plane structural distortions with respect to the rest of the flake. Given the non-reactive nature of the force fields employed in the MD simulations, we also indirectly prove that dangling bonds at the edge of the domains contribute mostly to the friction force observed in climbing substrate steps.

Results

Growth and characterization of vdW heterostructures

VdW heterostructure samples investigated in this work include MoS_2/graphite, MoS_2/h-BN, and graphene/h-BN with lattice mismatches of 26.8%, 24.6%, and 1.8%, respectively. Figs. 1**a**-**c** show the structures of these three heterostructures. All samples were prepared by an epitaxial growth technique described in our previous works[14-16] (see the Methods section for more details). Figs. 1**d**-**f** show typical AFM topographic images; these epitaxial interfaces are ultra-clean. The heights of monolayer MoS_2 on graphite and h-BN are 0.83 nm and 0.72 nm, respectively, and the height of monolayer graphene on h-BN is 0.35 nm; all in agreement with previous reports[16,17]. The arithmetic mean deviation of the assessed profiles (Ra) of substrate surfaces in Fig. 1d-f are 0.17nm, 0.13nm, and 0.02nm, which suggests atomically flat substrate surfaces and excludes the influence of the substrate roughness to the following experiments. We used selected area electron diffraction (SAED) to characterize the lattice alignment of our MoS_2/graphite and MoS_2/h-BN heterostructures. As illustrated in Fig. S1**b** and 1**e**, the hexagonal diffraction spots of both MoS_2 and graphite (h-BN) have the same orientation, indicating either 0° or 60° twisting angle between the as-grown MoS_2 and graphite (h-BN) substrate. Fig. S1**h** shows that the period of the moiré superlattice of as-grown graphene/h-BN heterostructure is ~16 nm, also suggesting a 0° twist angle. Raman and photoluminescence (PL) spectra in Fig. S1**c** and **f** also demonstrate a high sample quality. For more information, please refer to the Supplementary Note 1.

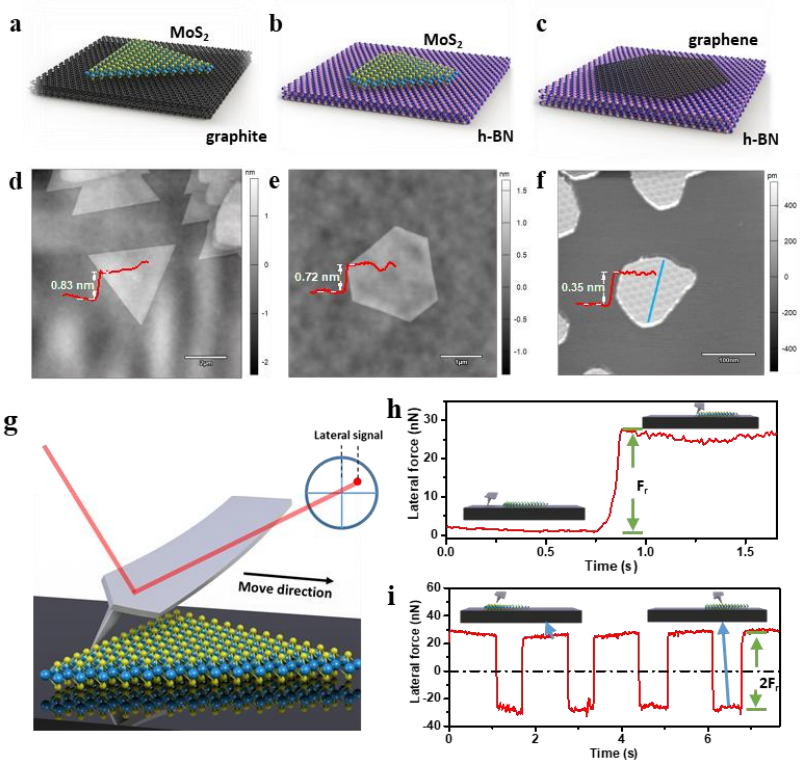

Fig. 1 | Friction characterizations of 2D heterostructures. a-c Atomic structures and **d-f** AFM images of three heterostructures: MoS_2/graphite, MoS_2/h-BN, and graphene/h-BN, respectively. **g** Diagram of friction force measurements. **h** and **i** Two different strategies for friction force characterizations of MoS_2/graphite and MoS_2/h-BN heterostructures: **h** by pushing from the edge of the domain, or **i** by dragging with the tip placed at the center of the domain, the sign of the force indicates the sliding direction.

Superlubricity behavior of vdW heterostructures

We performed friction force measurements by AFM in dry N_2 atmosphere to reduce contamination from the air. As illustrated in Fig. 1**d-f** and Fig. S2, the thickness of our samples is homogenous and the actual values indicate monolayer-thick samples, which exclude the presence of contamination. Fig. 1**g** shows a schematic of our measurements process. Based on a manipulation technique we developed previously[11,18], we can slide atop epitaxial domains on the substrate by using an AFM tip and monitor the lateral force during the sliding simultaneously (please refer to the Methods section and Supplementary Note 2 for more details). In the experiments, we explore two approaches to slide on-top domains on substrates by using AFM tips. The first is illustrated in Fig.

1**h**, where we laterally push the edge of the top domain and detect the difference of lateral force before and after on-top domain sliding. The second way is shown in Fig. 1**i.** For MoS_2/graphite and MoS_2/h-BN heterostructures, we could slide the top domains back and forth laterally by engaging the tip onto the center of the domain, with a load ranging from 0.4 to 5μN, since the friction force between the tip and MoS_2 is much greater than that between MoS_2 and graphite (or h-BN).

According to Amonton's law, the dependence of the friction force F_r on the load L is expressed by

$$F_r = \mu \cdot L,$$

where μ is the coefficient of friction (COF). By taking advantage of both approaches, we can change the applied tip load L_{tip} from zero to a few μN (near zero tip load is achieved by pushing the edge). The normal force experienced by the flake can be decomposed into two contributions

$$L = L_0 + L_{tip},$$

with L_0 being the adhesion between MoS_2 and graphite (or h-BN) and L_{tip} the load applied to the tip. It follows that:

$$F_r = \mu \cdot (L_0 + L_{tip}) = \mu \cdot L_0 + \mu \cdot L_{tip} = F_{r0} + \mu \cdot L_{tip}.$$

As shown in Fig. 2**a** and **b**, under N_2, the friction forces of aligned MoS_2/graphite and MoS_2/h-BN heterostructures are almost the same for different values of L_{tip}, which indicates constant F_{r0} and ultralow COF. As shown in Fig. 2, the coefficient of friction of both aligned MoS_2/graphite and MoS_2/h-BN heterostructure interfaces is well below 10^{-3}, which is considered the threshold for superlubricity[19]. To calculate the friction coefficient precisely from the slope in Fig. 2**a** and **b**, a much higher resolution and noise reduction of the AFM signal would be needed.

Nevertheless, we can use an alternative approach to estimate the COF. The adhesive force between MoS_2 domains and graphite or h-BN represents the major contribution to the load L[7]. Thus, we can estimate the magnitude of the COF, μ, by using:

$$\mu = F_{r0}/L_0$$

$$L_0 = G \cdot A$$

where G = 1.13GPa is the adhesive pressure between graphite and MoS_2 sheets[20]; and A is the area of the domain. From Fig. S3**a**, the area of our largest MoS_2 domain on graphite is A = 15.00 μm^2, giving an adhesive force $L_0 = 16.95$ mN. The corresponding

friction force is F_{r0} = 44.15 nN, then the COF of the aligned MoS_2/graphite heterostructure interfaces is μ_{MG} = 2.60×10^{-6}. This value is almost two orders of magnitude smaller than those reported in previous studies[7,21,22]. For the aligned MoS_2/h-BN heterostructure, according to Fig. S3**b,** the COF value is around μ_{MB} = 2.29×10^{-6}, similar to MoS_2/graphite.

To further explore the twist-angle dependence of superlubricity in large lattice mismatch heterostructures, we performed the friction test on the MoS_2/graphite heterostructure with different twist angles. Although the heterostructures can be rotated to any twist angle[18], they are only stable at large twist angles during sliding. We compare the friction force between aligned structures (0°/60°) and large twist angles of different MoS_2 domains. As shown in Fig.2**c,** the measured friction forces from MoS_2/graphite heterostructures before and after twisting show no significant angular dependence. This phenomenon is due to the fact that the in-plane interface friction force is almost zero even at 0° due to incommensurability, and the influence of the twist angle on the friction force has a negligible contribution to the total friction force. (please refer to the Supplementary Note 3 for more details).

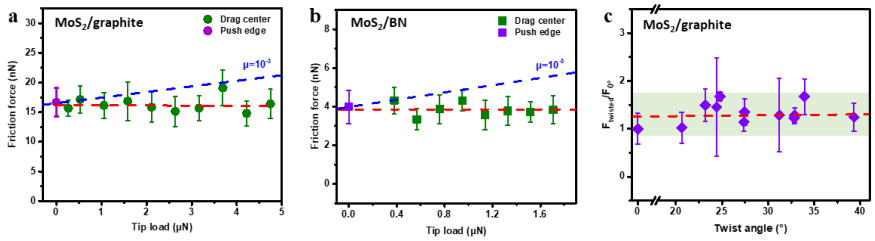

Fig. 2 | Superlubricity of MoS_2/graphite and MoS_2/h-BN heterostructure interfaces. a and **b** Friction force as a function of the tip load of MoS_2/graphite and MoS_2/h-BN heterostructures, obtained by AC200TS and AC240TS tips under N_2 gas environment. The red dashed lines are the fittings of all data points in **a** and **b**, respectively; the blue dashed line shows the limit of superlubricity. **c** Normalized friction force as a function of the twist angle of the MoS_2/graphite heterostructure. $F_{0°}$ and $F_{Twisted}$ are the friction forces of a MoS_2 domain before (aligned) and after twisting. The red dashed line is the fit. Error bars are standard deviations of data points.

Edge pinning effect of large lattice mismatch vdW heterostructures

Although the interface COFs of aligned MoS_2/graphite and MoS_2/h-BN heterostructure interfaces are small, there is still a constant friction force F_{r0}

independent of load within the normal load range considered. Previous results pointed out that the friction force could be affected by many parameters, such as edges, interface steps, and contaminations[23-25]. To determine the origin of this constant friction force, we define two parameters: shear strength S and domain edge pinning strength E. Considering the finite size of our samples, S and E are defined as follows:

$$S = F_r/A$$

$$E = F_r/P,$$

where A and P are the area and the perimeter of domains, respectively. We can expect three situations: 1) the in-plane interface sliding resistance contributes predominantly to the friction force and S is thus constant with respect to the area of domains; 2) the in-plane interface friction is negligible and the edge pinning effect dominates the friction process and E is constant with respect to the perimeter of the domains; 3) if both effects contribute significantly to the friction force, then both S and E cannot be constant.

We first measured the friction force of the aligned heterostructure samples with various contact areas under a dry N_2 atmosphere. The results are consistent even when different tips were used (Fig. S3), suggesting good consistency and repeatability of our calibration method. Fig. 3**a** shows a plot of the shear strength (S) of the aligned MoS_2/graphite heterostructure as a function of the domain area (A), clearly revealing a non-constant profile. In contrast, when we plot the data as E vs. P, as shown in Fig. 3**b**, the edge pinning strength E is constant with $E = 1.99^{+0.35}_{-0.25}$ nN/μm. These results indicate that the interface (in-plane) friction within aligned MoS_2/graphite is negligible, and the edges of the MoS_2 domains are pinned to the surface of graphite. Aligned MoS_2/h-BN exhibits similar behavior, as shown in Fig. 3**c** and **d**, where $E = 1.94^{+0.80}_{-0.59}$ nN/μm being very close to that of MoS_2/graphite. It is also worth noting that the thickness of MoS_2 domains has no apparent effect on the friction force due to the negligible interface friction (please also refer to Fig. S2**d**). Please note that all edges of MoS_2 domains in our experiment have the same zig-zag direction (supported by Fig. S1 and S5). So here E is actually the zig-zag edge pinning strength. As described above, the friction force of large lattice mismatch MoS_2/graphite and MoS_2/h-BN heterostructures mainly comes from the pinned edges. Therefore, the friction coefficient of edge-free, single-crystal MoS_2/graphite and MoS_2/h-BN heterostructure interfaces should be significantly lower than 10^{-6}.

The behavior of the aligned graphene/h-BN heterostructure, which has a small lattice mismatch (1.8%), is different from the MoS_2/graphite and MoS_2/h-BN heterostructures. From Fig. 3**e** and 3**f**, we can see that the shear strength of the graphene/h-BN heterostructure is constant and equal to $S = 2.20 \pm 0.39$ MPa, suggesting that the in-plane interface friction is dominant. The dominancy of in-plane friction in aligned graphene/h-BN can be understood considering its near-commensurate nature at small twist angles, where the period of moiré superlattice is larger than in the MoS_2-based heterostructures[16,26,27]. It needs to be mentioned that the shear strength value of the graphene/h-BN heterostructure in our experiment is larger than that of Ref. 10. The reason for this discrepancy can be attributed to the different thickneses of the graphene layers in the heterostructures, which can influence the sliding energy profile[28], the z-direction fluctuations, and the structure of the moiré pattern[29]. Those properties will eventually determine the interface friction force.

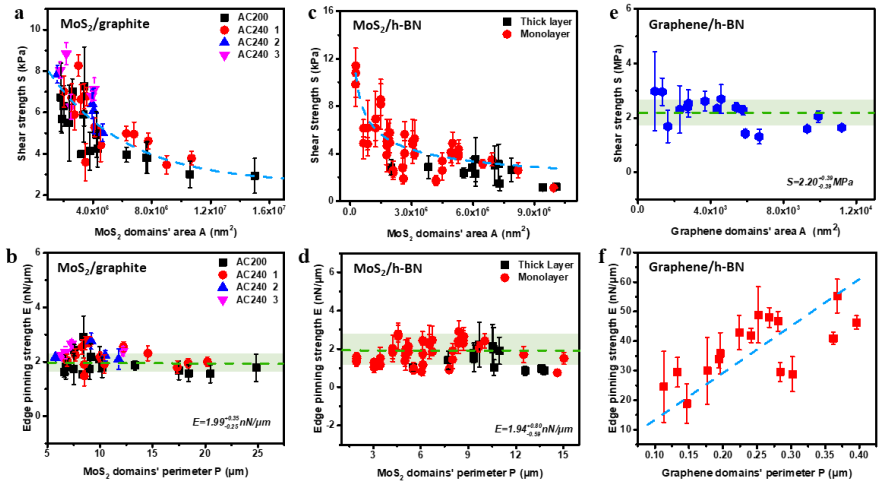

Fig. 3 | Source of friction for three different heterostructure interfaces. a and **b** are plots of friction characterization of MoS_2/graphite as a function of the domain area A and the perimeter P, respectively. **c** and **d** are similar plots for MoS_2/h-BN. **e** and **f** Friction characterization of graphene/h-BN as a function of A and P. Dash lines are linear fits. Error bars are standard deviations of data points.

Simulation results of the edge pinning effect for the MoS_2/graphite heterostructure

To understand the origin of the edge pinning effect for the MoS_2/graphene heterostructure, we performed a set of molecular dynamics simulations. The computational setup is illustrated in Fig. 4**a** and **b**. We considered triangular zigzag-

terminated MoS_2 flakes with different side lengths ranging from approximately 2 to 20 nm. Since no reactive force fields are available for the MoS_2/graphene system, we described the interlayer interactions by means of Stillinger-Weber[30] and AIREBO[31] potentials for MoS_2 and graphene, respectively. The interlayer interactions are modeled via a Lennard-Jones (LJ) potential, which was recently parameterized by using ab initio data[32]. According to this potential, the adhesive pressure between MoS_2 and graphite is G = 1.20 GPa, which is in good agreement with both experiment and *ab initio* calculations[20]. The Supplementary Note 6 reports an extensive analysis using density functional theory (DFT) calculations that shows no chemical bonding between MoS_2 edges and the graphene substrate, justifying the use of a non-reactive force field. Moreover, the sliding potential induced by the LJ coupling has been benchmarked against DFT calculations in a small test system. The classical force field captures the shape of the potential energy surface while it slightly underestimates the barrier height, as shown in the Supplementary Note 7. Thus, we expect the simulation to correctly reproduce the trends found in experiments albeit scaled. All systems have been equilibrated at room temperature, after which non-equilibrium simulations have been performed by applying a constant speed protocol and calculating the lateral force acting on the flake. For more details, please refer to the Methods section.

Fig. 4 summarizes the simulation results. The shear and edge pinning strength are reported as a function of the MoS_2 domain area and perimeter, respectively. As shown in Fig. 4**c**, S presents a decreasing profile as A increases, while E is almost constant. We also calculated the shear strength of an infinite heterostructure, $S_{infinite}$= 1.38 kPa, which is at least one order of magnitude smaller than that of our finite heterostructures. These trends are consistent with the experimental observations. To get a more in-depth insight into the underlying mechanisms, we analyzed the results in terms of structural and energy parameters. Fig. 4**d** reports the map of the atomic root mean square displacement (RMSD) with respect to the equilibrium positions for different atomic layers of MoS_2, and averaged over the MD trajectory. The mean displacement of edge atoms is significantly larger than for center atoms. Data distributions of the edge and center regions in Fig. S4**a** also show that edge atoms (particularly for atoms at the edge and at one lattice distance from it) have both a larger peak RMSD value and a broader distribution. Moreover, from Fig. 4**e** it is possible to notice that the main contribution to the RMSD comes from the out-of plane atomic distortions (see the Supplementary

Note 9 for the maps related to the other atomic layers). Potential energy maps of different atomic types within the MoS_2 layer (Fig. 4**f**) show that the edge S atoms present a distinct behavior in terms of potential energy than the center S atoms. In particular, sulfur atoms located at the edge are more mobile than central atoms due to the lower coordination and thus more prone to be trapped in the energy minima of the substrate, leading to the edge pinning effect. Edge Mo atoms also present differences with respect to the central ones, but the behavior is not as significant as for S atoms (please also refer to potential energy data in Fig. S4**b** and **c** for a more detailed discussion).

The MD simulations indicate that, during sliding, the dynamics of edge atoms present peculiar traits for distortions and potential energy fluctuations, ultimately providing the greatest contribution to the friction force. Indeed, in Fig. S5, using a high-resolution transmission electron microscopy, we observe more pronounced lattice distortions at the edges, which supports the simulation results.

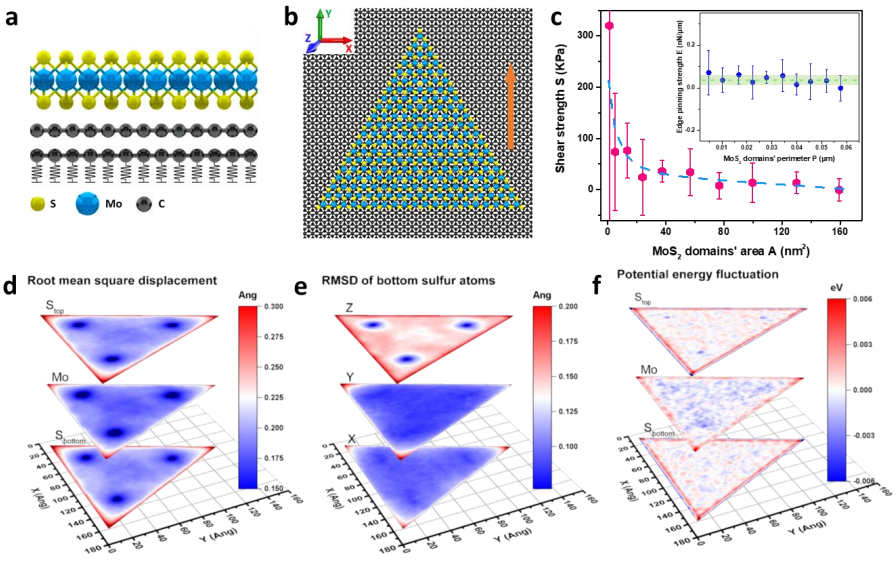

Fig. 4 | MD simulation results of MoS_2 flakes sliding on graphite. a and **b** Side and top views of the MD computational setup, respectively. **c** Calculated shear strength as a function of the MoS_2 flake area; the inset shows the calculated edge pinning strength as a function of the MoS_2 flake perimeter. Dashed lines are the fits. Error bars are standard deviations of data points, and the error bar of the shear strength of the smallest flake is 467.64 kPa. **d** Root mean square displacement maps of different atomic layers in the MoS_2 flake calculated with respect to the optimized geometry for a typical trajectory (flake size ~16 nm). **e** Maps of the root mean square displacement calculated on the three Cartesian components

separately, and for the bottom sulfur atoms only (for the maps of the other atomic layers, refer to the Supplementary Note 9). **f** Per-atom average potential energy fluctuation maps of different atomic layers in the MoS_2 flake. The three bright spots in **e** mark the position of the fixed atoms (see the Methods section for more details). For the potential energy, values are reported as the difference with respect to the mean value.

Step pinning effect at MoS_2/graphite heterostructure interfaces.

We have found experimentally that substrate steps can impede the sliding of MoS_2 domains even when they only have the height of a graphene monolayer (~0.4 nm). As shown in Fig. 5**a**, when we pushed a MoS_2 domain across a graphite step edge, we observed various resistance forces during different stages (I, II, III, IV). Stage III represents the MoS_2 domain crossing the step of graphite and finally locking on it. The resistance force increases almost tenfold before the MoS_2 domain locks on the graphite step. Here we define the interface step pinning strength P_{IS} as

$$P_{IS} = F_{max}/d$$

where F_{max} is the maximum force of stage III, and d is the length of the step edge under the MoS_2 domain. The interface step pinning strength in Fig. 5**a** is P_{IS}~100 nN/μm, which is two orders of magnitude larger than the edge pinning strength mentioned above. Therefore, the friction force will rise dramatically if interface steps are present. We also used MD simulations to monitor the friction force when a MoS_2 flake is pushed toward a graphite step with different angles with respect to the sliding direction, as shown in Fig. 5**b** and **c**. From Fig. 5**c**, we can see that, regardless of the orientation of the step, all profiles show a qualitatively similar behavior; the friction force will rise several times when the MoS_2 layer approaches the step. However, this increase in friction force is smaller than that observed in experiments. The difference between simulations and experiments can be ascribed to the fact that our model accounts only for non-bonded vdW interactions between flake and substrate (i.e., the model does not allow the formation of chemical bonds between MoS_2 and graphene atoms). Previous works show that chemical bonds on graphite steps have a strong influence on the friction force[33], so we attribute the step pinning effect to the interaction between the MoS_2 layer and the free chemical bonds on the graphite step.

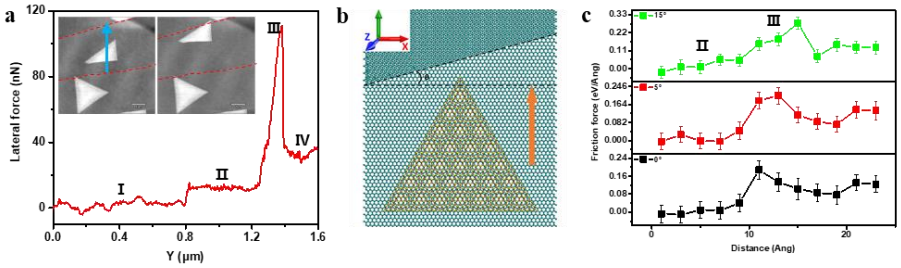

Fig. 5 | Effects of interface steps on friction force. a Lateral force measurement when pushing one MoS_2 domain across a monolayer step of graphite. The red dashed line marks the graphite step, and the blue arrow shows the tip route. The **I, II, III, and IV** tags mark the different stages of the tip movement: **I**, the tip is moving on graphite; **II**, the tip is pushing the MoS_2 domain; **III**, the MoS_2 domain is moving across the step of graphite; **IV**, the MoS_2 domain locks on the step and the tip jump onto the MoS_2 surface. **b** MD computational setup. The dashed line marks the graphite step and the direction normal to the sliding direction (orange arrow). **c** Average friction force experienced by the MoS_2 flake as a function of the distance traveled. The **II**, **and III** tags mark the same stages as **a**.

Conclusions

In conclusion, we demonstrated that large lattice mismatch MoS_2/graphite and MoS_2/h-BN heterojunction interfaces provide ultralow coefficients of friction, ~10^{-6}, without any twist angle dependence. Both experiments and molecular dynamics calculations indicated that pinned edges and interface steps in MoS_2/graphite and MoS_2/h-BN heterojunctions dominate the friction process, whereas small lattice mismatch in graphene/h-BN results in a significant contribution to the interface friction. Our results show that the large lattice mismatch of two contact surfaces and absence of interface steps are key components to designing a near-frictionless sliding pair.

Methods

Sample preparation. MoS_2 domains were grown by three-temperature-zone chemical vapor deposition. S (Alfa Aesar, 99.9%, 4 g) and MoO_3 (Alfa Aesar, 99.999%, 50 mg) powders were used as sources, loaded separately in two inner tubes and placed at zone-I and Zone-II, respectively. Substrates were loaded in zone-III. During the growth, Ar/O_2 (gas flow rate: 75/3 sccm) was flowed as carrying gases and temperatures for the S-source, MoO_3-source and wafer substrate are 115 °C, 530 °C, and 930 °C, respectively. Graphite and h-BN substrates were mechanically exfoliated from HOPG, Graphenium graphite (*Manchester Nanomaterials*), and bulk h-BN in this experiment.

Plasma enhanced chemical vapor deposition (PECVD) growth of the graphene/h-BN

heterostructure. h-BN flakes were prepared by mechanical exfoliation of h-BN crystals onto 300-nm SiO_2/Si substrate by Scotch tape (3M). Before growth, the substrate was annealed in hydrogen at 400 °C for 30 min to remove tape residues. Subsequently, the epitaxial growth was carried out by PECVD at a substrate temperature of ~500 °C with pure CH_4 as the carbon source, and the gas pressure and plasma power were 0.2 torr and 100 W, respectively. The growth period was about 1.5h.

Sample characterizations. AFM measurements were performed on Asylum Research Cypher S with AC240TS-R3 and AC200TS-R3 tips. PL and Raman characterizations were performed in a Horiba Jobin Yvon LabRAM HR-Evolution Raman system. The laser wavelength was 532 nm. SAED was performed in a TEM (Philips CM200) operating at 200 kV. Please refer to the Supplementary Information for the characterization results.

Environment control and cantilever calibration. We placed Cypher S in a specialized glove box. Under dry N_2 conditions, O_2 and H_2O were below 0.5ppm; the pressure of the glove box was set to 4 mbar. During the experiment, the temperature inside the Cypher carbinet was 35±1 ℃. We used standard Sader's method to calibrate the cantilever in the vertical direction and a non-contact method for the lateral direction[34,35]. During our measurements, two types of silicon AFM tips (AC200TS-R3 and AC240TS-R3) with different spring constants were used. The velocity of the tips was 0.6μm/s. For more details, please see the Supplementary Note 2.

MD simulations. Crystal structures for MoS_2[36] and graphite[37] were retrieved from the Crystallography Open Database[38]. The unit cell of bulk MoS_2 was transformed into a monolayer structure by removing half of the atoms in the cell and adding 20 Å of vacuum along the direction perpendicular to the basal plane in order to avoid interactions between images. The structure was replicated in the *a* and *b* directions and triangular flakes with zigzag edges (ending with sulfur atoms) and varying sides were cut out. The flake structures were then optimized according to the Stillinger-Weber potential for MoS_2[30]. A bilayer graphene structure was obtained in a similar way and then optimized using the AIREBO description[31]. The flake structures were then placed on top of the substrates within an orthogonal cell and finally optimized via an energy minimization with the conjugate gradient method. The interlayer interactions were modeled using solely a Lennard-Jones potential. Since the parameterization available in literature[30] proved to be unsuitable for describing the stacking interaction of MoS_2

and graphene correctly, we refined the actual parameters using DFT calculations as a reference. More details about the procedure can be found elsewhere[32]. All structures were then thermalized at 300 K for 50 ps using a Nosé-Hoover thermostat[39,40]. In order to obtain results with statistical significance, ten independent runs were performed for each setup by initializing the atomic velocities to the target temperature with different seeds for the random number generator. After this, sliding simulations of 2 ns were carried out by imposing a constant speed of 1 m/s to three atoms (whose relative positions were not allowed to change) within the top S layer and equidistant from the corners of the flake. In order to prevent the whole system from moving, the positions of the C atoms belonging to the bottommost graphene layer were tethered to their initial positions by applying harmonic potentials with a spring constant of 0.3 N/m. A verification of the validity of the results in the low-speed limit by means of quasistatic simulations is presented in the Supplementary Note 8. During sliding, a Nosé-Hoover thermostat set to 300 K and with a damping constant of 100 time units was coupled to all non-rigid atoms. For the flake atoms, the temperature is computed after removing the velocity of the center of mass of the flake. Forces acting on the externally controlled group of atoms and along the sliding direction were stored and then averaged over the production trajectory. Final averages and standard deviations over the ten independent trajectories were then calculated and reported in the main text. For the simulations involving the graphitic step, in order to mimic the AFM setup, the motion of the MoS_2 flake was obtained by imposing a constant speed to three atoms at the center of the flake edge opposite to the graphitic step. For all MD simulations a time step of 0.2 fs was employed. All calculations were carried out using the LAMMPS package[41]. The schematics of the computational setup in Figs. 4 and 5 were obtained using the VMD software[42].

Acknowledgments

G.Z. thanks the supports from NSFC (No. 11834017 and 61888102), the Strategic Priority Research Program of CAS (No. XDB30000000), the Key Research Program of Frontier Sciences of CAS (No. QYZDB-SSW-SLH004), and the National Key R&D program (No. 2016YFA0300904). M.L. thanks the supports from ESI Fund, OPR DE International Mobility of Researchers MSCA-IF III at CTU in Prague (No: CZ.02.2.69/0.0/0.0/20_079/0017983). D.S. is supported by NSFC (Nos. 51572289 and 61734001). K.W. and T.T. acknowledge support from the Elemental Strategy Initiative

conducted by the MEXT, Japan, A3 Foresight by JSPS and the CREST (JPMJCR15F3), JST. M.L., P.N. and T.P. acknowledge support from the project Novel nanostructures for engineering applications CZ.02.1.01/0.0/0.0/16_026/0008396. This work was supported by The Ministry of Education, Youth and Sports from the Large Infrastructures for Research, Experimental Development and Innovations project „e-Infrastructure CZ – LM2018140“. T.P., V.E.P.C. and A.S. acknowledge support from the European Union's Horizon2020 research and innovation program under grant agreement No. 721642: SOLUTION. The data and materials are available from the corresponding authors upon request. The authors acknowledge the use of the IRIDIS High Performance Computing Facility, and associated support services at the University of Southampton, in the completion of this work.

Author contributions

Guangyu Zhang supervises the research; Mengzhou Liao performed the AFM measurements and data analysis; Luojun Du, Jiaohao Yuan, ShuoPei Wang and Hua Yu performed the sample growth, TEM and spectroscopic characterizations; Jian Tang and Lin Gu performed TEM measurement; Kenji Watanabe and Takashi Taniguchi offered BN flakes; Paolo Nicolini, Victor E. P. Claerbout and Andrea Silva performed the MD simulations; Mengzhou Liao, Paolo Nicolini and Guangyu Zhang wrote, and all authors commented on the manuscript.

References

1 Holmberg, K., Andersson, P. & Erdemir, A. Global energy consumption due to friction in passenger cars. *Tribol Int* **47**, 221-234, (2012).
2 Holmberg, K. & Erdemir, A. Influence of tribology on global energy consumption, costs and emissions. *Friction* **5**, 263-284, (2017).
3 Shinjo, K. & Hirano, M. Dynamics of Friction - Superlubric State. *Surf Sci* **283**, 473-478, (1993).
4 Geim, A. K. & Grigorieva, I. V. Van der Waals heterostructures. *Nature* **499**, 419-425, (2013).
5 Dienwiebel, M. *et al.* Superlubricity of graphite. *Phys Rev Lett* **92**, 126101, (2004).
6 Zheng, Q. *et al.* Self-retracting motion of graphite microflakes. *Phys Rev Lett* **100**, 067205, (2008).
7 Li, H. *et al.* Superlubricity between MoS2 Monolayers. *Adv Mater* **29**, 1701474-n/a, (2017).
8 Filippov, A. E., Dienwiebel, M., Frenken, J. W., Klafter, J. & Urbakh, M. Torque and twist against superlubricity. *Phys Rev Lett* **100**, 046102, (2008).
9 Ribeiro-Palau, R. *et al.* Twistable electronics with dynamically rotatable heterostructures. *Science* **361**, 690-693, (2018).
10 Song, Y. *et al.* Robust microscale superlubricity in graphite/hexagonal boron nitride layered heterojunctions. *Nature Materials* **17**, 894-899, (2018).
11 Wang, D. *et al.* Thermally Induced Graphene Rotation on Hexagonal Boron Nitride. *Phys Rev Lett* **116**, 126101, (2016).

12 Leven, I., Krepel, D., Shemesh, O. & Hod, O. Robust Superlubricity in Graphene/h-BN Heterojunctions. *The Journal of Physical Chemistry Letters* **4**, 115-120, (2013).

13 Mandelli, D., Leven, I., Hod, O. & Urbakh, M. Sliding friction of graphene/hexagonal –boron nitride heterojunctions: a route to robust superlubricity. *Sci Rep-Uk* **7**, 10851, (2017).

14 Yu, H. *et al.* Precisely Aligned Monolayer MoS2 Epitaxially Grown on h-BN basal Plane. *Small* **13**, 1603005-n/a, (2017).

15 Du, L. J. *et al.* Modulating PL and electronic structures of MoS2/graphene heterostructures via interlayer twisting angle. *Applied Physics Letters* **111**, (2017).

16 Yang, W. *et al.* Epitaxial growth of single-domain graphene on hexagonal boron nitride. *Nature Materials* **12**, 792, (2013).

17 Radisavljevic, B., Radenovic, A., Brivio, J., Giacometti, V. & Kis, A. Single-layer MoS2 transistors. *Nat Nanotechnol* **6**, 147-150, (2011).

18 Liao, M. *et al.* Twist angle-dependent conductivities across MoS2/graphene heterojunctions. *Nature Communications* **9**, 4068, (2018).

19 Müser, M. H. in *Fundamentals of Friction and Wear on the Nanoscale NanoScience and Technology* (eds Enrico Gnecco & Ernst Meyer) Ch. Chapter 11, 209-232 (Springer International Publishing, 2015).

20 Li, B. *et al.* Probing van der Waals interactions at two-dimensional heterointerfaces. *Nature Nanotechnology*, (2019).

21 Martin, J. M., Donnet, C., Lemogne, T. & Epicier, T. Superlubricity of Molybdenum-Disulfide. *Physical Review B* **48**, 10583-10586, (1993).

22 Berman, D., Deshmukh, S. A., Sankaranarayanan, S. K., Erdemir, A. & Sumant, A. V. Friction. Macroscale superlubricity enabled by graphene nanoscroll formation. *Science* **348**, 1118-1122, (2015).

23 Dietzel, D., Feldmann, M., Schwarz, U. D., Fuchs, H. & Schirmeisen, A. Scaling laws of structural lubricity. *Phys Rev Lett* **111**, 235502, (2013).

24 de Wijn, A. S. (In)commensurability, scaling, and multiplicity of friction in nanocrystals and application to gold nanocrystals on graphite. *Physical Review B* **86**, 085429, (2012).

25 Muser, M. H., Wenning, L. & Robbins, M. O. Simple microscopic theory of Amontons's laws for static friction. *Phys Rev Lett* **86**, 1295-1298, (2001).

26 Yankowitz, M. *et al.* Emergence of superlattice Dirac points in graphene on hexagonal boron nitride. *Nature Physics* **8**, 382, (2012).

27 Wang, E. *et al.* Gaps induced by inversion symmetry breaking and second-generation Dirac cones in graphene/hexagonal boron nitride. *Nature Physics* **12**, 1111, (2016).

28 Gao, W. & Tkatchenko, A. Sliding Mechanisms in Multilayered Hexagonal Boron Nitride and Graphene: The Effects of Directionality, Thickness, and Sliding Constraints. *Physical Review Letters* **114**, 096101, (2015).

29 Mandelli, D., Ouyang, W., Urbakh, M. & Hod, O. The Princess and the Nanoscale Pea: Long-Range Penetration of Surface Distortions into Layered Materials Stacks. *Acs Nano* **13**, 7603-7609, (2019).

30 Ding, Z. W., Pei, Q. X., Jiang, J. W., Huang, W. X. & Zhang, Y. W. Interfacial thermal conductance in graphene/MoS2 heterostructures. *Carbon* **96**, 888-896, (2016).

31 Brenner, D. W. *et al.* A second-generation reactive empirical bond order (REBO) potential energy expression for hydrocarbons. *J Phys-Condens Mat* **14**, 783-802, (2002).

32 Silva, A., Claerbout, V. E. P., Polcar, T., Kramer, D. & Nicolini, P. Exploring the Stability of Twisted van der Waals Heterostructures. *Acs Appl Mater Inter*, (2020).

33 Chen, Z., Khajeh, A., Martini, A. & Kim, S. H. Chemical and physical origins of friction on surfaces with atomic steps. *Sci Adv* **5**, eaaw0513, (2019).

34 Sader, J. E., Chon, J. W. M. & Mulvaney, P. Calibration of rectangular atomic force microscope cantilevers. *Rev Sci Instrum* **70**, 3967-3969, (1999).

35 Wagner, K., Cheng, P. & Vezenov, D. Noncontact method for calibration of lateral forces in scanning force microscopy. *Langmuir* **27**, 4635-4644, (2011).

36 Schonfeld, B., Huang, J. J. & Moss, S. C. Anisotropic Mean-Square Displacements (Msd) in Single-Crystals of 2h-Mos2 and 3r-Mos2. *Acta Crystallogr B* **39**, 404-407, (1983).

37 Zemann, J. Crystal structures, 2nd edition. Vol. 1 by R. W. G. Wyckoff. *Acta Crystallographica* **18**, 139-139, (1965).

38 Grazulis, S. *et al.* Crystallography Open Database (COD): an open-access collection of crystal

structures and platform for world-wide collaboration. *Nucleic Acids Res* **40**, D420-D427, (2012).

39 Nose, S. A Unified Formulation of the Constant Temperature Molecular-Dynamics Methods. *J Chem Phys* **81**, 511-519, (1984).

40 Hoover, W. G. Canonical Dynamics - Equilibrium Phase-Space Distributions. *Phys Rev A* **31**, 1695-1697, (1985).

41 Plimpton, S. Fast Parallel Algorithms for Short-Range Molecular-Dynamics. *J Comput Phys* **117**, 1-19, (1995).

42 Humphrey, W., Dalke, A. & Schulten, K. VMD: Visual molecular dynamics. *Journal of Molecular Graphics* **14**, 33-38, (1996).